Spin Control and Coherent Optics in Semiconductor Nanostructures

Dissertation

presented to the Faculty of Physics of the
TU Dortmund University, Germany,
in partial fulfillment of the requirements
for the degree of

Doktor rer. nat

by

Matthias Salewski

technische universität
dortmund

Dortmund, November 2017

Accepted by the Faculty of Physics of the TU Dortmund University, Germany.

Day of the oral examination: 8th December 2017

Examination board:
PD Dr. Ilya A. Akimov (primary reviewer)
Prof. Dr. Manfred Bayer (secondary reviewer)
Prof. Dr. Metin Tolan
Dr. Bärbel Siegmann

Contents

Motivation **1**

I Physical background **3**

1 Semiconductors **5**
1.1 Solid state basics . . . 5
1.1.1 Pauli exclusion principle . . . 6
1.1.2 Spin-orbit interaction . . . 6
1.1.3 Electronic band structure . . . 7
1.2 Nanostructures . . . 9
1.2.1 Quantum wells . . . 10
1.2.2 Quantum dots . . . 12
1.3 Light-matter interaction . . . 13
1.3.1 Photon polarization . . . 13
1.3.2 Optical orientation . . . 15
1.3.3 Magneto-optical effects . . . 16
1.4 Electronic excitations . . . 17
1.4.1 Exciton complexes . . . 17
1.4.2 Exciton interaction with optical fields . . . 19

2 Coherent optical phenomena **21**
2.1 Independent two-level system . . . 21
2.1.1 Optical Bloch equations . . . 21
2.1.2 Density matrix formalism . . . 23
2.2 Four-wave mixing . . . 24
2.2.1 Photon echo . . . 25
2.2.2 Double-sided Feynman diagrams . . . 27
2.2.3 Two-dimensional Fourier transform spectroscopy . . . 27
2.3 Coherent spectroscopy of semiconductor nanostructures . . . 29
2.3.1 Photon echo timing sequence . . . 30
2.3.2 Microcavity systems . . . 30
2.3.3 Spin degree of freedom . . . 31

3 Spin physics and ferromagnetism 33
3.1 Spin physics in semiconductors . . . 33
3.1.1 Spin relaxation . . . 33
3.1.2 Zeeman effect . . . 34
3.1.3 Hanle effect . . . 35
3.2 Ferromagnetism . . . 35
3.2.1 Magnetic interactions . . . 35
3.2.2 Hysteresis loop . . . 37
3.2.3 Magnons and phonons . . . 37
3.3 Combining semiconductors with magnetic materials . . . 38

4 Experimental methods 41
4.1 Laser and magnet cryostat . . . 41
4.2 Photoluminescence spectroscopy . . . 42
4.2.1 Time-integrated photoluminescence . . . 42
4.2.2 Time-resolved photoluminescence . . . 44
4.3 Magneto-optical Kerr effect . . . 44
4.3.1 Time-resolved pump-probe spectroscopy . . . 44
4.3.2 Static magneto-optical characterization . . . 44
4.4 Four-wave mixing with heterodyne detection . . . 46

II Spin orientation in a ferromagnet-semiconductor hybrid 49

5 Long-range p-d exchange interaction in a Co-CdTe hybrid structure 51
5.1 The Co-CdTe hybrid samples . . . 51
5.2 Ferromagnet-induced photoluminescence circular polarization . . . 53
5.3 Ferromagnet-induced spin polarization of the quantum well heavy holes . 55
5.4 Origin of ferromagnet-induced photoluminescence circular polarization . . 58
5.4.1 Magnetic circular dichroism . . . 58
5.4.2 Ferromagnetic stray fields . . . 59
5.4.3 Spin-dependent capture . . . 60
5.4.4 Role of p-d exchange interaction . . . 61
5.4.5 Diffusion of magnetic atoms or cluster formation . . . 62
5.4.6 Resonant tunneling through deep centers in the (Cd,Mg)Te spacer 63
5.5 Magnetization curve of the ferromagnetic Co thin film . . . 63
5.6 Evaluation of the p-d exchange interaction . . . 65
5.7 Elliptically polarized phonons as origin of the long-range p-d exchange . . 67
5.8 Conclusions . . . 69

III Coherent dynamics of optical excitations 71

6 Rabi oscillations from excitons in (In,Ga)As quantum dots 73
6.1 The (In,Ga)As quantum dot samples . . . 73
6.1.1 Tamm-plasmon microcavity . . . 73
6.1.2 Distributed Bragg reflector microcavity . . . 75
6.2 Enhanced light-matter interaction inside low-Q microcavities . . . 76
6.2.1 Rabi oscillations induced by the rephasing pulse . . . 77
6.2.2 Coherent dynamics . . . 80
6.2.3 Time-resolved photoluminescence . . . 81
6.3 Inhomogenity effects on the photon echo transients . . . 83
6.3.1 Rabi oscillations induced by the initial rotation pulse . . . 83
6.3.2 Theoretical description . . . 85
6.3.3 Simulated two-dimensional Fourier transform spectroscopy . . . 88
6.4 Conclusions . . . 88

7 High resolution spectroscopy of electron spins in a CdTe quantum well 91
7.1 Four-level system with electron ground state . . . 91
7.1.1 Selection rules . . . 91
7.1.2 Hamiltonian . . . 92
7.2 Theory of the three pulse photon echo . . . 94
7.2.1 Temporal evolution of the density matrix . . . 94
7.2.2 Two-dimensional rephasing spectra . . . 98
7.2.3 Two-dimensional Raman coherence spectra . . . 99
7.3 Experimental results . . . 100
7.3.1 The CdTe/(Cd,Mg)Te quantum well sample . . . 101
7.3.2 Coherent optical spectroscopy in zero magnetic field . . . 102
7.3.3 Coherent optical spectroscopy in a transverse magnetic field . . . 104
7.3.4 Pump-pobe spectroscopy in a transverse magnetic field . . . 107
7.4 Conclusions . . . 109

8 Summary and outlook 111

Bibliography 115

List of figures 136

List of publications 137

Conference contributions 139

Acknowledgments 141

Motivation

The methods and ideas that led to this work trace back to the fundamental studies of light and, as an early milestone, Maxwell's prediction of an electromagnetic wave in 1865 [Max65]. Later, at the turn of the century, Planck and Einstein showed that nature is composed of discrete energy packets, and that this quantization is inherent in light and matter [Pla01, Ein05]. It took more than 25 years in order to develop a self-consistent interpretation that takes the paradox of the wave-particle dualism into account. Its revolutionary statement: probability exists not only due to a lack of knowledge but it is, in the form of the quantum mechanical wave function, an entity of nature. Thus, quantum physics provides not only the mechanical conception of nature at the smallest scales but influences general philosophical thinking and human knowledge [Boh58, Hei79].

Some of the numerous research areas developed since the early days of atomic physics are devoted to semiconductors in their various forms. Until now, they enabled significant technological breakthroughs such as the transistor in modern electronics (Nobel prize 1956), the charged-coupled device (CCD) in digital photography (Nobel prize 2009), heterostructure lasers and integrated circuits (Nobel prize 2000), or light-emitting diodes (Nobel prize 2014). Nowadays funding of basic research is often driven by the constant miniaturization of processors and the strive for quantum information technologies [Bou00]. In a quantum computer the classical bit (0 and 1) is substituted by a two-level system ($|0\rangle$ and $|1\rangle$) whose wave function is a superposition (linear combination) of the two eigenstates. A memory composed of n entangled *qubits* could be used to store 2^n numbers at once, leading to a tremendous increase of the performance of mathematical operations that cannot be achieved in existing technologies. Furthermore, while currently energy dissipation and the associated heating are major limiting factors for technological progress, these detrimental effects are largely suppressed in the *coherent* regime. Coherence is the phase difference between the oscillators associated with the eigenstates $|0\rangle$ and $|1\rangle$ that is existing in a superposition state. One of the many approaches for implementing a qubit exploits the charge or spin of electrons (and/or holes) in semiconductor quantum dots [Bay02]. Considerations as to whether spins can play a role beyond magnetic storage are extensively discussed in the research field of *spintronics* [Aws02]. If, e.g., semiconductors (whose electrical and optical properties can be tailored almost arbitrarily) could be also rendered magnetic, all-in-one-chip solutions for information processing could become possible.

The materials studied for this thesis are semiconductor quantum dots and wells, also

combined with ferromagnetic or plasmonic metals to hybrids. Two focus areas can be defined. The first one deals with the magnetic manipulation of spins inside a novel spintronic device (Ch. 5). Special attention is devoted to the exchange interaction between carrier spins in a semiconductor and magnetic ions in a nearby ferromagnet. The second area is about the storage of optical information, i.e., conversion of the optical field into a material excitation, storing this excitation, and its release after a controllable time delay. The strong oscillator strength of optical resonances in semiconductors is inevitably linked to a short lifetime of the excitation and, therefore, a short optical memory. Inhomogoneous broadening of the optical oscillators shortens the storage time even more. This obstacle can be overcome by echo techniques that allow one to recover the information as long as the *coherence* of the individual absorber is preserved. Coherence and its loss with the excitation field is extensively studied in quantum dots that are embedded in microcavity structures (Ch. 6). In previous works by *Langer et al.* it was shown that the information stored in the optical field can be transferred to the spin system, where it is decoupled from the optical vacuum field and may persist much longer [Lan12, Lan14]. The approach can be used to measure the spin dynamics of carriers in the ground state without creating a macroscopic spin polarization, as in conventional pump-probe experiments using a circularly polarized pump pulse (Ch. 7). However, the comparison of both techniques allows for fundamental studies of the spin ensemble with unique insights into local relaxation processes.

The thesis starts with an introductory part I providing general concepts of semiconductors, coherent optical pehenomena, spin physics, and magnetism. Also, it contains an overview of the experimental methods that were used in part II on a ferromagnet-semiconductor hybrid structure and part III on coherent optical excitations. Driven by the hope to contribute in some form to novel future technologies the present thesis exists simply for the sake of science, which is a good thing by itself.

Part I

Physical background

Chapter 1

Semiconductors

As implied by its name, a semiconductor combines at once properties from a metal and an insulator. While being insulating at low temperatures near $T = 0\,\mathrm{K}$ it becomes conducting for a certain temperature $T = E_\mathrm{g}/k_\mathrm{B}$ which lies below its melting point. k_B is the Boltzmann constant and E_g is the band gap energy that separates the lattice electrons from reaching a conducting state. Section 1.1 will introduce the electronic band structure arising in a crystal with the focus on semiconductor materials from the binary compounds of groups II-VI and III-V. Interesting properties arise from structures with reduced dimensionality, as outlined in Sec. 1.2. Light-matter interaction and electronic excitations in semiconductors will be discussed in the final two sections of this chapter.

1.1 Solid state basics

The electronic properties of semiconductors arise from single atoms that arrange in a crystal lattice. As our starting point, we recapitulate the fundamental atomic quantum numbers from quantum mechanics [Boh51]:

(i) $n = 1, 2, 3, ...$ is the principle quantum number describing the shell of the atom.

(ii) $l = 0, 1, 2, ..., n-1$ is the angular momentum quantum number describing the atomic orbitals (s, p, d,...). It results from the eigenvalue $\hbar^2 l(l+1)$ of the orbital momentum quantum operator $\hat{\boldsymbol{l}}^2 = \hat{\boldsymbol{l}}_x^2 + \hat{\boldsymbol{l}}_y^2 + \hat{\boldsymbol{l}}_z^2$. $\hbar$ is the reduced Planck constant.

(iii) $s = 1/2$ is the pure quantum intrinsic angular momentum of the electron called spin. It results from the eigenvalue $\hbar^2 s(s+1)$ of the spin operator $\hat{\boldsymbol{s}}^2 = \hat{\boldsymbol{s}}_x^2 + \hat{\boldsymbol{s}}_y^2 + \hat{\boldsymbol{s}}_z^2$.

Apart of $\hat{\boldsymbol{l}}^2$ and $\hat{\boldsymbol{s}}^2$ one can measure one of the operator components along a specified quantization axis, e.g., the z-axis with its eigenvalues in units of $\hbar$ reading $l_z = -l, -l+1, ..., l-1, l$, and $s_z = -1/2$ (spin down $\downarrow$) or $s_z = +1/2$ (spin up $\uparrow$), respectively.

In multi-electron systems, angular momenta of several electrons experience so-called *Russell-Saunders coupling* that leads to the total orbital quantum number L and total

spin quantum number S, i.e. [Stö06]

$$\hat{\boldsymbol{L}} = \sum_i \hat{\boldsymbol{l}}_i, \qquad \hat{\boldsymbol{S}} = \sum_i \hat{\boldsymbol{s}}_i. \tag{1.1}$$

Consequently, eigenvalues of the operator projections on the z-axis are called L_z and S_z, respectively, and have the unit $\hbar$.

1.1.1 Pauli exclusion principle

Let us consider the interaction between two electrons with spin wave function $|\uparrow\rangle$ or $|\downarrow\rangle$. Electrons are *fermions* with the property that the total wave function has to be *antisymmetric* with respect to the interchange of coordinates and spins. This can be achieved in two ways. Either the spatial part is symmetric and the spin part is antisymmetric or vice versa. Two cases have to be distinguished for the two electron-system. (i) The spins are pointing in opposite directions, i.e. $S = 0$, $S_z = 0$. The spin part of the total wave function is then the antisymmetric *singlet state*

$$\frac{1}{\sqrt{2}} \left(|\uparrow\downarrow\rangle - |\downarrow\uparrow\rangle \right). \tag{1.2}$$

(ii) For parallel spin orientation, i.e. $S = 1$, $S_z = 1{,}0, -1$, the spin function is the symmetric *triplet state*

$$|\uparrow\uparrow\rangle\,, \qquad \frac{1}{\sqrt{2}} \left(|\uparrow\downarrow\rangle + |\downarrow\uparrow\rangle \right), \qquad \text{and } |\downarrow\downarrow\rangle\,. \tag{1.3}$$

The antisymmetrization postulate for fermions is expressed in the *Pauli exclusion principle*, stating that two electrons cannot be in identical states, i.e., have identical quantum numbers.

1.1.2 Spin-orbit interaction

The coupling of momenta in systems with many electrons does not only lead to Eqs. (1.1), but *spin-orbit interaction* is giving rise to a total angular momentum operator

$$\hat{\boldsymbol{J}} = \hat{\boldsymbol{L}} + \hat{\boldsymbol{S}}. \tag{1.4}$$

The eigenvalues of $\hat{\boldsymbol{J}}^2$ and $\hat{\boldsymbol{J}}_z$ are accordingly J and $J_z = m\hbar$, respectively. In this notation we introduced the *magnetic quantum number* $m = -J, -J+1, ..., J-1, J$, because $\hat{\boldsymbol{J}}$ is associated with a magnetic moment $\hat{\boldsymbol{m}}$ whose expectation value measured along the z-axis is

$$\langle \hat{\boldsymbol{m}}_z \rangle = -\mu_\mathrm{B} \frac{g_\mathrm{e} J_z}{\hbar}. \tag{1.5}$$

Here, g_e is the *Landé g factor* of the electron and $\mu_\mathrm{B} = e\hbar/(2m_\mathrm{e}) = 5.788 \cdot 10^{-5}\,\mathrm{eV/T}$ is called Bohr magneton (e is the elemental charge and m_e is the electron mass). From the electron point of view, the charged nucleus moves around the electron and creates an

effective magnetic field that interacts with the electron spin. The field strongly increases with the number of protons in the nucleus as $\propto Z^2$. Spin-orbit interaction leads to a fine structure in atomic spectra and has many consequences in solid state physics. It contributes significantly to the band structure of semiconductors (Sec. 1.1.3) and enables the optical orientation and detection of electron spins (Sec. 1.3.2). In magnetic solids it is the main reason for magnetocrystalline anisotropy (Sec. 3.1.2).

1.1.3 Electronic band structure

Consider a single atom of the group IV semiconductor germanium with electron configuration $4s^2 4p^2$: The atom aims to fill up its 4p orbital which has place for four more electrons. This can be achieved if the atom establishes covalent bonds with four other germanium atoms. These four atoms try themselves to fill up their 4p orbital and establish new bonds; and so on, until a crystal is created. As a result, the electronic energy structure changes and the atomic orbitals are replaced by filled bonding and empty anti-bonding states of the sp^3 hybrid orbitals for covalent binding [Fox10, Yu10]. This happens for each single Ge–Ge bond. However, the Pauli exclusion principle prevents that more than two electrons are existing in the same quantum state and thus, the degeneracy of bonding and anti-bonding states is lifted. In the limit of an infinite lattice energy bands arise - the p-type fully populated valence band and the s-type empty conduction band which are separated by the band gap energy E_g.

The creation of energy bands of the compound semiconductors studied in this thesis occurs in analogy to the one described for the elemental semiconductor germanium. Taking the III-V gallium arsenide (GaAs), the Ga atoms outer shell reads $4s^2 4p$ while for As it is $4s^2 4p^3$. In sum the number of valence electrons, i.e. those electrons from the not completely filled p orbital, is the same as if two germanium atoms bond to each other.[1] The same is true for II-VI cadmium tellurid (CdTe) with Cd electron configuration $4d^{10} 5s^2$ and Te $5s^2 5p^4$ although, in contrast to III-V semiconductors, the valence band contains also metal d-states from the Cd 4d orbital. They are, however, far away from the band gap and all valence band states relevant for this thesis are p-type [Wei88].

The characteristics of the energy bands can be better understood when considering the periodic nature of semiconductor crystals. For the sake of simplicity we discuss only CdTe, since the conclusions made are also true for (In,Ga)As. As shown in Fig. 1.1(a), CdTe crystallizes in the cubic zinc blende structure which consists of two relatively to each other shifted face-centered cubic lattices [Ash76, Kit04]. Each atom is surrounded by four nearest neighbors of the opposite kind of atom. The challenge is now to calculate the kinetic energy of the electrons traveling through this periodically arranged crystal. Due to their interaction with the lattice nuclei this kinetic energy is not just $1/2 m_\mathrm{e} v^2$, with velocity v, but the electron mass changes to an effective mass m_e^* which is strongly dependent on the electron's speed and direction of motion, i.e. magnitude and direction

[1] Note that this does not change if a fraction x of the group III Ga atoms is replaced by the same group Indium (In) atoms in order to form $\mathrm{In}_x\mathrm{Ga}_{1-x}\mathrm{As}$.

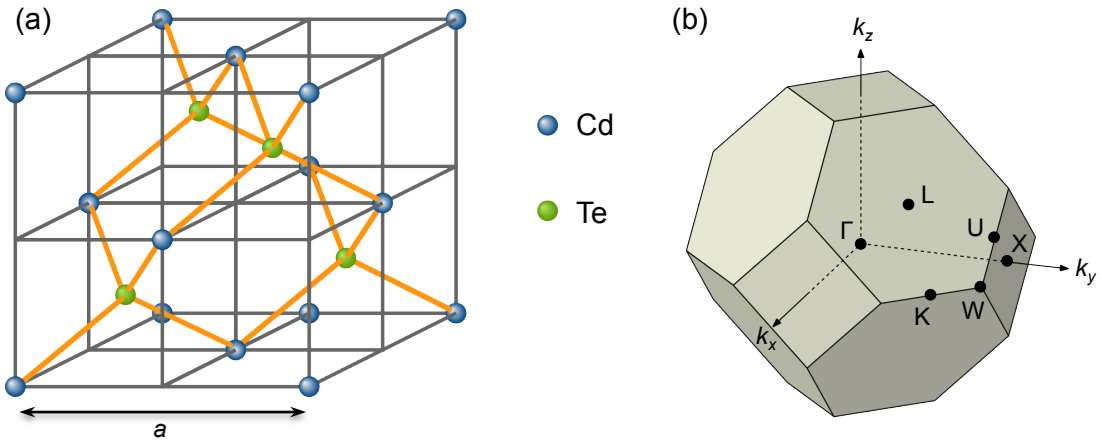

Figure 1.1: (a) Cubic zinc blende structure of CdTe in real space composed of two relatively to each other shifted face-centered cubic (fcc) lattices with $a \approx 0.64\,\text{nm}$ [Str12]. For cubic zinc blende GaAs the lattice parameter $a \approx 0.56\,\text{nm}$ [Str11]. (b) The first Brillouin zone of an fcc lattice, with the points of high symmetry labeled in k-space.

of $\boldsymbol{k}$ [Dav12]. Interesting are those directions in which the crystal looks the same after shifting it along the vector $\boldsymbol{R}$, i.e. $\exp(-i\boldsymbol{k}\cdot\boldsymbol{R}) = 1$. All wave vectors $\boldsymbol{k}$ that are satisfying this relation form the so called reciprocal lattice. The Wigner-Seitz cell of this lattice is called the first Brillouin zone. As seen from Fig. 1.1(b) this cell has points of high symmetry, e.g. the point of origin Γ, or the center of the big hexagonal face L and the small square face X. Now it is possible to plot the electron energy for these symmetry points which correspond to wave vectors $\boldsymbol{k}$ in the real crystal lattice. This representation known as dispersion relaxation is shown in Fig. 1.2 exemplary for CdTe. Note the two equivalent ways of how to read the x-axis: (i) Between Γ and any other symmetry point the wave vector of a well defined direction changes its magnitude $|\boldsymbol{k}|$, and (ii) between two points on the surface of the Brillouin zone the wave vector changes its direction. In Fig. 1.2(a) the bands at points of high symmetry are labeled by their irreducible representations in the double group notation of the T_d crystal symmetry [Yu10]. CdTe is a direct band gap semiconductor since the minimum of the conduction band and the maximum of the valence band are both located at the Γ point. Figure 1.2(b) shows a closeup around the Γ point and labels important nomenclatures. The s-type conduction band is twice degenerated in spin and its minimum is located at the band gap energy $E = E_\text{g}$. The maximum of the p-type valence band has $E = 0$ and consists of the heavy hole (hh) and light hole (lh) bands whose degeneracy is lifted for $\boldsymbol{k} \neq 0$. The split-off (so) band is separated by an energy distance Δ_so which is called the spin-orbit splitting. The values for CdTe as shown in Fig. 1.2 are $E_\text{g} = 1.59\,\text{eV}$ and $\Delta_\text{so} = 0.91\,\text{eV}$ [Cha72].

The wave functions describing the electron and hole states in the periodic potential of the crystal are given by Bloch waves [Blo28]

$$\psi_m(\boldsymbol{r},\boldsymbol{k}) = u_m(\boldsymbol{r})\mathrm{e}^{i\boldsymbol{k}\boldsymbol{r}}, \tag{1.6}$$

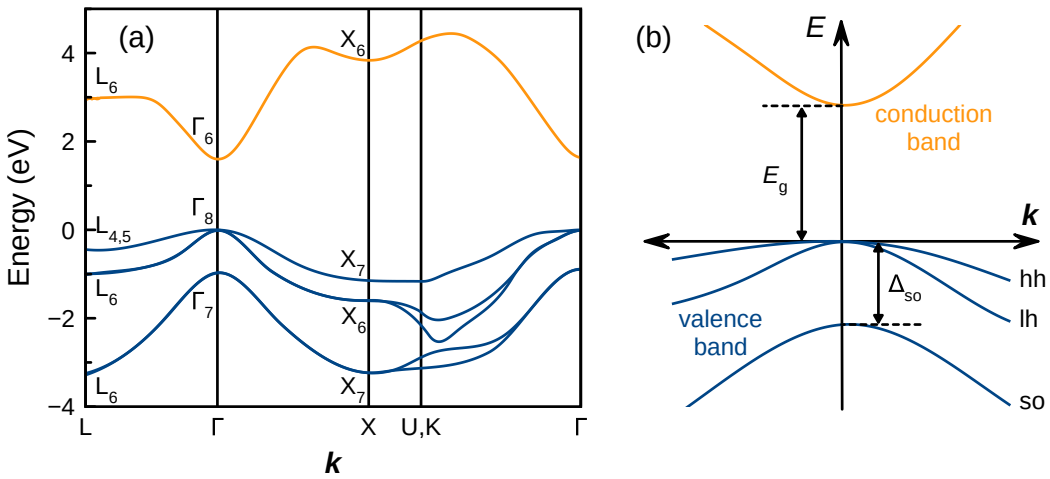

Figure 1.2: Electronic band structure of CdTe in the principle symmetry directions (a) and around the Γ point (b). Values for $T = 15\,\mathrm{K}$ adapted from [Cha72]. The minimum of the conduction band is separated by an energy gap $E_\mathrm{g} = 1.59\,\mathrm{eV}$ from the maximum of the valence Band. The heavy hole (hh) and light hole (lh) sub-bands are degenerate in energy for $\boldsymbol{k} = 0$, while the split-off sub-band is shifted by $\Delta_\mathrm{so} = 0.91\,\mathrm{eV}$.

where $u_m(\boldsymbol{r})$ are Bloch amplitudes which are invariant under the symmetry transformations of the crystal. For the conduction band the angular momentum $L = 0$ and spin $S = 1/2$, i.e. $J = 1/2$. The valence band has $L = 1$ and $S = 1/2$, so the total angular momentum has two possible values, $J = 1/2$ and $J = 3/2$. The $J = 3/2$ band consists of the heavy hole ($m = \pm 3/2$) and light hole bands ($m = \pm 1/2$) and $J = 1/2$ is the split-off band. The corresponding Bloch amplitudes can be found in Refs. [Dya84, Bas86]. In the vicinity of high symmetry points, Eq. (1.6) is a solution of the static Schrödinger equation with eigenenergies

$$E(\boldsymbol{k}) \sim \frac{\hbar^2 \boldsymbol{k}^2}{2m_\mathrm{e}^*}, \tag{1.7}$$

which differs from the dispersion relation of a free electron only in the substitution by an effective mass, i.e $m_\mathrm{e} \mapsto m_\mathrm{e}^*$. In Fig. 1.2(b) it is seen that Eq. (1.7) is a good approximation around $\boldsymbol{k} = 0$. Now it becomes also obvious that the light and heavy hole have their names from their different curvatures in the dispersion relation.

1.2 Nanostructures

The artificial production of semiconductors allows one to create structures in which the motion of electrons and holes is confined in one or more directions. Based on the Heisenberg uncertainty principle, the confinement of an electron to a region of the $\boldsymbol{z}$-axis with length Δz causes an uncertainty in its linear momentum $\Delta p_z \sim \hbar/\Delta z$. This uncertainty causes an additional kinetic energy $(\Delta p_z)^2/2m_\mathrm{e}^*$ which is significant if it

becomes greater than the kinetic energy of the particle due to its thermal motion $k_\mathrm{B}T/2$ [Fox10]. This relation can be transformed to

$$\Delta z \lesssim \sqrt{\frac{\hbar^2}{m_\mathrm{e}^* k_\mathrm{B} T}} \tag{1.8}$$

in order to estimate the scales at which quantum effects appear. With a typical electron effective mass $m_\mathrm{e}^* = 0.1 m_\mathrm{e}$ [Kli12a] it follows that $\Delta z \lesssim 5\,\mathrm{nm}$ at room temperature. The confinement is technologically realized by the growth of heterostructures that contain layers of different semiconductor materials. If their band gap energies E_g are different one can fabricate potential wells in which charge carriers are spatially confined. In this thesis so called type-I heterostructures are studied in which electrons and holes are located in the same layer. Their fabrication is mainly enabled by epitaxial deposition techniques, e.g. molecular beam epitaxy (MBE) [Her89]. In MBE processes atomic or molecular beams from different semiconductors are deposited on a monocrystalline substrate in an ultra-high vacuum chamber. The beams are created by high temperature evaporation on effusion cells behind mechanical shutters that allow one to tailor the composition of the constituents.

1.2.1 Quantum wells

A crystal with confinement in one dimension is called *quantum well* (QW). They are technologically realized by MBE growth of two semiconductor materials with comparable lattice constant a (mismatch $< 5\%$). In the non-confined plane the electron motion can be described by a Bloch wave. In order to consider confinement along the z-axis, Eq. (1.6) has to be multiplied with an envelope wave function $\phi_n(z)$ so that it reads

$$\psi_n(\boldsymbol{r},\boldsymbol{k}_\parallel) = u(\boldsymbol{r})\mathrm{e}^{i(k_x x + k_y y)} \cdot \phi_n(z). \tag{1.9}$$

The eigenergies of the system are given by

$$E(n,\boldsymbol{k}) = E_n + E(\boldsymbol{k}_\parallel). \tag{1.10}$$

$E(\boldsymbol{k}_\parallel)$ is known from Eq. (1.7) and E_n follows from the calculation of a wave function $\phi_n(z)$ in a potential well [Boh51]. For infinite potential wells the solution reads

$$E_n = \frac{\hbar^2}{2m^*}\left(\frac{n\pi}{d_\mathrm{QW}}\right)^2, \tag{1.11}$$

where d_QW is the width of the quantum well and $n = 1, 2, 3, ...$ Mind the different meaning of n with respect to the principle quantum number introduced in the beginning of Sec. 1.1. It becomes immediately clear that the degeneracy of the light and heavy hole for $\boldsymbol{k} = 0$ is in a QW structure lifted by $\hbar\omega_\mathrm{lh,hh}$ due to $m_\mathrm{lh}^* > m_\mathrm{hh}^*$. Moreover, a decrease in the QW thickness results in an increase of the confinement energy.

In the more realistic case of finite potential wells the wave functions $\phi_n(z)$ penetrate exponentially decaying into the barrier and there exist only a finite number of quantized

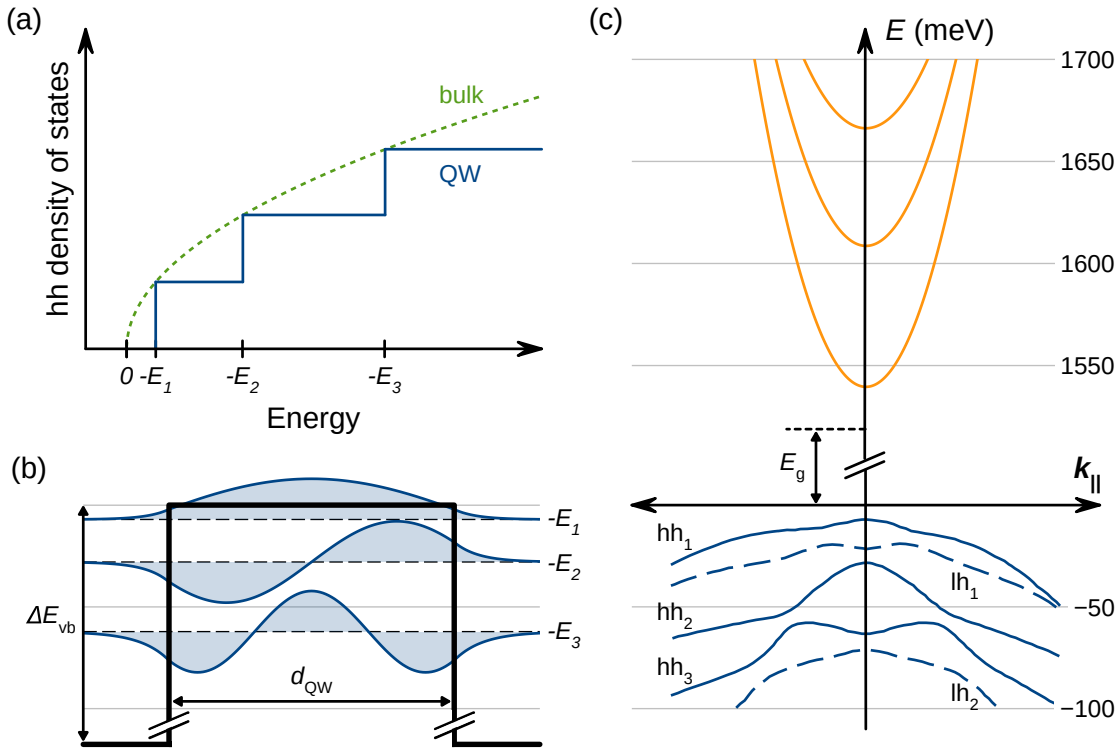

Figure 1.3: Electronic band structure of a GaAs/$Ga_{0.7}Al_{0.3}As$ quantum well (QW) with width $d_{QW} = 10\,nm$. (a) The density of states for the heavy hole (hh) band in a bulk and QW structure. (b) The first three hh wave functions $\phi_n(z)$ (n = 1,2,3) in the potential well of the valence band for $\boldsymbol{k}_{\parallel} = 0$. The decay constant in the barrier for hh_1 is $d_0 \approx 0.8\,nm$. (c) In-plane dispersion relation of the conduction (orange lines) and valence bands (blue lines) adapted from [Coh90]. The parameters for the calculations in (b) are: $E_g = 1519\,meV$, $\Delta E_{vb} = 142\,meV$, $m^*_{hh,GaAs} = 0.38m_e$, and $m^*_{hh,GaAlAs} = 0.4785m_e$.

states. Figure 1.3 shows calculations for a 10 nm wide GaAs/$Ga_{0.7}Al_{0.3}As$ QW. As a consequence of the quantization the density of states changes from the $E^{1/2}$ behavior in a bulk crystal to a step-like function in the QW, as shown in Fig. 1.3(a). Such a behavior can be observed in the absorption spectra of thin heterostructures with confinement effects [Din74]. Within the confining potential in Fig. 1.3(b) standing waves form at the quantization energies E_n. Using a $\boldsymbol{k} \cdot \boldsymbol{p}$ perturbation model [Wei91] Cohen and Marques (1990) calculated the in-plane dispersion relation for conduction and valence band which is shown in Fig. 1.3(c). Here, it is nicely seen that both bands are shifted away from the band edge of a bulk semiconductor which makes the QW emission energy for luminescence larger.

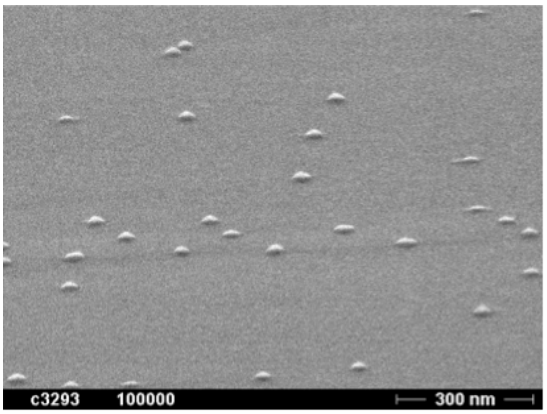

Figure 1.4: Scanning electron microscope (SEM) image of (In,Ga)As QDs on the surface of the wetting layer before the capping and annealing process. The QD density is about $2 \times 10^9\,\mathrm{cm}^{-2}$, and their height and lateral sizes before overgrowth are about 2.3 and 25 nm, respectively. The sample and the SEM image originate from the group of *Höfling*, Technische Universität Würzburg.

1.2.2 Quantum dots

Spatial confinement can be realized for up to three dimensions in order to create *quantum dots* (QDs). It is no surprise that the size reduction leads in the limit to the energy spectrum of a single atom. However, already 10^4–10^6 atoms in a typical QD of $\sim 10\,\mathrm{nm}$ size reveal discrete energy levels, i.e. [Bim99]

$$E = E(n_x,n_y,n_z). \tag{1.12}$$

This is the equivalent to Eq. (1.11) in three dimensions. Although the energy in Eq. (1.12) is no longer a function of the wave vector one should keep in mind that the atoms in a QD are arranged in a crystalline structure. Therefore, the electron and hole wave function

$$\psi_{n_x,n_y,n_z}(\boldsymbol{r}) = u(\boldsymbol{r}) \cdot \phi_{n_x,n_y,n_z}(\boldsymbol{r}) \tag{1.13}$$

contains a Bloch amplitude, $u(\boldsymbol{r})$, which allows one to refer the discrete energy levels in QDs to the energy band structure of a bulk crystal [Wog97]. However, due to valence band mixing hh and lh states are no longer single eigenstates and, e.g., spherical QDs have to be described in terms of molecular orbitals [Xia89].

The technique used for fabrication of the (In,Ga)As QDs studied in this thesis is based on self-organization during so called Stranski and Krastanow growth of strained heterostructures [Bra16]. Here, a thin layer of InAs, the so called "wetting layer", is grown on top of a thick GaAs buffer layer along the z-axis. The strong lattice mismatch, $a_{\mathrm{InAs}} = 1.07 a_{\mathrm{GaAs}}$, results in a strain that leads to the self-organized formation of InAs QDs on top of the wetting layer [Mar94]. They are typically of pyramidal shape with a width significantly larger than their height, as seen in the scanning electron microscope image in Fig. 1.4. Therefore, as well as in QWs, the z-axis is the main quantization axis and orbitals have to be considered only for the in-plane confinement of pyramidal QDs. Technical, the confinement of electrons and holes in all directions is realized when the dots are overgrown by a GaAs cap layer. An *in situ* annealing causes an inter-diffusion of Ga and In atoms resulting in a change of the QD's shape and a blue shift in its spectrum [Kos96]. Fluctuations in QD size, shape, and composition lead to a strong inhomogeneous broadening of the optical transitions.

1.3 Light-matter interaction

Most of the phenomena observed in the experiments performed for this thesis are based on unequal population of different states in semiconductor nanostructures. Often, these unequal populations are created using the photoexcitation of charge carriers. This section deals with the creation and detection of such populations in terms of light-matter interaction based on the polarization of the involved photons.

1.3.1 Photon polarization

Classically, light is a transverse electromagnetic wave which is described by synchronized oscillations of the magnetic and electric field vectors in Cartesian coordinates. One distinguishes between three basic geometrical orientations of these oscillations, i.e., right and left handed circular polarization ($\sigma^{\pm}$) with a circular motion of the $\boldsymbol{E}$-vector of the electromagnetic wave around the propagation axis, and linear polarization (π) with $\boldsymbol{E}$ oscillating in a single direction. The quantum mechanical particle equivalent of an electromagnetic wave is the *photon* which carries a spin orbital momentum with projection $L_z = \pm\hbar$ along the direction of its relativistic motion. However, it is possible to deduce all possible polarization states of the electromagnetic wave from two eigenstates when exploiting the spinor formalism for a quantum mechanically two-level system [Stö06].

In a two-level system every quantum mechanical state

$$|\Psi\rangle = \alpha\,|a\rangle + \beta\,|b\rangle \tag{1.14}$$

can be constructed from the two eigenvectors

$$|a\rangle = \begin{pmatrix} 1 \\ 0 \end{pmatrix} \quad \text{and} \quad |b\rangle = \begin{pmatrix} 0 \\ 1 \end{pmatrix}. \tag{1.15}$$

The complex coefficients α and β are the probability amplitudes of the eigenstates $|a\rangle$ and $|b\rangle$, respectively, and satisfy the normalization condition $|\alpha|^2+|\beta|^2 = 1$. It is possible to obtain a representation of Eq. (1.14) in Cartesian coordinates as

$$\boldsymbol{\mathcal{S}} = \begin{pmatrix} \langle\boldsymbol{\sigma}_x\rangle \\ \langle\boldsymbol{\sigma}_y\rangle \\ \langle\boldsymbol{\sigma}_z\rangle \end{pmatrix} = \begin{pmatrix} \alpha^*\beta + \beta^*\alpha \\ i[\beta^*\alpha - \alpha^*\beta] \\ \alpha^*\alpha - \beta^*\beta \end{pmatrix}, \tag{1.16}$$

with the help of the *Pauli spin matrices*

$$\boldsymbol{\sigma}_x = \begin{pmatrix} 0 & 1 \\ 1 & 0 \end{pmatrix}, \quad \boldsymbol{\sigma}_y = \begin{pmatrix} 0 & -i \\ i & 0 \end{pmatrix}, \quad \boldsymbol{\sigma}_z = \begin{pmatrix} 1 & 0 \\ 0 & -1 \end{pmatrix}, \tag{1.17}$$

and their expectation values $\langle\boldsymbol{\sigma}_i\rangle = \langle\Psi|\,\boldsymbol{\sigma}_i\,|\Psi\rangle$, where $i = x, y, z$. Without limiting the generality of the foregoing, the complex coefficients α and β can be expressed by two angles, i.e.,

$$\alpha = \cos\frac{\Theta}{2} \quad \text{and} \quad \beta = e^{i\varphi}\sin\frac{\Theta}{2} \quad \Rightarrow \quad \boldsymbol{\mathcal{S}} = \begin{pmatrix} \sin\Theta\cos\varphi \\ \sin\Theta\sin\varphi \\ \cos\Theta \end{pmatrix}. \tag{1.18}$$

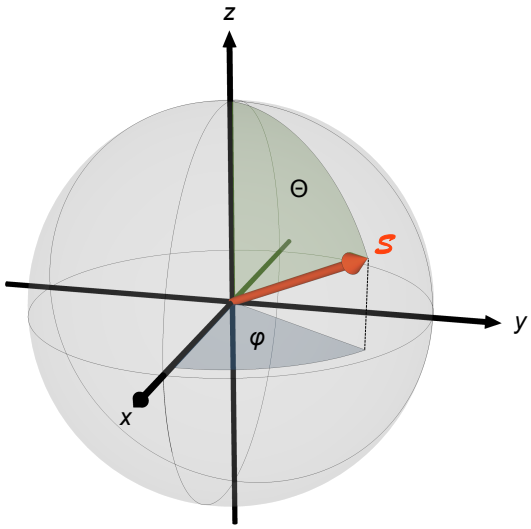

Figure 1.5: Three-dimensional representation of a quantum mechanical state $|\Psi\rangle$ in a two-level system according to Eqs. (1.14) and (1.18) in form of a spin polarization vector $\boldsymbol{\mathcal{S}}$.

Θ and the phase difference φ define the inclination and azimuth for the spin polarization vector $\boldsymbol{\mathcal{S}}$ in spherical coordinates, as demonstrated in Fig. 1.5. Now it is easily seen that the north and south pole of the sphere correspond each to one of the two eigenstates, while projections onto the x-y-plane correspond to coherent superpositions.

The object in Fig. 1.5 is called *Bloch sphere* for a quantum mechanical two-level system, e.g. the electron spin with eigenstates $|\uparrow\rangle$ and $|\downarrow\rangle$, and *Poincaré sphere* for the polarization states of a photon.[1] The north and south pole of the Poincaré sphere correspond to 100% circularly polarized light $\sigma^{\pm}$ with $L_z = \pm\hbar$, respectively. If $\boldsymbol{\mathcal{S}}$ is oriented parallel (anti-parallel) to the x-axis the light is 100% horizontally (vertically) linear polarized. In analogy, the y-axis corresponds to 45° tilted linear polarization. In the positive (negative) half sphere the polarization is right (left) handed elliptical. Note that $\boldsymbol{\mathcal{S}}$ is a vector in configurational space which should not be mixed with the real space orientation of the electric field $\boldsymbol{E}$.

The three elements of $\boldsymbol{\mathcal{S}}$ multiplied by the total beam intensity I and the degree of polarization ρ (with $0 \leq \rho \leq 1$) are known as *Stokes parameters*. Normalized on the intensity one measures, e.g., the degree of circular polarization

$$\rho_{\mathrm{c}} = \frac{I_+ - I_-}{I_+ + I_-}, \tag{1.19}$$

where I_+ and I_- are the intensities of right and left circular polarized radiation. The degrees of linear polarization, ρ_π and $\rho_{\pi'}$ for a 45° tilted basis, are measured accordingly.

[1] In the latter case the two angles in Eq. (1.18) are typically substituted by $2\psi = \varphi$ and $2\chi = 90° - \Theta$. The reason for the factor of 2 is that the two circularly polarized photon basis states are orthogonal (90°), while for electron spins the two basis states include an angle of 180° [Stö06].

1.3.2 Optical orientation

When studying the absorption of photons in semiconductors one has to consider that the basic conservation laws of physics are not only about energy but also linear and angular momentum. While the linear momentum is rather small and can be neglected, the spin angular momentum is of significant importance.[1] The absorption of a circularly polarized photon with spin angular momentum projection $L_z = \pm\hbar$ requires a change in the electron angular momentum projection by $\pm\hbar$. In fact, due to spin-orbit interaction also the spins become oriented by the absorbed light [Per84].

The transition between a ground state with Bloch amplitude $|u_m\rangle$ and an excited state with $|u_{m'}\rangle$ can only be addressed if a dipole moment

$$\boldsymbol{d}_{mm'} = \langle u_m | \, \hat{\boldsymbol{d}} \, | u_{m'} \rangle \tag{1.20}$$

is existing, where $\hat{\boldsymbol{d}} = -e\hat{\boldsymbol{r}}$ is the dipole momentum operator with electron charge $-e$ and displacement operator $\hat{\boldsymbol{r}}$. One generally neglects the electric quadrupole and magnetic dipole interactions since they are smaller by the fine structure constant $\approx 1/137$. The dipole moments from Eq. (1.20) are shown in Refs. [Zak82, Dya84] for the interband transitions between the valence and conduction bands in cubic zinc blende crystals. Since in the nanostructures[2] studied for this thesis the transitions involving heavy hole states are of primary interest, we recall here the corresponding results. The Bloch amplitudes with quantization along the growth direction $\boldsymbol{z}$ read for the conduction band electrons

$$u_{+1/2} = S\uparrow, \qquad u_{-1/2} = S\downarrow, \tag{1.21}$$

and for the valence band heavy holes

$$u_{+3/2} = -\frac{1}{\sqrt{2}}(X + iY)\uparrow, \qquad u_{-3/2} = \frac{1}{\sqrt{2}}(X - iY)\downarrow. \tag{1.22}$$

S is a function with spherical symmetry $x^2 + y^2 + z^2 = 1$, and X,Y,Z are functions of the coordinates which transform as the coordinates under rotations. The arrows denote spin functions that are normalized and orthogonal for different spin directions. Thus, it is clear that $\langle u_{\pm 1/2} | \, \hat{\boldsymbol{d}} \, | u_{\mp 3/2} \rangle = 0$. The only matrix elements not equal to zero are

$$\boldsymbol{d}_+ \equiv \langle u_{+1/2} | \, \hat{\boldsymbol{d}} \, | u_{-3/2} \rangle \propto -\frac{1}{\sqrt{2}}(\boldsymbol{x} + i\boldsymbol{y}), \tag{1.23a}$$

$$\boldsymbol{d}_- \equiv \langle u_{-1/2} | \, \hat{\boldsymbol{d}} \, | u_{+3/2} \rangle \propto \frac{1}{\sqrt{2}}(\boldsymbol{x} - i\boldsymbol{y}), \tag{1.23b}$$

where $\boldsymbol{x}$ and $\boldsymbol{y}$ are unit vectors. The result shows that there are dipoles rotating clockwise and counterclockwise in the plane perpendicular to the quantization z-axis, as shown in Fig. 1.6. Correspondingly, they can be addressed by circularly polarized light, $\sigma^{\pm}$, with wave vector along the z-axis.

[1] In modern optics there is also an orbital angular momentum of light associated with the azimuthal phase of the complex electric field [Lea02]. However, it is not relevant for the optical orientation.

[2] An additional optical selection rule arises for structures with quantization effects: the conservation of the quantum number n, i.e. only transitions with $\Delta n = 0$ are allowed.

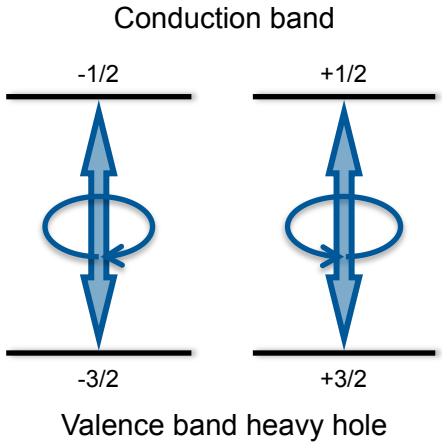

Figure 1.6: Dipole moments rotating in the plane perpendicular to the quantization z-axis for transitions between the heavy hole valence band and the conduction band that are. The energy states are labeled in accordance to the projection of the total angular momentum J_z in units of $\hbar$. The dipole moments can be optically addressed by circular polarized light $\sigma^{\pm}$ with its wave vector parallel to the z-axis.

Exemplary, we discuss the optical orientation in a semiconductor QW by absorption of left handed circularly polarized light (σ^-) whose energy corresponds to the first heavy hole-conduction band transition. According to Fig. 1.6, only dipole moments on the right hand side are addressed. Immediately after absorption the average electron spin along the quantization axis is $S_0 = +1/2$ (in units of $\hbar$). In order to equal in sum the spin momentum of the photon, the average total angular momentum projection of photocreated holes points into the opposite direction and has the value -3/2. Instead of the average electron spin S_0, one can express the initial degree of electron spin orientation

$$\mathcal{P}_0 = \frac{N_{+1/2} - N_{-1/2}}{N_{+1/2} + N_{-1/2}} = +100\%, \tag{1.24}$$

where $N_{\pm 1/2}$ is the number of electrons with spin $\pm 1/2$ [Par69, Par71]. Note that $\mathcal{P}_0 < 1$ for far above barrier excitation where the conduction band electrons lose their spin orientation much faster during thermalization to the band edge [Zak82]. By considering the recombination rates, the measured degree of circular polarization $\rho_c \propto \mathcal{P}_0^2$ [Par69]. An experimental study of electron spin optical orientation in GaAs QWs can be found in Ref. [Pfa05].

1.3.3 Magneto-optical effects

Light-matter interaction with linearly polarized light can be used to detect spin polarization in semiconductors or magnetization in ferromagnetic materials (Sec. 3.1.2). The knowledge about the rotation of polarized light after transmission, respectively reflection, traces back to the groundbreaking experiments of Faraday and Kerr in the 19th century [Far46, Ker77]. The phenomena result from the fact that the complex refractive index $\tilde{n}(\omega) = n(\omega) + i\kappa(\omega)$ and thus the real refractive index n and the extinction coefficient κ of a medium can differ for right and left circularly polarized light, when the medium is magnetized or spin polarized.

Magneto-optical effects can be described in terms of the formalism developed in Sec. 1.3.1. We consider a linear polarized beam, e.g., $\boldsymbol{\mathcal{S}}$ is parallel to the x-axis in Fig. 1.5.

The precession angle φ increases linearly with the light path through the sample if the *phase velocities* for right and left circularly polarized light are different. This effect is known as *magnetic-circular birefringence* and can be measured as a Kerr- of Faraday-rotation angle of the linear polarized light after interaction with the sample. Another effect is *magnetic-circular dichroism* which results from different *absorption* of right and left circular polarized light [Ste70]. In the frame of Fig. 1.5, $\boldsymbol{\mathcal{S}}$ moves into the direction of north or south pole and the polarization of the light becomes elliptically.

1.4 Electronic excitations

The strong light-matter interaction in semiconductors enables the creation of various electronic excitations that will be discussed in this section.

1.4.1 Exciton complexes

In Sec. 1.1.3 we have discussed energy bands that are completely filled by electrons and such, that are completely empty. Following the selection rules in Fig. 1.6, the absorption of a photon with energy $\hbar\omega > E_\mathrm{g}$ causes the "jump" of an electron from the valence band into the conduction band where it can move freely. Simultaneously, the electron leaves in the valence band an unoccupied state, called *hole*, which can move there freely as a *quasiparticle*.[1] Thus, photon absorption is always considered as the creation of an electron-hole pair from the crystal ground state which is defined as "vacuum" state $|0\rangle$. Since electrons and holes are oppositely charged particles they feel an attractive mutual Coulomb interaction. Due to their creation in the same moment at the same spot it is very likely that they will form a bound state $|\mathrm{X}\rangle$, *exciton*, with binding energies $-\mathrm{Ry}^*/n_\mathrm{B}^2$ [Kno63]. Here Ry^* is the exciton Rydberg energy and n_B is a principal quantum number in analogy to the hydrogen atom. Excitons were predicted by *Frenkel* [Fre31a, Fre31b] and first observed in a bulk crystal of copper oxcide (Cu_2O) by *Gross and Karryev* [Gro52a, Gro52b]. Due to its extremely large Rydberg energy, $\mathrm{Ry}^* \approx 90\,\mathrm{meV}$, excitons with principle quantum numbers as large as $n_\mathrm{B} = 25$ could be recently measured in Cu_2O [Kaz14]. Such highly excited excitons have giant wave functions of more than two micrometers distance between the electron and the hole. The Rydberg energies in the semiconductors studied for this thesis are much smaller (CdTe 12 meV and GaAs 4.2 meV) and thus, the observation of higher excited states is typically not or only hardly possible [Fox10, Kli12a]. The resulting excitons are called *Wannier-Mott type* with spatial dimensions that exceed the lattice constant a by more than 10 times for $n_\mathrm{B} = 1$ (cf. Fig. 1.1(a)). Optically allowed exciton states are given by the total angular momentum projection J_z of heavy holes and electrons and can be written as

$$|+1\rangle_z = |-1/2, +3/2\rangle \qquad \text{and} \qquad |-1\rangle_z = |+1/2, -3/2\rangle \tag{1.25}$$

[1] Elementary excitations in solids are called quasiparticles because they can only exist in matter and not in vacuum.

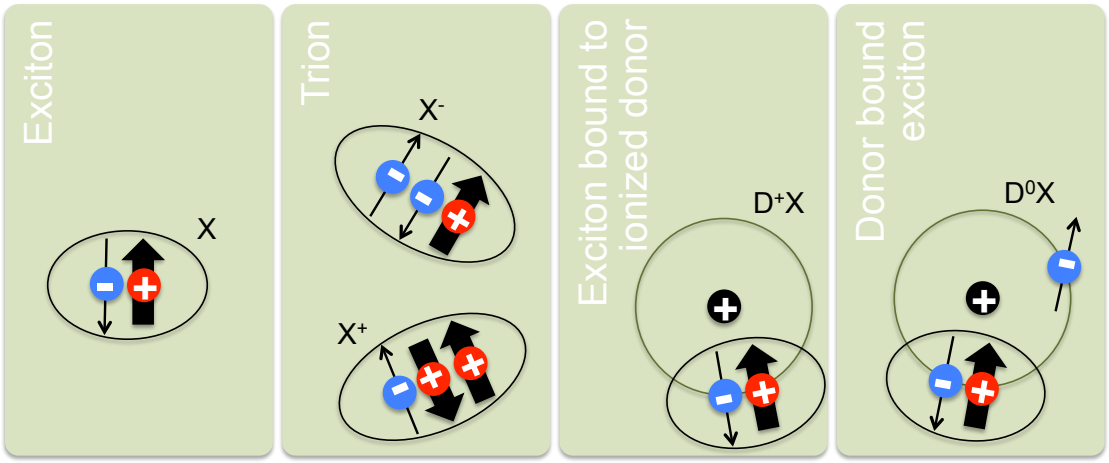

Figure 1.7: Most relevant excitations in semiconductors as discussed in the text. Electrons and holes are shown with their spins. For the case of an acceptor bound exciton, A^0X, the plus and minus signs in the D^0X picture have to be exchanged.

where $\boldsymbol{z}$ is the quantization axis. The states $|\pm 2\rangle_z = |\pm 1/2, \pm 3/2\rangle$ are called "dark" excitons because their dipole matrix elements with the ground state are zero (cf. Sec. 1.3.2).

The exciton binding energy in nanostructures increases while the exciton size given by the Bohr radius a_B^* decreases [Kli12a]. Moreover, the lifted degeneracy of the valence band at $\boldsymbol{k} = 0$ (cf. Sec. 1.2.1) causes a distinction between hh and lh excitons in QWs. Due to composition and well width fluctuations in the growth process of QWs, excitons can become localized at low temperature leading to an inhomogeneous broadening of the spectrum. For QDs it is important to distinguish whether their size is bigger or smaller than a_B^*. In the case of weak confinement Coulomb effects are dominating, while for strong confinement in very small QDs the quantization energy is much larger than the Coulomb energy [Sto10].

Further kinds of relevant semiconductor excitations are *excitons bound to shallow impurities*. They can appear when the crystal is doped, i.e., single atoms of the semiconductor lattice are substituted by atoms with one electron more (or less) in its outer shell. A neutral donor D^0 is a center with its energy level just below the conduction band. It can easily ionize by giving a free electron to the conduction band, i.e. $D^+ + e$ [Kli12a]. In analogy, neutral acceptors A^0 with their energy level just above the valence band can take an electron from it so that $A^- + h$ results. If excitons bind to these impurities they form D^0X (A^0X) and D^+X, respectively. A^-X is typically not excited since it is energetically more favorable to form a free electron and a neutral acceptor [Kli12b].

Third, we mention *trions* in semiconductors with reduced dimensionality. They can form due to slight (even unintentional) doping of the barriers from where donors and acceptors diffuse into the potential well region [Kli12a]. Excitons have then a high probability to bind an acceptor hole, X^+, or an donor electron, X^- [Khe93, Hau98]. Their

binding energy is larger than for a neutral exciton. Concerning total angular momentum, trions are indistinguishable from donor bound excitons. For example, the first excited state from X^- and D^0X is given by the hh total angular momentum $|\pm 3/2\rangle_z$ since the electron spins cancel each other out, as shown in Fig. 1.7. In the case of electron hole recombination the complexes return into their ground state given by a resident electron.

1.4.2 Exciton interaction with optical fields

Excitons in semiconductors are created by optical excitation. The physical properties of excitons are significantly influenced if the coupling to the optical field is strong, i.e., its energy spectra have to be described in terms of an additional quasiparticle called *exciton-polariton* [Kav08]. Efficient coupling at the nanoscale plays a decisive role for the realization of single photon emitters and other nonclassical light sources of importance in quantum information technologies [Lod15, Alb13]. Various structural concepts based on photonic crystals, patterned microcavities or plasmonic structures have been intensely studied in that respect [Ben11].

Another interesting system is a Tamm-plasmon (TP) resonator in which confinement of the optical field is obtained between a distributed Bragg reflector (DBR) and a thin metal layer, leading to the appearance of a TP photonic mode [Kal07]. In addition, TP structures support surface plasmon polaritons (SPPs), evanescent electromagnetic waves at the metal-semiconductor interface which can propagate along this interface. Thus, plasmonic structures allow one to overcome the diffraction limit of classical optics and enable the miniaturization of photonic circuits comparable to that achievable in electronics [Rae88]. Especially interesting in a TP resonator is the coupling between SPPs and TP cavity modes [Afi13, LG14, Azz16]. Therefore these structures are appealing for the generation of SPPs via optical or electrical pumping of a close active layer containing, e.g., semiconductor QDs. The integration of semiconductors into plasmonic structures is appealing for compensating losses in the metal [Gub17]. In plasmonic circuits the metal mirror may be used as an electrode to apply a bias voltage for controlling the charging state of the QDs or pumping the optically active layer electrically [Ges14]. As active material in the resonator single or multiple QW [Gro11, Sym13, Ges14, Seb15] or QD [Gaz11, Bra15, Gub17] layers as well as organic materials [Brü12, Che14] and single layers of transition metal dichalcogenides [Lun16] were used. So far, efforts have mainly been focused on time-integrated and time-resolved studies of the emission under non-resonant excitation. Thereby the Purcell effect of single QD excitons coupled to a localized TP mode [Gaz11], enhancement of the spontaneous emission [Bra15], and coherent laser emission [Sym13, Brü12] were demonstrated. Photoluminescence and coherent optical spectroscopy (Sec. 2.3.2) of QDs embedded into low-Q TP and DBR microcavities are the subjects of Ch. 6.

Chapter 2

Coherent optical phenomena

Immediately after photoexcitation by an ultrashort optical pulse the excitation in the semiconductor (electron-hole pair) has a well-defined phase relationship within itself and with the electromagnetic field that created it [Sha99]. The time during which this phase is preserved is called the *coherent regime*. This chapter gives an introduction to the concept of optical coherence in the independent two-level system. Ways to measure coherence even in inhomogeneously broadened ensembles of emitters will be discussed in the context of transient four-wave mixing. Huge possibilities arise in the field of optical spectroscopy, especially for energy systems with more than two levels.

2.1 Independent two-level system

Although the electronic states in a semiconductor are considerably more complicated than those in atoms, one can consider an exciton in the simplest approximation as an independent two-level system (TLS). In such a system the transition between the two eigenstates, $|0\rangle$ and $|1\rangle$, with energy

$$\hbar\Omega_0 = E_1 - E_0 \tag{2.1}$$

is unique and can be driven (nearly) resonantly by photon absorption. It allows one to create an individual quantum mechanical state which can be written as

$$|\Psi_j(t)\rangle = a_j(t)\,|0\rangle + b_j(t)\,|1\rangle\,, \tag{2.2}$$

where the complex coefficients $a_j(t)$ and $b_j(t)$ are the time-dependent probability amplitudes of being in the state $|0\rangle$ and $|1\rangle$, respectively. $|\Psi_j(t)\rangle$ can be expressed by a three-dimensional "pseudo" spin polarization vector $\boldsymbol{\mathcal{S}}$ in analogy to the spinor formalism in Sec. 1.3.1 [All75].

2.1.1 Optical Bloch equations

The basic dynamical equations of TLS are practically the same as those appropriate to spins in a magnetic field [Blo46]. Here, however, the field is not magnetic but results from

an electromagnetic wave traveling along the z-axis. It is convenient to use the *rotating wave approximation*, i.e., to describe the dynamics of the "pseudo" spin polarization vector $\boldsymbol{\mathcal{S}}$ in a frame rotating with the frequency of the light ω. The *optical Bloch equations* are then given by [All75]

$$\frac{\mathrm{d}}{\mathrm{d}t}\begin{pmatrix}\mathcal{S}_x\\ \mathcal{S}_y\\ \mathcal{S}_z\end{pmatrix} = \begin{pmatrix}\mathcal{S}_x\\ \mathcal{S}_y\\ \mathcal{S}_z\end{pmatrix} \times \begin{pmatrix}\chi(t)\\ 0\\ -\Delta\end{pmatrix} - \begin{pmatrix}\frac{1}{T_2} & & 0\\ & \frac{1}{T_2} & \\ 0 & & \frac{1}{T_1}\end{pmatrix}\begin{pmatrix}\mathcal{S}_x\\ \mathcal{S}_y\\ \mathcal{S}_z - \mathcal{S}_0\end{pmatrix}, \tag{2.3}$$

where $\chi(t)$ is the *Rabi frequency* resulting from the interaction of the system's dipole moment $\boldsymbol{d}_{01}$ with the external electromagnetic field $\boldsymbol{E}(t)$. $\Delta = \Omega_0 - \omega$ is the detuning of the transition frequency from the angular frequency of the light. For resonant excitation ($\Delta = 0$) the electromagnetic field rotates $\boldsymbol{\mathcal{S}}$ around the x-axis with the Rabi frequency $\chi(t)$. In the frame of Fig. 1.5 this motion changes the inclination angle Θ which reflects the physical entity

$$\Theta(\tau_\mathrm{p}) = \int_0^{\tau_\mathrm{p}} \chi(t)\mathrm{d}t, \tag{2.4}$$

called *pulse area*. τ_p is the the pulse duration which becomes $\to \infty$ for continuous wave. In absence of light ($\boldsymbol{E}(t) = 0$) $\boldsymbol{\mathcal{S}}$ rotates around the z-axis if the detuning $\Delta \neq 0$. If neither $\boldsymbol{E}(t) = 0$ nor $\Delta = 0$, the vector $\boldsymbol{\mathcal{S}}$ rotates around a vector lying in the x-z-plane with the *generalized Rabi frequency*

$$\tilde{\Omega} = \sqrt{\chi^2 + \Delta^2}. \tag{2.5}$$

Relaxation processes are in Eqs. (2.3) phenomenologically considered by two time constants: The longitudinal relaxation with T_1 corresponds to the lifetime of the population, and the transverse time T_2 is linked with the coherence.[1] The equilibrium state $(0, 0, \mathcal{S}_0)^T$ represents the ground state $|0\rangle$.

In the frame of Eqs. (1.18) the coherence decay with T_2 corresponds to a loss of the phase angle φ between the ground and excited states. The physical reason for this loss is twofold: due to recombination with T_1 and elastic scattering processes on the timescale τ_c, and can be summarized as [Kli12a]

$$\frac{1}{T_2} = \frac{1}{2T_1} + \frac{1}{\tau_c}. \tag{2.6}$$

The factor 2 comes from the conversion of polarization (electric field) to population (intensity).

In GaAs-like semiconductors scattering with polar optical phonons (Sec. 3.2.3) plays a major role in the dissipation of energy and momentum [Sha99]. Moreover, Coulomb interactions between electrons and/or holes can lead to scattering with other electronic excitations and scattering at impurities or lattice defects. Further scattering processes specific to QWs are inter-subband scattering, capture of carriers from the barriers into

[1] Transverse with respect to the (longitudinal) quantization z-axis. The designation comes from the description of spin dynamics in presence of an external magnetic field $\boldsymbol{B}$ along the z-axis [Blo46].

QWs, and real space transfer of carriers from QWs into the barriers. Taking many-body effects into account, the Eqs. (2.3) have to be replaced by the more complex *semiconductor Bloch equations* [Che01, Bal12]. However, the treatment as a TLS is sufficient for the study of localized excitons where many-body interactions are strongly suppressed [Nol90].

2.1.2 Density matrix formalism

Generally, the dynamics of a quantum state $|\Psi(t)\rangle$ follow from the Lindblad form of the Schrödinger equation $i\hbar\,|\dot{\Psi}(t)\rangle = \hat{\mathcal{H}}\,|\Psi(t)\rangle$, i.e.

$$i\hbar\dot{\rho} = [\hat{\mathcal{H}},\rho] + \Upsilon, \tag{2.7}$$

where $\hat{\mathcal{H}}$ is the Hamiltonian of the system, Υ describes relaxation processes with T_1 and T_2, and $\rho = |\Psi(t)\rangle\langle\Psi(t)|$ is the density matrix. For an ensemble of independent TLS $|\Psi_j(t)\rangle$ one can write

$$\rho = \begin{pmatrix} \rho_{00} & \rho_{01} \\ \rho_{10} & \rho_{11} \end{pmatrix} = \sum_j \xi_j \begin{pmatrix} |a_j(t)|^2 & a_j(t)b_j^*(t) \\ a_j^*(t)b_j(t) & |b_j(t)|^2 \end{pmatrix}, \tag{2.8}$$

where ξ_j is the fraction of the system with state vector $|\Psi_j(t)\rangle$. Diagonal elements correspond to population probabilities and off-diagonal elements indicate polarization. The latter describe dipole moments $\hat{\boldsymbol{d}}$ which oscillate under coherent excitation at the eigenfrequency Ω_0 and represent a macroscopic radiation field given by

$$\boldsymbol{P} = \mathrm{Tr}(\hat{\boldsymbol{d}}\rho), \tag{2.9}$$

where Tr is the trace of the matrix. The Hamiltonian $\hat{\mathcal{H}}$ can be written as the sum [Dem08a]

$$\hat{\mathcal{H}} = \hat{\mathcal{H}}_0 + \hat{\mathcal{V}}(t), \quad \hat{\mathcal{H}}_0 = \begin{pmatrix} E_0 & 0 \\ 0 & E_1 \end{pmatrix}, \quad \hat{\mathcal{V}}(t) = \begin{pmatrix} 0 & -\boldsymbol{d}_{01}\boldsymbol{E}(\boldsymbol{r},t) \\ -\boldsymbol{d}_{01}^*\boldsymbol{E}(\boldsymbol{r},t)^* & 0 \end{pmatrix}. \tag{2.10}$$

$\hat{\mathcal{H}}_0$ is the Hamiltonian of the isolated system, and $\hat{\mathcal{V}}(t)$ is the perturbation operator which describes the interaction of the only non-zero optical transition dipole element $\boldsymbol{d}_{01}$ (cf. Sec. 1.3.2) with an electric field

$$\boldsymbol{E}(\boldsymbol{r},t) = \boldsymbol{\mathcal{E}}_0(t)e^{i(\boldsymbol{kr}-\omega t)} + \text{c.c.} \tag{2.11}$$

$\boldsymbol{\mathcal{E}}_0(t)$ is the (real) electric field amplitude in the direction of the polarization vector and c.c. stands for complex conjugated. When calculating the perturbation one has to consider that the dipole element $\boldsymbol{d}_{01} \propto e^{i\Omega_0 t}$. Therefore, the product in Eq. (2.10) contains a term with the rapidly varying phase factor $e^{i(\omega+\Omega_0)t}$ which will be omitted in the rotating wave approximation. Thus, the off-diagonal elements of $\hat{\mathcal{V}}(t)$ reduce to $(\hbar/2)\chi(t)e^{i(\boldsymbol{kr}-\omega t)}$ with the *Rabi frequency*

$$\chi(t) = \frac{2\,|\boldsymbol{d}_{01}\boldsymbol{\mathcal{E}}_0(t)|}{\hbar} \tag{2.12}$$

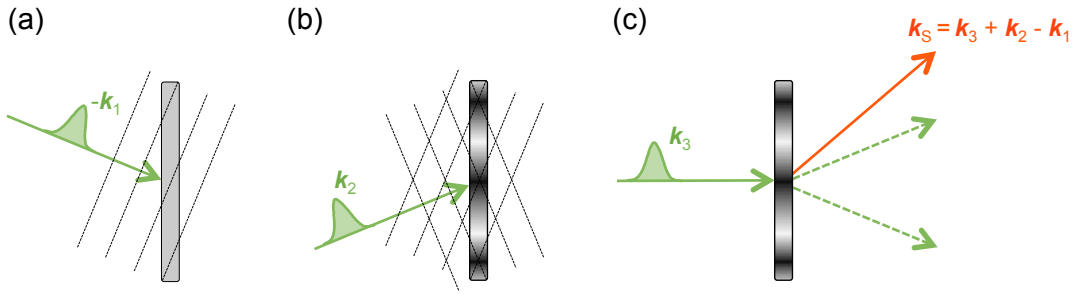

Figure 2.1: Grating picture of transient four-wave mixing in the rephasing configuration. (a) The first pulse creates a macroscopic polarization in the sample. The dashed lines designate phase fronts. (b) The second pulse converts the coherence into a population grating depending on the pulse phase relative to the coherence. Darker (lighter) regions represent excited (ground) state population. (c) The third pulse scatters in the background free phase matching direction $\boldsymbol{k}_{\mathrm{S}} = \boldsymbol{k}_3 + \boldsymbol{k}_2 - \boldsymbol{k}_1$.

at resonance $\omega = \Omega_0$. Finally, we note that the elements of the density matrix correspond to the expectation values of the $\boldsymbol{\mathcal{S}}$ vector in the optical Bloch equations (2.3), i.e.

$$\boldsymbol{\mathcal{S}} = \begin{pmatrix} \rho_{10}^{\Omega} + \rho_{01}^{\Omega} \\ i[\rho_{10}^{\Omega} - \rho_{01}^{\Omega}] \\ \rho_{11} - \rho_{00} \end{pmatrix}. \tag{2.13}$$

Here, the substitution $\rho_{01} = \rho_{01}^{\Omega} e^{i(\Omega_0 - \Delta)}$ takes the rotating wave approximation into account [Jon03].

2.2 Four-wave mixing

Techniques of nonlinear spectroscopy measure, in most cases, the third-order macroscopic polarization induced by the optical fields, i.e. [She84]

$$\boldsymbol{P}^{(3)} \propto \chi^{(3)} \boldsymbol{E}^3, \tag{2.14}$$

where $\chi^{(3)}$ is the susceptibility tensor of rank three. We assume that $\boldsymbol{E}^3$ is the product of three separate light fields in the form of Eq. (2.11). In a four-wave mixing process the three excitation fields "mix" inside of the medium to produce the fourth signal field oscillating at the light frequency ω with wave vectors $\pm\boldsymbol{k}_1 \pm \boldsymbol{k}_2 \pm \boldsymbol{k}_3$.

Of particular interest is transient FWM with pulsed excitation in the rephasing configuration $\propto \boldsymbol{E}_1^* \boldsymbol{E}_2 \boldsymbol{E}_3$. The first pulse excites a coherent polarization whose radiation field interferes with the second pulse forming an interference pattern with wave vector $\boldsymbol{k}_1 - \boldsymbol{k}_2$ (Figs. 2.1(a) and 2.1(b)). The third pulse scatters from the resulting population grating in the background free, phase-matching direction $\boldsymbol{k}_{\mathrm{S}} = \boldsymbol{k}_3 + \boldsymbol{k}_2 - \boldsymbol{k}_1$ (Fig. 2.1(c)). The simplest configuration is the two-beam degenerate transient FWM where $\boldsymbol{k}_2 = \boldsymbol{k}_3$. In this case, the second pulse counts twice and will be self-diffracted from the interference

pattern in the $2\boldsymbol{k}_2 - \boldsymbol{k}_1$ direction. The signal decays exponentially with the dephasing rate $\gamma = 1/T_2$ as a function of time after the last pulse. In addition, as the delay between the first and second pulses τ_{12} is increased, the strength of the emitted signal will decay due to the relaxation of the coherence that is established by the first pulse. One can summarize:

$$P^{(3)} \propto e^{-\frac{t-\tau_{12}}{T_2}} e^{-\frac{\tau_{12}}{T_2}}. \tag{2.15}$$

$\hbar\gamma = \hbar/T_2$ is called the homogeneous linewidth and can be measured in linear spectroscopy ($P^{(1)}$) as half-width of the Lorentzian absorption lineshape.

2.2.1 Photon echo

An obvious limitation for the determination of the homogeneous lineshape γ is inhomogeneous broadening, as present in the semiconductor nanostructures studied for this thesis (cf. Sec. 1.4.1). This is due to different local environments leading to slightly different individual transition frequencies Ω_0. In the ensemble one assumes a continuous distribution of transition frequencies according to the Gaussian

$$G(\Omega_0) = \frac{\sigma}{\sqrt{2\pi}} e^{-\frac{\sigma^2(\Omega_0-\overline{\Omega}_0)^2}{2}}, \tag{2.16}$$

where $\overline{\Omega}_0$ is the central frequency of the inhomogeneous ensemble with a half-width in frequency corresponding to $\Gamma = 1/\sigma$. It defines the width of the absorption spectrum and can be much wider than in the case of pure homogeneous broadening. However, it is in principle conceivable to isolate one system from the inhomogeneous ensemble and to extract γ from methods of linear spectroscopy with high spatial and spectral resolution [Gam96].

More feasible is the *photon echo* (PE) approach in four-wave mixing rephasing configuration. The idea is based on the Hahn echo for spins in nuclear magnetic resonance [Hah50] and was firstly realized in a ruby crystal [Kur64]. The scenario can be nicely described in the picture of the "pseudo" spin vector $\boldsymbol{\mathcal{S}}$ using the optical Bloch equations (2.3) and their visualization in Fig. 2.2(a). A short spectrally broad laser pulse with $\Theta_1 = \pi/2$ creates a macroscopic polarization which subsequently dephases due to inhomogeneity. A second optical rephasing pulse with $\Theta_2 = \pi$ retrieves the macroscopic polarization with emission of a PE pulse delayed by a time exactly equal to the interval between the rephasing and excitation pulse, τ_{12} (Fig. 2.2(b)). The scenario can be extended to three pulses, rather than two. This can be regarded as splitting of the pulse sequence $\pi/2$-π into $\pi/2$-$\pi/2$-$\pi/2$. In this case, the second pulse orients the $\boldsymbol{\mathcal{S}}$ vectors in a direction along the z-axis corresponding to population. The third, rephasing pulse after time delay τ_{23} initiates the retrieval of the macroscopic polarization with subsequent emission of a PE pulse. Typically, the temporal profile of the PE pulse has a Gaussian shape reflecting the inhomogeneous frequency distribution of the excited ensemble,

$$P^{(3)} \propto e^{-\frac{(t-2\tau_{12}-\tau_{23})^2}{2\sigma^2}} e^{-\frac{2\tau_{12}}{T_2}} e^{-\frac{\tau_{23}}{T_1}}. \tag{2.17}$$

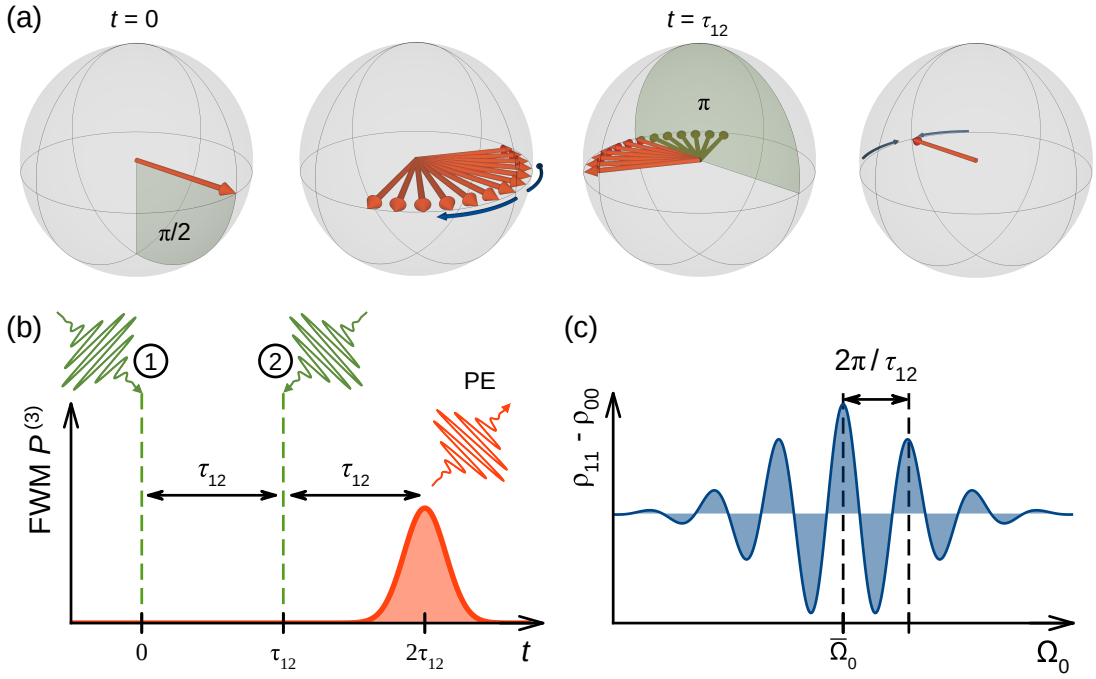

Figure 2.2: Principle of the photon echo (PE). (a) Dynamics of the pseudo spin vectors according to the optical Bloch equations (2.3) for two laser pulses with area $\Theta = \pi/2$ and π, respectively. (b) Pulse sequence and third-order nonlinear polarization $P^{(3)}$ in the rephasing configuration according to Eq. (2.17) with $\tau_{23} = 0$. (c) Spectral grating of the population inversion $\rho_{11} - \rho_{00}$ just after action of the second pulse. The period $2\pi/\tau_{12}$ corresponds to the phase of the individual oscillators.

The photon echo can thus be used to determine the dephasing rate $1/T_2$ by scanning τ_{12} and the total population decay rate $1/T_1$ by scanning τ_{23}. It can be shown that the existence of the two-pulse echo in semiconductors is not attributed to the π-character of pulse 2 [Bal12]. Therefore, one observes in experiments with three pulses actual two photon echoes – the first after pulses 1 and 2, and a second one following on the third pulse. They will be distinguished as *primary* and *stimulated photon echo*.

There is an equivalent explanation in the frequency domain image that is more helpful for the understanding of the rephasing process [Cun12]. The first, spectrally broad pulse excites all the oscillators resonantly into a coherent state. They start to evolve in time and accumulate a phase that is proportional to their unique eigenfrequency and the delay τ_{12}. The second pulse transforms this phase distribution into a spectral grating of the population matrix elements ρ_{00} and ρ_{11} in which it can be stored as long as T_1 (Fig. 2.2(c)). When the third pulse (the second pulse counted twice, respectively) arrives, it causes the oscillators to resume their temporal evolution. However, the first pulse is complex conjugated with respect to the others, and therefore, the oscillators evolve in the opposite direction. The net phase for all frequency groups returns to zero and coherent emission is observed in form of a photon echo. In fact, the oscillators are always

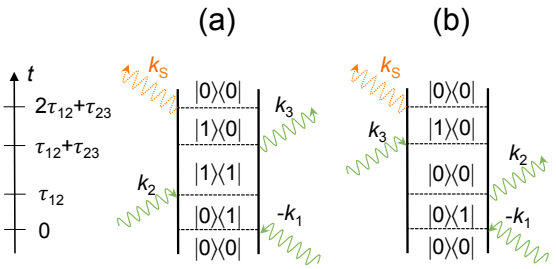

Figure 2.3: Double-sided Feynman diagrams for an independent two-level system representing contributions to the phase-matched direction $\boldsymbol{k}_3 + \boldsymbol{k}_2 - \boldsymbol{k}_1$. The path in (a) is given by an absorption of the second pulse and laser pulse stimulated emission of the third one. The situation in (b) is vice versa.

emitting; however, at times other than the echo time, the emissions are not in phase and average to zero.

2.2.2 Double-sided Feynman diagrams

The temporal evolution of the density matrix during a FWM experiment can be traced in a double-sided Feynman diagram [Muk95]. Figure 2.3 shows an example for an independent TLS. The time evolves in vertical direction upwards. Two vertical lines represent the elements of the density matrix, the left line corresponds to "ket" and the right one to "bra". Wavy lines represent the interaction with a light field. Their arrows are pointing on one of the vertical lines in the case of photon absorption and in the opposite direction in case of photon emission. An arrow pointing to the right represents a contribution of $\boldsymbol{\mathcal{E}}_j e^{i(\boldsymbol{k}_j \boldsymbol{r} - \omega t)}$ to the polarization. An arrow pointing to the left represents the complex conjugated contribution $\boldsymbol{\mathcal{E}}_j^* e^{-i(\boldsymbol{k}_j \boldsymbol{r} - \omega t)}$.

2.2.3 Two-dimensional Fourier transform spectroscopy

Measurements of transient FWM are generally performed in the time domain as function of the pulse delays. However, Fourier transform of the time variables allows one to transfer the measurements in the frequency domain. The particular case of two-dimensional spectroscopy can be best explained when renaming the delay $\tau_{12} \mapsto t_1$ ($\tau_{23} \mapsto t_2$), as shown in Fig. 2.4(a). The signal is emitted over the time t_3. For inhomogeneous broadening of the optical transitions, the transient FWM signal is considered in the rephasing configuration, and the resulting photon echoes are described by the optical field

$$S_I(t_1,t_2,t_3) = A_{\mathrm{PE}}(t_1,t_2,t_3) e^{-\frac{(t_3-t_1)^2}{2\sigma^2}} e^{i\omega(t_3-t_1)}. \tag{2.18}$$

The amplitude of the photon echo $A_{\mathrm{PE}}(t_1,t_2,t_3)$ depends on the delay times t_1, t_2, and t_3 as well as on the polarization configuration of the exciting pulses. The phase of the optical field is given by $\omega(t_3 - t_1)$, where $\omega = \overline{\Omega}_0$ is tuned in resonance with central frequency of the inhomogeneous ensemble. A two-dimensional *rephasing spectrum* can be generated by scanning t_1, recording the signal as function of t_3, and taking Fourier transforms with respect to t_1 and t_3 (Fig. 2.4). The result is a plot in two frequency

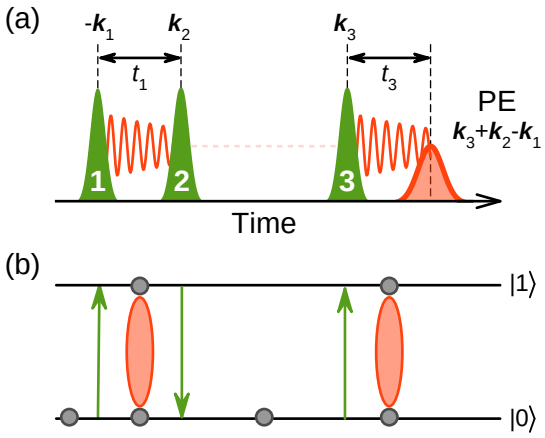

Figure 2.4: Principle of two-dimensional Fourier transform spectroscopy in the rephasing configuration. (a) Temporal pulse sequence for the photon echo (PE) signal that is detected in $\boldsymbol{k}_3 + \boldsymbol{k}_2 - \boldsymbol{k}_1$ direction. (b) Excitation sequence in the two-level system. The first pulse creates a coherent superposition which is oscillating in time, as indicated by decaying sinosoid. The second pulse converts the superposition to a population in the ground state (cf. Fig. 2.3(b)) that does not oscillate. The third pulse converts the population back to a coherent superposition.

dimensions according to [Cun13]

$$S_I(\Omega_1,\Omega_3) = \int\int S_I(t_1,t_3)e^{i(\Omega_1 t_1 - \Omega_3 t_3)}\mathrm{d}t_1\mathrm{d}t_3, \tag{2.19}$$

where Ω_1 and Ω_2 correspond to the absorption (the transform of t_1) and emission (the transform of t_3) optical frequencies. The technique of two-dimensional Fourier transform spectroscopy (2DFTS) has rapidly developed during the last decade and has been successfully applied for the investigation of atomic, molecular, and condensed matter systems such as organic and inorganic semiconductors [Muk95, Zha07, Yan07, Sto09, Kas11]. One of the appealing features of 2DFTS is the intuitive visualization of the underlying physics, as it not only enables one to extract energy levels but also provides a clear understanding of the dynamics and correlations between optical excitations [Cun09]. Note that 2DFTS measurements demand not only knowledge about the optical field's amplitude but also about the phase and its correlation to the phase delay between all excitation pulses. The experimental implementation requires therefore active interferometric phase stabilization between all involved pulses [Zha05]. Measurement of the optical phase is typically accomplished by heterodyne detection of the nonlinear signal with a reference pulse.

Systems with more than two states interacting with light attract particular interest. The most representative examples are V-type (Λ-type) energy level orders where the single ground (excited) state is optically coupled to an excited (ground) state doublet [Har68, Scu97]. These level schemes make it possible to observe several fascinating phenomena such as quantum beats, coherent population trapping, and electromagnetically induced transparency, which may be used for applications in quantum information technology [Fle05, Ham10]. A main feature of a Λ scheme as shown in Fig. 2.5(b) is the possibly long coherence time of the ground states, $|1\rangle$ and $|2\rangle$. There are two optically allowed transitions, $|1\rangle \rightarrow |3\rangle$ and $|2\rangle \rightarrow |3\rangle$, which can be addressed by orthogonally polarized optical pulses (indicated by red and blue arrows, respectively). A sequence of two such pulses allows one to shuffle the optical coherence between $|1\rangle$ and $|3\rangle$ into a

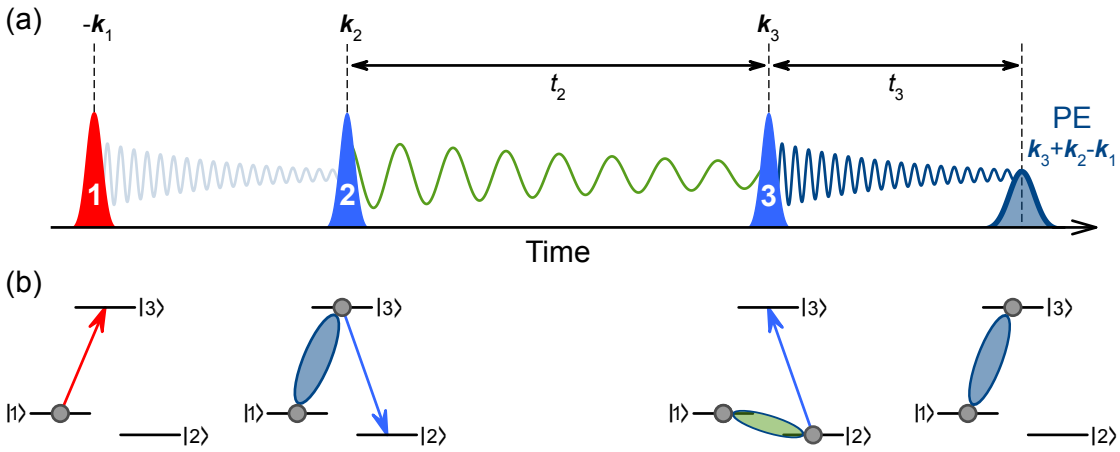

Figure 2.5: Principle of two-dimensional Raman coherence spectroscopy. (a) Temporal pulse sequence of the photon echo (PE) signal that is detected in $\boldsymbol{k}_3+\boldsymbol{k}_2-\boldsymbol{k}_1$ direction. (b) Excitation sequence in the Λ-type energy system. Orthogonally polarized pulses (transitions) are indicated by the colors red and light blue. Coherent superpositions oscillate as function of time, as indicated by the decaying sinusoid.

non-radiative coherence between $|1\rangle$ and $|2\rangle$. Oscillations in time associated with this non-radiative coherence are much slower than for the optical coherences, as indicated by the decaying sinusoids with different frequencies in Fig. 2.5(a). A 2DFTS *Raman coherence spectrum* can be generated by scanning t_2, recording the signal as function of t_3, and taking Fourier transforms with respect to t_2 and t_3, i.e.

$$S_I(t_1,\Omega_2,\Omega_3) = \int\int S_I(t_1,t_2,t_3)e^{-i(\Omega_2 t_2+\Omega_3 t_3)}\mathrm{d}t_2\mathrm{d}t_3. \tag{2.20}$$

Keep in mind that the frequency Ω_1 is phase conjugated with respect to the frequencies Ω_2 and Ω_3. For a different time ordering of the conjugated pulse with wave vector $\boldsymbol{k}_1$ one receives non-rephasing spectra, S_{II}, or double-quantum coherence spectra, S_{III} [Cun09].

2.3 Coherent spectroscopy of semiconductor nanostructures

Coherent optical spectroscopy has been widely used for the investigation of the energy levels of charge, vibration, and spin states in condensed matter systems [Dem08b, Cun13]. It comprises many elaborated techniques that can be roughly divided in two main categories: the first set uses continuous wave light sources of tunable wavelength with narrow spectral width, i.e. long coherence time, which enable direct acquisition of coherent spectra in the frequency domain [Fle05]. The second set is based on recording the temporal dynamics of the system's response to short light pulse excitation. Here, the third order nonlinearity probed by transient FWM is of particular interest since it allows to investigate the coherence properties even in the presence of large inhomogeneous

broadening (cf. Sec. 2.2). The first photon echo experiments in semiconductors measured the exciton dynamics in GaAs QWs [Sch85, Web91] and CdS_xSe_{1-x} mixed crystals [Nol90]. This section provides an outlook for the FWM spectroscopy of (In,Ga)As QDs and CdTe QWs studied in Ch. 6 and Ch. 7, respectively.

2.3.1 Photon echo timing sequence

Manipulation of electronic states by laser pulses requires precise timing of the pulse sequence. A particular example is ultrafast coherent control of exciton complexes confined in QDs [De 13] which may be used for manipulating quantum states [Kim11, Bio00, Li03] or even storing quantum information [Kro04, Lan14]. PE for an inhomogeneous ensemble of TLS in QDs were reported in Refs. [Bor01, Moo13, Tah14]. To be of practical use, the echo formation time needs to be determined with high accuracy. What seems to be easy for the scenario of a weakly inhomogeneous ensemble of TLS shown in Fig. 2.2(b) turns out to become complicated in QDs for several reasons: (i) Due to the many-body interactions a description by a distribution of independent TLS is as a rule not appropriate, but complex coherent transients are recorded [Sha99, Che01]. However, localization of excitons strongly reduces exciton-exciton interactions (cf. Sec. 2.1.1). Therefore, QDs with particularly strong three-dimensional localization can be often reasonably well considered as TLS with long coherence times. (ii) In addition, fluctuations in QD size, shape and composition lead to a considerable inhomogeneous broadening of the optical transitions in QDs. Also excitation with ultrashort pulses having a broader spectrum than the inhomogeneity is in many cases prohibited because of the demand of addressing a specific optical transition. The relatively narrow energy spacing of different electronic excitations limits the spectral width that the laser pulses may have, to avoid excitation of multiple transitions.

Therefore a careful consideration of the optical frequency detuning with respect to the TLS optical resonance is mandatory when considering the PE transient formation, even in the limit of small excitation levels. Generally, it is expected that for strongly inhomogeneous TLS ensembles the PE temporal profile may undergo significant distortion compared to the standard τ_{12}-$2\tau_{12}$ sequence, showing either retarded or advanced echo pulses [All75]. This is due to the non-negligible inhomogeneity-induced dephasing of oscillators during the action of optical excitation pulse, so that the finite pulse duration should be taken into account. Surprisingly, these variations of the PE transients in TLS were only reported in ruby [Sam78], where the characteristic excitation and depolarization times are in the range of tens of nanoseconds, i.e. orders of magnitude longer than in semiconductor nanostructures. In Sec. 6.3 we show the first demonstration of PE transients from QDs that deviate from the conventional τ_{12}-$2\tau_{12}$ picture.

2.3.2 Microcavity systems

Transient FWM and 2DFTS were used to investigate the coherent optical response of exciton-polaritons (cf. Sec. 1.4.2) in QW and QD based microcavities with high quality factors in the strong coupling regime [Koh12, Alb13, Wil15]. QDs were also imple-

mented in low-Q cavities based on two DBR mirrors in order to increase the strength of the transient FWM signal and to study the corresponding coherent optical phenomena [Fra16, Mer16]. In the strong field regime, Rabi-oscillations can be used for direct evaluation of the light-matter interaction strength. Rabi oscillations of exciton complexes were demonstrated in QDs using various techniques [Sti01, Zre02, Ram10, Gam13]. In Ch. 6 they are measured by photon echoes from QDs embedded in low-Q microcavities.

2.3.3 Spin degree of freedom

The spin level structure of ground and excited states contributes to the formation of two- and three-pulse photon echoes [Lam69, Che79, Mor79]. In semiconductors, Λ-type energy schemes (cf. Fig. 2.5(b)) can be obtained for optical excitation of localized excess carriers, e.g., electrons in the conduction band or holes in the valence band, using their spin degree of freedom. In the case of resident electrons, the negatively charged exciton (trion) and the donor-bound exciton are possible optically excited states. Coherent population trapping and electromagnetically induced transparency have been demonstrated for donor-bound excitons in bulk GaAs [Fu05, Sla10], as well as trions in n-type CdTe QWs [Wan12] and QDs charged with resident carriers [Xu08, Bru09, Han14]. These studies have exploited high resolution spectroscopy with continuous-wave lasers. Spin control of resident carriers using ultrafast laser pulses has also been successfully demonstrated [Gre06, Car07, Pre08]. However, most of the FWM and 2DFTS experiments on charged excitations in semiconductors have not exploited the spin degree of freedom in the ground state so far [Bro94, Bri99, Moo14, Fra16]. Recently, it was demonstrated that the ground state splitting of a trion in a transverse magnetic field leads to quantum beats in the photon echoes at the Larmor precession frequency [Lan12]. This allows to perform a coherent transfer of optical excitation into a spin ensemble and to observe long-lived stimulated photon echoes [Lan14, Sal14, Pol16b]. Coherent-optically detected magnetic resonance enabling the high-resolution spectroscopy of electron spins is the subject of Ch. 7.

Chapter 3

Spin physics and ferromagnetism

Phenomena based on magnetism are known by every child, whether it is the invisible force repulsing or attracting permanent magnets or the needle of a compass turning in the direction of the earth's magnetic field. In the 19th century physicists like André Marie Ampère or James Clerk Maxwell found out that magnetism is created when electric charges are in motion. As a consequence, the Bohr model of an atom led in the early 20th century to the idea that the current of the orbiting electron is associated with a magnetic moment $\boldsymbol{m}$ (cf. Eq. (1.5)). Later, the elementary concept of the *spin* was added to the list of electron's angular momenta. It is most of all the mysterious nature of the electron spin which is fundamental for the nowadays understanding of magnetism (cf. Pauli exclusion principle, Sec. 1.1.1).

Basics of spin physics were already introduced in the beginning of Sec. 1.1. This chapter aims to discuss basic spin physics in semiconductors and ferromagnetic materials and introduces the concept of combining constituents of both materials in order to form spintronic devices.

3.1 Spin physics in semiconductors

Spin-orbit coupling (cf. Sec. 1.1.2) is in semiconductors of particular interest. Having already addressed its contribution to the band structure (Sec. 1.1.3) and optical orientation (Sec. 1.3.2), here we discuss mechanisms of spin relaxation and show how the Zeeman effect can be used in order to measure the associated decay times.

3.1.1 Spin relaxation

Generally, non-equilibrium spin can be created by optical or electrical methods [icvac04]. Once the pumping is turned off the initial non-equilibrium spin polarization (cf. Eq. (1.24)) will relax to zero. In bulk materials, the electron spin relaxation time τ_{se} ranges from $\sim 1\,\mathrm{ps}$ in ferromagnets up to $\sim 10\,\mathrm{ns}$ in semiconductors [Stö06]. The reason for spin relaxation can be understood as a result of fluctuating in time magnetic fields originating, e.g., from spin-orbit or, in ferromagnets, exchange interaction (Sec. 3.2.1).

Important for the semiconductors studied in this thesis is the *Dyakonov-Perel mechanism* which is related to spin-orbit splitting of the conduction band [Dya71, Dya72]. The electron spin precesses around an effective magnetic field created by the nuclei unless its direction changes randomly. If it happens the spin starts to precess around the new field direction and the process repeats until the initial spin orientation S_0 will be completely forgotten. The initial hole "spin" orientation J_0 relaxes rapidly due to the much stronger spin-orbit coupling in the valence band, i.e. $\tau_{\mathrm{se}} \gg \tau_{\mathrm{sh}}$, where τ_{sh} is the hole spin relaxation time. Effective magnetic fields can also arise from from lattice vibrations (Sec. 3.2.3), as described by the *Elliott–Yafet mechanism* [Dya08]. However, for the cryogenic temperatures used in our experiments this contribution is rather weak. Another reason for spin relaxation is hyperfine interaction between the electron and nuclear spin systems.

3.1.2 Zeeman effect

The relaxation of spins is influenced by external magnetic fields. The interaction between the total angular momentum $\hat{\boldsymbol{J}}$ and an external magnetic field $\boldsymbol{B}$ is described by the *Zeeman effect* and its Hamiltonian can be written as

$$\hat{\mathcal{H}}_B = \frac{g_{\mathrm{e}}\mu_{\mathrm{B}}}{\hbar}\boldsymbol{B}\hat{\boldsymbol{J}}. \tag{3.1}$$

By choosing the quantization z-axis in the direction of the external field $\boldsymbol{B}$ one observes that the magnetic field lifts the degeneracy of the substates of the total angular moment by

$$\Delta E_B = g_{\mathrm{e}}\mu_{\mathrm{B}}B = \hbar\omega_{\mathrm{L}}. \tag{3.2}$$

The introduced frequency ω_{L} is called *Larmor frequency* and determines a precession of the angular momentum components perpendicular to the magnetic field axis. The dynamic can be described in terms of a spin polarization vector $\boldsymbol{\mathcal{S}}$ (cf. Sec. 1.3.1) using the Bloch equations [Blo46].[1] As for the optical Bloch equations (2.3), relaxation is considered with respect to longitudinal and transverse spin components, $T_{1,\mathrm{e(h)}}$ and $T_{2,\mathrm{e(h)}}$, respectively. They are linked to the spin relaxation mechanisms with $\tau_{\mathrm{se(h)}}$ discussed in the previous section as follows. The components of the random field perpendicular to the external field $\boldsymbol{B}$ create damping torque towards the z-axis pushing the spin vector in a direction (anti-)parallel to the external field. The components of the random fields directed along $\boldsymbol{B}$ cause spin relaxation of the perpendicular spin components. Ensemble of carrier spins lose their macroscopic spin polarization typically during the time $T^*_{2,\mathrm{e(h)}}$ which is faster than $T_{2,\mathrm{e(h)}}$ [Yak08].

[1] There is a beautiful analogy to a gyroscope precessing in the plane perpendicular to the earth's gravitational field $\boldsymbol{F}_{\mathrm{G}}$. The mechanical angular momentum $\boldsymbol{L} = \boldsymbol{r} \times \boldsymbol{p}$ moves according to Newton's classical equation of motion

$$\mathrm{d}\boldsymbol{L}/\mathrm{d}t = \boldsymbol{r} \times \boldsymbol{F}_{\mathrm{G}}, \tag{3.3}$$

where $\boldsymbol{r}$ is the position vector and $\boldsymbol{p}$ is the linear momentum.

3.1.3 Hanle effect

The optical orientation of electron spins after absorption of circularly polarized light can be destroyed by the application of a transverse magnetic field. The electron spins oriented along the z-axis start to precess in the z-y plane when $\boldsymbol{B} \parallel \boldsymbol{x}$ is applied. It manifests itself in a depolarization of luminsecense described by a Lorentzian [Dya84]

$$\rho_\mathrm{c}(B) = \frac{\rho_\mathrm{c}(0)}{1 + \left(\frac{B}{B_{1/2}}\right)^2}, \tag{3.4}$$

with the degree of circular polarization ρ_c from Eq. (1.19). The half-width of the Hanle curve (3.4) is given by

$$B_{1/2} = \frac{\hbar}{\mu_\mathrm{B} g_\mathrm{e} \tau_\mathrm{e}}, \tag{3.5}$$

where τ_e is the overall electron spin lifetime, i.e.,

$$\frac{1}{\tau_\mathrm{e}} = \frac{1}{\tau_\mathrm{se}} + \frac{1}{\tau_\mathrm{r}} \tag{3.6}$$

with electron lifetime in the excited state τ_r and pure spin relaxation time τ_se (cf. Sec. 3.1.1). The longer the electron spin lifetime τ_e, the smaller the magnetic field necessary to rotate the spin and depolarize the PL.

Equation (3.5) represents the simplest case of electron spin depolarization in a magnetic field. For the interaction with nuclear spins [Mer02] or magnetostatic stray fields generated by the domain structure of a nearby ferromagnet [Dzh95] the Hanle curve becomes artificially broadened and a fit to a Lorentzian according to Eq. (3.4) will underestimate the spin lifetime. For the case of an isotropic distribution of random fields there is the relation [Pet08, Gre12]

$$B_{1/2} = \frac{2\sqrt{3}\hbar}{\mu_\mathrm{B} g_\mathrm{e} T^*_{2,\mathrm{e}}}, \tag{3.7}$$

where $T^*_{2,\mathrm{e}}$ is the transverse electron spin dephasing time. Moreover, the interaction with stray magnetic fields reflects itself in an increase of ρ_c under application of a longitudinal magnetic field, recently called the "inverted" Hanle effect [Das11].

3.2 Ferromagnetism

This section provides a brief introduction to the basic properties of ferromagnetic materials. The first two sections follow Ref. [Stö06].

3.2.1 Magnetic interactions

The strongest magnetic interaction arises from the electrostatic Coulomb repulsion between electrons in combination with the Pauli exclusion principle (cf. Sec. 1.1.1). It is

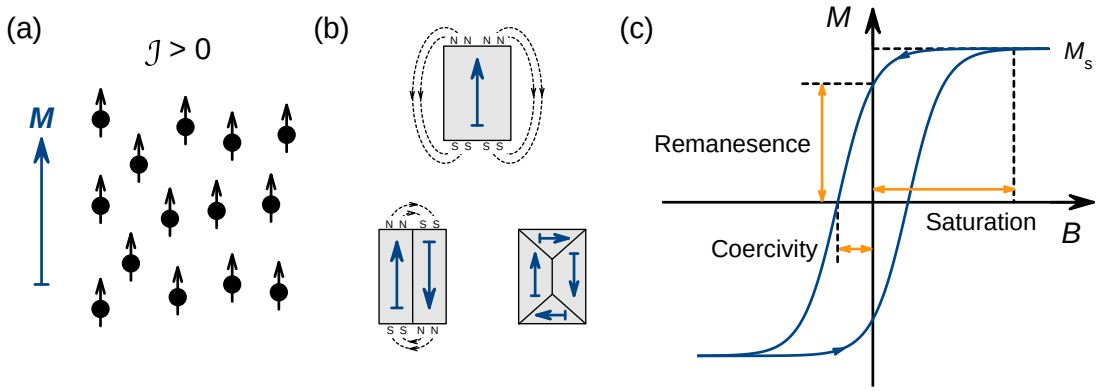

Figure 3.1: Principles of ferromagnetism. (a) Structure of the parallel oriented spin lattice with exchange constant $\mathcal{J} > 0$ resulting in the macroscopic magnetization $\boldsymbol{M}$. (b) Formation of ferromagnetic domains in order to reduce the stray field and thereby the magnetostatic energy. (c) Magnetization $\boldsymbol{M}$ as function of the external magnetic field $\boldsymbol{B}$ with the main parameters of the resulting hysteresis loop.

called *exchange interaction* and leads in atoms to an energy splitting of the singlet-triplet states. In condensed matter, exchange interaction is the origin for correlated magnetism with multi-faceted behavior such as ferro-, antiferro- or ferrimagnetism. It can be described by a simple Heisenberg model taking only nearest neighbors into account,

$$\hat{\mathcal{H}}_{\text{ex}} = -2\mathcal{J} \sum_{i<j} \hat{\boldsymbol{S}}_i \hat{\boldsymbol{S}}_j, \tag{3.8}$$

where $\mathcal{J}$ is the exchange constant depending on the overlap of the wave functions of the electrons and $\hat{\boldsymbol{S}}_{i,j}$ are total spin operators of adjacent atoms. In one dimension, the three dimensional spin operator $\hat{\boldsymbol{S}}$ has to be replaced by $\hat{\boldsymbol{S}}_z$ along the quantization z-axis leading to the so called Ising Hamiltonian. Depending on the sign of $\mathcal{J}$, there will be a parallel ($\mathcal{J} > 0$, shown in Fig. 3.1(a)) or antiparallel ($\mathcal{J} < 0$) spin alignment in the groundstate, leading to the phenomenon of ferro- and antiferromagnetism, respectively. Ferrimagnets have two antiferromagnetically coupled magnetic sublattices, whose magnetizations are generally not compensated. The exchange leads to effective magnetic fields that can reach in ferromagnets up to several 1000 T.

Spin-orbit interaction was already introduced in Se. 1.1.2. In ferromagnets it the primary source of *magnetocrystalline anisotropy*. The orbital moment prefers to lie along a specific lattice direction caused by surrounding charges in the crystal. Spin-orbit interaction locks the spins along this direction and, as a result, the magnetic alignment in the material is not free, but has one preferred direction, called the *easy axis*. In magnetic films of several nanometer thickness *shape anisotropy* becomes relevant and the easy axis is typically oriented in-plane.

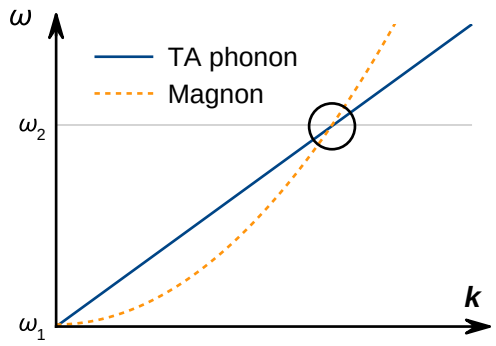

Figure 3.2: Dispersion relation of magnons $\propto k^2$ and transverse accoustical (TA) phonons $\propto k$. The second crossing point with energy $\hbar\omega_2$ is highlighted by the circle.

3.2.2 Hysteresis loop

External magnetic fields in combination with magnet-optical effects (cf. Sec. 1.3.3) can be used to study a ferromagnet's magnetization, i.e., the volume density of magnetic moments, $\boldsymbol{M} = \mathrm{d}\boldsymbol{m}/\mathrm{d}V$. For example, without external disturbance, the magnetization in a ferromagnet breaks up into domains with different magnetization directions which cancel out on a macroscopic scale (Fig. 3.1(b)). The $\boldsymbol{M}$ increases under application of an external magnetic field $\boldsymbol{B}$ until the saturation value $\boldsymbol{M}_\mathrm{s}$ for which the domain structure is removed, and $\boldsymbol{M}$ is pointing entirely in the direction of $\boldsymbol{B}$. When $\boldsymbol{M} \neq 0$ remains although the external field is switched off, one speaks about remanescence magnetization. The coercivity field is the field that must be applied in the opposite direction in order to reduce the magnetization to zero. Field scans in both direction can provide a hysteresis loop as shown in Fig. 3.1(c).

When applying the field along various directions of the crystal lattice one can study the magnetocrystalline anisotropy. Its energy is determined by the field required to rotate the magnetization by 90° away from the easy axis.

3.2.3 Magnons and phonons

In ferromagnetic materials pure spin dephasing involves typically the transfer of angular momentum into the spin system of the crystal lattice. In the ground state of a simple ferromagnet all spins are aligned in parallel. Due to exchange interaction (cf. Sec. 3.2.1) waves appear in the coupled spin system when at least one spin is displaced from its equilibrium position [Lev68, Kit04]. The resulting oscillations are called *spin waves* or, in the quasiparticle equivalent for quantized vibrations of the spin lattice, *magnons*. Their angular momentum corresponds to a single electron spin flip $\Delta s_z = \hbar$.

Another important type of vibrations arises from elastic strain inside the crystal lattice. If the nuclei are displaced from their equilibrium position they feel restoring forces which cause vibrations. Since all nuclei in the lattice are coupled to each other, elastic waves with wave vector $\boldsymbol{k}$ can travel through the crystal [Ash76, Kit04]. The energy of a lattice vibration is quantized and the quantum of energy is called *phonon*. In the quasiparticle picture they travel through the crystal carrying linear "quasimomentum"

$\hbar\boldsymbol{k}$. With respect to $\boldsymbol{k}$, longitudinal and transverse modes of lattice oscillations are existing. In crystals with two atoms per unit cell one has to distinguish between nearest neighbors with oscillations in phase ("acoustical") and out of phase ("optical"). Note that phonons are pure lattice phenomena which appear not only in ferromagnets, but all kinds of solids.

Currently the role of phonons on the magnetization properties of condensed matter systems attracts particular interest and is actively discussed in literature [Jur17b]. One of the examples, discussed in Ch. 5, dates back to *Kittel* who predicted in 1958 the coupling of magnons and transverse acoustic (TA) phonons in ferromagnetic crystals [Kit58]. Figure 3.2 shows that two crossing points are existing in the dispersion relation. The higher energetic one at frequency ω_2 is of primary interest since in the Debye model the density of states is $\propto \omega^2$ [Kit04].

3.3 Combining semiconductors with magnetic materials

External magnetic fields can be used in order to orient the magnetization of a ferromagnetic thin film, as typically done in nowadays magnetic memory and storage technologies [Pri98]. The ferromagnet spin-polarization is translated into electronic transport by exploiting the giant magnetoresistance effect.[1] Temporal switching of the external writing field by miniaturized electromagnets is limited to nanoseconds, leading in contemporary computers to data rates $\sim 1\,\mathrm{GHz}$. Ultrafast demagnetization induced by femtosecond laser pulses showed that magnetization manipulation in ferromagnets is also possible by pure optical methods [Bea96]. Laser heating of the magnetic system and circular polarization acting simultaneously as a magnetic field led in fact to all-optical magnetization switching on a timescale of tens of nanoseconds [Sta07, Vah09]. However, there is a difference to the manipulation of a pure quantum mechanical spin state. Spins suffer from the rather complicated band structure of metals consisting of many broad overlapping bands, resulting in strong interactions of electrons with the lattice and each other. In semiconductor nanostructures the band structure is clearer and selection rules allow for spin orientation and detection by pure optical methods.[2] Interactions are reduced by localization and remarkably long spin lifetimes $\sim 1\,\mathrm{ms}$ have been reported [Kro04]. Nowadays the research field of *spintronics* discusses the combination of magnetic materials with semiconductors in a single structure with various applications in electronics and quantum information [Wol01]. For example, this could initiate a new generation of computers based on advanced functional elements where magnetic memory and processor are located on a single chip [icvac04, Zak05, Joh08, Die10].

The most prominent approach in this direction is given by diluted magnetic semiconductors (DMS), frequently realized by magnetic doping of II-VI semiconductors with

[1] When the magnetic moments of the ferromagnetic layers are parallel, the spin-dependent scattering of the carriers is minimized, and the material has its lowest resistance. When the ferromagnetic layers are antialigned, the spin-dependent scattering of the carriers is maximized, and the material has its highest resistance [Pri98].

[2] It should be noted that also electrical contacts can be used for spin injection [icvac04].

elements such as paramagnetic Mn^{2+} ions [Fur88, Nag88, Die10, Gaj11]. Many features such as the giant Zeeman splitting of the electronic bands ($g_e \sim 100$) and the giant Faraday rotation are induced by the strong $\mathcal{J}_{s(p)\text{-}d}$ exchange interaction between the electrons (holes) and magnetic ions. Moreover, optically induced coherent precession of the Mn^{2+} magnetic moments can be observed [Cro97a].

The inclusion of magnetic ions in the same spatial region reduces the mobility of carriers in semiconductor QWs. An alternative approach for magnetic semiconductors is therefore based on hybrid systems where a thin ferromagnetic film is placed at the top of the semiconductor. Such structures with well defined profile along the growth axis can be fabricated with monolayer precision. One expects to detect emergent functional properties in such structures which should appear after bringing primary constituents together, i.e., magnetic as in ferromagnets (FM) with optical and electrical tunability as in semiconductors (SC) [Dzh95, Kaw01, Han03, Cro05, Lou07, Jon07, Cio09, Son11]. For this it is required to establish strong exchange interaction between the charge carriers in the SC and magnetic ions in the FM. Control over the concentration of charge carriers and the penetration of their wave function into the FM layer should consequently change the magnitude of exchange coupling between the FM and SC [Kor03]. Therefore, the resulting effects can be divided into two main categories: (i) spin polarization of charge carriers in SC by magnetized FM layer and (ii) inverse action of spin polarized carriers to control the FM magnetization. Previously it was demonstrated that the stray fields of a FM layer influence the spin polarization of conduction band electrons in bulk GaAs [Dzh95] and DMS [Cro97b, Hal07, Das11]. In its turn, illumination of GaAs changed the coercive force of nickel FM layer (photocoercivity), which was attributed to optical control of exchange coupling at the interface between the FM and SC [Dzh95].

For a two-dimensional hole gas (2DHG, the p-system) in a QW the overlap of the hole wave function with the magnetic atoms in a nearby FM layer (the d-system) is believed to result in p-d exchange interaction [Kor03, Mye04, Zai10, Pan09]. In particular, the 2DHG spin system becomes polarized in the effective magnetic field from the p-d exchange [Kor03, Pan09]. Recently it was shown that in addition to this equilibrium 2DHG polarization there is an alternative mechanism involving spin-dependent capture of carriers from the SC into the FM [Kor12, Roz15]. For ferromagnetic (Ga,Mn)As on top of an (In,Ga)As QW, electron capture induces electron spin polarization in the QW, representing a dynamical effect in contrast to the exchange-induced equilibrium polarization. In Ch. 5 we present an extensive study of a new hybrid structure, consisting of a Co layer and a CdTe II–VI semiconductor QW, separated by a nanometre thick barrier.

Chapter 4

Experimental methods

This chapter provides an overview of the experimental techniques that where used in the scope of this thesis. Section 4.1 presents the mode-locked laser system and cryostat used in the majority of the presented experiments. Subsequently the setups for measuring photoluminescence, magneto-optical Kerr effect, and four-wave mixing are discussed.

4.1 Laser and magnet cryostat

Most of the experimental setups used for this thesis are based on the tunable mode-locked *MIRA 900* laser operating in the picosecond pulse regime. Pumped by a 10 W continuous-wave laser at 532 nm the gain medium, titanium-doped sapphire (Ti:sapphire), covers a spectral range between 700 and 980 nm. This is suitable for the (near-)resonant studies of CdTe quantum wells (~ 775 nm) and (In,Ga)As quantum dots (~ 915 nm) in this thesis. The laser pulses are emitted at a repetition rate of 75.75 MHz, corresponding to a repetition period of 13.2 ns. Figure 4.1(a) shows the auto-correlation intensity $|E(t)|^2$ of a Gaussian pulse $E(t) \propto \exp(-t^2/(2\tilde{\tau}_\mathrm{p}^2))$ in the time-domain at the wavelength 776 nm. Considering that the convolution of two Gaussian pulses with the same standard deviation $\tilde{\tau}_\mathrm{p}$ gives a new Gauss with standard deviation $\sqrt{2}\tilde{\tau}_\mathrm{p}$, one extracts from the full width at half maximum (FWHM) in Fig. 4.1(a) the laser pulse duration

$$\tau_\mathrm{p} = 2\sqrt{\ln 2}\tilde{\tau}_\mathrm{p} = 2.3\,\mathrm{ps} \tag{4.1}$$

in the intensity scale. It has to be multiplied by $\sqrt{2}$ for the electric field scale, relevant in the heterodyne detected four-wave mixing experiments (cf. Sec. 4.4). Assuming a Fourier transform limited pulse, $\delta f_0 \tau_\mathrm{p} = 0.441$, one expects a spectral bandwidth of

$$h\delta f_0 = 0.79\,\mathrm{meV}, \tag{4.2}$$

where h is the Planck constant. This value is in good agreement with the measured spectrum in Fig. 4.1(b) for which FWHM = 0.85 meV is extracted. Thus, the laser pulses in the experiments are assumed to be free of chirp.

Most of the measurements were performed in a helium bath cryostat with a split-coil superconducting magnet system generating magnetic fields up to several Tesla. Windows

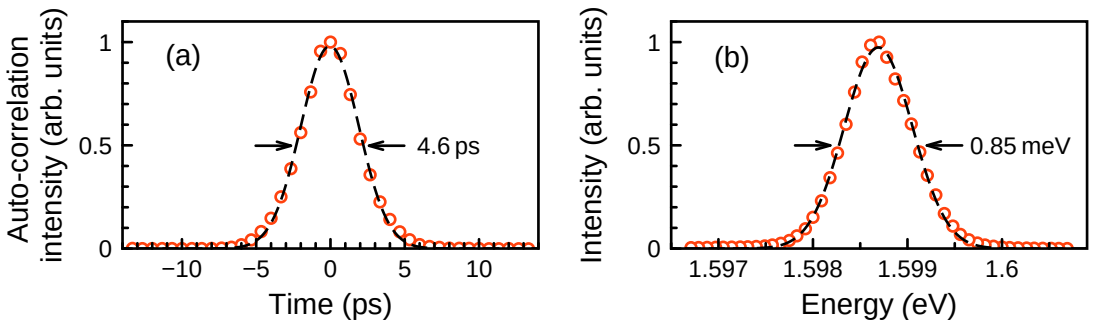

Figure 4.1: Characterization of the picosecond pulses from the mode-locked Ti:sapphire laser *MIRA 900*. (a) Auto-correlation intensity of a Gaussian laser pulse with a laser energy 1.598 eV. (b) Laser pulse spectrum measured with a monochromator and CCD camera. Black dashed lines depict Gaussian fits with FWHM written next to the arrows.

from four sides provide optical access of the laser with wave vector $\boldsymbol{k}$ to the sample mounted in a variable temperature insert (VTI). Magnetic fields $\boldsymbol{B}$ can be applied in Faraday ($\boldsymbol{B} \parallel \boldsymbol{k}$) or Voigt geometry ($\boldsymbol{B} \perp \boldsymbol{k}$). Pumping on the liquid helium in the VTI allows one to achieve minimal temperatures of the helium bath down to $T_{\mathrm{bath}} = 2\,\mathrm{K}$. The sample is mounted on a special holder that provides several optional features: The magnetic field near the sample can be measured with high accuracy using a Hall sensor. If necessary, a lens with high aperture can collect a maximal amount of photoluminescence. The sample can be rotated around an axis parallel to the incident light or vertically with respect to the experimental table. The latter allows one to measure in a tilted magnetic field geometry. Oblique field measurements are alternatively realized using a second helium bath cryostat without superconductig magnet system, but two orthogonal, external electromagnets surrounding the VTI. This makes it possible to scan both field components independently.

4.2 Photoluminescence spectroscopy

The setup for measuring photoluminescene (PL) is sketched in Fig. 4.2. It can be used for time-integrated or time-resolved measurements as discussed in the following.

4.2.1 Time-integrated photoluminescence

The beam of a tunable Ti–sapphire laser is focused on a sample into a spot with diameter of 100-500 μm. For time-integrated PL measurements, continuous wave lasers, e.g., HeNe or frequency doubled Nd:YAG, can be used alternatively for the excitation. The power densities do not exceed $100\,\mathrm{Wcm}^{-2}$. The emitted light is passed into a single grating spectrometer (resolution $\sim 0.1\,\mathrm{nm}$) equipped with an avalanche photodiode (APL), or nitrogen-cooled charged coupled device (CCD camera).

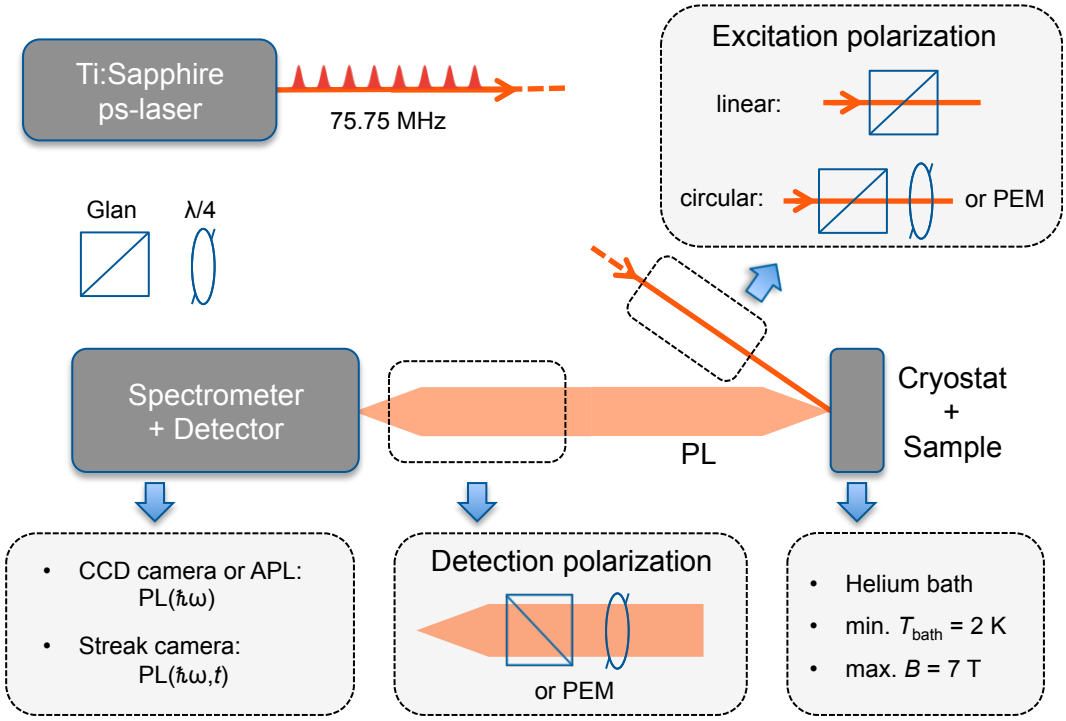

Figure 4.2: Setup for measuring photoluminescence (PL). For time resolved measurements the streak camera is triggered with the laser repetition frequency of 75.75 MHz. Glan is the abbreviation for Glan-Taylor prism, $\lambda/4$ denotes a quarter-wavelength retardation plate. Abbreviations: PEM = photo-elastic modulator; CCD = charged coupled device; APL = avalanche photodiode.

For measurements of the circular polarization degree (cf. Eq. (1.19))

$$\rho_{\mathrm{c}}^{\mathrm{exc}} = \frac{I_{+}^{\mathrm{exc}} - I_{-}^{\mathrm{exc}}}{I_{+}^{\mathrm{exc}} + I_{-}^{\mathrm{exc}}}, \tag{4.3}$$

where I_{+}^{exc} and I_{-}^{exc} are the intensities of right and left circularly polarized polarized PL, the PL passes a detection polarization scheme. Either it consists of a half-wavelength retarder in front of a linear polarizer, or a photo-elastic modulator (PEM) in conjunction with a two-channel photon counting system. Circular or linear polarized excitation is indicated with exc = σ or π, respectively, and realized by the polarization optics in the excitation laser path (cf. inset in Fig. 4.2).

For optical orientation and Hanle effect measurements we use a σ^{+} circularly polarized excitation beam (exc = +). Here, a PEM can be introduced in the excitation path, while one of the circular polarization components (σ^{+}) is measured in the detection path. This allows the suppression of effects related to dynamic nuclear polarization. The modulation parameter

$$\eta = \frac{I^{+} - I^{-}}{I^{+} + I^{-}} \tag{4.4}$$

can be measured also with a PEM in the excitation path, whereas the total intensity is measured using a depolarization wedge in the detection path.

4.2.2 Time-resolved photoluminescence

The setup for time-resolved PL (TRPL) is also based on the sketch in Fig. 4.2. The repetition rate of the mode-locked Ti–sapphire laser, 75.75 MHz, is used as a trigger for the streak camera providing a time resolution of 20 ps. The laser beam is focused into a spot with a diameter of approximately 200 μm and the pulse fluences does not exceed 1 μJcm^{-2}. The degree of polarization follows the definition of Eq. (4.3). However, no PEM is used here. The linear and circular polarization of optical excitation and detection are selected by rotating $\lambda/2$ and $\lambda/4$ plates, respectively, in conjunction with a Glan–Thompson prism. The same single grating spectrometer is used as for time-integrated PL measurements.

4.3 Magneto-optical Kerr effect

Magneto-optical effects (cf. Sec. 1.3.3) can be studied using time-resolved pump-probe spectroscopy or time-integrated measurements of the magnetization curves.

4.3.1 Time-resolved pump-probe spectroscopy

Spin dynamics can be studied with a pump-probe setup illustrated in Fig. 4.3. The output of a mode-locked laser splits into two beams, pump and probe, respectively. A pulse delay τ between both beams can be controlled by reflectors mounted on a motorized mechanical translation stage in the path of pump. Before entering the sample, the pump beam is modulated with a photoelastic modulator (PEM), switching periodically its polarization between left- and right-handed circular at a frequency of 42 kHz. The probe beam enters the sample being linearly polarized. The power ratio between probe and pump should be in the order of 1:10. After reflection from the sample, probe is sent through a Glan-Taylor prism (Glan) and the two orthogonal linear polarized outputs are focused on the diodes of a balanced photo-detector. A half-wavelength plate allows one to tune its output-current to zero when pump is blocked and the external magnetic field is switched off. Afterwards, pump-induced polarization changes can be measured when filtering the resulting output-current for the PEM frequency using a lock-in amplifier.

4.3.2 Static magneto-optical characterization

The magnetization curves of a ferromagntic thin film (cf. Fig. 3.1(c)) are measured with a single Ti–sapphire laser beam. The magnetic field is applied along the growth axis z of the sample in the Faraday geometry for the polar magneto-optical Kerr effect (P-MOKE) and in the plane of the samples in the Voigt geometry for the longitudinal (L-MOKE). The linearly polarized laser beam is focused on the sample into a spot with a diameter of approximately 300 μm and the power does not exceed 1 mW. The reflected beam passes

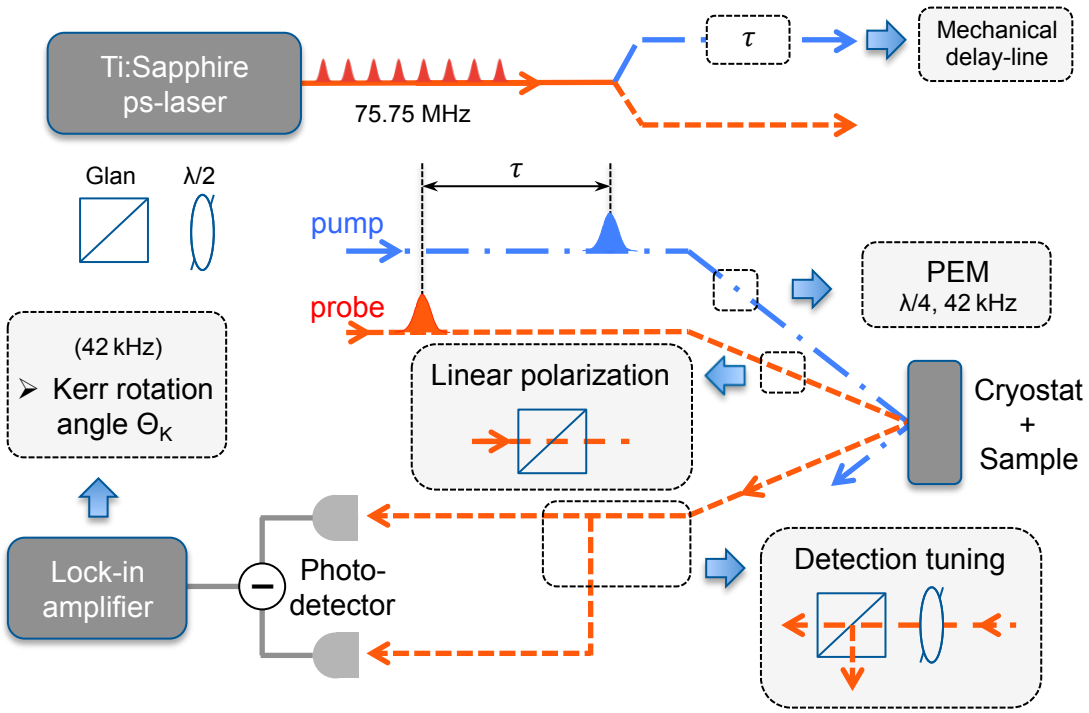

Figure 4.3: Setup for measuring degenerate pump-probe Kerr rotation (reflection geometry). The laser beam with picosecond pulses at a repetition rate of 75.75 MHz is split into a pump and a probe beam. A mechanical delay-line is used to control their time delay τ. Pump is modulated by a photoelastic modulator (PEM) which periodically switches its polarization from left-handed to right-handed circular at a frequency of 42 kHz. Probe is linearly polarized before entering the magnet-cryostat. The detection scheme uses a Glan-Taylor prism (Glan) which divides the probe into an orthogonal linear polarized basis. A half-wavelength plate ($\lambda/2$) allows to tune the output of a balanced photo-detector to zero. Pump-induced polarization changes after the reflection of probe from the sample can be precisely measured when filtering the resulting output-current for the PEM frequency using a lock-in amplifier.

through a PEM in conjunction with a linear analyzer and a photodetector (silicon photodiode). The main axis of the PEM is perpendicular to the initial polarization of the incident light, whereas the analyzer axis is rotated by 45°. The rotation angle of the polarization is proportional to the measured signal, which is homodyne-detected at double the resonance frequency of the PEM (80 kHz) using a lock-in amplifier. In addition, MOKE signals are measured using a spectrally broad white-light source (tungsten lamp). In this way one confirms that the Kerr signals from a ferromagnet-semciconductor hybrid structure originate from the ferromagnetic thin film with a weak spectral dependence in the region of interest, 700-800 nm (Ch. 5).

4.4 Four-wave mixing with heterodyne detection

While the pump-probe signal corresponds to the component radiating in the probe direction, degenerate four-wave mixing (FWM) is measured in an (almost) background free, diffracted direction (cf. Sec. 2.2). In some experiments, however, all excitation beams are co-linear and the diffracted and reflected beams are degenerated in $\boldsymbol{k}$, e.g., in the groups of *Langbein* [Lan06] and *Kasprzak* [Fra16]. This geometry has the benefit to ensure phase matching, i.e. $|2\boldsymbol{k}_2 - \boldsymbol{k}_1| > |\boldsymbol{k}_i|$ (i = 1,2), even for thick samples. The signal is still distinguishable when frequency shifting pulses 1 and 2 in the range of several tens of MHz by acousto–optic modulators (AOMs) [Bor08]. This shift is negligible compared to the overall pulse width $\sim 0.1\,\mathrm{THz}$ of a picosecond laser source. It enables, however, the *heterodyne detection* of the signal frequency $f_\mathrm{S} = 2f_2 - f_1$ using lock-in techniques.

The experimental setup used for the measurements for this thesis is schematically shown in Fig. 4.4. It uses the mode-locked Ti:sapphire laser and magnet cryostat described in Sec. 4.1. The laser splits into four different beams using non-polarizing beam splitter cubes. Three of them are required for the FWM generation, and the fourth one is used as a reference pulse in the heterodyne detection. Three delays between all four pulses can be scanned by reflectors mounted on mechanical translation stages. The distance between the first and second pulse, τ_{12}, and second and third pulse, τ_{23}, is controlled using two 27 cm long translation stages which cover a maximum delay of 1.8 ns. The reference delay-line measures 15 cm length and covers maximal 1 ns. The FWM experiment is performed in the reflection geometry. The first pulse with wave vector $\boldsymbol{k}_1$ impacts the sample at an incidence angle of $\sim 6°$. Pulses 2 and 3 are spatially overlapped after the delay lines ($\boldsymbol{k}_2 = \boldsymbol{k}_3$) and hit the sample in the same spot at slightly bigger incident angle of $\sim 7°$. The beams are focused by a spherical mirror with a focal distance of 200 mm, resulting in a spot diameter on the sample of $\sim 200\,\mu$m. Polarization and intensity of the pulses can be controlled individually with polarization optics consisting of half-wavelength retarders and linear polarizers (Glan). The retarders are mounted in motorized rotation stages that allow precise scans of the beam power (respectively, pulse energy).

The FWM signal is collected along the $\boldsymbol{k}_\mathrm{S} = 2\boldsymbol{k}_2 - \boldsymbol{k}_1$ direction. The phase matching condition is not sensitive to the z-component of the wave vector $\boldsymbol{k}_\mathrm{S}$ since the signal originates from the quantum well or quantum dot layer which has a thickness that is significantly smaller than the wavelength of light in the corresponding semiconductor material. Interferometric heterodyne detection is used, where the FWM signal and reference beam are overlapped at a balanced detector [Cho92, Bor08]. In front of the photo diodes, the electric fields E_S and E_ref are spatially overlapped in a 50:50 beam splitter. Considering its field transmission/reflection scheme [Bor08], the two outputs of the beam splitter read $E_\pm = (E_\mathrm{ref} \pm E_\mathrm{S})/\sqrt{2}$. The balanced photo-detector generates a photo-current

$$I_\mathrm{d} \propto |E_+|^2 - |E_-|^2 \propto \mathrm{Re}[E_\mathrm{S} E_\mathrm{ref}^*]. \tag{4.5}$$

The optical frequencies of pulse 1 and the reference pulse are shifted by +40 MHz and

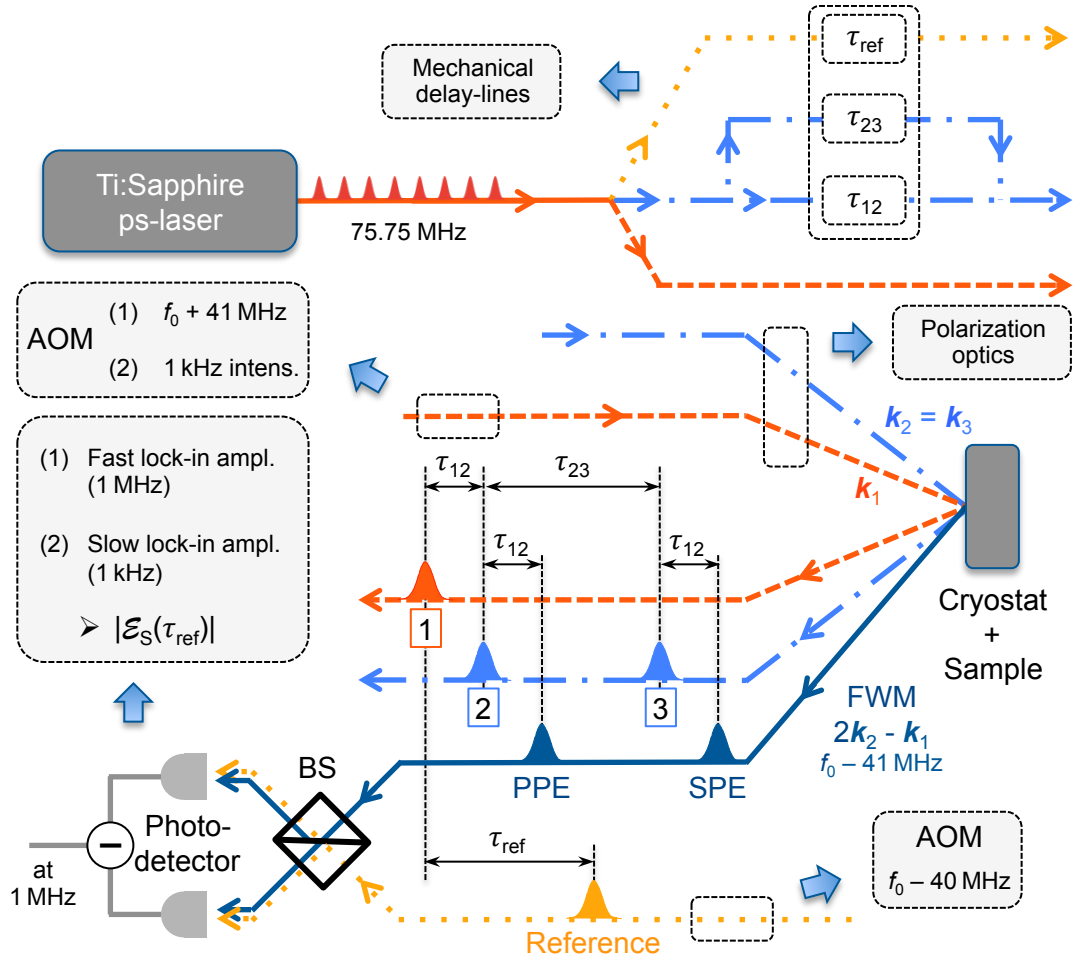

Figure 4.4: Setup for measuring degenerate transient four-wave mixing (FWM) in reflection geometry. The laser beam with picosecond pulses at a repetition rate of 75.75 MHz is split into four beams. One of them serves as a reference pulse (orange dotted) for heterodyne detection, and the others are required for the FWM (dark blue solid) generation: The first (red dashed) and second (light blue dot-dashed) pulses create the primary photon echo (PPE), while together with the third pulse (light blue dot-dashed) they create the stimulated photon echo (SPE). The time delays, τ_{12} and τ_{23}, defining the temporal appearance of the photon echoes are controlled by two mechanically delay-lines. A third delay-line controls the measurement time τ_{ref} at which the cross-correlation $|\mathcal{E}_S|$ between reference and FWM electric field amplitudes is measured. $|\mathcal{E}_S(\tau_{\mathrm{ref}})|$ is extracted from the output of a balanced photo-detector after filtering it with two lock-in amplifiers. The required modulation comes from two acousto-optical modulators (AOMs) giving radio-frequency shifts in the centre-optical laser frequency f_0 for pulses 1 and reference. $\boldsymbol{k}_i$ is the wave vector of pulse $i = 1,2,3$. BS denotes a 50:50 non-polarizing beam splitter.

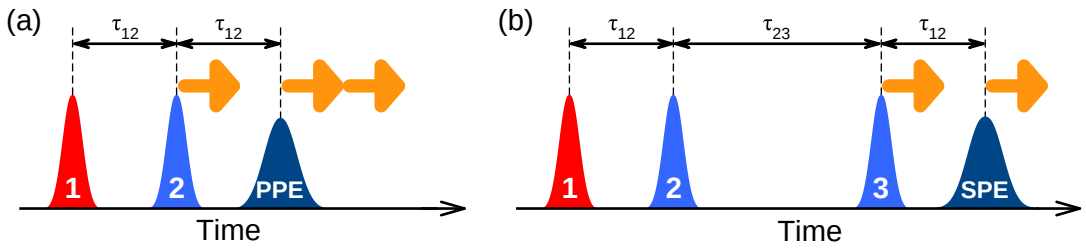

Figure 4.5: FWM pulse sequence for the explanation of a dual delay-line scan. (a) For one step in the τ_{12} delay the reference has to make two steps in τ_{ref} in order to remain fixed on the primary photon echo (PPE) amplitude, as indicated by the orange arrows. (b) For one step in the τ_{23} delay the reference has to make one steps in τ_{ref} in order to remain fixed on the secondary photon echo (SPE) amplitude.

$-41\,\mathrm{MHz}$ with two AOMs. Therefore, the frequency of the resulting interference signal $\mathrm{Re}[E_{\mathrm{S}}E^{*}_{\mathrm{ref}}]$ is

$$|2f_2 - f_1 - f_{\mathrm{ref}}| = 1\,\mathrm{MHz}. \tag{4.6}$$

Note that there is also a sum of the frequencies (81 MHz) which is filtered out by a digital filter. The 1 MHz component is selected from I_{d} using a high-frequency lock-in amplifier. The signal-to-noise ratio is further reduced by a second lock-in amplifier filtering for frequencies 1 kHz that are imprinted by an intensity modulation from the AOM in the path of pulse 1. The phase of the signal is locked at short times because all of the pulses originate from the same laser source. However, random fluctuations of the optical phase in the different beam paths at time scales longer than 1 ms are not suppressed because no active stabilization of the beam paths is implemented in the setup. Therefore, only the amplitude of the signal is accessible in the measurement procedure. Still, heterodyne detection provides a high-sensitivity, background free measurement of the cross-correlation function for the absolute value of the FWM electric field amplitude

$$|\mathcal{E}_{\mathrm{S}}(\tau_{\mathrm{ref}})| \propto \left| \int_{-\infty}^{\infty} E_{\mathrm{S}}(t) E_{\mathrm{ref}}(t - \tau_{\mathrm{ref}}) \mathrm{d}t \right| \tag{4.7}$$

when scanning the reference pulse delay time τ_{ref}. In general, $\tau_{\mathrm{ref}} = 0$ is defined as the temporal overlap between pulses 1 and reference (cf. Fig. 4.4). In Ch. 7, however, it is defined relative to the arrival time of pulse 3.

We study inhomogeneously broadened systems where the FWM signal is given by photon echoes (cf. Sec. 2.2.1). Figure 4.4 shows that pulses 1 and 2 create the primary photon echo (PPE), while together with pulse 3, they create the stimulated photon echo (SPE). Measurements of the coherence time T_2 (PPE) and lifetime T_1 (SPE) are performed by dual delay-line scans, as sketched in Figs. 4.5(a) and 4.5(b). In order to keep the reference fixed on the PPE (SPE) amplitude, an increase of τ_{12} (τ_{23}) by one step has to be compensated by increasing the reference delay τ_{ref} for two steps (one step).

Part II

Spin orientation in a ferromagnet-semiconductor hybrid

Chapter 5

Long-range p-d exchange interaction in a Co-CdTe hybrid structure

This chapter is about investigations of a new ferromagnet-semiconductor (FM-SC) hybrid structure consisting of a Co layer and a CdTe semiconductor quantum well (QW), described in Sec. 5.1. The experimental proof of a FM-SC exchange coupling in Secs. 5.2, 5.3, and 5.4 is obtained by measurements of the photoluminescence (PL) polarization with the experimental technique described in Sec. 4.2. FM induced circular polarization is compared with direct measurements of the Co thin-film magnetization is Sec. 5.5. The magnitude of the exchange splitting is measured in Sec. 5.6. A theoretical concept describing the observed phenomena is presented in Sec. 5.7.

An introduction to modern spintronic devices can be found in Sec. 3.3. The results of this chapter have been published in a similar form in Refs. [Kor16, Aki17].

5.1 The Co-CdTe hybrid samples

A schematic presentation of the studied ferromagnet-semiconductor hybrid structures is shown in Fig. 5.1(a). A 10 nm thick CdTe QW sandwiched between $Cd_{0.8}Mg_{0.2}Te$ barriers was grown by molecular-beam epitaxy (MBE) on top of a (100)-oriented GaAs substrate. The bottom barrier has a width of 3.2 μm while the cap layer is gradually changing in width, defining the spacer thickness d_s. Without contact to the ambient atmosphere, the structures were transferred into a second MBE chamber for the deposition of the Co layer. As for the cap layer, various thicknesses of the Co layer, d_{Co}, were produced by a time-controlled linear movement of the main shutters in each of the two MBE chambers.[1]

A set of structures with widely varying parameters was grown, as listed in Tab. 5.1.

[1] A more detailed description of the sample preparation can be found in the online version of Ref. [Kor16].

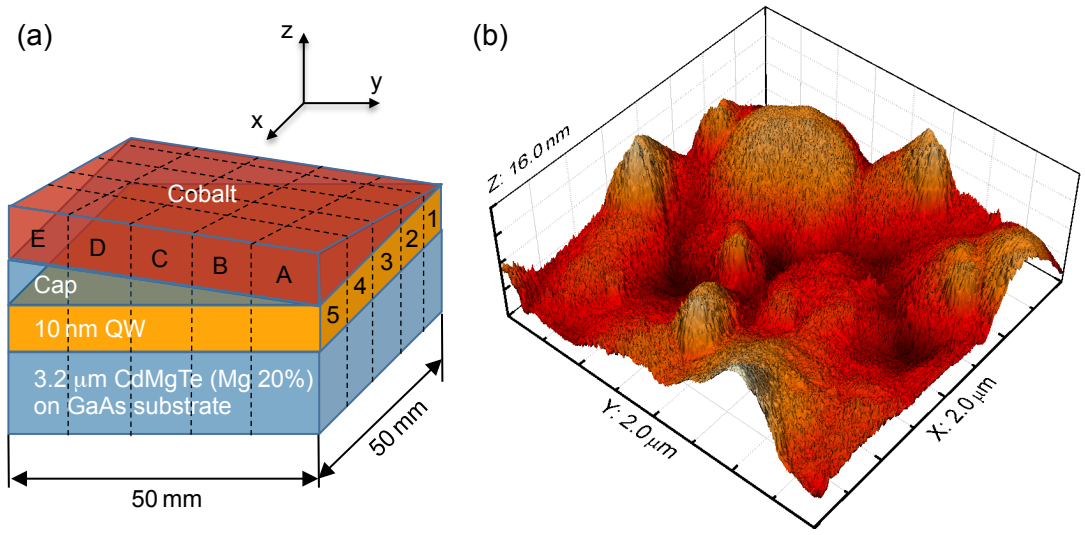

Figure 5.1: (a) Sketch of the double gradient structure 2. (b) Atomic force microscopy image of structure 2 with a Co-film thickness $d_{\mathrm{Co}} = 5\,\mathrm{nm}$. Note the different scaling on the z axis.

In structure 1 the (Cd,Mg)Te spacer thickness d_{s} increases continuously from 5 nm to 15 nm over a lateral structure size of 5 cm (wedge shape), and the Co film has a thickness of 7 nm. The semiconducting parts of the other structures are similar to those of structure 1, except for the spacer thickness d_{s}, which varies over a 3 cm lateral dimension from a thickness of zero to 10 nm for structure 2, from zero to 14 nm for structure 3, and from 10 up to 40 nm for structure 4. In addition, the Co-film thickness, d_{Co} is varied in discrete steps of 1 nm from zero to 6 nm normal to the spacer thickness gradient, followed by an area with a constant Co-film thickness of 16 nm. Atomic force microscopy on structure 2 with a 5 nm thick Co layer shows a non-uniform Co growth, with islands having lateral sizes of tens of nanometres (Fig. 5.1(b)). In the following experimental data are mainly presented for structure 2, if not mentioned otherwise. However, the key observations concerning the proximity effect are similar for all structures.

	Code	Spacer thickness d_{s} (nm)	Co thickness d_{Co} (nm)
Structure 1	120313B	5–15	5
Structure 2	070714A	0–10 and 50	0–6[a] and 16
Structure 3	070214A	0–14 and 54	0–6[a] and 16
Structure 4	051415A	10–40	10

[a] In dicrete steps of 1 nm

Table 5.1: Parameters of the various hybrid structures studied in this chapter.

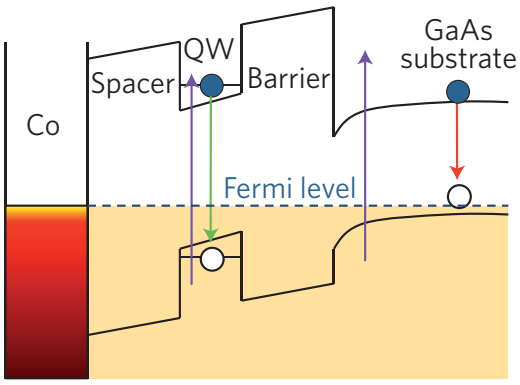

Figure 5.2: Band structure of the investigated structures. The violet arrow indicates the excitation energy, whereas the green and red arrows correspond to PL from the QW and GaAs substrate, respectively.

5.2 Ferromagnet-induced quantum well photoluminescence circular polarization

The magnetization of the Co layers is oriented in the plane of the structure ($\boldsymbol{M}_{\mathrm{Co}} \perp \boldsymbol{z}$).[1] An out-of-plane magnetization component can be induced by applying an external magnetic field in the Faraday geometry $\boldsymbol{B}_{\parallel}$ (longitudinal field parallel to the structure growth axis $\boldsymbol{z} \parallel [001]$). In all cases, the Co layers are semitransparent for laser light exciting the sample along $\boldsymbol{z}$ in either linear (π) polarization, or unpolarized using a depolarizing wedge. The band structure of the hybrid system is sketched in Fig. 5.2. For photon energies less than the band gap energy $E_{\mathrm{CdMgTe}} = 2\,\mathrm{eV}$ of the barrier, only the QW is excited. The photoluminescence (PL) emitted by the QW is analyzed with respect to its circular polarization σ^+ and σ^-, to determine the degree of circular polarization $\rho_{\mathrm{c}}^{\pi}(B_{\parallel})$ of the PL under π-excitation according to Eq. (4.3). Moreover, the modulus of the polarization difference

$$\delta\rho_{\mathrm{c}}^{\pi}(B_{\parallel}) = \left|\overline{\rho}_{\mathrm{c}}^{\pi}(B_{\parallel})\right| = \left|\frac{\rho_{\mathrm{c}}^{\pi}(+B_{\parallel}) - \rho_{\mathrm{c}}^{\pi}(-B_{\parallel})}{2}\right| \tag{5.1}$$

for oppositely oriented fields is used as a measure of the field-induced signal.

Figure 5.3(a) shows $\delta\rho_{\mathrm{c}}^{\pi}$ recorded for $B_{\parallel} = 10\,\mathrm{mT}$ (orange dots) as a function of the detection energy for a spacer thickness $d_{\mathrm{s}} = 10\,\mathrm{nm}$ at a temperature $T_{\mathrm{bath}} = 2\,\mathrm{K}$. For comparison the total PL intensity[2] $I_0 = I_+^{\pi} + I_-^{\pi}$ is shown (blue line), exhibiting two main lines, centered at 1.63 eV (X) and at $\sim 1.60\,\mathrm{eV}$ (e–A^0), with a wide flank towards lower energies. The X-line is assigned to the heavy-hole exciton transition of the QW. The e–A^0-line, on the other hand, is associated with electrons recombining with holes bound to acceptors. This assignment is supported by time-resolved PL (TRPL) data, where the X-line decays within 50 ps, whereas the e–A^0 PL is observed for much longer

[1] Compare with the MOKE measurements discussed in Sec. 5.5.

[2] $I_{\mathrm{det}}^{\mathrm{exc}}$ is the PL intensity with polarization of the excitation (detection) exc (det) = π or $\sigma^{\pm} \equiv \pm$, respectively.

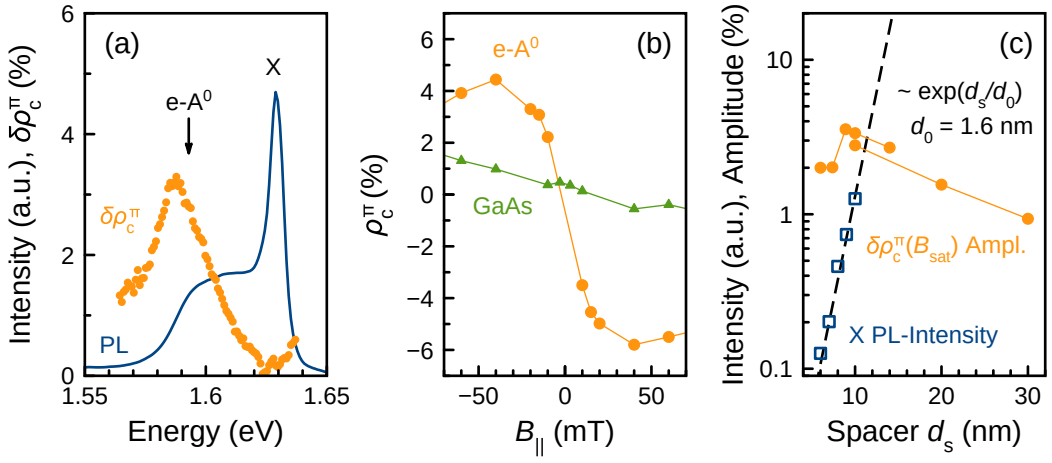

Figure 5.3: (a) PL spectrum (blue line) and polarization difference $\delta\rho_c^\pi$ (orange circles) between the circular polarizations ρ_c^π according to Eq. (5.1) measured for $B_\parallel = 10\,\mathrm{mT}$ at $T_\mathrm{bath} = 2\,\mathrm{K}$; data recorded for linearly polarized pulsed excitation with a photon energy of 1.69 eV and an excitation density $20\,\mathrm{W\,cm^{-2}}$. CdMgTe spacer thickness $d_\mathrm{s} = 10\,\mathrm{nm}$ and Co thickness $d_\mathrm{Co} = 4\,\mathrm{nm}$. (b) $\rho_c^\pi(B_\parallel)$ detected at the lower energy flank of the e–A^0 transition in the QW around 1.59 eV, as indicated by the vertical arrow in (a) (orange circles) and the GaAs substrate at 1.49 eV (green triangles); an up-down field scan revealed no hysteresis. (c) Dependence of the exciton PL intensity on spacer thickness d_s for $d_\mathrm{Co} = 4\,\mathrm{nm}$ (blue squares). The dashed line is an exponential fit, $\exp(d_\mathrm{s}/d_0)$, with characteristic length $d_0 = 1.6\,\mathrm{nm}$. The orange circles show the spacer thickness dependence of the proximity effect amplitude $\rho_c^\pi(B_\mathrm{sat})$ for the different structures, which seems to be slowly varying.

times, of the order of nanoseconds (Fig. 5.4(a)). From the typical exciton binding energy of 10 meV and the 30 meV distance between the two lines, one deduces a hole–acceptor binding energy of $E_{A^0} \approx 40\,\mathrm{meV}$, which agrees well with values reported for a hole bound to a shallow acceptor in CdTe [Cro66, Bar98]. The circular polarization $\rho_c^\pi(B_\parallel)$ of the PL varies considerably (Fig. 5.3(a)), with a maximum difference at the e–A^0-line. Variation of the laser photon energy $\hbar\omega_\mathrm{exc}$ in the range 1.62 eV–1.69 eV leads to no strong change of ρ_c^π. Figure 5.3(b) shows the magnetic field dependence of $\rho_c^\pi(B_\parallel)$ for excitation at $\hbar\omega_\mathrm{exc} = 1.69\,\mathrm{eV}$ and detection at $\hbar\omega_\mathrm{PL} = 1.59\,\mathrm{eV}$.[1] Up-and-down field scans show a non-hysteretic behavior of $\rho_c^\pi(B_\parallel)$, saturating for field strengths of $B_\mathrm{sat} = 20\,\mathrm{mT}$ at amplitude $\rho_c^\pi(B_\mathrm{sat}) \approx 4\%$, which is an order of magnitude larger than without the Co layer (see Fig. 5.10). Figure 5.3(b) also shows the dependence $\rho_c^\pi(B_\parallel)$ detected at $\hbar\omega_\mathrm{exc} = 1.494\,\mathrm{eV}$, corresponding to the e–A^0 PL transition in the GaAs substrate (green triangles), which is separated by more than 3 μm from the FM. In contrast to the QW emission, a much smaller polarization without any saturation is observed. Therefore the

[1] The sign of ρ_c^π was determined by comparing with the sign of polarization in a diluted magnetic semiconductor (DMS) $Cd_{0.64}Mn_{0.06}Mg_{0.30}Te/Cd_{0.94}Mn_{0.06}Te$ QW structure for the same direction of magnetic field. In the DMS the sign of the circular polarization is positive (σ^+) for $B_\parallel > 0$ [Gaj78, Fur88].

PL polarization from the CdTe QW is clearly induced by the proximity of the FM.

TRPL gives insight into the kinetics of the spin polarization after linearly polarized, pulsed excitation. Spectrally resolved PL intensity transients are shown in Fig. 5.4(a), from which one derives the temporal dependence of the FM-induced $\delta\rho_c^\pi(t)$ in Fig. 5.4(b) for a magnetic field of 40 mT, applied in the Faraday geometry: $\delta\rho_c^\pi(t)$ increases continuously with time. Initially being non-polarized, the photo-excited carriers acquire spin polarization with a characteristic rise time of $\tau_{fm} \approx 2$ ns, obtained from an exponential fit (dashed line). In combination with the decay times of 50 ps for the X-line and a few ns for the e–A^0-line, this allows one to explain the absence of polarization for the X-line: the exciton does not live long enough to acquire polarization from the FM.[1]

To understand the origin of the FM-induced PL polarization from the QW one has to address the following three questions: Are the electrons or the holes in the QW polarized? Which mechanism causes the QW circular polarization? Is there an effective exchange magnetic field exerted by the FM that polarizes the QW carriers?

5.3 Ferromagnet-induced spin polarization of the quantum well heavy holes

As discussed, application of a longitudinal magnetic field $B_\parallel$ causes polarization of the PL. Next, an additional transverse magnetic field $B_\perp$ in the Voigt geometry will be applied according to Fig. 5.5(a) with the goal to depolarize the FM-induced PL polarization. Figure 5.5(b) shows that for $B_\parallel = 4$ mT the polarization difference $\delta\rho_c^\pi$ of the QW PL is about 1%, and not sensitive to $B_\perp$ up to 20 mT. This means that any out-of plane component M_z of the FM magnetization remains fixed in this range of Voigt fields. However, there is a further important consequence. The data also indicate heavy-hole polarization as source of the non-zero $\delta\rho_c^\pi$. Indeed, if $\delta\rho_c^\pi$ arose from electron spin orientation, the Hanle effect should be observed for the electron spins: for electrons with spins polarized along the z-axis the magnetic field $B_\perp$ would induce Larmor precession about $B_\perp$. This precession would decrease the z-component of the electron spin, leading to a PL depolarization $\delta\rho_c^\pi(B_\perp)$ in complete analogy with the Hanle effect observed for optical injection of polarized electron spin. Indeed, under circularly polarized excitation the degree of polarization $\rho_c^\sigma(B_\perp)$ decreases with $B_\perp$ (orange circles in Figs. 5.5(c) and 5.6) with a halfwidth $B_{\perp,1/2} = 18$ mT. However, this decrease is absent for $\delta\rho_c^\pi(B_\perp)$ in the same field range (Fig. 5.5(b)). Moreover, Fig. 5.5(c) shows that application of a 4 mT longitudinal field does not change the Hanle curve (the blue triangles), which means that the magnetization of the FM does not create a magnetic field (for example, due to s–d exchange) that could influence the Larmor precession of the electron spin. Therefore, the out-of-plane magnetization M_z of the FM neither orients electron spins, nor affects their Larmor precession frequency. Thus, one concludes that the FM-induced polarization $\delta\rho_c^\pi$ is directly related to spin polarization of the heavy holes: the in-plane g-factor of the heavy holes is close to zero, such that the $B_\perp$ field cannot depolarize

[1] Another possible contribution will be discussed in Sec. 5.7.

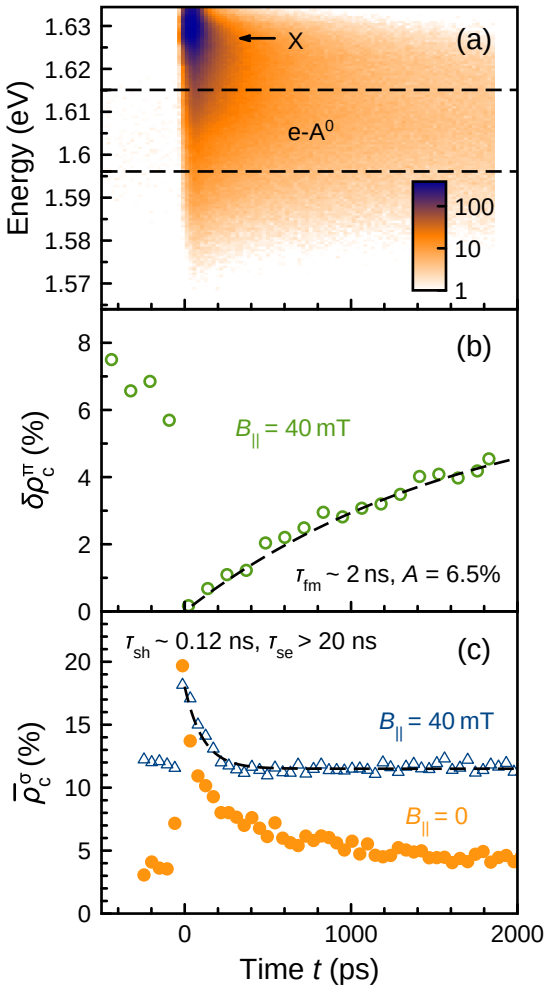

Figure 5.4: Time-resolved spin dynamics. (a) Contour plot of the PL intensity decay from the QW. The dasehd lines indicate the region of interest for polarization measurements corresponding to the e–A^0 transition. (b) Dynamics of the FM-induced proximity effect. The time evolution of the difference of circular polarization degree $\delta\rho_c^\pi$ according to Eq. (5.1) for $B_\parallel = 40\,\mathrm{mT}$ under linearly polarized excitation is shown. The dashed line is a fit according to $\delta\rho_c^\pi(t) = A[1-\exp(-t/\tau_{\mathrm{fm}})]$ with $\tau_{\mathrm{fm}} \approx 2\,\mathrm{ns}$ and $A = 6.5\,\%$. (c) Optical orientation kinetics. The average circular polarization under excitation by σ^+-polarized light $\overline{\rho}_c^\sigma(t)$ according to Eq. (5.2) is shown for $B_\parallel = 40\,\mathrm{mT}$ (blue triangles) and $B_\parallel = 0$ (green circles). The black dashed line gives a double exponential fit to the data for $B_\parallel = 40\,\mathrm{mT}$ with $\overline{\rho}_c^\sigma(t) = \rho_{0,\mathrm{h}}\exp(-t/\tau_{\mathrm{sh}}) + \rho_{0,\mathrm{e}}\exp(-t/\tau_{\mathrm{se}})$, where $\rho_{0,\mathrm{h}} = 7\,\%$, $\tau_{\mathrm{sh}} = 0.12\,\mathrm{ns}$, $\rho_{0,\mathrm{e}} = 11.5\,\%$, and $\tau_{\mathrm{se}} > 20\,\mathrm{ns}$.

them [Deb13].

TRPL data allow one to determine the electron and hole spin dynamics for comparison with the nanosecond kinetics of the proximity effect. Figure 5.4(c) shows the optical orientation

$$\overline{\rho}_c^\sigma(t, B_\parallel) = \frac{\rho_c^\sigma(+B_\parallel, t) + \rho_c^\sigma(-B_\parallel, t)}{2} \tag{5.2}$$

at $B_\parallel = 40\,\mathrm{mT}$, averaged for opposite magnetic field directions, to exclude any contribution from the FM-induced polarization. One finds two decay components with strongly different spin relaxation times, τ_{se} and τ_{sh}. The shorter one, $\tau_{\mathrm{sh}} = 0.12\,\mathrm{ns}$, corresponds to holes, whereas the much longer time, $\tau_{\mathrm{se}} > 20\,\mathrm{ns}$, corresponds to electrons (cf. Sec. 3.1.1). Note that the zero-field decay of $\rho_c^\sigma(t)$ in Fig. 5.4(c) contains an additional contribution with $\tau_{\mathrm{deph}} \approx 1\,\mathrm{ns}$ due to electron spin dephasing in the randomly oriented stray fields of the FM. The stray fields also determine the 18 mT width of the Hanle

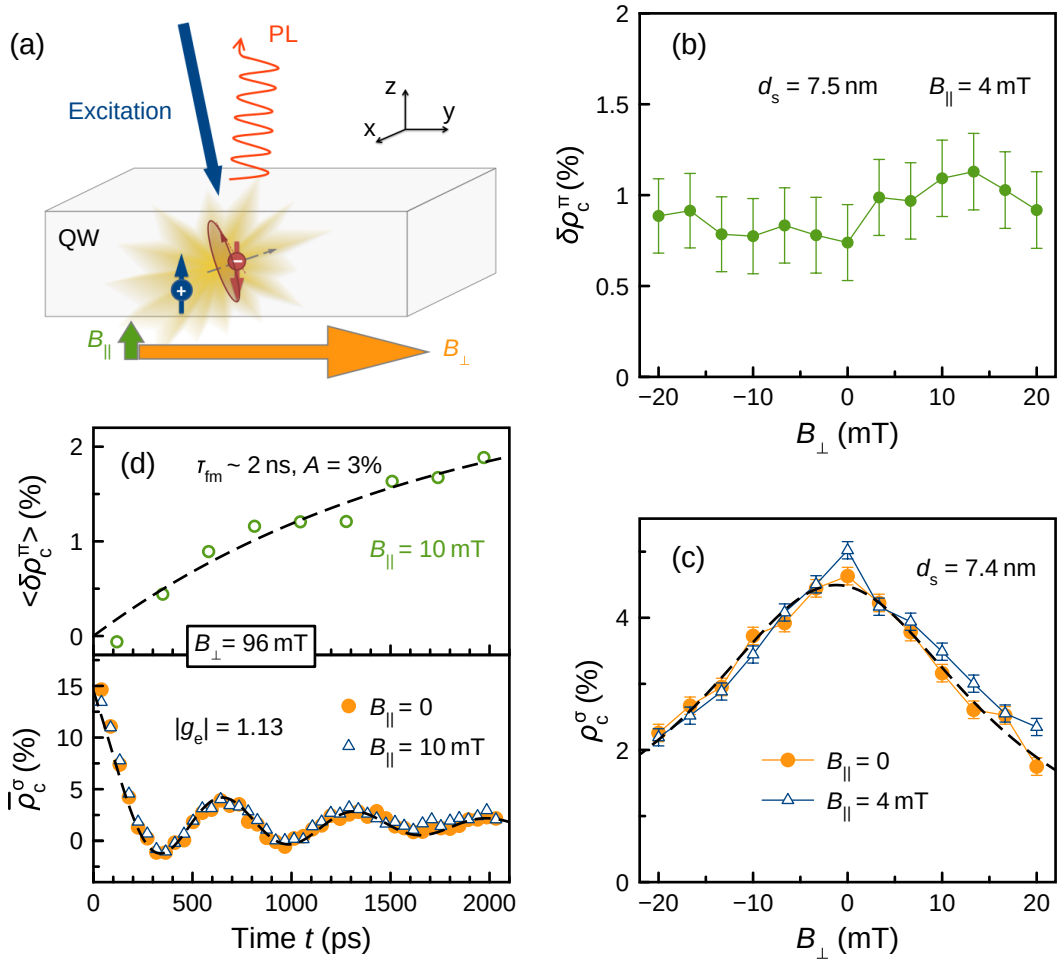

Figure 5.5: FM-induced spin polarization of the QW heavy holes bound to acceptors. (a) Sketch of the experiment in crossed magnetic fields. (b) Structure 1. Dependence of $\delta\rho_c^\pi(B_\perp)$ on the magnetic field in Voigt geometry in presence of a longitudinal field $B_\parallel = 4\,\mathrm{mT}$. (c) Hanle effect $\rho_c^\sigma(B_\perp)$ in the absence of a longitudinal field (orange circles) and in the presence of a longitudinal field $B_\parallel = 4\,\mathrm{mT}$ (blue triangles). The black dashed line shows a Lorentz-fit with half-width $B_{\perp,1/2} = 18\,\mathrm{mT}$. (d) Structure 2, $d_s = 10\,\mathrm{nm}$. Upper panel: kinetics of the proximity effect according to Eq. (5.3) at $B_\perp = 96\,\mathrm{mT}$, $B_\parallel = 10\,\mathrm{mT}$. Fit according to Fig. 5.4(b) with $\tau_{fm} \approx 2\,\mathrm{ns}$ and $A = 3\,\%$. Bottom panel: kinetics $\rho_c^\sigma(t)$ of the optical orientation in a magnetic field of $B_\perp = 96\,\mathrm{mT}$ for $B_\parallel = 0$ (orange circles) and $B_\parallel = 10\,\mathrm{mT}$ (blue triangles). The dashed line is a fit according to $\rho_c^\sigma(t) = \rho_{0,h}\exp(-t/\tau_{sh}) + \rho_{0,e}\exp(-t/T_{2,e}^*)\cos(g_e\mu_B B_\perp t/\hbar) + C$, with $\rho_{0,h} = 8\,\%$, $\tau_{sh} = 0.15\,\mathrm{ns}$, $\rho_{0,e} = 5\,\%$, $|g_e| = 1.13$, $T_{2,e}^* = 1\,\mathrm{ns}$, $C = 1.5\,\%$. $T_{bath} = 2\,\mathrm{K}$. Error bars represent standard deviations.

curve, as will be discussed in Sec. 5.4.2. The dephasing determines the spin dynamics and leads to the faster decay of $\rho_c^\sigma(t)$ at $B_\parallel = 0$. Application of a $B_\parallel = 40\,\mathrm{mT}$ Faraday

field suppresses the stray field impact. The comparison of $\rho_c^\sigma(t,B_\parallel = 40\,\mathrm{mT})$ with $\delta\rho_c^\pi(t)$ in Figs. 5.4(c) and 5.4(b), respectively, shows that the FM-induced polarization kinetics is much faster ($\tau_{\mathrm{fm}} \approx 2\,\mathrm{ns}$) than the electron spin kinetics ($\tau_{\mathrm{se}} > 20\,\mathrm{ns}$). This is in agreement with the hole spin-flip being much faster than that of the electron. However, it is still considerably slower than the hole spin-flip time of $\tau_{\mathrm{sh}} = 0.12\,\mathrm{ns}$. This faster spin relaxation of the optically oriented holes can be explained by the higher laser photon energy (1.70 eV) with which free holes are excited. Optically excited hot holes become depolarized before they are trapped by acceptors. Remember in this context the the unusual proximity effect shown in Fig. 5.3(c) where only the e–A^0 transition shows a FM-induced polarization. Hence $\rho_c^\pi(t)$ reflects the spin kinetics of holes bound to acceptors, whose spin-flip time can be considerably longer than τ_{sh}. Additional information on the free valence band holes measured by the pump-probe technique can be found in Ref. [Aki17].

Further evidence of the heavy-hole polarization comes from TRPL data in oblique magnetic field. Therefore, the TRPL measurements from Figs. 5.4(b) and 5.4(c) were repeated under additional application of a Voigt field $B_\perp$. In order to isolate the proximity effect, $\delta\rho_c^\pi$ form Eq. (5.1) is averaged for opposite Voigt magnetic field directions, i.e.,

$$\langle\delta\rho_c^\pi(t)\rangle = \frac{\delta\rho_c^\pi(t,B_\parallel,+B_\perp) + \delta\rho_c^\pi(t,B_\parallel,-B_\perp)}{2}. \tag{5.3}$$

For $B_\parallel = 10\,\mathrm{mT}$, the non-oscillating signal in the upper panel of Fig. 5.5(d) increases with time $\tau_{\mathrm{fm}} \approx 2\,\mathrm{ns}$ in spite of the large magnetic field $B_\perp = 96\,\mathrm{mT}$ applied in the Voigt geometry. In contrast, the optical orientation signal $\overline{\rho}_c^\sigma(t,B_\parallel = 10\,\mathrm{mT})$ in the bottom panel of Fig. 5.5(d), oscillates in time in accordance with the electron g factor, $|g_e| = 1.13 \pm 0.01$, and tends to zero.

In conclusion, the out-of-plane magnetization component of the FM is robust in magnetic fields $B_\perp < 100\,\mathrm{mT}$ and the FM-induced PL polarization $\rho_c^\pi(B_\parallel)$ in a longitudinal field originates from spin polarization of heavy holes bound to acceptors.

5.4 Origin of ferromagnet-induced quantum well photoluminescence circular polarization

This section can be taken as a catalog of potential mechanisms responsible for the strong polarization of holes bound to acceptors. Each of the mechanisms will be discussed and compared with the experimental results. It turns out that the results are based on equilibrium spin polarization due to thermal population of spin levels split by p-d exchange interaction (Sec. 5.4.4) which is surprisingly long-ranged.

5.4.1 Magnetic circular dichroism

Magnetic circular dichroism (MCD) is the dependence of the absorption coefficient on the photon helicity. Assuming that MCD is present in the FM layer, the QW would not become excited by linearly (or un-) polarized light and, in fact, one would not measure

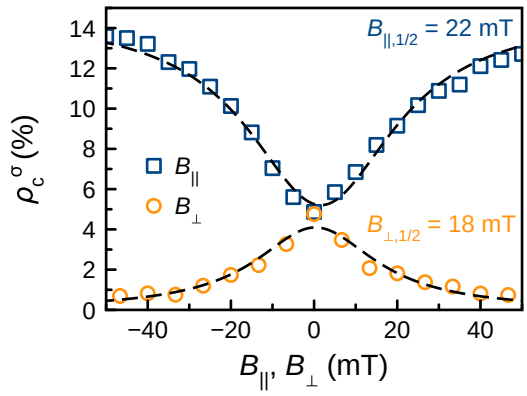

Figure 5.6: Magnetic field dependence of the circular polarization ρ_c^σ. Hanle effect (orange circles) in Voigt geoemtry and "inverted" Hanle effect (blue squares) on strcuture 1 at a temperature $T_{\text{bath}} = 10\,\text{K}$. The black dashed lines show Lorentz-fits with half-width $B_{\perp,1/2} = 18\,\text{mT}$ and $B_{\|,1/2} = 22\,\text{mT}$, respectively.

ρ_c^π, as assumed so far. This would lead to spin polarized electrons that should have became visible already in the TRPL measurements of the previous sections.

In order to check potential influence from MCD on the polarization with a time-integrated technique, detection was done at the e-A^0 PL transition (1.494 eV) of the GaAs substrate, and the laser was scanned with alternating helicity $\sigma^\pm$ across the QW resonances in the range from 1.59 to 1.63 eV with a Faraday-field of $B_\| = \pm 70\,\text{mT}$ applied. Only negligible changes of the PL intensity $< 0.3\%$ were found. Moreover, MCD would lead to spin polarized electrons. Therefore, MCD is not important in the small field range $\sim B_{\text{sat}}$ and the observed $A \approx 4\%$ polarization results from the FM-induced spin polarization of two-dimensional holes. In Sec. 5.6, ρ_c^π will be investigated for much bigger field strengths where MCD plays indeed a role.

5.4.2 Ferromagnetic stray fields

The nearby FM creates a stray magnetic field which can deeply penetrate into the SC [Kor08]. Zeeman interaction can cause a spin splitting in the QW that is leading in equilibrium to a spin polarization of the SC carriers.

As discussed in Sec. 3.1.3, magnetic stray fields affect the dependencies of the circular polarization degree ρ_c^σ on a magnetic field in Voigt geometry (the Hanle effect) and cause an "inverted" Hanle effect in Faraday geometry. Results of such measurements are shown in Fig. 5.6. The Hanle curve (orange circles) results from electron spin precession about $B_\perp$ while the hole depolarization is negligible due to the transversal hole g factor close to zero. Figure 5.6 shows that the half-width of the depolarization curve is $B_{\perp,1/2} = 18\,\text{mT}$ in structure 1 for the 7-10 nm range of spacer thickness. Also shown is the "inverted" Hanle effect (blue squares) where a magnetic field in Faraday geometry increases the circular polarization. The similar characteristic half-width $B_{\|,1/2} = 22\,\text{mT}$ points towards the presence of stray magnetic fields in the QW region due to the domain structure of the FM [Dzh95] or interface roughness [Das11]. Stray fields with a strength $\mu_0 M_s d_{\text{Co}}/w$ appear on length scales comparable with the domain size w [Kor08]. Note that the fringe fields due to hyperfine interaction with the nuclei are about 0.5 mT in CdTe QWs and can be neglected [Zhu07]. As mentioned before, the effect of the stray

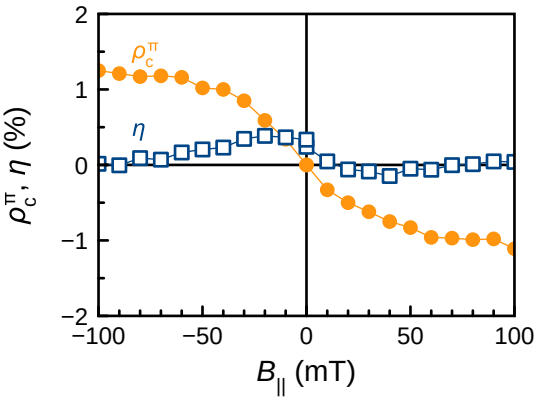

Figure 5.7: Sample 1 excited resonantly at the exciton (1.619 eV) with the detection done at the acceptor transition e–A^0 (1.602 eV). The dependence of the intensity modulation parameter $\eta(B_\parallel)$ on longitudinal field (blue squares, laser with alternate helicity without polarizers in the detection channel) is compared with the FM-induced polarization $\rho_c^\pi(B_\parallel)$ (orange circles, π-excitation). $T_{\mathrm{bath}} = 4\,\mathrm{K}$.

fields is also seen in the TRPL data in the lower panel of Fig. 5.5(d), where they lead to dephasing of the optical orientation of electrons with a characteristic time $\tau_{\mathrm{deph}} = T_{2,\mathrm{e}}^* = (1.0 \pm 0.4)$ ns. The strength of the stray field can be calculated with Eq. (3.7) for the case of an isotropic distribution of random fields. Taking into account $|g_\mathrm{e}| = 1.13$ one obtains theoretically $B_{\parallel,1/2} = B_{\perp,1/2} = (35 \pm 14)\,\mathrm{mT}$, which agrees with the experimentally observed value of $B_{\parallel,1/2}$. The difference in measurements, $B_{\parallel,1/2} \neq B_{\perp,1/2}$, indicates an anisotropic distribution of the FM random fields. Small local fields in the ten mT range can affect the electron spin precession kinetics. However, the polarization of electrons (and of holes whose longitudinal g factor has a similar value [Deb13]) due to the thermal distribution between the spin sublevels at $T = 2\,\mathrm{K}$ cannot exceed 0.5% at this field strength, i.e., it is too small to explain the experiment.

If the longitudinal field orients all the domains to a uniform magnetization the stray field penetrates even deeper into the SC [Kor08]. However, the field strength $\mu_0 M_\mathrm{s} d_{\mathrm{Co}}/L$ is in this case much smaller than for a large number of domains, since $w \ll L \approx 5\,\mathrm{mm}$, where L is the sample size. Thus, stray magnetic fields cannot provide a notable spin polarization.

5.4.3 Spin-dependent capture

According to Ref. [Kor12] the observed proximity effect may be non-equilibrium due to spin-dependent carrier capture from the SC into the FM. Then, the magnetization of the FM decides about the spin orientation of carriers which can tunnel dynamically through the barrier and do not contribute in the subsequent radiative recombination within the QW [Aki14]. In this case, the total PL intensity I_0 (the sum of the right- and left-circular polarized PL components) in a longitudinal magnetic field would depend on the helicity $\sigma^\pm$ of the exciting light. The intensity modulation parameter

$$\eta = \frac{I_0^+ - I_0^-}{I_0^+ + I_0^-} \tag{5.4}$$

is determined by the parameter $\mathcal{P}_0(\hbar\omega)$ characterizing the selection rules for the involved optical transitions at the laser energy $\hbar\omega$ (cf. Sec. 1.3.2). According to Ref. [Kor12],

$\eta(B_\parallel) = \mathcal{P}_0 \cdot \rho_c^\pi(B_\parallel)$ is equal to $\rho_c^\pi(B_\parallel)$ for heavy hole exciton excitation when $\mathcal{P}_0 \approx 1$. Figure 5.7 shows the modulation parameter $\eta(B_\parallel)$ when the laser photon energy is tuned to the X-resonance at 1.62 eV and detected at the e–A^0 transition (1.60 eV). $\eta(B_\parallel)$ is several times smaller than $\rho_c^\pi(B_\parallel)$. Moreover, one finds that $\eta(B_\parallel)$ is small over the whole range of laser photon energies $1.62 - 1.70$ eV. Thus one concludes that spin-dependent capture by the FM cannot be the main source of the FM-induced hole spin polarization.

5.4.4 Role of p-d exchange interaction

Heavy-hole spin polarization in the effective magnetic field of the p-d exchange interaction with magnetic atoms was predicted in Ref. [Kor03]. When the FM magnetization is saturated ($M = M_s$), the equilibrium polarization of the holes obeys the Curie law [Kit04]

$$\mathcal{P}(T) = \frac{N_{+3/2} - N_{-3/2}}{N_{+3/2} + N_{-3/2}} \approx \frac{\Delta E_{ex}(M_s)}{2k_B T}. \tag{5.5}$$

Here k_B is the Boltzmann constant, $\Delta E_{ex}(M_s)$ is the spin splitting of the heavy holes in the FM exchange field, and $N_{+3/2}$ ($N_{-3/2}$) is the concentration of QW heavy holes with momentum projection $+3/2$ ($-3/2$) onto the growth direction. We assume that $\mathcal{P}(T) \ll 1$. One can expect from Eq. (5.5) that the hole spin polarization decreases with increasing T. The experiment confirms this trend (Fig. 5.8(b)). An estimation for $T = 6$ K shows that 4 % spin polarization corresponds to a splitting $\Delta E_{ex}(M_s)$ of about 50 μeV. A direct evaluation of the p-d exchange energy is presented in Sec. 5.6.

The p-d exchange from the overlap of the QW holes and Co d-shell orbitals is expected to scale like $\Delta E_{ex}(d_s) \sim \exp(-d_s/d_0)$ owing to wave function penetration through the rectangular potential barrier. The same exponential behavior holds for the rate of hole tunnelling through the barrier, with a characteristic barrier width $d_0 = \hbar/2\sqrt{2m_{hh}\Delta}$, which is less than 1 nm for a heavy hole mass $m_{hh} > 0.1m_e$, and a barrier height $\Delta = 0.1$ eV (cf. Fig. 1.3(b)). Thus, the possible coupling mechanism is undoubtedly short-ranged. At first sight, this is in agreement with the steep decrease of PL intensity with decreasing barrier thickness owing to carrier tunnelling from the QW into the FM (the red squares Fig. 5.3(c)), from which one can derive $d_0 = 1.6$ nm. However, the spin polarization does not follow a similar steep decrease at all. The green circles in Fig. 5.3(c) show that $\rho_c^\pi(d_s)$ at $B_\parallel = B_{sat}$ seems to be slowly varying with d_s. Furthermore, and maybe even more surprising, the proximity effect observed here is long-ranged and persists over more than 30 nm, in contrast to our expectations based on wave function overlap.

It should be noted that in systems other than the one studied here a long-range proximity effect may occur, for example, due to spin-dependent capture by the FM. Previously this effect has been observed in a ferromagnetic GaMnAs/QW hybrid for electrons, but not for holes [Kor12]. The tunnel capture rates γ_+ (γ_-) of electrons with spin up (down) through the nonmagnetic spacer also have an exponential dependence on spacer thickness. The non-equilibrium polarization in the QW, however, is determined by

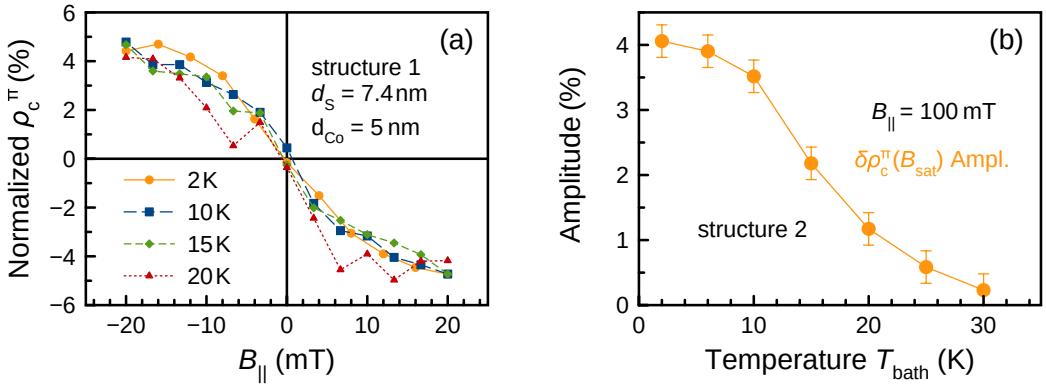

Figure 5.8: Temperature dependence of the proximity effect. (a) $\rho_c^\pi(B_\parallel)$ in structure 1 for various temperatures T_{bath}. The curves for $T_{\mathrm{bath}} = 10{,}15{,}20\,\mathrm{K}$ are normalized on the scaling for $T_{\mathrm{bath}} = 2\,\mathrm{K}$ in order to make the temperature dependence of the saturation field B_{sat} visible. (b) Temperature depence of the saturation amplitude $\delta\rho_c^\pi(B_{\mathrm{sat}})$ in structure 2. Note that the measurements are performed as function of the helium bath temperature T_{bath} which is several Kelvin below the actual temperature of the crystal lattice T in the illumination area (cf. Sec. 5.6).

the ratio γ_+/γ_-, so that the exponential dependence cancels. In the case here, the spin-dependent capture is weak in absolute terms, as it is related to holes, and the proximity effect comes mainly from the p-d exchange interaction. Therefore one concludes that the results indicate a long-range mechanism of p-d exchange coupling.

5.4.5 Diffusion of magnetic atoms or cluster formation

p-d exchange interaction is also relevant for diffusion of magnetic atoms into the QW region. Similar to the behavior in diluted magnetic semiconductors [Fur88], nearby magnetic atoms could enhance the effective Landé g factors of spins, so that $g_{\mathrm{eff}} \gg 1$. Since $|g_{\mathrm{e}}|$ did not show any enhancement (cf. $\overline{\rho}_c^\sigma$ in Fig. 5.5(d)) any diffusion into the QW region appears to be unlikely. A further possibility for the small saturation field $B_{\mathrm{sat}} \sim 20\,\mathrm{mT}$ of $\rho_c^\pi(B_\parallel)$ (cf. Fig. 5.3(b)) could be superparamagnetic Co cluster formation; i.e. nanometre-sized particles with a single ferromagnetic domain structure [Bea59]. For clarification, the polarization dependencies $\rho_c^\pi(B_\parallel)$ were measured at different temperatures in the range from 2 up to 30 K. Figure 5.8(a) shows that all curves coincide when the measured amplitudes are normalized. The magnetiziation of a paramagnet follows a Brillouin function $M(x)$ whose saturation magnetic field depends on the ratio

$$x = \frac{m_{\mathrm{c}} B_\parallel}{k_{\mathrm{B}} T}, \tag{5.6}$$

where k_{B} is the Boltzmann constant and m_{c} is the magnetic moment. If $\rho_c^\pi(B_\parallel)$ would arise from paramagnetic clusters or Co impurities one would expect a polarization saturation field $B_{\mathrm{sat}} \propto k_{\mathrm{B}} T$. This, however, is not seen in Fig. 5.8(a) where the saturation

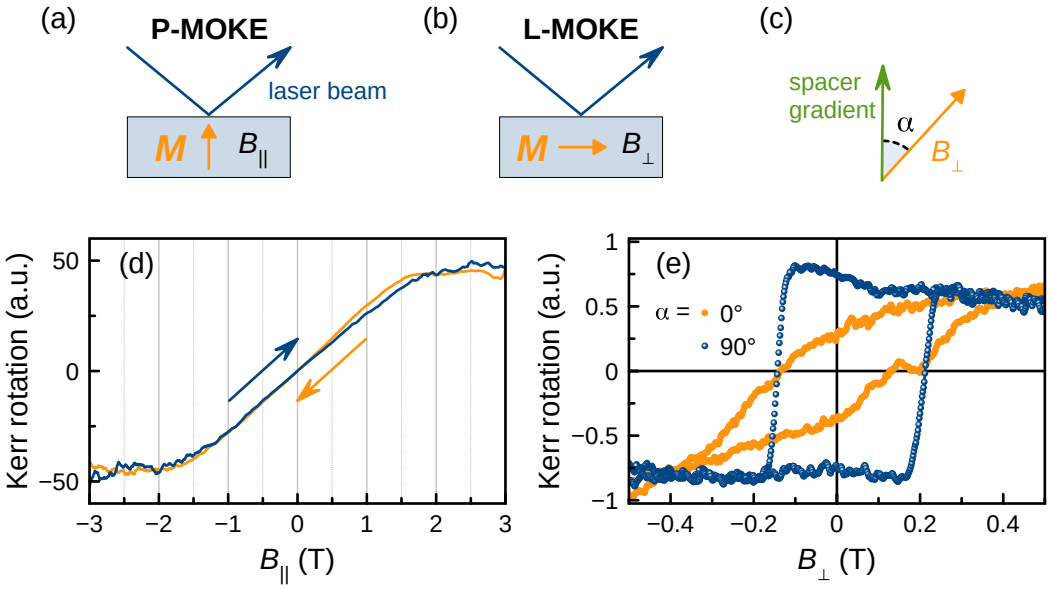

Figure 5.9: Magneto-optical Kerr effect in (a), (d) polar (P-MOKE) and (b), (e) longitudinal (L-MOKE) configuration. L-MOKE is measured for different orientations, α, of the spacer gradient with respect to the external magnetic field $B_\perp$ (c).

takes place at $B_{\mathrm{sat}} \sim 20\,\mathrm{mT}$ over the entire temperature range. This also means that the ferromagnetism of the Co layer is not sensitive to temperatures up to 30 K. The decrease of polarization with increasing temperature in Fig. 5.8(b) is related to the decreasing sensitivity of the "QW detector" to ferromagnetism.

5.4.6 Resonant tunneling through deep centers in the (Cd,Mg)Te spacer

Another possible reason of the FM-induced spin polarization is related to resonant transfer of spin coupling through overlapping deep paramagnetic centers in the (Cd,Mg)Te barrier. Assuming a localization radius of such a center of about $a_{\mathrm{t}} \sim 1\,\mathrm{nm}$ one can estimate the concentration required to make such a coupling efficient to be $N_{\mathrm{t}} \sim 1/a_{\mathrm{t}}^3 \sim 10^{21}\,\mathrm{cm}^{-3}$. Such a large concentration of parametric centers was never reported for (Cd,Mg)Te. Moreover, its presence should significantly influence the Larmor precession frequency of the CdTe QW electrons, which was not observed so far. Therefore, it is highly unlikely that this possibility can explain the experiment.

5.5 Magnetization curve of the ferromagnetic Co thin film

While having already addressed the question for the origin of the FM-induced QW PL circular polarization, the FM itself was not investigated so far. The magneto-optical Kerr effect (MOKE) is often used to measure the magnetic hysteresis loop of thin magnetic

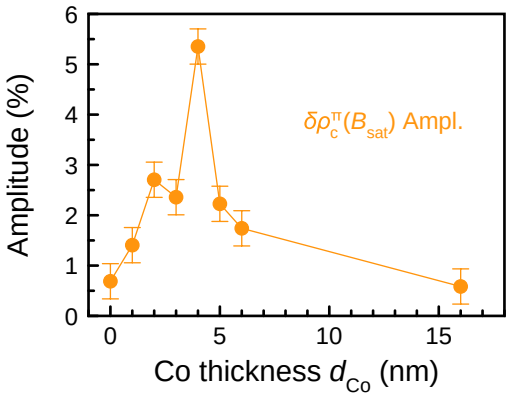

Figure 5.10: Time-integrated amplitude $\delta\rho_c^{\pi}$ for $B_{sat} = 40\,\mathrm{mT}$ as function of the Co thickness d_{Co} for a spacer thickness $d_s = 10\,\mathrm{nm}$ and $T_{bath} = 2\,\mathrm{K}$.

films (cf. Sec. 3.2.2). Such measurements exhibit for the Co-CdTe hybrid system an easy axis of magnetization in-plane, as shown in Fig. 5.9. In polar (P-MOKE) configuration (see Fig. 5.9(a) and (d)) the Faraday magnetic field $B_{\|}$ orients the magnetization slowly out-of plane with a saturation field $\mu_0 M_s \approx 1.7\,\mathrm{T}$, which is a typical value for Co [Chi05]. In full accordance with the expectations for magnetic thin films [Stö06], the magnetization by an in-plane magnetic field $B_{\perp}$ (L-MOKE) saturates much faster. Figure 5.9(e) shows magnetic hysteresis loops with a coercivity $B_c \approx 120\,\mathrm{mT}$ for the spacer gradient direction perpendicular and parallel to the magnetic field (see Fig. 5.9(c)).

These data are in contrast with the proximity effect: The PL polarization degree ρ_c^{π} in Faraday magnetic field saturates at $B_{\|} = 20\,\mathrm{mT}$ (cf. Fig. 5.3(b)) and is weakly sensitive to an in-plane magnetic field with $B_{\perp} < 100\,\mathrm{mT}$. In MOKE, no magnetization changes can be seen within the 20 mT accuracy. One concludes that the Kerr technique and the PL polarization technique detect ferromagnets with different properties - the easy-plane for the former and the perpendicular anisotropy for the latter method. The ferromagnet detected by the Kerr effect can be ascribed to the Co film itself, whereas the other ferromagnet could be related to interfacial ferromagnetism with properties differing substantially from the Co film. The interfacial ferromagnet layer is expected to be thinner than the Co film thickness, so that it is hard to be seen by the Kerr technique. In contrast, the ferromagnet-QW exchange coupling may be sufficient to induce spin polarization of nearby QW charge carriers. Interfacial ferromagnetism was discovered in a Ni-GaAs hybrid [Dzh95] and was discussed later in a number of papers [Nie13, Wil10]. The origin of the ferromagnet responsible for the proximity effect in the structures studied here needs further investigation in future. Currently, Co-related oxides can be excluded as origin because the structures 2 and 3 were grown without exposure to air before ferromagnet sputtering. Therefore, possible origins are Co-(Cd,Mg)Te intermixing and/or interfacial ferromagnetism. In Fig. 5.10 the amplitude $\delta\rho_c^{\pi}$ is shown as a function of the Co thickness d_{Co}. Interestingly, the FM proximity effect decreases not only for small Co thicknesses $d_{Co} < 4\,\mathrm{nm}$ (which is natural) but also for $d_{Co} > 4\,\mathrm{nm}$. The latter may be related to reorientation of the easy axis or change of the interfacial ferromagnetism, when the Co film becomes thick enough.

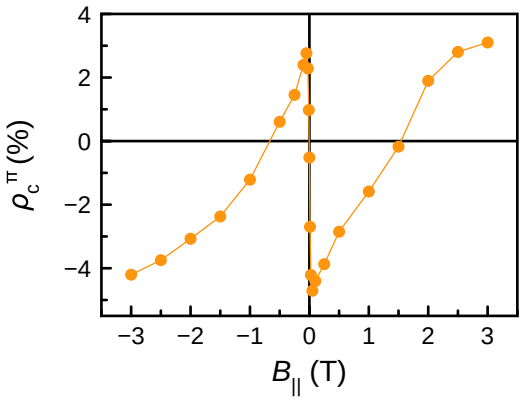

Figure 5.11: Magnetic field dependence of the FM induced circular polarization $\rho_c^{\pi}(B_{\parallel})$. The polarization is averaged over the spectral range of the e-A^0 PL band (1.57-1.62 eV). Excitation photon energy $\hbar\omega_{\mathrm{exc}} = 1.7\,\mathrm{eV}$. $T_{\mathrm{bath}} = 2\,\mathrm{K}$.

5.6 Evaluation of the p-d exchange interaction

Big efforts have been spend in measuring directly the magnitude of the exchange energy ΔE_{ex} [Aki17]. The idea is quite simple: Measurements of the spin-splitting for various magnetic fields $> B_{\mathrm{sat}}$ and extrapolation of these data to zero magnetic field reveals a finite offset with a magnitude of ΔE_{ex} [Kor12]. In Ref. [Aki17] it is shown that the hole spin-flip at the acceptor observed in spin-flip Raman scattering grants robust access to the effective p-d exchange constant. In contrast, pump-probe Kerr rotation in oblique magnetic fields reveals only Larmor oscillations from electrons and free valence band holes; the latter only weakly coupled to the Co thin film for magnetic fields $\mu_0 M_{\mathrm{s}} \gg B_{\mathrm{sat}}$ from the interfacial FM. In this section it will be shown that also polarization resolved PL can be used to measure ΔE_{ex}.

First, $\rho_c^{\pi}(B_{\parallel})$ is measured to a larger magnetic field range up to 3 T, when the out-of plane magnetization of the Co thin layer is present. Figure 5.11 shows FM induced $\rho_c^{\pi}(B_{\parallel})$ dependence averaged in the spectral range of $1.57 - 1.62\,\mathrm{eV}$. In strong magnetic fields $B_{\parallel} > 0.25\,\mathrm{T}$ the polarization increases with $B_{\parallel}$ and changes the slope around 2 T, which is close to the saturation field of Co discussed in Sec. 5.5. At first glance such behavior could be attributed to spin polarization of holes due to exchange interaction with Co where the exchange constant $\mathcal{J}_{\mathrm{pd}}$ has the opposite sign as that of the interfacial FM. However, care should be taken because there is a significant contribution of MCD (cf. Sec. 5.4.1). For this reason, TRPL measurements according to Fig. 5.4(b) are repeated with special attention to the sign of the amplitude $\overline{\rho}_{\mathrm{c}}^{\pi}(t)$, i.e., $\delta\rho_{\mathrm{c}}^{\pi}(t) = |\overline{\rho}_{\mathrm{c}}^{\pi}(t)|$ according to Eq. (5.1). Figure 5.12(a) shows the transients for different magnetic fields $B_{\parallel} = 0.5,\ 1.7,\ 2.5\,\mathrm{T}$. For the bigger field values an offset becomes relevant and the data have to be approximated with the expression

$$\overline{\rho}_{\mathrm{c}}^{\pi}(t) = \rho_{\mathrm{MCD}} + A\left(1 - e^{-\frac{t}{\tau_{\mathrm{fm}}}}\right). \tag{5.7}$$

Here, the instantaneous polarization degree ρ_{MCD} results from the difference in absorption of σ^+ and σ^- polarized light in the Co layer, the amplitude A corresponds to the equilibrium polarization of acceptor holes induced by external magnetic field $B_{\parallel}$ and FM

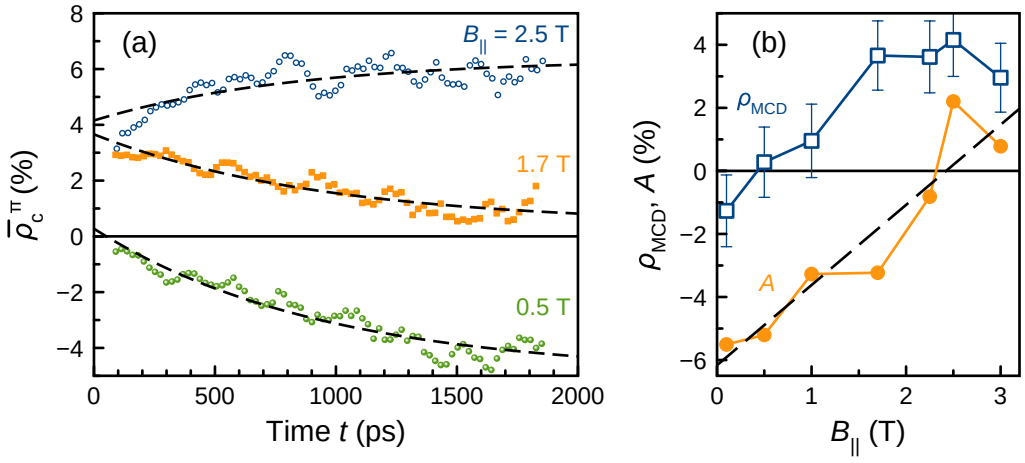

Figure 5.12: (a) Transients of the circular polarization $\bar{\rho}_c^{\pi}(t)$ according to Eq. (5.1) for different magnetic fields $B_{||} = 0.5$, 1.7, 2.5 T. Dashed lines are fits with Eq. (5.7). (b) Magnetic field dependence of ρ_{MCD} and A. The dashed line is a fit of A with Eq. (5.8) with $\Delta E_{\mathrm{ex}} = (50{\pm}10)\,\mu$eV and $|g_{\mathrm{A}}| = 0.4 \pm 0.1$. $T = 5$ K.

induced effective exchange field, and τ_{fm} is the spin relaxation time of polarized carriers, which is required to reach the equilibrium populations of the spin sub-levels.

The magnetic field dependencies of ρ_{MCD} and A evaluated from fits according to Eq. (5.7) are shown in Fig. 5.12(b). It follows that MCD saturates at $B_{||} \approx 1.7$ T, while the amplitude A continuously grows with $B_{||}$. The increase of A in magnetic field is related with additional equilibrium polarization of holes due to their thermalization between the spin sub levels. For small splittings ($A \ll 1$) the field dependence of A can be approximated by

$$A(B_{||}) = \frac{\mu_{\mathrm{B}} g_{\mathrm{A}} B_{||} - \Delta E_{\mathrm{ex}}}{2 k_{\mathrm{B}} T}, \tag{5.8}$$

where g_{A} is the Landé factor of the acceptor which determines the splitting of the heavy hole states. The total Zeeman splitting of holes is determined by the external magnetic field through $\mu_{\mathrm{B}} g_{\mathrm{A}} B_{||}$ and the effective exchange field through ΔE_{ex}. The sign of the different contributions is opposite as follows from Fig. 5.11. Since the amplitude A does not saturate in magnetic fields $B_{||} > 1.7$ T, one concludes that the contribution of the Co film to the proximity effect is negligible. Equation (5.8) is very sensitive to the actual temperature of the crystal lattice T in the illumination area. Much less sensitive on the temperature is $\Delta E_{\mathrm{ex}} \approx 50\,\mu$eV evaluated from spin-flip Raman scattering [Aki17]. From the fit in Fig. 5.12(b) one obtains $\Delta E_{\mathrm{ex}} = (50 \pm 10)\,\mu$eV and $g_{\mathrm{A}} = 0.4 \pm 0.1$ when taking the temperature $T = 5$ K. This value is about 3 K larger than the bath temperature $T_{\mathrm{bath}} = 2$ K. However, laser heating of the crystal lattice due to optical excitation is in agreement with previous studies on optical orientation of Mn ions in GaAs [Aki11].

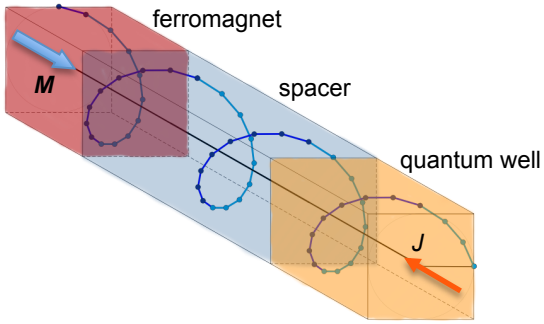

Figure 5.13: Illustration of a circularly polarized transverse phonon mode in the FM-SC hybrid structure. The phonon $\sigma^{-}_{\mathrm{phon}}$ is propagating along the FM magnetization $\boldsymbol{M}$. J denotes the spin polarization of acceptor holes pointing in the opposite direction as $\boldsymbol{M}$ because of $\rho^{\pi}_{\mathrm{c}}(B_{\parallel}) < 0$ for $B_{\parallel} > 0$.

5.7 Elliptically polarized phonons as origin of the long-range p-d exchange coupling

In Sec. 5.4 several possible origins for a long-ranged proximity effect (i.e., magnetic stray fields or spin-dependent capture) could be excluded. The long-range p-d exchange between FM and SC may be mediated by elliptically polarized phonons generated in the ferromagnetic layer, as schematically shown in Fig. 5.13. Such effective p-d exchange coupling has not been discussed previously in the literature. Subsequently, acoustic phonons are considered as an example. However, the coupling with elliptically polarized optical phonon modes [Sch76] is discussed in the supplementary section D of Ref. [Kor16].

It is well established that transverse acoustic (TA) phonons propagating through a FM along the magnetization direction $\boldsymbol{m} = \boldsymbol{M}/M_{\mathrm{s}}$ are elliptically polarized [Tuc72, Kit58]. This polarization arises from the strong hybridization of TA phonons (linear dispersion in momentum) and spin waves (dispersion quadratic in momentum) near the crossing points of their dispersion relations – that is, near a phonon–magnon resonance (cf. Fig. 3.2). There are two such crossing points at frequencies of $\omega_1 \sim 10^{10}\,\mathrm{s}^{-1}$ and $\omega_2 \sim 10^{12}\,\mathrm{s}^{-1}$ ($\hbar\omega_{1,2} \leq 1\,\mathrm{meV}$), with two orthogonal phonon polarizations per crossing. Only the phonon mode with polarization vector rotating in the same direction as the magnetization vector in the spin wave participates in the coupling, whereas the other one couples only weakly to magnons. The coupled rotary phonon mode shows a strong damping (over a decay length $\sim 2\,\mathrm{nm}$), whereas the other one survives [Kit58]. The authors of Refs. [Sin60] and [Sve79] measured in $Co_{0.92}Fe_{0.08}$ dispersion relations of magnons and phonons, respectively. The fact that they could not observe crossing points is not relevant for this work, since the p-d exchange interaction is based on the interfacial FM.

Recently, it was found that TA phonons (shear waves) can easily cross the interface between a FM and a SC, without an appreciable destructive effect [Bom13]. According to the continuity boundary conditions for displacement and stress, elliptically polarized modes will also propagate in the SC. The elliptically polarized phonons transfer angular momentum from the FM into the SC and will interact with hole spins owing to the strong spin–orbit interaction in the valence band [Ivc95]. The effect obviously occurs

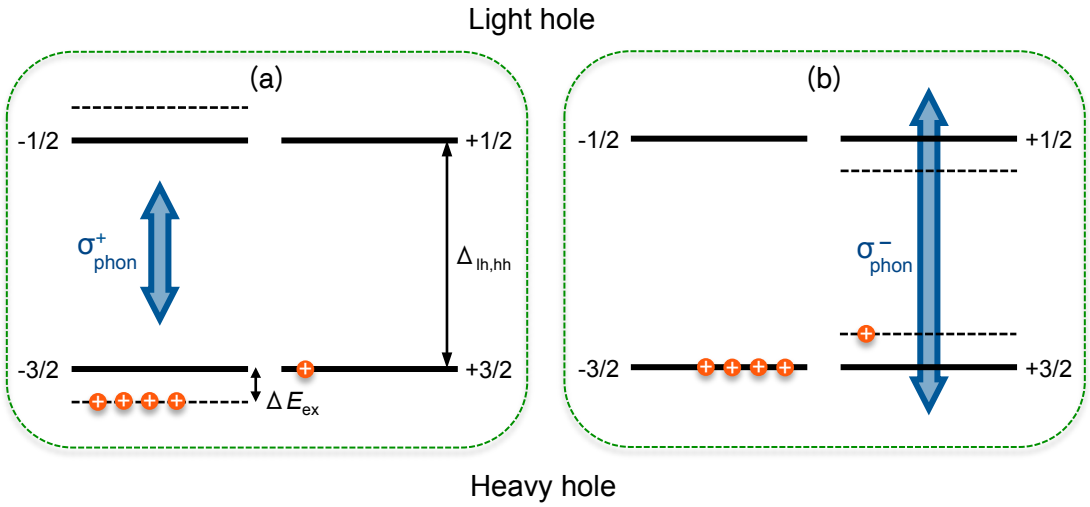

Figure 5.14: Energy diagram for the "phonon a.c. Stark effect" in semiconductors. (a) A right circularly polarized phonon $\sigma^{+}_{\mathrm{phon}}$ with energy $\hbar\omega_{1,2} < \Delta_{\mathrm{lh,hh}}$ couples the heavy hole ground $-3/2$ state and the light hole excited $-1/2$ state, inducing a spin-dependent shift of the hole spin levels by ΔE_{ex}. (b) $\sigma^{-}_{\mathrm{phon}}$ phonon with energy $\hbar\omega_{1,2} > \Delta_{\mathrm{lh,hh}}$ coupling the heavy hole ground $+3/2$ state and the light hole excited $+1/2$ state. In both cases, the heavy hole $-3/2$ state is in thermal equilibrium stronger populated than the heavy hole $+3/2$ state.

over much larger spacer thicknesses than any mechanism based on wave function overlap because there is no energy barrier for phonons.

One assumes transverse phonons propagating along the magnetization $\boldsymbol{M} \parallel \boldsymbol{z} \parallel [001]$ through the FM–SC hybrid interface, as sketched in Fig. 5.13. The angular momentum of a phonon with polarization $\sigma^{-}_{\mathrm{phon}}$ ($\sigma^{+}_{\mathrm{phon}}$) is parallel (antiparallel) to $\boldsymbol{M}$. For the selection rules in Fig. 5.14 the phonon results in a lifting of the Kramers degeneracy of the heavy hole $\pm 3/2$ doublet in zero external magnetic field. The shift is maximal when the energy of the magnon-phonon resonance is close to the energy splitting between the heavy ($\pm 3/2$) and light ($\pm 1/2$) holes, i.e. $\hbar\omega_{1,2} \approx \Delta_{\mathrm{lh,hh}}$. For the acceptor bound holes $\Delta^{\mathrm{A}}_{\mathrm{lh,hh}} \sim 1\,\mathrm{meV}$ is indeed close to the phonon resonance [Sap94], in contrast to the $\sim 10\,\mathrm{meV}$ energy splitting between the free hole subbands. This is another reason why the proximity effect is not detected at the X-transition.[1] Figures 5.14(a) and 5.14(b) show that phonons with energy $\hbar\omega_{1,2} < \Delta_{\mathrm{lh,hh}}$ or $> \Delta_{\mathrm{lh,hh}}$ can create the same heavy hole spin polarization where the $-3/2$ state is stronger populated than the $+3/2$ state. The coupling may be considered as the phonon analogue of the a.c. Stark shift in optics, in which the action of circularly polarized light in a medium is equivalent to an effective magnetic field [CT72].

[1] The absence of FM-induced spin splitting for the QW electrons (and the related precession corresponding to the Larmor frequency) can then also be explained by the small spin–orbit interaction in the conduction band.

The optical Stark effect is a well established phenomenon in semiconductors [Jof89, Sim16, Yan16]. It takes place when an electromagnetic wave with σ^+ polarization couples the electronic states with angular momentum projection $-3/2$ in the valence band and $-1/2$ state in the conduction band (cf. Fig. 1.6). Due to the interaction with light these states experience an energy shift $\Delta \propto d_\pm^2/\delta$, where $\delta = E_\mathrm{g} - \hbar\omega$. Here, $\hbar\omega$ is the photon energy and E_g is the band gap energy of the SC, $d_\pm$ is the dipole matrix element of the optical transitions between valence and conduction bands. For photons with $\hbar\omega < E_\mathrm{g}$ repulsion between the electronic states takes place, i.e. $\Delta > 0$, and vice versa for $\hbar\omega > E_\mathrm{g}$.

For the phonon Stark effect, the resulting energy shift is different for the $\pm 3/2$ levels because the number of phonons with opposite circular polarizations is different especially near the magnon-phonon resonance. This dynamic, phonon-mediated interaction therefore induces an effective p-d exchange coupling between the FM and the QW along the growth axis z. Thus, we write the Ising Hamiltonian (cf. Sec. 3.2.1)

$$\hat{\mathcal{H}}_\mathrm{ex}^\mathrm{eff} = -\frac{1}{3\hbar}\Delta E_\mathrm{ex} \hat{\boldsymbol{m}}_z \hat{\boldsymbol{J}}_z, \tag{5.9}$$

where $\hat{\boldsymbol{m}}_z$ is the z-projection operator corresponding to the magnetization unit vector $\boldsymbol{m}$, and $\hat{\boldsymbol{J}}_z$ is the z-projection operator of the total angular momentum of the acceptor hole with $J_z = \pm 3/2$ in units of $\hbar$. Calculation of the energy shift of the QW hole levels requires precise knowledge of many quantities, such as interaction parameters, phonon propagation directions, and so on. However, an estimation of the effective p-d exchange in the supplementary section C of Ref. [Kor16] shows that the p-d exchange splitting is about $50\,\mu$eV, leading to a PL polarization of 5 %, in agreement with the experimental results.

5.8 Conclusions

This chapter investigated a new ferromagnet-semiconductor hybrid structure composed of a ferromagnetic Co thin film and a semiconducting CdTe quantum well, separated by a nanometre thick (Cd,Mg)Te barrier. Hybrid structures are appealing because they allow not only combination of the functionalites of the individual constitutions but also mutual control of the properties. Specifically, the exchange interaction between magnetic ions and charge carriers in semiconductors is considered as a prime tool for spin control. The exchange interaction depends typically on the wave function overlap $\sim d_0$ and is therefore short-ranged [Ala01, Kob14]. In the structure studied here, p-d exchange coupling is manifested by the spin splitting of acceptor bound holes in the effective magnetic field induced by the ferromagnet. Surprisingly, a long-ranged, robust coupling is observed that does not vary with barrier width up to more than 30 nm although $d_0 = 1.6$ nm was measured from the decrease of photoluminescence intensity with decreasing barrier thickness. Time-resolved photoluminescence circular polarization is used to determine the magnitude of the long-ranged exchange interaction $\Delta E_\mathrm{ex} \approx 50\,\mu$eV. The equilibrium spin polarization might be mediated by elliptically polarized phonons that can travel

through the barrier without significant damping. This approach has been used later to explain the influence of elliptically polarized optical phonons on magnetic properties of materials [Nov17, Jur17a].

Implementation of techniques for exploitation of elliptically polarized phonons in semiconductors could have profound consequences for spin systems in general, and not only in hybrids. First, it could enable one to control the spin levels through the phonon analogue of the optical a.c. Stark effect [CT72]. Second, one may demonstrate phonon-assisted spin pumping: the absorption of circularly polarized phonons would create spin orientation of the holes in the valence band, similar to the well-known interband optical pumping in solids [Lam68] and gases [Kas98].

Part III

Coherent dynamics of optical excitations

Chapter 6

Rabi oscillations from excitons in (In,Ga)As quantum dots

Transient four-wave mixing (TFWM) spectroscopy is used to study excitons from self-assembled (In,Ga)As quantum dots (QDs) embedded in low-Q microcavities – one based on two dielectric distributed Bragg reflectors (DBRs), and the other one based on a top metallic gold mirror with bottom DBR (Tamm-plasmon resonator). The chapter is structured as follows: First, the two samples, Tamm-plasmon (TP) and DBR structure, are described. Coherent optical response in form of the photon echo (PE) from the structures is shown in Sec. 6.2.1. The focus is here on Rabi oscillations from the rephasing otpical pulse that are used in order to estimate the enhancement factor for the driving optical field inside the TP structure. Coherent dynamics and time-resolved photoluminescence (TRPL) are studied in Secs. 6.2.2 and 6.2.3. Rabi oscillations from the initial rotation pulse are used in Sec. 6.3.1 for the demonstration that the PE timing is strongly influenced by the inhomogeneity of the QD ensemble. The analytical model in Sec. 6.3.2 is finally used to simulate the influence of the first pulse variation on two-dimensional Fourier transform spectroscopy (2DFTS) in Sec. 6.3.3.

Most of this chapter has been published in similar form in Refs. [Sal17a, Pol16a].

6.1 The (In,Ga)As quantum dot samples

The integration of QDs into microcavity structures enables efficient coupling between excitons and optical fields (cf. Sec. 1.4.2). Here we discuss the two sample that are studied in the experiments.

6.1.1 Tamm-plasmon microcavity

Figure 6.1 summarizes information about the investigated TP structure (code M5278). The sample was grown by molecular-beam epitaxy on a GaAs (001) semi-insulating substrate. It comprises 20 pairs of $\lambda/4n$ GaAs/AlAs layers forming the back DBR mirror with the stop-band located in the spectral region of interest ($\sim$ 1.2-1.4 eV). A

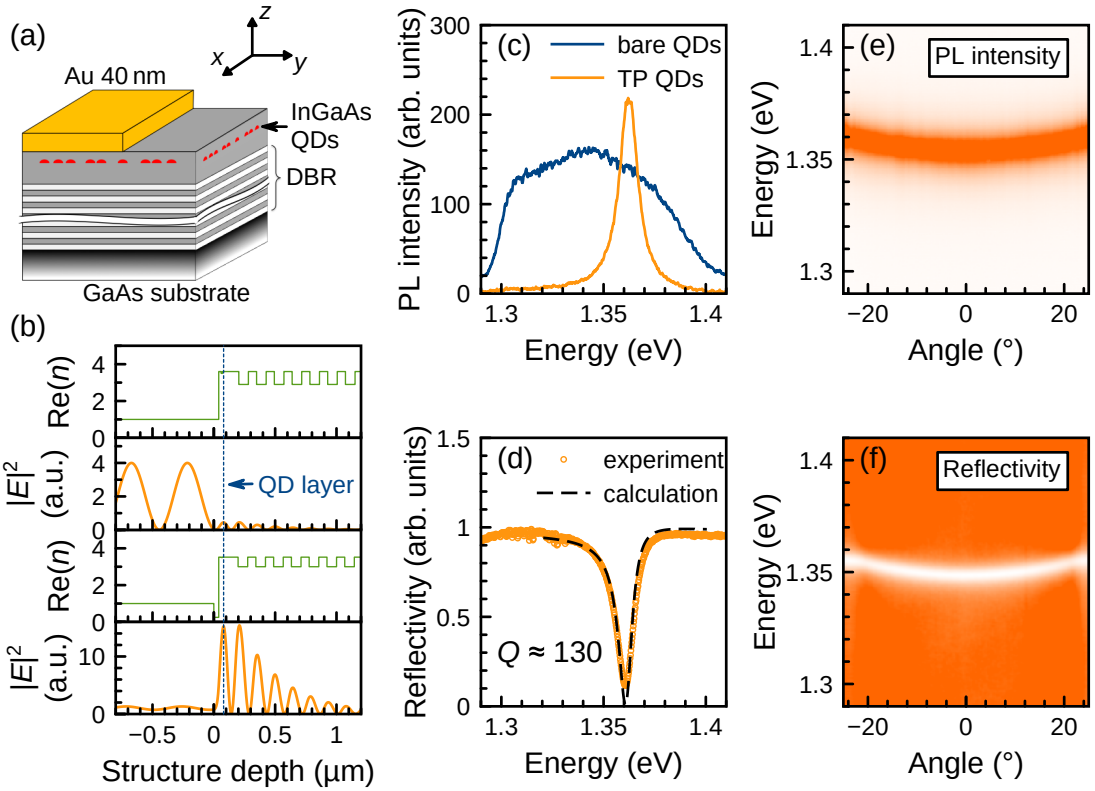

Figure 6.1: (a) Schematic presentation of the investigated TP structure. (b) Refractive index and electric field distribution under normal incidence of light (along the z-axis) for the uncovered part (top) and the metal-covered part (bottom) of the sample. In the TP microcavity the intensity of light at the QD layer position is increased by a factor of 34 compared to the bare waver. (c) PL spectra of the inhomogeneously broadened QD ensemble with and without TP microcavity. Photon excitation energy $\hbar\omega_{\mathrm{exc}} = 2.33\,\mathrm{eV}$, temperature $T = 2\,\mathrm{K}$. (d) Measured and calculated reflectivity spectra of the TP microcavity. Quality factor $Q \approx 130$, temperature $T = 8\,\mathrm{K}$. The calculation used a transfer matrix method with $d_{\mathrm{w}} = 118\,\mathrm{nm}$ (cf. supplemental material to Ref. [Sal17a]). Normalized angle resolved reflectivity and PL spectra in (e) and (f), respectively. Temperature $T = 10\,\mathrm{K}$. White corresponds to 0 and dark orange to signal strength 1.

single (In,Ga)As QD layer in the GaAs cavity layer is located about 125 nm above the DBR and 40 nm below the surface. The thickness of the GaAs layer d_{w} beneath the QDs is slightly varied by a wedge design which allows tuning the cavity resonance by the position of the excitation spot along the gradient axis x (Fig. 6.1(a)). Half of the sample is covered with a 40 nm thick gold layer, which leads to formation of the TP photon mode.

The QD layer is located at the maximum of the electric field distribution, 40 nm away from the gold layer (Fig. 6.1(b)). It is close enough to the gold to ensure that the coupling to the TP mode is strong, but far enough so that quenching of the PL due to

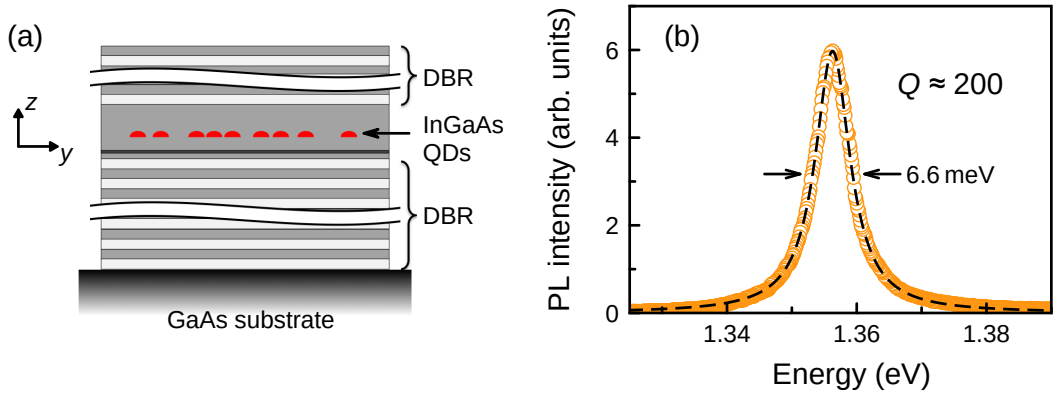

Figure 6.2: (a) Sketch of the (In,Ga)As QDs in the field maximum of a λ-microcavity with a top and bottom distributed Bragg reflector (DBR). (b) PL spectrum of the sample with quality factor $Q \approx 200$.

surface states, in particular at the uncovered surface, does not occur. The QD density is about $2 \times 10^9\,\mathrm{cm}^{-2}$, their height and lateral sizes before overgrowth are about 2.3 nm and 25 nm, respectively [Bra16]. In order to prevent tunneling of photoexcited carriers into the metal layer, a 10 nm $Al_{0.2}Ga_{0.8}As$ barrier was introduced between the QDs and the surface (20 nm below the surface).

The low temperature ($T = 2\,\mathrm{K}$) PL spectrum from the bare QDs under non-resonant excitation with photon energy $\hbar\omega_{\mathrm{exc}} = 2.33\,\mathrm{eV}$ shows a broad spectral band centered at about 1.35 eV (Fig. 6.1(c)). The large inhomogeneous broadening of $\sim 100\,\mathrm{meV}$ originates from fluctuations of QD size and composition in the ensemble. The emission from the same part of the sample, but covered with gold shows a resonant enhancement of the PL signal around the photon energy of the cavity mode that is also shown in the angle-resolved PL spectrum in Fig. 6.1(e). The PL has a significantly narrower bandwidth with a full width at half maximum of only 12 meV. The maximum of the PL peak and its width correspond to the dip in the cavity reflectivity spectrum (Figs. 6.1(d) and 6.1(f)). The latter is attributed to a TP photonic mode with energy $\hbar\omega_{\mathrm{TP}} = 1.36\,\mathrm{eV}$ and width $\Delta = 10.5\,\mathrm{meV}$, corresponding to a quality factor of $Q \approx 130$. Calculations using the transfer matrix method are in good agreement with the measured reflectivity spectrum for $d_{\mathrm{w}} = 118\,\mathrm{nm}$. The expected enhancement factor of the light intensity at the position of the QD layer is 34 (Fig. 6.1(b)).

6.1.2 Distributed Bragg reflector microcavity

The structure (code C3297) consists of a single layer of (In,Ga)As QDs which is inserted into a GaAs λ-microcavity, as schematically shown in Fig. 6.2(a). The QD density is about $1.8 \times 10^9\,\mathrm{cm}^{-2}$ and the barrier contains a Si δ-layer with donor density $8 \times 10^9\,\mathrm{cm}^{-2}$, separated from the QD-layer by 10 nm. The Bragg mirrors consist of alternating GaAs and AlAs layers with thicknesses of 68 nm and 82 nm, respectively. They have 5 and

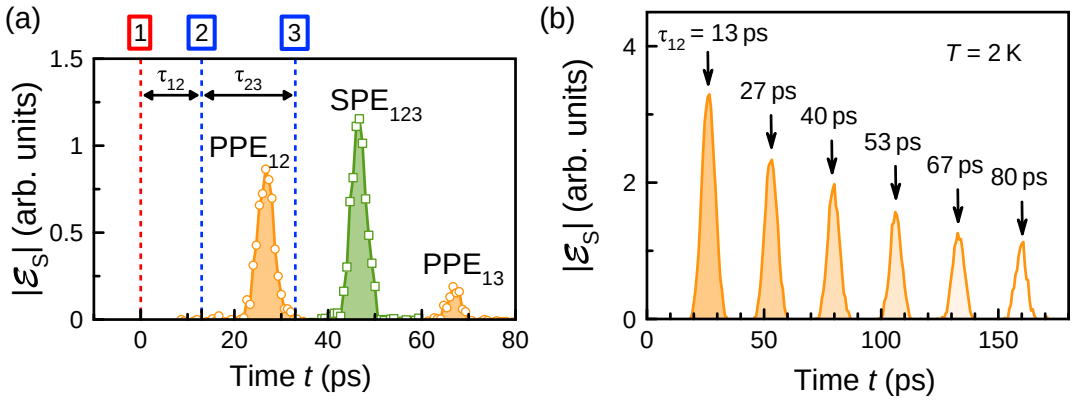

Figure 6.3: Photon echoes from the TP structure with pulse energies $\mathcal{P}_1 = 0.08\,\mathrm{nJ}$ and $\mathcal{P}_2 \approx \mathcal{P}_3 \approx 0.3\,\mathrm{nJ}$, temperature $T = 2\,\mathrm{K}$. (a) TFWM amplitudes measured at fixed delay times of $\tau_{12} = 13\,\mathrm{ps}$ and $\tau_{23} = 20\,\mathrm{ps}$. The primary photon echoes PPE_{12} and PPE_{13} appear at the time delays $t = 2\tau_{12}$ and $t = 2(\tau_{12}+\tau_{23})$, respectively, and the stimulated photon echo SPE_{123} appears $t = 2\tau_{12} + \tau_{23}$. (b) PPE_{12} for different time delays τ_{12} indicated at the arrows.

18 such pairs in the top and bottom mirror, respectively [Mai14]. With a microcavity Q-factor of ≈ 200, the photon lifetime is much shorter than the laser pulse duration of several picoseconds. Therefore, the main influence of the microcavity is to enhance the light-matter interaction for those QDs which have optical frequency in resonance with the cavity mode. Further, the broad exciton PL spectrum from the QDs with a width of 30 meV is modulated with the relatively narrow photon cavity mode to result in a relatively narrow emission band with full-width of 6.6 meV. The energy of the cavity mode depends on the sample spot due to the wedged cavity design. A PL spectrum measured at the studied sample spot discussed subsequently is shown in Fig. 6.2(b).

6.2 Enhanced light-matter interaction of quantum dots embedded in low-Q microcavities

The coherent optical response from the microcavity structures (cf. Sec. 2.3.2) is measured with the degenerate TFWM setup described in Sec. 4.4. The spectral width of the optical pulses of 0.8 meV is significantly smaller than the width of each of the resonator mode, i.e., the lifetime of the photonic mode inside the microcavity is shorter than the pulse duration of $\tau_\mathrm{p} \approx 2\,\mathrm{ps}$. Resonantly excited QDs can be considered as isolated two-level systems (TLS). Note that excitation of few-particle complexes such as biexcitons is excluded because the spectral width of the laser line is below the biexciton binding energy of about 2 meV. From these parameters one expects that the TFWM signal is represented by photon echoes due to the inhomogeneous broadening of the optical transitions in the QD ensemble. If the ensemble is embedded in the microcavity, the broadening is given by the spectral width of the photonic mode, as discussed in Sec.

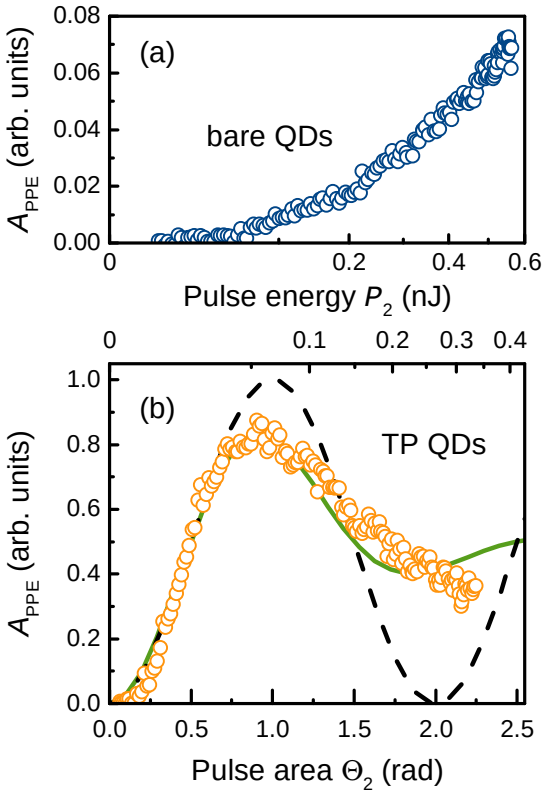

Figure 6.4: Dependence of the PPE amplitude A_{PPE} on the energy of the second pulse $\mathcal{P}_2$ for the bare QDs (a) and the TP microcavity (b) in a spot size of 200 μm. $\mathcal{P}_1 = 0.026$ nJ, $\tau_{12} = 67$ ps, $T = 2$ K. The scaling of the x-axis (bottom in (a) and top in (b)) is chosen such that it would scale linearly with the square root of $\mathcal{P}_2$. The bottom x-axis in (b) corresponds to the area of pulse 2. The dashed curve is a fit using Eq. (6.1). The solid curve follows from Eq. (6.2) when including the statistical distribution of dipole moments of the two-level systems with a standard deviation of 30%.

6.3.

An example of the TFWM signal $|\mathcal{E}_{\mathrm{S}}(t)|$ (cf. Eq. (4.7)) measured under resonant excitation in the TP mode is shown in Fig. 6.3(a). Here, the delay time between pulses 1 and 2 is set to $\tau_{12} = 13$ ps, while the delay time between pulses 2 and 3 is $\tau_{23} = 20$ ps. In full accordance with the expectation, one observes primary (PPE) and stimulated (SPE) photon echoes which appear at time delays of $t = 2\tau_{12}$ and $t = 2\tau_{12} + \tau_{23}$, respectively. In addition, Fig. 6.3(b) demonstrates that the PPE pulse appears at twice the delay between pulses 1 and 2. In what follows, the amplitudes of the echo at the peak-maximum of the PPE, A_{PPE}, or the SPE, A_{SPE}, are considered as the measured value.

6.2.1 Rabi oscillations induced by the rephasing pulse

The dependence of the PPE amplitude on the intensity of the excitation pulses can be used to compare the strength of light-matter interaction in the systems with bare QDs and TP QDs. For simplicity, one considers the dependence of the two-pulse PE on the energy of the second pulse, $\mathcal{P}_2$, shown in Figs. 6.4(a) and 6.4(b) for the bare QDs and the TP microcavity, respectively, for identical experimental conditions. Two main observations can be made: First, in the TP microcavity, one achieves significantly stronger PPE amplitudes for low pulse energies $\mathcal{P}_2 \leq 0.1$ nJ. Second, in the TP microcavity, one

observes a non-monotonous behavior which resembles the one expected for Rabi oscillations. Both features indicate a considerable enhancement of the light-matter interaction in the TP cavity which enable us to work in the nonlinear regime already at moderate intensities.

For isolated TLS in absence of decoherence processes and when optical pulses with rectangular intensity profile are assumed, the amplitude of the PPE follows the simple relation [Ber11]

$$A_{\mathrm{PPE}} \propto \sin^2\left(\frac{\chi_2 \tau_{\mathrm{p}}}{2}\right), \tag{6.1}$$

where $\chi_2 = 2|E_2 d|/\hbar$ is the Rabi frequency which is determined by the electric field amplitude of the second pulse E_2 and the dipole matrix element of the TLS d. In the experiment τ_{p} is fixed while $E_2 \propto \sqrt{\mathcal{P}_2}$ is varied. The expression can be used to evaluate the electromagnetic field amplitude inside the microcavity $E_2^{\mathrm{TP-QD}}$. This approximation should be valid also in the strong field limit because the lifetime of the cavity mode is the shortest time scale compared to the duration of the excitation pulses and the radiative lifetime in the QDs. For $\mathcal{P}_2 \leq 0.15\,\mathrm{nJ}$, the PPE oscillatory behavior in the TP-QD structure is reasonably well reproduced by Eq. (6.1) with the π-rotation occurring at $\mathcal{P}_2 \approx 0.06\,\mathrm{nJ}$. However, for larger pulse areas significant damping of the Rabi oscillations takes place. This is mainly due to a statistical distribution of the dipole moments d in the QD ensemble which results in a variation of the pulse area $\Theta_2 = \chi_2 \tau_{\mathrm{p}}$ and blurring of the Rabi oscillations [Bor02]. Assuming a Gaussian distribution with a standard deviation $\sigma\Theta_2$ centered around Θ_2, one obtains

$$A_{\mathrm{PPE}} \propto \frac{1}{\sqrt{2\pi}\sigma\Theta_2} \int_0^\infty \sin^2\left(\frac{\Theta}{2}\right) e^{-\frac{(\Theta_2-\Theta)^2}{2\sigma^2\Theta_2^2}}\,\mathrm{d}\Theta. \tag{6.2}$$

The best fit to the experimental data is obtained for $\sigma = 0.3$ as shown by the solid curve in Fig. 6.4(b). This value is in good agreement with previous results on similar QD ensembles [Bor02]. In addition, other mechanisms, such as the interaction with acoustic phonons, can lead to damping of the Rabi oscillations. The latter is expected to be strongest for pulses with durations of several ps, as used in the experiment [Krü05, Rei14]. A more detailed discussion of the oscillation damping, including mechanisms like spatial intensity variation of the optical pulse within the excitation spot and excitation induced dephasing, can be found in Ref. [Pol17b].

In contrast to the TP microcavity structure, A_{PPE} for the bare wafer follows a quadratic dependence on $\sqrt{\mathcal{P}_2}$ which indicates that the pulse area is significantly below π even for pulse energies as large as $\mathcal{P}_2 \approx 0.5\,\mathrm{nJ}$. Thus a significant enhancement of the light-matter interaction is clearly present in the TP cavity. A direct comparison of the intensities allows one to estimate the enhancement factor of the electromagnetic field for the coherent excitation of the QDs. Taking into account that the PPE signal depends on both $\mathcal{P}_1$ and $\mathcal{P}_2$, one estimates that the pulse area Θ_2 is enhanced by a factor of 6, i.e., the amplitude of the electromagnetic field $E_2^{\mathrm{TP}} \approx 6E_2^{\mathrm{b}}$. This is in accordance with the calculated increase of the light intensity by a factor of 34 in the TP microcavity as compared with the bare QD system (cf. Fig. 6.1(b)).

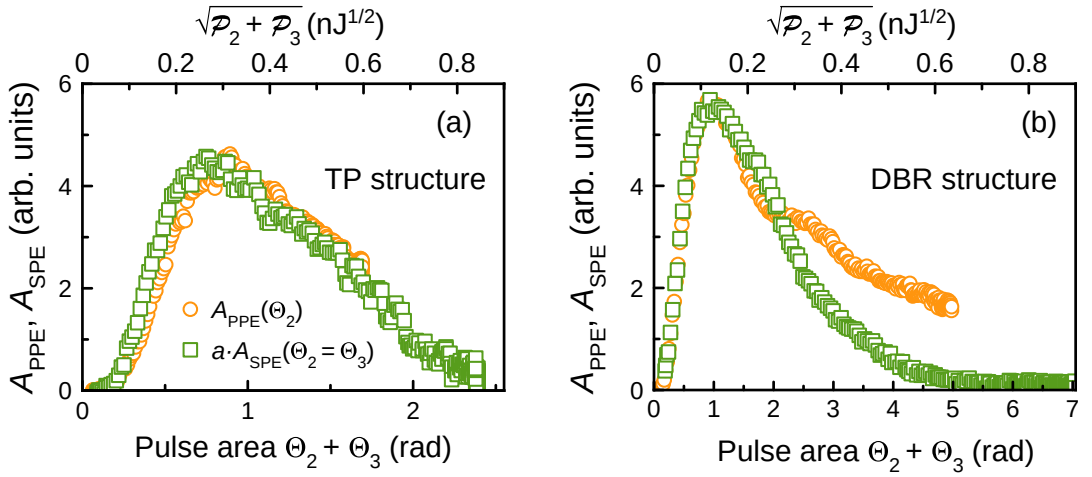

Figure 6.5: Dependence of the PPE amplitude, A_{PPE}, on the energy of the second pulse $\mathcal{P}_2$ and dependence of the SPE amplitude, A_{SPE}, on the sum of the second and third pulse energy with $\mathcal{P}_2 = \mathcal{P}_3$ ($\Theta_2 = \Theta_3$). The SPE amplitude is scaled by a factor a in order to match the first maximum of the PPE amplitude. (a) Rabi oscillations from the TP microcavity with experimental parameters: $\mathcal{P}_1 \approx 0.013\,\mathrm{nJ}$, $\tau_{12} = 13\,\mathrm{ps}$, $\tau_{23} = 33\,\mathrm{ps}$, $a = 2$. (b) Rabi oscillations from the DBR microcavity. $\mathcal{P}_1 \approx 0.003\,\mathrm{nJ}$, $\tau_{12} = \tau_{23} = 67\,\mathrm{ps}$, $a = 1.7$. $T = 2\,\mathrm{K}$.

The enhanced light-matter interaction in the microcavity structures can also be used for the observation of Rabi oscillations from the SPE amplitude which are given by [Ber11]

$$A_{\mathrm{SPE}} \propto \sin(\Theta_2)\sin(\Theta_3) \tag{6.3}$$

when making the same simplifying assumptions as for Eq. (6.1). Figure 6.5 compares Rabi oscillations in the two-pulse PE (A_{PPE}) with Rabi oscillations from the three-pulse PE (A_{SPE}) for both resonator types. It follows from Eqs. (6.1) and (6.3) that $A_{\mathrm{PPE}}(\Theta_2)$ should have the same dependence on the pulse area $\Theta_2+\Theta_3$ as $A_{\mathrm{SPE}}(\Theta_2 = \Theta_3)$. While both structures meet the expectations for small pulse areas, strong deviations are observed for $\Theta_2 + \Theta_3 > 2\pi$. Surprisingly, A_{SPE} does not converge to the mean value of $\sin^2$ but goes to zero. However, a closer study of this effect taking into account, e.g., enhanced excitation induced dephasing in the SPE configuration is out of the scope of this thesis.

The comparison between Figs. 6.5(a) and 6.5(b) reveals that the light-matter interaction in the DBR structure is even stronger than in the TP structure. Therefore, the same pulse energy covers in the DBR structure an about 3 times bigger pulse area than in the TP structure. It allows one to observe even a second maximum, $P_{\mathrm{PPE}}(\Theta_2 = 3\pi)$, in Fig. 6.5(b). For this reason, the DBR structure is used for the detailed discussion of Rabi oscillations from the first pulse (Θ_1) following in Sec. 6.3.1.

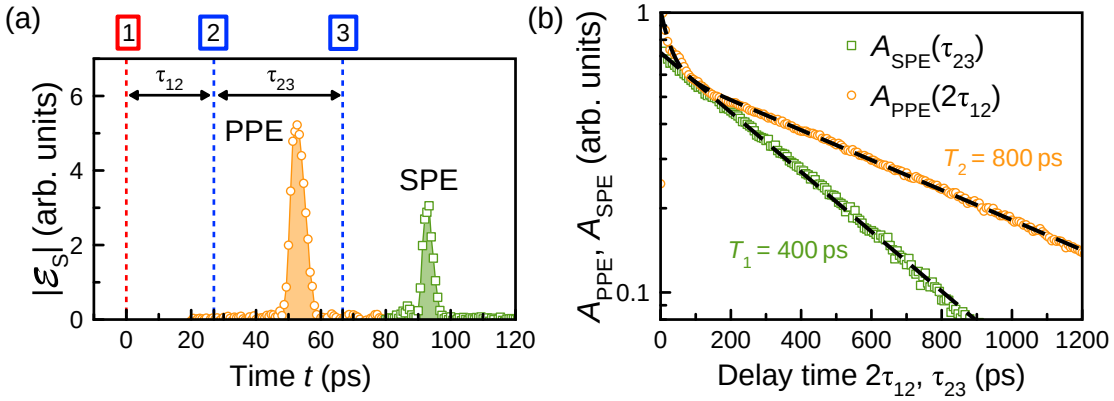

Figure 6.6: Photon echoes from the DBR structure at temperature $T = 2\,\mathrm{K}$ and excitation energy $\hbar\omega_{\mathrm{exc}} = 1.35\,\mathrm{eV}$. (a) TFWM amplitudes measured at fixed delay times of $\tau_{12} = 27\,\mathrm{ps}$ and $\tau_{23} = 40\,\mathrm{ps}$. Pulse energies $\mathcal{P}_1 = 0.013\,\mathrm{nJ}$ and $\mathcal{P}_2 \approx \mathcal{P}_3 \approx 0.040\,\mathrm{nJ}$. The primary photon echo PPE and stimulated photon echo SPE signals appear at the time delays $t = 2\tau_{12}$ and $t = 2\tau_{12} + \tau_{23}$, respectively. (b) PPE amplitude as function of the time delay $2\tau_{12}$ and SPE amplitude as function of τ_{23}. From the exponential fits follows the relation $2T_1 = T_2$. Pulse energies $\mathcal{P}_1 = 0.005\,\mathrm{nJ}$ and $\mathcal{P}_2 \approx \mathcal{P}_3 \approx 0.018\,\mathrm{nJ}$.

6.2.2 Coherent dynamics

Studying the transient decay of the photon echo signals gives insight into the coherent dynamics and the relaxation processes in the QD systems. Figure 6.6(a) shows the coherent optical response from the QDs inside the DBR microcavity in order to remind the reader on the time delays between the pulses, τ_{12} and τ_{23}, respectively. The PPE signal appears at exactly $2\tau_{12}$ and the SPE signal at $2\tau_{12} + \tau_{23}$. Figure 6.6(b) shows the echo amplitudes A_{PPE} and A_{SPE} as function of the pulse delays $2\tau_{12}$ and τ_{23}, respectively. The same measurements are shown in Figs. 6.7(a) and 6.7(b) for the bare QDs and QDs in the TP resonator, respectively. The PPE decay reflects an irreversible loss of optical coherence (i.e., of the medium's polarization) due to interaction of the TLS with the environment and/or radiative damping. It follows from measurements on both samples that the signal can be described by a double exponential decay $A_{\mathrm{PPE}} \propto A\exp\left(-2\tau_{12}/T_2'\right) + B\exp\left(-2\tau_{12}/T_2\right)$ including a short coherence time $T_2' = 30\,\mathrm{ps}$ and an approximately 10 times longer coherence time T_2. The short dynamics are attributed to fast energy relaxation of QD excitons excited in higher energy states, e.g. in p shell states, into the ground state [Kur09]. On the other hand, the long-lived signal with T_2 decay time corresponds to the coherent response of excitons in the ground s shell [Bor01]. The excitation of excitons in different energy shells is possible due to the strong inhomogeneous broadening of the optical transition energies in the studied QDs. Apparently, the long component decays faster in the TP microcavity with $T_2^{\mathrm{TP}} = 170\,\mathrm{ps}$, while in the bare QDs $T_2^{\mathrm{b}} = 350\,\mathrm{ps}$, i.e the coherent decay is twice slower. For the DBR structure one evaluates $T_2^{\mathrm{DBR}} = 800\,\mathrm{ps}$. All times are summarized in Tab. 6.1.

The SPE decay gives insight into the population decay dynamics and allows the

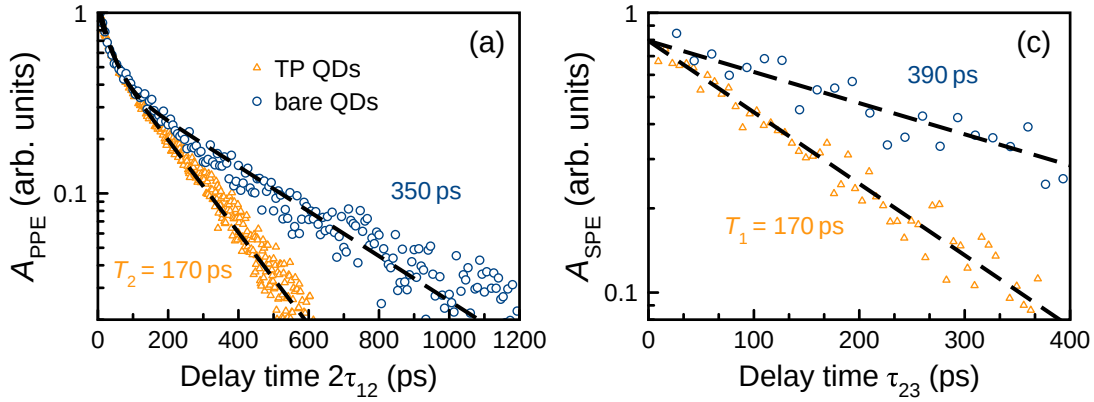

Figure 6.7: Normalized coherent dynamics on the bare QDs (circles) and the QDs in the TP microcavity (triangles). $T = 2\,\mathrm{K}$. (a) PPE amplitude as function of the pulse delay τ_{12} in order to measure the coherence time T_2. (b) SPE amplitude as function of the pulse delay τ_{23} in order to measure the lifetime T_1. $\tau_{12} = 26.7\,\mathrm{ps}$. The pulse areas in (a) and (b) did not exceed π. The dashed curves are fits with double (a) and single (b) exponential decays, respectively.

evaluation of the exciton lifetime T_1. From Fig. 6.7(b) one obtains for the bare QDs $T_1^{\mathrm{b}} = 390\,\mathrm{ps}$ and for the TP microcavity $T_1^{\mathrm{TP}} = 170\,\mathrm{ps}$. The simple relation from Eq. (2.6) allows to calculate the pure dephasing time τ_c. τ_c turns out to be shorter for the excitons confined in the QDs in the TP microcavity, $\tau_c^{\mathrm{TP}} = 340\,\mathrm{ps}$, as compared with the bare QDs, $\tau_c^{\mathrm{b}} = 635\,\mathrm{ps}$. As this time exceeds the exciton lifetime, the pure dephaing is neverheless weak. For the fully dielectric DBR structure in Fig. 6.6(b) one extracts $T_1^{\mathrm{DBR}} = 400\,\mathrm{ps}$. Thus, the pure dephasing is negligible and the ground state exciton coherence is radiatively limited, i.e. $T_2^{\mathrm{DBR}} = 2T_1^{\mathrm{DBR}}$. Note, that T_1^{DBR} has approximately the same magnitude as for bare QDs. From the comparison we conclude that the exciton coherence in the bare QDs is somewhat reduced by charges at the surface 40 nm separated from the dot layer. The gold layer of the TP cavity induces further decoherence which can be attributed to the interaction between excitons and plasmons.

6.2.3 Time-resolved photoluminescence

The lifetime measurements deduced from the SPE in Fig. 6.7(b) show that for the TP microcavity T_1 is approximately halved compared to the bare QDs. This shortening most likely is due to the Purcell effect [Gaz11]. However, one has to consider also non-radiative processes due to tunneling of photoexcited carriers from the QDs into the nearby metal as potential origin. Further insight can be obtained from PL transients measured using a streak camera for below-barrier pulsed excitation with photon energy $\hbar\omega_{\mathrm{exc}} = 1.494\,\mathrm{eV}$. These measurements are shown in Fig. 6.8. The PL signals decay with lifetimes $\tau_0^{\mathrm{b}} = 1350\,\mathrm{ps}$ and $\tau_0^{\mathrm{TP}} = 590\,\mathrm{ps}$ for the bare QDs and the TP structure, respectively. Interestingly, the PL decay times τ_0 are significantly larger as compared to

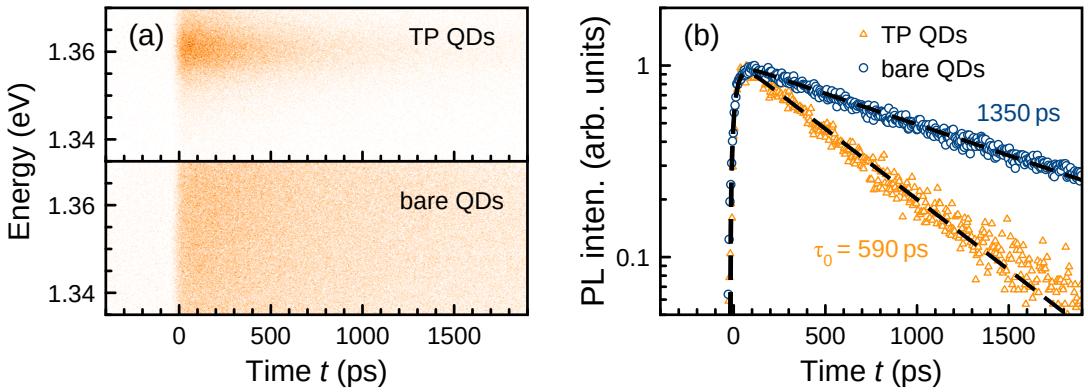

Figure 6.8: Time-resolved PL from the Tamm structure for excitation with below barrier excitation $\hbar\omega_{\mathrm{exc}} = 1.494\,\mathrm{eV}$. $T = 2\,\mathrm{K}$. (a) Contour plot of the PL intensity decay. (b) Normalized dynamics of the spectrally integrated signal with dashed lined fit function $\propto \exp(-t/\tau_0) \cdot [1 - \exp(-t/\tau_{\mathrm{rise}})]$ for the bare QDs (circles) and the QDs in the TP microcavity (triangles). In both cases, $\tau_{\mathrm{rise}} = 30\,\mathrm{ps}$. In the colormaps, white indicates the zero level and orange corresponds to the maximum signal.

the T_1-values from the SPE decay. This leads to the surprising observation that the decay rate from SPE measurements increases in the TP structure about three times stronger than the decay rate from PL measurements, i.e. $\Delta T_1^{-1} \approx 3\Delta\tau_0^{-1}$. The explanation comes from the fact that the two techniques measure indeed different population dynamics. SPE is a coherent phenomenon following resonant excitation. If for some reason exciton relaxation occurs, it will not contribute to the echo signal. In contrast, PL from the ground state is an incoherent process after relaxation of the involved carriers. While the rise time τ_{rise} of this signal is in the few ten ps-range, the PL decay time is significantly extended by several factors. For the chosen conditions a carrier reservoir is excited also in the wetting layer, from where carriers have to be transferred to the QDs. After being captured by the dots, relaxation can occur either by phonon emission or by carrier-carrier scattering. In the latter case a carrier, e.g. an electron, relaxes at the expense of the other carrier, the hole. Thereby populations in higher states and potentially even again in the wetting layer are created slowing down the carrier recombination. Also other processes such as formation of dark excitons may contribute.

Non-radiative processes lead to shortening of the lifetime. PL transients with extended dynamical range allow one to give an upper estimate for the non-radiative decay, $\tau_{\mathrm{NR}}^{\mathrm{TP}}$, in the TP microcavity which should contribute to the SPE decay rate. Neglecting non-radiative processes, $\tau_{\mathrm{NR}}^{\mathrm{b}}$, in the bare QDs, on gets

$$\frac{1}{\tau_0^{\mathrm{b}}} = \frac{1}{\tilde{\tau}_0^{\mathrm{b}}} + \frac{1}{\tau_{\mathrm{NR}}^{\mathrm{b}}} = \frac{1}{\tilde{\tau}_0^{\mathrm{b}}} = \frac{1}{1350\,\mathrm{ps}}, \tag{6.4}$$

where $\tilde{\tau}_0^{\mathrm{b}}$ is the radiative decay time. The maximal possible enhancement of non-radiative

processes in the TP microcavity would be

$$\frac{1}{\tau_0^{\mathrm{TP}}} = \frac{1}{\tilde{\tau}_0^{\mathrm{b}}} + \frac{1}{\tau_{\mathrm{NR}}^{\mathrm{TP}}} \iff \tau_{\mathrm{NR}}^{\mathrm{TP}} = 1\,\mathrm{ns}. \tag{6.5}$$

Thus, one finds $\tau_{\mathrm{NR}}^{\mathrm{TP}} \geq 1\,\mathrm{ns}$ as the lower limit for the non-radiative decay time in the TP microcavity. $\tau_{\mathrm{NR}}^{\mathrm{TP}}$ should be also visible in the SPE experiment, but in fact

$$\frac{1}{T_1^{\mathrm{TP}}} > \frac{1}{T_1^{\mathrm{b}}} + \frac{1}{\tau_{\mathrm{NR}}^{\mathrm{TP}}}, \tag{6.6}$$

with the limit from Eq. (6.5). Therefore, the shortening of T_1 from the 350 ps in the bare QDs to the 170 ps in the TP microcavity cannot be initiated by non-radiative processes, but has to be attributed to the Purcell effect with an enhancement factor of about 2.

Acceleration of the spontaneous emission rate T_1^{-1} by a factor of 2 represents a significant change of the radiative emission dynamics. In $\lambda/2$ microcavities with ideal planar metal mirrors the Purcell factor is limited to 3, while in structures with DBR mirrors the modification of the spontaneous emission rate is typically smaller than $\pm 20\%$ [Bro90, Bay01]. For planar resonators the spontaneous emission becomes mostly redistributed spatially, while the vacuum field becomes only weakly squeezed leading to a moderate enhancement of the local density of photon modes and the associated emission rate at best. Here, in addition SPPs may become relevant for the shortening of T_1. On the other hand, the resonator-induced enhancement of light-matter interaction is much stronger for resonant excitation of coherent processes which is related to the selective excitation of the contributing QDs.

	T_1 (ps)	T_2 (ps)	τ_c (ps)	τ_0 (ps)
bare QDs	390	350	635	1350
TP-QDs	170	170	340	590
DBR	400	800	∞	–

Table 6.1: Decay constants evaluated from Figs. 6.6, 6.7, and 6.8. T_2 follows from the PPE, T_1 from the SPE, and τ_0 from the time resolved PL measurements. τ_c follows from Eq. (2.6).

6.3 Inhomogenity effects on the photon echo transients

The strong inhomogeneous broadening of the QD ensemble influences the photon echo timing sequence (cf. Sec. 2.3.1). Here, we focus our investigations on the DBR structure where the light-matter interaction is stronger than in the TP structure (cf. Fig. 6.5).

6.3.1 Rabi oscillations induced by the initial rotation pulse

In the experiment, the temporal profiles of the PPE are measured as a function of the laser pulse energy $\mathcal{P}_1$. In order to demonstrate the maximal possible amount of oscillations Fig. 6.9 shows the PPE signal from the DBR structure as function of $\sqrt{\mathcal{P}_1}$.

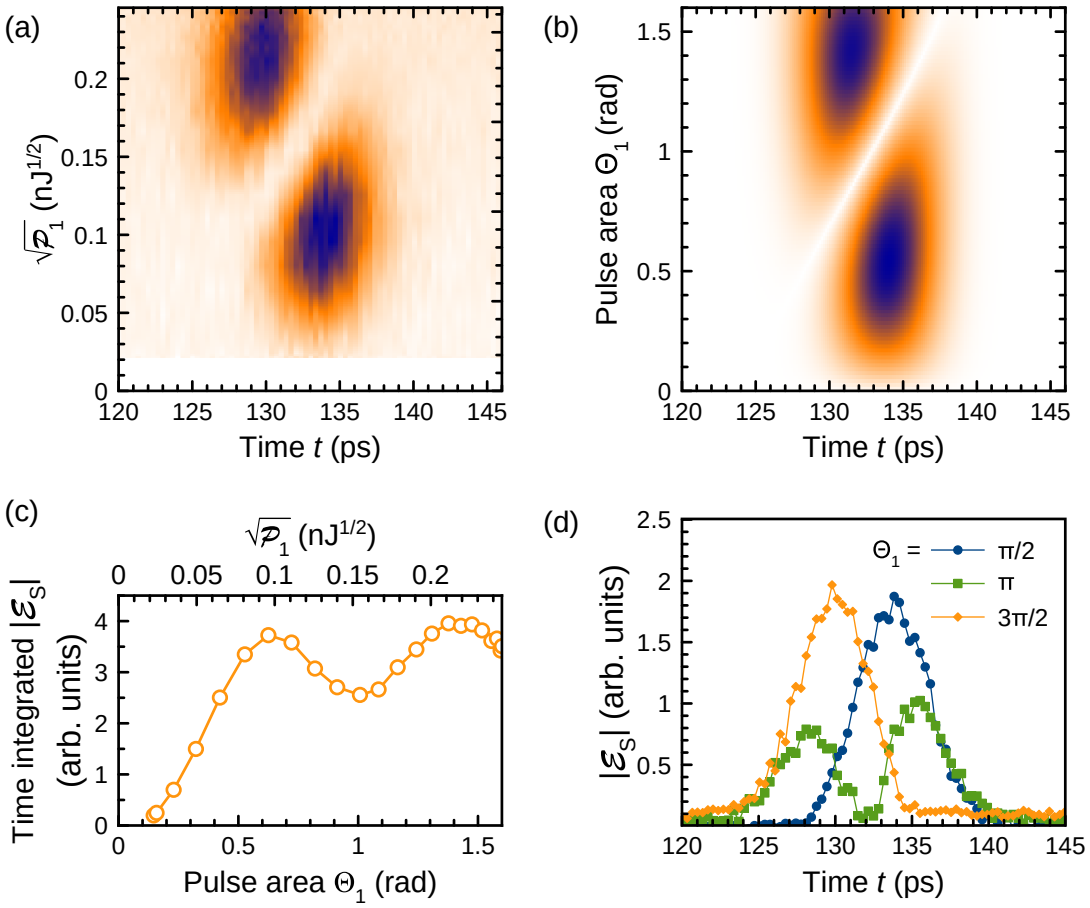

Figure 6.9: Experimental data from the DBR structure and theoretical calculations of the absolute value of the PPE amplitude. (a) Experimental dependence of the PPE temporal profile on the first pulse energy $\sqrt{\mathcal{P}_1}$. The delay between the centers of rephasing and excitation pulses is 66.7 ps. $\mathcal{P}_2 = 0.007$ nJ. (b) Theoretical modeling of the data from (a) using Eq. (6.8) with the following parameters: pulse duration $\tau_\mathrm{p} = 3.3$ ps, inhomogeneity $2\sqrt{2\ln 2}\hbar\Gamma = 6.6$ meV, and rephasing pulse area $\chi_2\tau_\mathrm{p} = \pi$. In the colormaps, white indicates the zero level and dark-blue corresponds to the maximum signal. (c) Time-integrated (TI) modulus of the PPE amplitude measured as function of the first pulse energy. (d) PPE transients for $\Theta_1 = \pi/2$, π, and $3\pi/2$.

The delay between the centers of rephasing and excitation pulses is set to $\tau_{12} = 66.7$ ps. Clearly, footprints of Rabi oscillations are observed in Fig. 6.9(a). Most strikingly, sizable temporal shifts of the PPE maxima for $\pi/2$ and $3\pi/2$-excitation pulses (around 0.1 nJ$^{1/2}$ and 0.2 nJ$^{1/2}$, respectively) as well as a splitting of the PE profile around π-pulse amplitude (around 0.15 nJ$^{1/2}$) become evident in Fig. 6.9(d), where the corresponding PPE transients are plotted. The time-integrated PPE signal also manifests Rabi oscillations, as seen from Fig. 6.9(c), but the oscillations are much less pronounced than in the time-resolved data. Note, that variation of the second pulse amplitude does not lead to any additional modification of the PPE temporal profile.

6.3.2 Theoretical description

In order to describe the PPE from a QD ensemble one calculates the temporal evolution of a set of 2×2 density matrices interacting with two sequent laser pulses and analyzes the resulting macroscopic polarization of the medium $\boldsymbol{P}$. The general approach starting from the Lindblad equation $i\hbar\dot{\rho} = [\hat{\mathcal{H}},\rho] + \Upsilon$ is discussed in Sec. 2.1.2. Here one considers the case, when the individual oscillator coherence time $T_2 \gg \tau_{12}$, which is justified by T_2 being ultimately limited by the exciton lifetime $T_1 = 400\,\mathrm{ps}$ (cf. Fig. 6.6(b)). Thus, the only consequence of relaxation in the system is the PPE exponential decay $\sim \exp(-2\tau_{12}/T_2)$. Therefore, one neglects relaxation considering $\Upsilon = 0$, for simplicity.

In the calculations we assume rectangular shaped pulses, each with with duration τ_p. Keep in mind that we deal with the case of strong inhomogeneous broadening where the detuning $\Delta = \Omega_0 - \omega$ of every individual oscillator with frequency Ω_0 from the light frequency ω is not necessarily zero during excitation (cf. Sec. 2.1.1). In the rotating wave approximation, this defines the optical nutation of the TLS on the Bloch sphere with a generalized Rabi frequency $\tilde{\Omega} = \sqrt{\chi^2 + \Delta^2}$. Accordingly, the analysis of the coherent optical response of the system includes the following steps: first, one calculates the interaction of the unperturbed system with the first excitation pulse ($\chi = \chi_1$) acting during the time τ_p, then the system evolves freely in absence of excitation ($\chi = 0$) during the time interval τ_{12}, followed by the excitation with the second rephasing pulse ($\chi = \chi_2$) during the time τ_p.Finally, one analyzes the macroscopic polarization of the QDs that is available for PPE pulse formation by integrating the individual responses over the inhomogeneous ensemble of TLS, defined by a Gaussian distribution with standard deviation Γ (cf. Eq. (2.16)). Within these approximations, it is possible to perform the analysis analytically and calculate the following expression for the excitation-dependent part of the PPE amplitude:

$$\begin{aligned} A_\mathrm{PPE}(t') \;\propto\; & \int_{-\infty}^{\infty} e^{-\frac{\Delta^2}{2\Gamma^2}} \frac{\chi_1\chi_2^2}{\tilde{\Omega}_1\tilde{\Omega}_2^2} \sin^2\left(\frac{\tilde{\Omega}_2\tau_\mathrm{p}}{2}\right) \\ & \times \left[\frac{2\Delta}{\tilde{\Omega}_1}\sin^2\left(\frac{\tilde{\Omega}_1\tau_\mathrm{p}}{2}\right)\sin\left(\Delta t'\right) + \sin\left(\tilde{\Omega}_1\tau_\mathrm{p}\right)\cos\left(\Delta t'\right)\right] \mathrm{d}\Delta. \end{aligned} \tag{6.7}$$

Here $t' = t - 2(\tau_{12} + \tau_\mathrm{p})$, and $\tilde{\Omega}_{1,2}$ are the generalized Rabi frequencies of the first and the second pulse, respectively. In this notation, delay between the exciting pulse centers used in experiment is $\tau_{12} + \tau_\mathrm{p}$ and expected PPE arrival time according to the standard treatment is $t' = 0$. This equation is similar to the one obtained for spin echoes measured in highly inhomogeneous fields [Blo55, Kil98]. It can be easily seen, that variation of the second, rephasing pulse amplitude and, hence, χ_2 does not affect the symmetry of the PPE profile. Thus, the discussion of Rabi oscillations from $\Theta_2 = \chi_2\tau_\mathrm{p}$ as function of the echo amplitude measured at precisely $2\tau_{12}$ is feasible (cf. Sec. 6.2.1). In what follows, only the effect coming from variation of the first, excitation pulse amplitude is considered.

Figure 6.10 shows results of theoretical calculations performed using the modulus of Eq. (6.7) for two ensembles with different widths of the inhomogeneity: $\tau_\mathrm{p}\Gamma = 0.12$ and

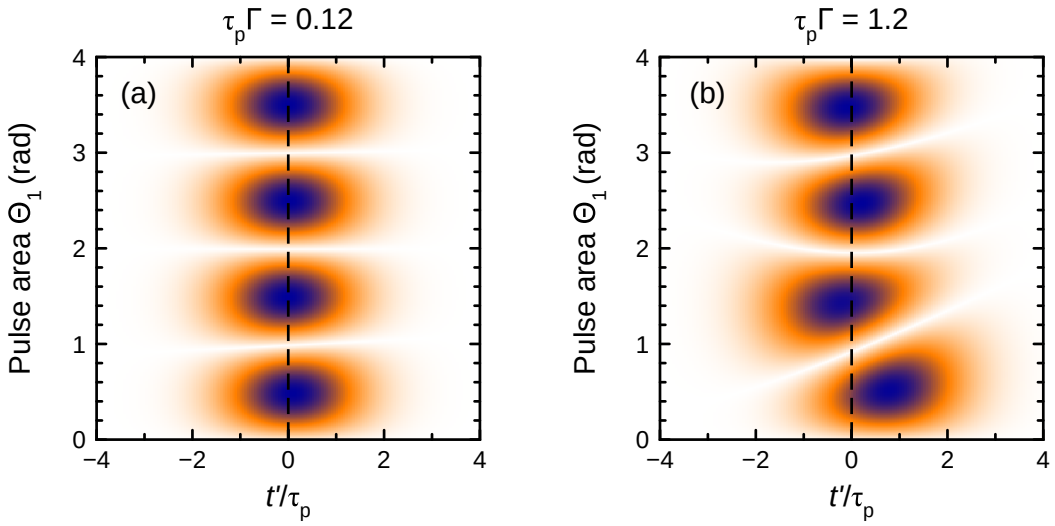

Figure 6.10: Theoretical calculation of the PE temporal profile as function of the excitation pulse area Θ_1 using the modulus of Eq. (6.7) for two ensembles with different inhomogeneity Γ: (a) $\tau_p\Gamma = 0.12$; and (b) $\tau_p\Gamma = 1.2$. The time scale is normalized by the pulse duration. White corresponds to zero signal level, dark-blue gives the maximum value.

1.2.[1] For an ensemble broadening much narrower than the pulse spectrum, $\tau_p\Gamma = 0.12$, clean Rabi oscillations are seen in the PPE temporal profile as function of the excitation pulse area $\Theta_1 = \chi_1\tau_p$, shown in Fig. 6.10(a). In particular the photon echo arrives as expected at twice the separation between rephasing and excitation pulse. This case is equivalent to an ideal Hahn echo, where the echo signal is generated at $2\tau_{12}$. When, however, the inhomogeneous ensemble width becomes comparable with the pulse spectral width ($\tau_p\Gamma = 1.2$), strong modifications of the temporal PPE profile appear, as can be seen in Fig. 6.10(b). The key feature of these modifications is the effective temporal shift of the PPE amplitude that is particularly prominent for the first two maxima of the Rabi oscillations when increasing the excitation power: for a $\pi/2$-pulse the PPE maximum is retarded relative to the expected PPE arrival time, while for a $3\pi/2$-pulse the PPE is advanced. These shifts do not depend on the pulses delay time τ_{12} in the limit of negligible damping and decrease with further increasing Θ_1 [Pol16c].

The temporal shifts of the PPE can be qualitatively explained using the Bloch sphere representation, as outlined in Fig. 6.11. In Fig. 6.11(a), the ideal case of a Hahn echo is given as a reference, where excitation with a negligibly short excitation $\pi/2$-pulse results in an unshifted echo signal. When the excitation pulse has a finite duration, as shown in Fig. 6.11(b), the oscillators experience dephasing during the pulse action, so that the excitation distributes the oscillators along the equator of the Bloch sphere followed by their precession in the equatorial plane. This precession extrapolated to negative times results in focusing all the Bloch vectors on the same meridian, which

[1] In the calculations, dimensionless units are used for convenience for the frequency and the time scales. In these units, the pulse spectral width is equal to 1.

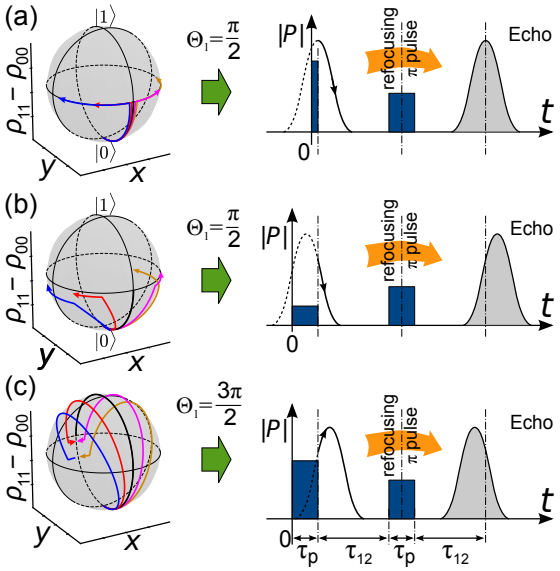

Figure 6.11: Explanation of the PE timing modifications using the Bloch sphere representation for different excitation pulse configurations: (a) ultrashort $\pi/2$-pulse: case of Hahn echo. (b) $\pi/2$-pulse: retarded echo. (c) $3\pi/2$-pulse: advanced echo. The colored lines on the Bloch spheres (left panels) denote different trajectories of the Bloch vectors of individual oscillators with different detuning from the laser frequency in directions indicated by the arrows. The right panels show the temporal evolution of the modulus of the macroscopic polarization, $|P|$, after excitation pulse action. The dashed lines denote extrapolation of $|P|$ to $t < \tau_p$.

corresponds to a situation where the maximum macroscopic polarization is shifted to $t < \tau_p$. In case of excitation by a $3\pi/2$-pulse as shown in Fig. 6.11(c), after pulse action all oscillators proceed along the equator towards each other, which leads to a shift of the macroscopic polarization maximum to $t > \tau_p$. Since the rephasing pulse acts essentially as a refocusing pulse, which in effect reverses the temporally coherent evolution of the ensemble oscillators, the dynamics of the macroscopic dipole moment around the expected echo arrival time, $2(\tau_{12} + \tau_p)$, is similar to a mirrored copy of its dynamics around the time $t = \tau_p$, as shown by the right panels of Fig. 6.11. Thus, the PPE pulse is retarded for the a $\pi/2$-excitation pulse and advanced for a $3\pi/2$-pulse, when the ensemble dephasing during pulse action is sufficiently strong. This can be achieved either by high inhomogeneity in the excited ensemble and/or long pulse duration.

The analysis of the experimental data has to consider that the measured signal is in fact the modulus of the cross-correlation of the PPE amplitude from Eq. (6.7) with the Gaussian reference pulse field (cf. Eq. (4.7)), i.e.

$$|\mathcal{E}_S(t)| \propto \left| \int_{-\infty}^{\infty} e^{-\frac{\tau^2}{2\tilde{\tau}_p^2}} A_{PPE}(t-\tau) \mathrm{d}\tau \right|. \tag{6.8}$$

From auto-correlation measurements it is known that $\tau_p = 2\sqrt{2\ln 2}\tilde{\tau}_p = 3.3\,\mathrm{ps}$ is the laser pulse duration in the electric field scale (cf. Sec. 4.1). The inhomogenity parameter $2\sqrt{2\ln 2}\hbar\Gamma = 6.6\,\mathrm{meV}$ is taken from the PL linewidth in Fig. 6.2(b). The theoretical simulation depicted in Fig. 6.9(b) is in good agreement with the experimental results in Fig. 6.9(a). Note that the inhomogenity $\tau_p\Gamma \approx 14$ is considerably larger than in Ref. [Pol16a] where the cross-correlation with the reference pulse was neglected. However, further mechanisms, e.g., excitation induced dephasing and the spread of Rabi frequencies, have to be considered for improved theoretical simulations [Pol17b].

6.3.3 Simulated two-dimensional Fourier transform spectroscopy

In a next step one simulates 2DFTS for the inhomogeneously broadened QD ensemble. As done in Sec. 2.2.3, the two temporal variables are redefined, i.e., $t_1 = \tau_{12}$ is the delay between the laser pulses, and $t_3 = t - \tau_{12}$ is the delay of the resulting PPE. Thus, Eq. (6.7) can be rewritten in the form

$$\begin{aligned} S_I(t_1,t_3) \quad \propto \quad & e^{i\omega(t_3-t_1)} e^{-\frac{t_3-t_1}{T_2}} \int_{-\infty}^{\infty} e^{-\frac{\Delta^2}{2\Gamma^2}} \frac{\chi_1 \chi_2^2}{\tilde{\Omega}_1 \tilde{\Omega}_2^2} \sin^2\left(\frac{\tilde{\Omega}_2 \tau_\mathrm{p}}{2}\right) \\ \times \quad & \left[\frac{2\Delta}{\tilde{\Omega}_1} \sin^2\left(\frac{\tilde{\Omega}_1 \tau_\mathrm{p}}{2}\right) \sin(\Delta[t_3 - t_1 - 2\tau_\mathrm{p}]) \right. \\ & \left. + \sin\left(\tilde{\Omega}_1 \tau_\mathrm{p}\right) \cos(\Delta[t_3 - t_1 - 2\tau_\mathrm{p}])\right] \mathrm{d}\Delta. \end{aligned} \tag{6.9}$$

Note, that $\exp[i\omega(t_3 - t_1)]$ and the exponentially decaying term with the dephasing time T_2 are added here. This is necessary since on has to integrate over the times t_1 and t_3 in order to obtain the rephasing spectra according to Eq. (2.19). The results of the numerical integration are shown in Fig. 6.12 for TLS ensemble excitation with different pulse areas Θ_1. The 2DFTS spectra are normalized to unity. Note, that the weak fringes in the plot are an artifact due to taking the Fourier transform over finite intervals. The reader should compare the pictures with the analytically calculated rephasing spectra for an ideal (Hahn echo) configuration in Fig. 7.3(a), for which no temporal shift of the PPE is expected. In the case of weak excitation (linear regime) of a strongly inhomogeneous system similar to the QD ensemble studied in this chapter, the real part in Fig. 6.12(a) is quite similar to the one in Fig. 7.3(a). Big changes are seen in the imaginary part of the two-dimensional spectrum: While it is zero for an ideal configuration (compare Eq. (7.12)) the temporal shift of the PPE gives rise to a significant imaginary part with a dispersive shape and sign reversal along the diagonal, as shown in Fig. 6.12(b). When increasing the power of the first excitation pulse further to a π-pulse also the real part of the two-dimensional spectrum undergoes strong changes: its sign becomes reversed compared to the weak power regime and it shows a double peak structure, while the imaginary part of the spectrum is now the dominant contribution (Figs. 6.12(c) and 6.12(d)).

6.4 Conclusions

In conclusion, the coherent optical response from self-assembled (In,Ga)As QDs embedded in a TP, as well as in a DBR planar microcavity has been demonstrated in form of photon echoes. Despite the low quality factor of about 100 a substantial enhancement of the selective optical excitation of QDs whose optical transitions are in resonance with the TP cavity mode has been shown. The intensity of the driving optical field is amplified by 6 times with comparison to bare QDs. Such enhancement allows one to observe Rabi oscillations in the photon echo and to perform coherent control of excitons with

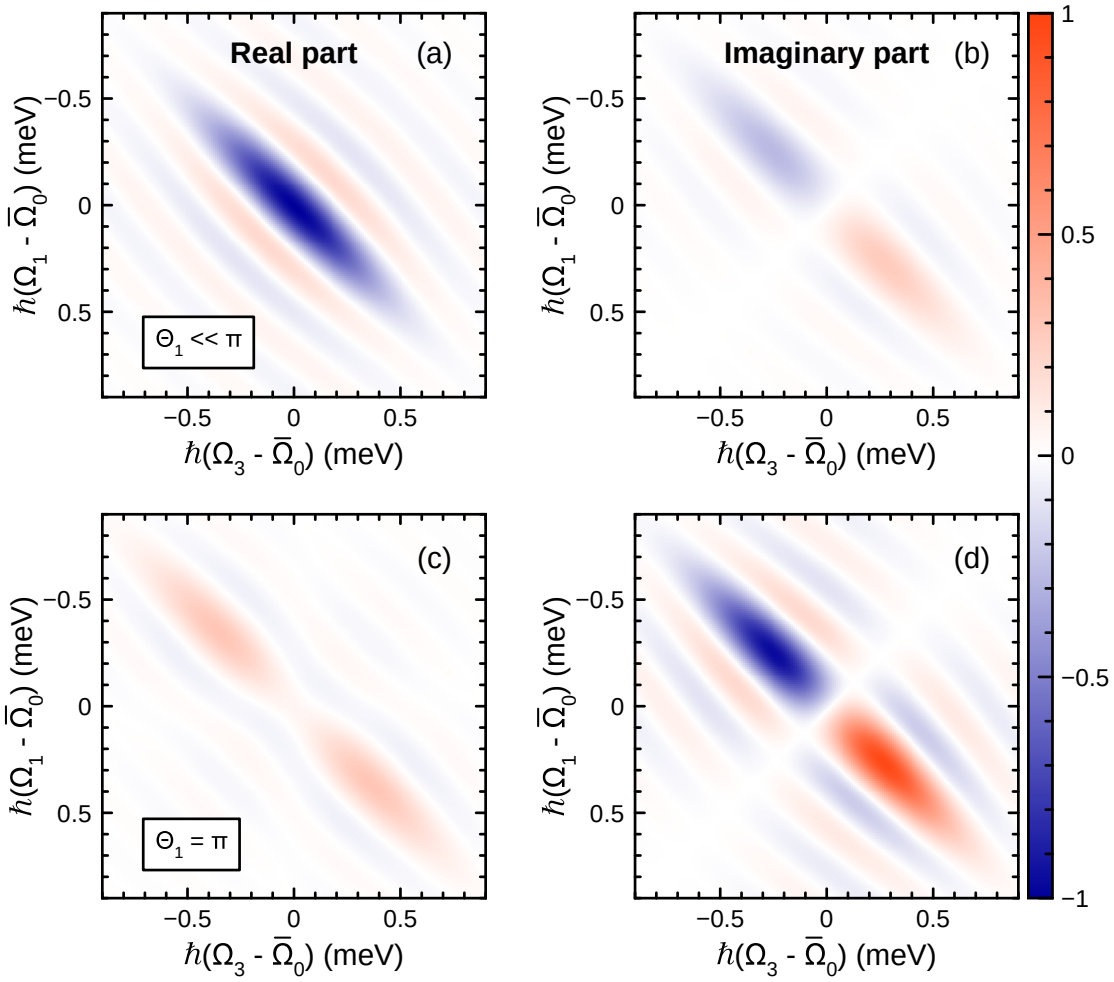

Figure 6.12: Results of 2DFTS simulations for (a), (b) linear excitation regime with weak intensity of the first pulse, $\Theta_1 = 0.01\pi$, and (c), (d) excitation in the non-linear regime with the first pulse being a π-pulse. All spectra are normalized to unity. (a), (c) show real parts, (b), (d) show imaginary parts. Parameters in the calculations are $2\sqrt{2\ln 2}\hbar\Gamma = 0.65\,\mathrm{meV}$ and $\tau_\mathrm{p} = 2.5\,\mathrm{ps}$.

picosecond optical pulses of moderate intensities, while the statistical distribution of dipole moments still represents a significant problem. The decoherence and population dynamics of excitons in TP structures also experience modifications. A decrease of the radiative recombination time from 350 to 170 ps due to the Purcell effect is observed. The presence of the metal layer gives rise to pure dephasing of the QD excitons with characteristic times of about 200 to 400 ps so that pure dephasing remains quite weak. Note, that the metal layer at the top of the TP microcavity can be used to control the charge state of QDs electrically [Bra15]. Therefore, such structures are appealing for investigations of long-lived photon echoes from charged QDs where the decay rate is governed by the spin relaxation of the resident electrons (cf. Refs. [Lan14, Bab17] and

Ch. 7).

The relation between QD ensemble spectral broadening and exciting pulse width was studied in the second main part of this chapter. Although the importance of the oscillator detuning from the optical frequency in forming the macroscopic coherent response in semiconductor QDs was addressed in literature already before [Pat05, Ram07], no consequence of the timing of the associated photon echo had been reported for such systems. The essential consequence of this study is that even significantly inhomogeneous semiconductor systems still demonstrate a comprehensible coherent behavior, but great care needs to be exercised to consider the consequences of the inhomogeneity in detail. When doing so, such systems are very well suited candidates for the coherent manipulations in coherent optoelectronics. In particular, the observed temporal shifts of the PPE amplitude need to be taken into account when a precise timing of the optical signals matters. The findings have strong impact on interpretation of two-dimensional Fourier transform images. The complex-valued envelope of the PPE-transients from strongly inhomogeneous systems results in a changeover of the corresponding 2DFTS image from a resonance profile to a dispersive profile. The results obtained here were used by Ref. [Mis17] in order to discuss the effect of shaping the first pulse in frequency while keeping its pulse area constant.

Chapter 7

High resolution spectroscopy of electron spins in a CdTe quantum well

The potentials of studying Λ-type energy schemes with electron ground state by two-dimensional Fourier transform spectroscopy (2DFTS) are investigated. Our test object is the four-level system arising from trions or donor-bound excitons in semiconductor nanostructures. After discussing the theory of long-lived photon echoes, we present a CdTe/(Cd,Mg)Te quantum well (QW) sample which can be used as a model system. Next, experimental results on heterodyne-detected transient photon echoes (PEs) are analyzed. Extracted fitting parameters are used to restore the absolute value of a two-dimensional spectrum with information about the ground state electron spin coherence. The results are compared with conventional spin coherence measurements using pump-probe Kerr rotation spectroscopy.

In contrast to Ch. 6, the results are discussed in the "language" of 2DFTS by renaming the pulse delays $\tau_{12} \mapsto t_1$ and $\tau_{23} \mapsto t_2$ (cf. Sec. 2.2.3). In the experimental part $\tau_{\mathrm{ref}} \mapsto t_3$, i.e., the time over which the signal is emitted. Most of the results presented in this chapter have been or will be published in a similar form in Ref. [Sal17b, Sal17c].

7.1 Four-level system with electron ground state

Λ-type energy schemes are realized in a large variety of atomic and solid state objects with pseudospin in the ground and excited states [Scu97]. Here, we discuss negatively charged trion complexes, i.e., X^- and D^0X as present in semiconductor nanostructures (cf. Sec. 1.4.1).

7.1.1 Selection rules

Negatively charged trion complexes in a semiconductor QW can be considered as four-level systems. The ground state is given by an electron with doublet spin orientation

$\pm 1/2$ along the quantization z-axis. The lowest-energy states that can be optically excited are the localized trion or the donor-bound exciton, whose projection of total angular momentum $\pm 3/2$ is given by the heavy hole. Higher energy states, e.g., the neutral exciton or the light hole exciton transitions, can be neglected for the optical pulses with spectral width $\sim 1\,\mathrm{meV}$ used in our experiments. The optical transitions shown in Fig. 7.1(a) correspond to the matrix elements (1.23) calculated in Sec. 1.3.2.

The application of a transverse magnetic field $\boldsymbol{B} \parallel \boldsymbol{x}$ leads to a coupling between the electron spin states, $|1\rangle_z$ and $|2\rangle_z$, and trion states, $|3\rangle_z$ and $|4\rangle_z$. The selection rules in Fig. 7.1(a) only remain valid if the field strength is small and the laser pulses are short [Lan12]. In this case only the electron spins perform notable Larmor oscillations, as indicated by the red arrows. Without these restrictions[1] one has to express the system in the eigenvalues along the x-direction

$$|1\rangle_x = \frac{1}{\sqrt{2}}(-|u_{+1/2}\rangle + |u_{-1/2}\rangle), \tag{7.1a}$$

$$|2\rangle_x = \frac{1}{\sqrt{2}}(|u_{+1/2}\rangle + |u_{-1/2}\rangle), \tag{7.1b}$$

$$|3\rangle_x = \frac{1}{\sqrt{2}}(-|u_{+3/2}\rangle + |u_{-3/2}\rangle), \tag{7.1c}$$

$$|4\rangle_x = \frac{1}{\sqrt{2}}(|u_{+3/2}\rangle + |u_{-3/2}\rangle), \tag{7.1d}$$

where u_m are the Bloch amplitudes from Eqs. (1.21) and (1.22). The only transition matrix elements not equal to zero are

$$\boldsymbol{d}_\mathrm{V} \equiv \langle 1|\,\hat{\boldsymbol{d}}\,|3\rangle_x = \langle 2|\,\hat{\boldsymbol{d}}\,|4\rangle_x \propto -\frac{1}{\sqrt{2}} i\boldsymbol{y}, \tag{7.2a}$$

$$\boldsymbol{d}_\mathrm{H} \equiv \langle 1|\,\hat{\boldsymbol{d}}\,|4\rangle_x = \langle 2|\,\hat{\boldsymbol{d}}\,|3\rangle_x \propto \frac{1}{\sqrt{2}}\boldsymbol{x}, \tag{7.2b}$$

where i indicates a phase difference between the transition dipole moments. The resulting selection rules shown in Fig. 7.1(b) are consistent with the those of charged InAs QDs published in Ref. [Tru13]. Since the heavy hole transverse g factor is close to zero [Mar99, Deb13], only the Zeeman splitting for the electron spin states is shown. In the geometry of the experiment, optical transitions are allowed using light with linear polarization directed parallel (H $\parallel \boldsymbol{x}$) or perpendicular (V $\parallel \boldsymbol{y}$) to the magnetic field.

7.1.2 Hamiltonian

The Hamiltonians for Figs. 7.1(a) and 7.1(b) can be written as $\hat{\mathcal{H}} = \hat{\mathcal{H}}_0 + \hat{\mathcal{V}} + \hat{\mathcal{H}}_B$, where $\hat{\mathcal{H}}_0$ describes the isolated system, $\hat{\mathcal{V}}$ the interaction with an electromagnetic field (cf. Eq. (2.10)), and $\hat{\mathcal{H}}_B$ results from the Zeeman effect (cf. Sec. 3.1.2).

[1] There is still the restriction that the Zeeman splitting between the heavy hole states, $\hbar\omega_{\mathrm{L,hh}}$, is smaller than the splitting of heavy and light hole, $\Delta_{\mathrm{lh,hh}}$. Mixing between all four valence band states becomes relevant for magnetic fields $B > 5\,\mathrm{T}$ [Bar11].

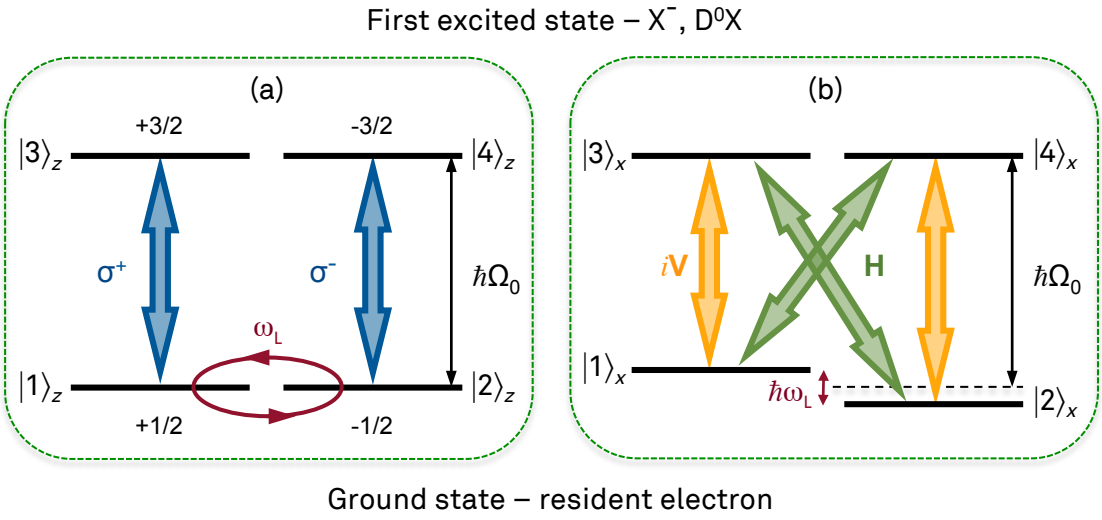

Figure 7.1: Energy level diagram and optical transitions for the trion (X^-) or the donor-bound exciton (D^0X) in a CdTe QW with growth direction $\boldsymbol{z}$. Ω_0 corresponds to the optical resonance frequency. (a) Selection rules in the basis of $\boldsymbol{z}$ where $\sigma^\pm$ denotes circularly polarized light with wave vector along $\boldsymbol{z}$. The application of a small magnetic field $\boldsymbol{B} \parallel \boldsymbol{x}$ couples the electron spin states as indicated by the red arrows. The selection rules remain valid in the short pulse approximation where the pulse duration τ_p is significantly shorter than the electron spin Larmor precession period, i.e. $\omega_\mathrm{L}\tau_\mathrm{p} \ll 1$. In the general case (b), $\boldsymbol{x}$ is a good quantization axis. $\hbar\omega_\mathrm{L}$ is the Zeeman energy splitting of the electron spins which is considerably larger than for the hole spins (almost-degenerate excited states). Optical transitions are excising for horizontally (H $\parallel \boldsymbol{x}$) or vertically (V $\parallel \boldsymbol{y}$) linear polarized light. i indicates a phase difference between the transition dipole moments. A typical value for the experiments is $B = 260\,\mathrm{mT}$ which leads to $\omega_\mathrm{L}\tau_\mathrm{p} \approx 0.17$ and $\hbar\omega_\mathrm{L} \approx 24\,\mu\mathrm{eV}$.

In the short pulse approximation, $\omega_\mathrm{L}\tau_\mathrm{p} \ll 1$, one can write the Hamiltonian for the system in Fig. 7.1(a) with the circularly polarized dipole elements $\boldsymbol{d}_\pm$ from Eqs. (1.23) as

$$\hat{\mathcal{H}}^\mathrm{circ} = \begin{pmatrix} 0 & \frac{\hbar\omega_\mathrm{L}}{2} & -\boldsymbol{d}_+\boldsymbol{\mathcal{E}_0}e^{i\omega t} & 0 \\ \frac{\hbar\omega_\mathrm{L}}{2} & 0 & 0 & -\boldsymbol{d}_-\boldsymbol{\mathcal{E}_0}e^{i\omega t} \\ -\boldsymbol{d}_+^*\boldsymbol{\mathcal{E}_0}^*e^{-i\omega t} & 0 & \hbar\Omega_0 & 0 \\ 0 & -\boldsymbol{d}_-^*\boldsymbol{\mathcal{E}_0}^*e^{-i\omega t} & 0 & \hbar\Omega_0 \end{pmatrix}, \tag{7.3}$$

where Ω_0 corresponds to the optical resonance frequency, $\boldsymbol{\mathcal{E}}_0$ is the electric field amplitude in the direction of the polarization vector, and ω is the light frequency (cf. Eq. (2.11)). The system in Fig. 7.1(b) is described by a Hamiltonian with the linearly polarized dipole elements $\boldsymbol{d}_\mathrm{V,H}$ from Eqs. (7.2), i.e.,

$$\hat{\mathcal{H}}^\mathrm{lin} = \begin{pmatrix} -\frac{\hbar\omega_\mathrm{L}}{2} & 0 & -\boldsymbol{d}_\mathrm{V}\boldsymbol{\mathcal{E}_0}e^{i\omega t} & -\boldsymbol{d}_\mathrm{H}\boldsymbol{\mathcal{E}_0}e^{i\omega t} \\ 0 & +\frac{\hbar\omega_\mathrm{L}}{2} & -\boldsymbol{d}_\mathrm{H}\boldsymbol{\mathcal{E}_0}e^{i\omega t} & -\boldsymbol{d}_\mathrm{V}\boldsymbol{\mathcal{E}_0}e^{i\omega t} \\ -\boldsymbol{d}_\mathrm{V}^*\boldsymbol{\mathcal{E}_0}^*e^{-i\omega t} & -\boldsymbol{d}_\mathrm{H}^*\boldsymbol{\mathcal{E}_0}^*e^{-i\omega t} & \hbar\Omega_0 & 0 \\ -\boldsymbol{d}_\mathrm{H}^*\boldsymbol{\mathcal{E}_0}^*e^{-i\omega t} & -\boldsymbol{d}_\mathrm{V}^*\boldsymbol{\mathcal{E}_0}^*e^{-i\omega t} & 0 & \hbar\Omega_0 \end{pmatrix}. \tag{7.4}$$

As before, we assume that the excited states are almost degenerated and the Zeeman spin splitting of heavy holes is negligible.

7.2 Theory of the three pulse photon echo

The four-level system from Fig. 7.1(b) can be investigated in three pulse photon echo experiments with various polarization schemes.

7.2.1 Temporal evolution of the density matrix

The temporal evolution of the 4×4 density matrix ρ is given by the Lindblad equation $i\hbar\dot{\rho} = [\hat{\mathcal{H}},\rho] + \Upsilon$ (cf. Sec. 2.1.2). For the calculation of the three pulse PE one separates the interaction with a light pulse from the temporal evolution after the light pulse; the latter is given by relaxation processes Υ and, eventually, Larmor oscillations in the magnetic field. Successive calculations for pulse 1, 2, and 3 allows one to obtain an expression for the macroscopic polarization $P \propto A_{\mathrm{PE}}$ which can be measured in a transient four-wave mixing (TFWM) experiment. As initial conditions one assumes that before excitation with pulse 1, the system is in the ground state and the only non-zero density matrix elements are $\rho_{11} = \rho_{22} = 1/2$, i.e. $\hbar\omega_{\mathrm{L}} \ll k_{\mathrm{B}}T$, where k_{B} is the Boltzman constant and T is the temperature. *Langer et al.* [Lan14] calculated the temporal evolution of ρ for the Hamiltonian $\hat{\mathcal{H}}^{\mathrm{circ}}$ from Eq. (7.3) in the short pulse approximation, i.e., the pulse duration τ_{p} is significantly shorter than the trion lifetime, the decoherence times, and the electron spin precession period in the transverse magnetic field. In the following, we limit our considerations to the energy system shown in Fig. 7.1(b). However, $\hat{\mathcal{H}}^{\mathrm{lin}}$ from Eq. (7.4) together with the same assumptions as mentioned above produces equivalent results to Ref. [Lan14] (cf. supplementary section I of Ref. [Sal17b]). For the case that the splitting of the electron spin sub-levels in the ground state is smaller than the spectral width of the excitation laser pulses ($\tau_{\mathrm{p}}\omega_{\mathrm{L}} \ll 2\pi$) and the inhomogeneous broadening ($\omega_{\mathrm{L}}\sigma \ll 1$), the echo signals can be well approximated by Gaussian pulses with an amplitude $A_{\mathrm{PE}}(t_1,t_2)$ that depends on t_1 and t_2 only (cf. (2.17)).

An elegant way to track the temporal evolution of ρ during the three pulse photon echo experiment is given by double-sided Feynman diagrams (cf. Sec. 2.2.2). The three main polarization configurations are shown in Fig. 7.2. Following the Feynman diagrams, it is seen that the polarization of the resulting photon echo depends on the polarization of the second and third pulse. For HHH, the possible optical transitions take place between the two independent two-level pairs $|1\rangle_x$-$|4\rangle_x$ and $|2\rangle_x$-$|3\rangle_x$, while for HVV and HVH all transitions are involved, and the coherent superposition between one pair of states is transferred to the other pair after each excitation event in a steplike process.

The first H-polarized pulse addresses the two optical transitions between $|1\rangle_x$ and $|4\rangle_x$ at frequency $\Omega_0 - \omega_{\mathrm{L}}/2$ and between $|2\rangle_x$ and $|3\rangle_x$ at frequency $\Omega_0 + \omega_{\mathrm{L}}/2$ (cf. Fig. 7.1(b)). Pulse 1 creates two independent coherent superpositions between the

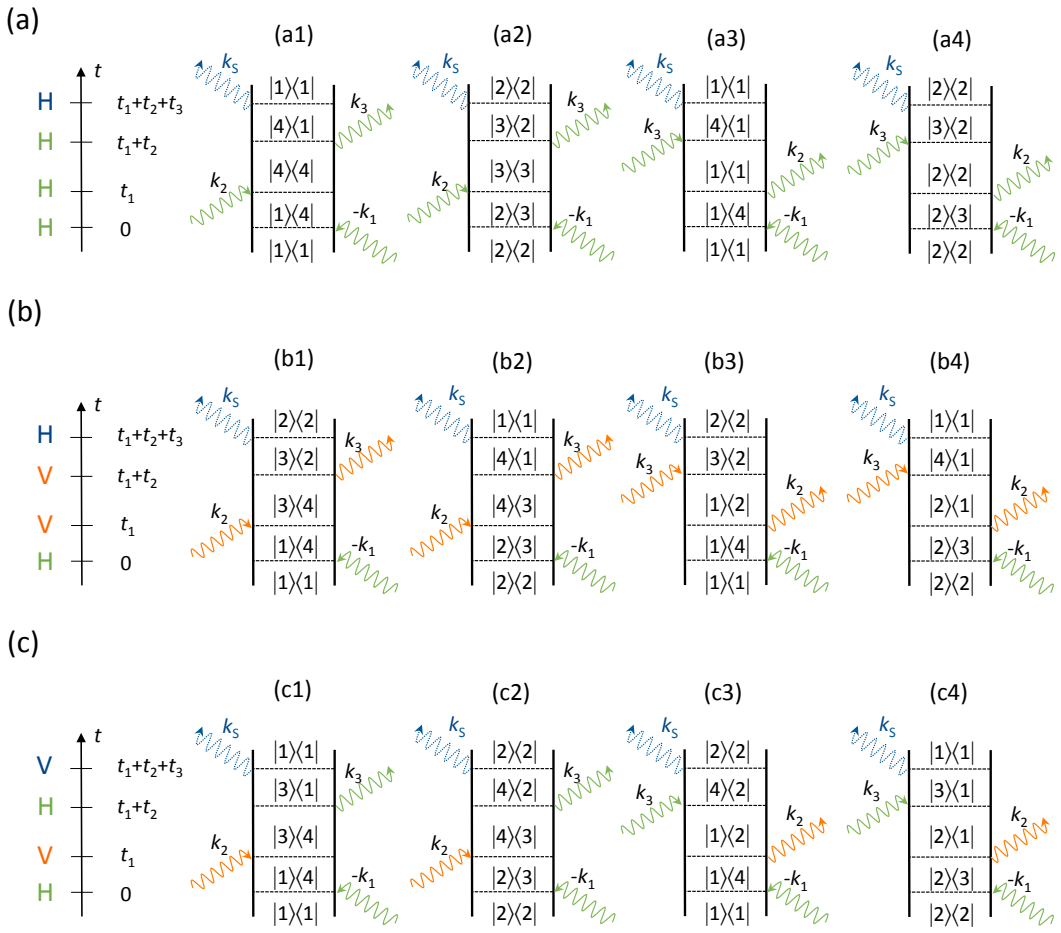

Figure 7.2: Double-sided Feynman diagrams for the HHH (a), HVV (b), and HVH (c) polarization configurations. For VVV, VHH, and VHV the resulting diagrams are identical to the one shown here if the state vectors $|3\rangle$ and $|4\rangle$ are exchanged. For the sake of simplicity, we neglect the subscript x indicating the quantization axis of the state vectors (cf. Fig. 7.1(b)).

pairs of states $|1\rangle_x$-$|4\rangle_x$ and $|2\rangle_x$-$|3\rangle_x$, which can be considered as optical coherences. In the density matrix formalism, they correspond to the ρ_{14} and ρ_{23} elements of the density matrix, respectively. The second and third pulses are H or V polarized. Possible quantum mechanical pathways for the evolution of the system follow from the double-sided Feynman diagrams in Figs. 7.2(a), 7.2(b), and 7.2(c), respectively, and will be discussed in the following.

HHH co-polarized configuration

The second pulse addresses the same pairs of optical transitions and, in that way, the optical coherences ρ_{14} and ρ_{23} are transformed into the excited state populations ρ_{44} and

ρ_{33} [diagrams (a1) and (a2) in Fig. 7.2(a)] as well as the ground state populations ρ_{11} and ρ_{22} [diagrams (a3) and (a4) in Fig. 7.2(a)]. The populations carry the information about the optical phase $\phi_\pm = (\Omega_0 \pm \omega_\mathrm{L}/2)t_1$ between the pulses 1 and 2, i.e., $\rho_{33} \propto \sin^2(\phi_-/2)$ and $\rho_{44} \propto \sin^2(\phi_+/2)$, where $\rho_{11} + \rho_{33} = \rho_{22} + \rho_{44} = 1/2$ holds. The third pulse induces the coherences ρ_{41} and ρ_{32} and results in the emission of an H-polarized PE signal whose amplitude is given by

$$\begin{aligned} A_\mathrm{PE}^{\parallel} &\propto \rho_{14} + \rho_{23} \\ &\propto e^{-\frac{2t_1}{T_2}} e^{-\frac{t_2}{\tau_\mathrm{r}}} \left[2\cos^2\left(\frac{\omega_\mathrm{L} t_1}{2}\right) + e^{-\frac{t_2}{\tau_\mathrm{sh}}} \sin^2\left(\frac{\omega_\mathrm{L} t_1}{2}\right)\right] \\ &\quad + e^{-\frac{2t_1}{T_2}} e^{-\frac{t_2}{T_{1,\mathrm{e}}}} \sin^2\left(\frac{\omega_\mathrm{L} t_1}{2}\right). \end{aligned} \tag{7.5}$$

T_2 and τ_r are the coherence time and the radiative lifetime of the optically excited X^- or $\mathrm{D}^0\mathrm{X}$ complex, τ_sh is the pure spin relaxation time of the hole[1] for X^- or $\mathrm{D}^0\mathrm{X}$, and $T_{1,\mathrm{e}}$ is the longitudinal spin relaxation time of the electron in the ground state.

At zero magnetic field the frequencies of the optical transitions $\Omega_0 \pm \omega_\mathrm{L}/2$ in the left and right arms of Fig. 7.1(b) are the same and the excited state populations are identical, i.e. $\rho_{33} = \rho_{44}$. Then, the optical response is governed by the radiative lifetime τ_r when t_2 is varied. This population decay due to spontaneous recombination is seen in the first term on the left hand side of Eq. (7.5).

When a magnetic field is applied $\rho_{33} - \rho_{44} \propto \sin(\omega_\mathrm{L} t_1/2)\sin(\Omega_0 t_1)$; i.e., for a given Ω_0, there are non-zero spin populations

$$J_x = \frac{\rho_{33} - \rho_{44}}{2} \quad \text{and} \quad S_x = \frac{\rho_{11} - \rho_{22}}{2} = -J_x \tag{7.6}$$

in the excited and ground states, respectively. Note that S_x and J_x carry the information about $\phi_\pm$ and correspondingly contribute to the coherent optical response [Lan14]. In Eq. (7.5) this is given by the second and third term. The decay is now governed by the pure spin relaxation of the photoexcited complex τ_sh and the longitudinal spin relaxation of the resident electron in the ground state $T_{1,\mathrm{e}}$, respectively. Note that the last term is not influenced by the radiative lifetime τ_r. In the investigated structures $T_{1,\mathrm{e}} \gg \tau_\mathrm{r}$ so that the last term is responsible for the observation of long-lived stimulated photon echoes.

In the simple case $t_2 = 0$ the signal is

$$A_\mathrm{PE}^{\parallel} \propto e^{-\frac{2t_1}{T_2}}, \tag{7.7}$$

which is independent of the magnetic field.

[1] Note that we do not distinguish between longitudinal and transverse spin relaxation for holes, $T_{1,\mathrm{h}}$ and $T_{2,\mathrm{h}}$, respectively, since the heavy hole transverse g factor is close to zero.

HVV cross-polarized configuration

Here, the second pulse accomplishes a stimulated steplike Raman process where the optical coherences ρ_{14} and ρ_{23} are transferred into (i) the X^- or D^0X spin coherence ρ_{34} [diagrams (b1) and (b2) in Fig. 7.2(b)] and (ii) the electron spin coherence ρ_{12} [diagrams (b3) and (b4) in Fig. 7.2(b)]. The third pulse induces a back transformation of the excited trion and ground electron spin coherences into the optical coherences ρ_{32} and ρ_{41}. This mechanism exploits off-diagonal density matrix elements. Thereby, the Raman process initiates a shift of the optical frequency of the emitted signal by $+\omega_L$ or $-\omega_L$ when starting from ρ_{11} or ρ_{22}, respectively. This leads to Larmor precession with the frequency ω_L as manifested by the H-polarized PE signal with amplitude

$$\begin{aligned} A_{PE}^{\perp} &\propto \rho_{14} + \rho_{23} \\ &\propto e^{-\frac{2t_1}{T_2}} \left[e^{-\frac{t_2}{\tau_T}} \cos(\omega_L t_1) + e^{-\frac{t_2}{T_{2,e}^*}} \cos(\omega_L (t_1 + t_2)) \right]. \end{aligned} \tag{7.8}$$

Here, one assumes that $\omega_L t_1 \gg 2\pi$, i.e. the Larmor precession is fast compared to the delay between the pulses 1 and 2. In Eq. (7.8) $T_{2,e}^*$ is the transverse spin dephasing time of the electron ensemble in the ground state and τ_T is the spin lifetime of the trion, which is determined by the spin relaxation of the hole in the trion and its radiative decay, i.e.

$$\frac{1}{\tau_T} = \frac{1}{\tau_{sh}} + \frac{1}{\tau_r}. \tag{7.9}$$

The two subgroups (i) and (ii) are linked to the two terms of Eq. (7.8). The Raman coherence in the photoexcited state corresponds to the first term, decaying with the spin lifetime of the trion τ_T. The Raman coherence in the ground state decays with the transverse electron spin relaxation time $T_{2,e}^*$. In our case $T_{2,e}^* \gg \tau_T$ so that the second term represents the long-lived coherent optical signal.

For $t_2 = 0$ the signal transforms into

$$A_{PE}^{\perp} \propto e^{-\frac{2t_1}{T_2}} \cos(\omega_L t_1). \tag{7.10}$$

HVH cross-polarized configuration

The situation is very similar to the HVV configuration, however, for the first subgroup [diagrams (c1) and (c2) in Fig. 7.2(c)], i.e. the Raman coherences in the photoexcited state, there is no energy shift by $\pm\hbar\omega_L$ for the emitted photon (excitation and emission field have the same otpical frequency). For this reason the first term in

$$\begin{aligned} A_{PE}^{\times} &\propto \rho_{13} + \rho_{24} \\ &\propto e^{-\frac{2t_1}{T_2}} \left[e^{-\frac{t_2}{\tau_T}} + e^{-\frac{t_2}{T_{2,e}^*}} \cos(\omega_L (t_1 + t_2)) \right], \end{aligned} \tag{7.11}$$

does not oscillate. Note that the PE signal from Eq. (7.11) is V-polarized. The long-lived component from the Raman coherence in the ground electron spin state remains

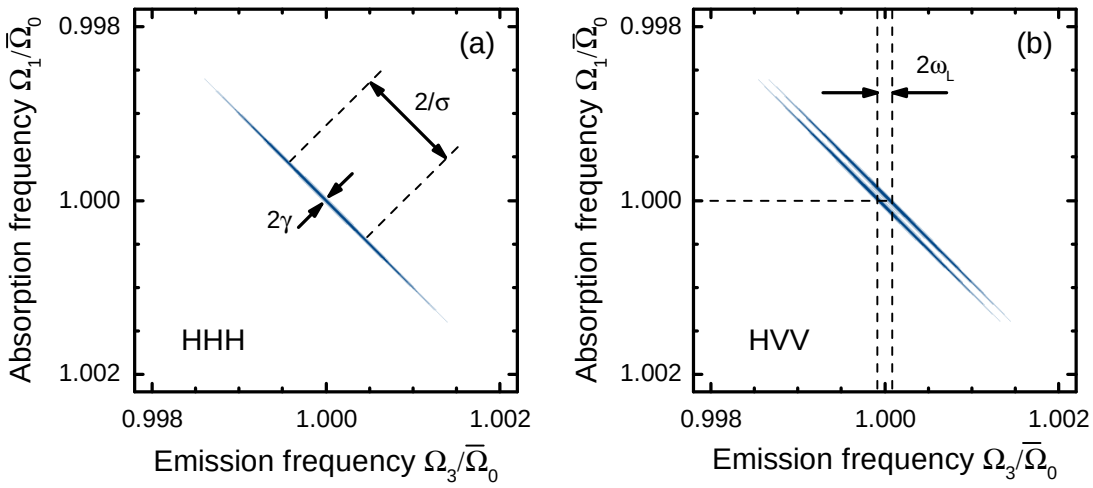

Figure 7.3: Contour plots of the 2D Fourier rephasing spectra $S_I(\Omega_1,\Omega_3)$ in the co-polarized HHH (a) and in cross-polarized HVV (b) polarization configurations after Eqs. (7.12) and (7.13), respectively. The following parameters are used: $\hbar\overline{\Omega}_0 = 1.6\,\mathrm{eV}$, $\hbar\Gamma = \hbar/\sigma = 1\,\mathrm{meV}$, $\hbar\gamma = \hbar/T_2 = 10\,\mu\mathrm{eV}$, $\hbar\omega_\mathrm{L} = 100\,\mu\mathrm{eV}$.

the same as in the HVV polarization, including the shift of the optical frequency of the emitted signal by $\pm\omega_\mathrm{L}$, respectively [diagrams (c3) and (c4) in Fig. 7.2(c)]. For $t_2 = 0$ the signal does not differ from $A^{\perp}_{\mathrm{PPE}}$.

7.2.2 Two-dimensional rephasing spectra

Two-dimensional rephasing spectra follow from Fourier transforms of the signal optical field with respect to t_1 and t_3 as discussed in Sec. 2.2.3. The optical field with amplitude A_PE can be found in Eq (2.18). Here, we calculate Eq. (2.19) for the simple case of $t_2 = 0$. Together with Eq. (7.7) one gets for the co-polarized configuration

$$S^{\parallel}_I(\Omega_1,\Omega_3) \quad \propto \quad e^{-\frac{\sigma^2(\Omega_1-\overline{\Omega}_0)^2}{2}} \frac{\gamma}{4\gamma^2+(\Omega_1-\Omega_3)^2}, \tag{7.12}$$

and with Eq. (7.10) for the cross-polarized configuration

$$S^{\perp}_I(\Omega_1,\Omega_3) \quad = \quad S^{+}_I + S^{-}_I, \tag{7.13a}$$

$$S^{\pm}_I(\Omega_1,\Omega_3) \quad \propto \quad e^{-\frac{\sigma^2(\Omega_1-\overline{\Omega}_0)^2}{2}} \frac{\gamma}{4\gamma^2+(\Omega_1-\Omega_3\pm\omega_\mathrm{L})^2}. \tag{7.13b}$$

$\overline{\Omega}_0$ is the central frequency of the inhomogeneous ensemble with a half-width in frequency corresponding to $1/\sigma$. Here, it is assumed that the inhomogeneous broadening $\Gamma = 1/\sigma$ is significantly larger than the homogeneous broadening $\gamma = 1/T_2$. This condition is fulfilled for the optical transitions to the localized X^- and D^0X complexes [Nol90, Koc93,

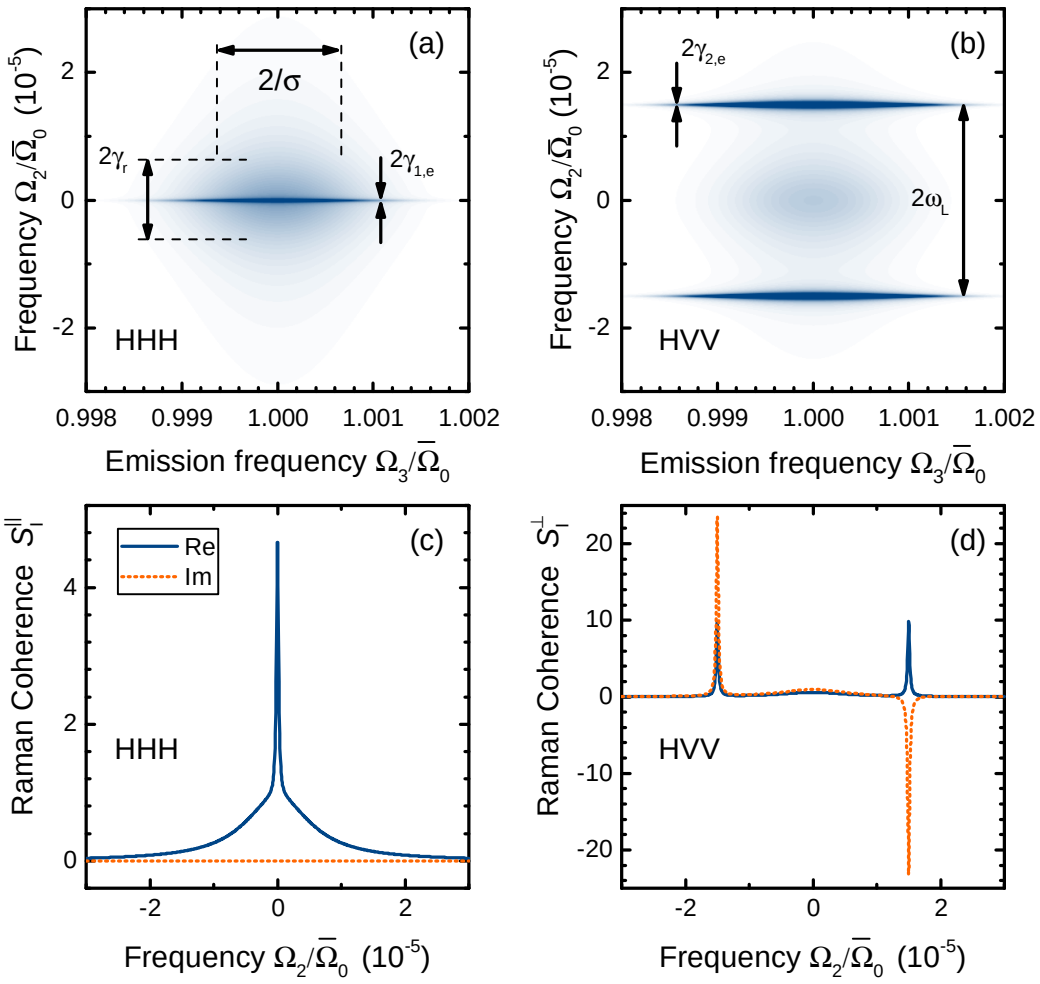

Figure 7.4: Contour plots of the absolute value of the Raman coherence 2D Fourier spectra in the co-polarized HHH (a) and cross- polarized HVV (b) polarization configuration and their cross-sections at the optical frequency $\Omega_3 = \overline{\Omega}_0$ (c) and (d), respectively. The following parameters are used: $\hbar\overline{\Omega}_0 = 1.6\,\mathrm{eV}$, $\hbar\Gamma = \hbar/\sigma = 1\,\mathrm{meV}$, $\hbar\gamma_\mathrm{r} = \hbar\gamma_\mathrm{T} = 10\,\mu\mathrm{eV}$, $\hbar\gamma_{1,\mathrm{e}} = \hbar\gamma_{2,\mathrm{e}} = 0.3\,\mu\mathrm{eV}$, $\hbar\omega_\mathrm{L} = 24\,\mu\mathrm{eV}$ and $t_1 = 26.7\,\mathrm{ps}$.

Moo14, Pol17a]. The rephasing spectra for the co- and cross-polarized configurations are plotted in Figs. 7.3(a) and 7.3(b), respectively. The splitting of the diagonal line by the energy $\hbar\omega_\mathrm{L}$ in the cross-polarized configuration clearly demonstrates the stimulated Raman process with an increase (S_I^+) and a decrease (S_I^-) of the emission frequency compared to single excitation.

7.2.3 Two-dimensional Raman coherence spectra

Of particular interest are Raman coherence spectra according to Eq. (2.20). They are obtained by taking the Fourier transforms of the optical field from Eq. (2.18) with

respect to t_2 and t_3.

For the co-polarized configuration using Eq. (7.5) one obtains

$$S_I^{\parallel}(t_1,\Omega_2,\Omega_3) \propto e^{-\frac{2t_1}{T_2}} e^{-i\Omega_3 t_1} e^{-\frac{\sigma^2(\Omega_3-\overline{\Omega}_0)^2}{2}} (S_{I,\mathrm{T}}^{\parallel} + S_{I,\mathrm{e}}^{\parallel}), \tag{7.14a}$$

$$S_{I,\mathrm{T}}^{\parallel} = 2\cos^2\left(\frac{\omega_\mathrm{L} t_1}{2}\right) \frac{\gamma_\mathrm{r}}{\gamma_\mathrm{r}^2+\Omega_2^2} + \sin^2\left(\frac{\omega_\mathrm{L} t_1}{2}\right) \frac{\gamma_\mathrm{T}}{\gamma_\mathrm{T}^2+\Omega_2^2}, \tag{7.14b}$$

$$S_{I,\mathrm{e}}^{\parallel} = \sin^2\left(\frac{\omega_\mathrm{L} t_1}{2}\right) \frac{\gamma_{1,\mathrm{e}}}{\gamma_{1,\mathrm{e}}^2+\Omega_2^2}, \tag{7.14c}$$

where $\gamma_\mathrm{r} = 1/\tau_\mathrm{r}$, $\gamma_\mathrm{T} = 1/\tau_\mathrm{T}$ and $\gamma_{1,\mathrm{e}} = 1/T_{1,\mathrm{e}}$. The corresponding 2DFTS image is shown in Fig. 7.4(a) for the case when $\gamma_\mathrm{r} = \gamma_\mathrm{T} \gg \gamma_{1,\mathrm{e}}$. In this case, two Lorentzian peaks are centered at $\Omega_2 = 0$ (see the cross section at $\Omega_3 = \overline{\Omega}_0$ in Fig. 7.4(c)). Their widths are given by γ_r and $\gamma_{1,\mathrm{e}}$ and their relative amplitudes depend on $\omega_\mathrm{L} t_1$. The spectrum can be used to evaluate the lifetimes of the excited states (γ_r) and the time of population relaxation between the ground states $|1\rangle_x$ and $|2\rangle_x$ ($\gamma_{1,\mathrm{e}}$).

For the cross-polarized configuration using Eqs. (2.18), (7.8), and (2.20), the solution reads

$$S_I^{\perp}(t_1,\Omega_2,\Omega_3) \propto e^{-\frac{2t_1}{T_2}} e^{-i\Omega_3 t_1} e^{-\frac{\sigma^2(\Omega_3-\overline{\Omega}_0)^2}{2}} (S_{I,\mathrm{T}}^{\perp} + S_{I,\mathrm{e}}^{\perp}), \tag{7.15a}$$

$$S_{I,\mathrm{T}}^{\perp} = 2\cos(\omega_\mathrm{L} t_1) \frac{\gamma_\mathrm{T}}{\gamma_\mathrm{T}^2+\Omega_2^2}, \tag{7.15b}$$

$$S_{I,\mathrm{e}}^{\perp} = \frac{\gamma_{2,\mathrm{e}} e^{i\omega_\mathrm{L} t_1}}{\gamma_{2,\mathrm{e}}^2+(\Omega_2+\omega_\mathrm{L})^2} + \frac{\gamma_{2,\mathrm{e}} e^{-i\omega_\mathrm{L} t_1}}{\gamma_{2,\mathrm{e}}^2+(\Omega_2-\omega_\mathrm{L})^2}, \tag{7.15c}$$

where $\gamma_{2,\mathrm{e}} = 1/T_{2,\mathrm{e}}^*$. This 2DFTS spectrum is shown in Fig. 7.4(b). It is worth mentioning that in the HVV configuration, only the imaginary part is present for $\omega_\mathrm{L} t_1 = \pi/2$. It contains two peaks with different sign (dispersive shape) at frequencies $\Omega_2 = \pm\omega_\mathrm{L}$ (see Fig. 7.4(d)). The widths of these peaks are given by $\gamma_{2,\mathrm{e}}$. Thus, the 2DFTS spectra measured in cross-polarized configuration allow one to evaluate the coherence times and the energy splitting between the ground state levels $\hbar\omega_\mathrm{L}$. The measurement of the splitting works even if it significantly undercuts the homogeneous spectral width of the optical transitions (γ). Thus, this method can be used for high resolution spectroscopy of the ground state. The advantage is the possibility to determine the splitting of the ground states for excitation at a particular photon energy $\omega = \Omega_1$.

7.3 Experimental results

An excellent example and demonstration of the powerful technique described in the previous section is the determination of the spin splittings of different complexes that exist simultaneously in the very same sample, e.g., X^- and D^0X in a CdTe/(Cd,Mg)Te QW. This information cannot be obtained using pure spin resonance techniques where the optical excitation with Ω_1 is absent. Therefore, in this particular case, one performs optically detected magnetic resonance using coherent optical spectroscopy. Eventually, the

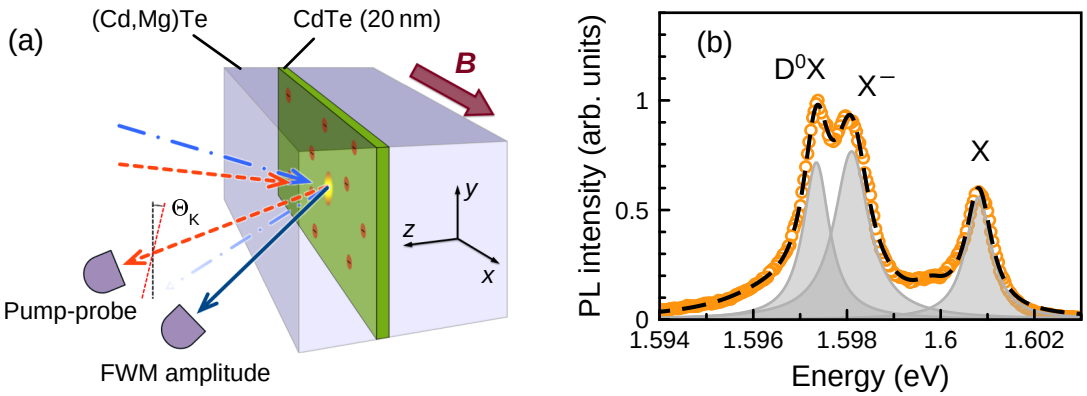

Figure 7.5: (a) Sketch of the 20 nm-thick CdTe QW sample and schematic illustration of the four-wave mixing (FWM) and pump-probe experiment in a transverse magnetic field $\boldsymbol{B}$. Θ_K denotes the Kerr rotation angle. (b) PL spectrum (orange dots) of the sample measured without magnetic field at temperature $T = 2\,\mathrm{K}$ for above-barrier excitation with photon energy 2.33 eV. Three pronounced transients are observed as indicated by the grey shaded Lorentzian lines.

optical coherence initiated by the laser pulse plays an essential role during the excitation and the final emission process at Ω_1 and Ω_3 optical frequency, respectively. Otherwise, the Raman coherence cannot be restored, which is in contrast to conventional time-resolved pump-probe Faraday rotation measurement [Cro97a, Zhu07, Yug09].

7.3.1 The CdTe/(Cd,Mg)Te quantum well sample

The investigated sample (code 032112B) comprises a 20 nm-thick high quality CdTe QW sandwiched between $Cd_{0.76}Mg_{0.24}Te$ barriers (Fig. 7.5(a)). The QW was grown by molecular-beam epitaxy on a (100)-GaAs substrate, onto which a 4.5 μm-thick (Cd,Mg)Te buffer was deposited followed by 5 short-period superlattices and a 100 nm $Cd_{0.76}Mg_{0.24}Te$ barrier. The structure was not intentionally doped with donors; however, the unavoidable background of impurities results in localized resident carriers that originate from the barriers as well as from electrons bound to donors in the QW. The density of these electrons, $n_e \leq 10^{10}\,\mathrm{cm}^{-2}$, in the QW is low so that the exciton Bohr radius $a_B \ll 1/\sqrt{n_e}$, which allows one to consider each resident electron as isolated and noninteracting with other electrons. At cryogenic temperatures the resident electrons are localized on potential fluctuations. Alternately, the electrons can become trapped by donors.

The photoluminescence (PL) spectrum measured at the temperature $T = 2\,\mathrm{K}$ is shown in Fig. 7.5(b). It consists of three pronounced spectral lines which are attributed to the exciton (X), the negatively charged trion (X^-), and the donor-bound exciton (D^0X). The D^0X binding energy is found to exceed the X^- binding energy for a QW of the same width [Pag98]. Other complexes such as the acceptor bound exciton (A^0X), exciton bound to ionized donor (D^+X), or positively charged trion (X^+) could not explain the results of the magneto-optical measurements presented later in this chapter.

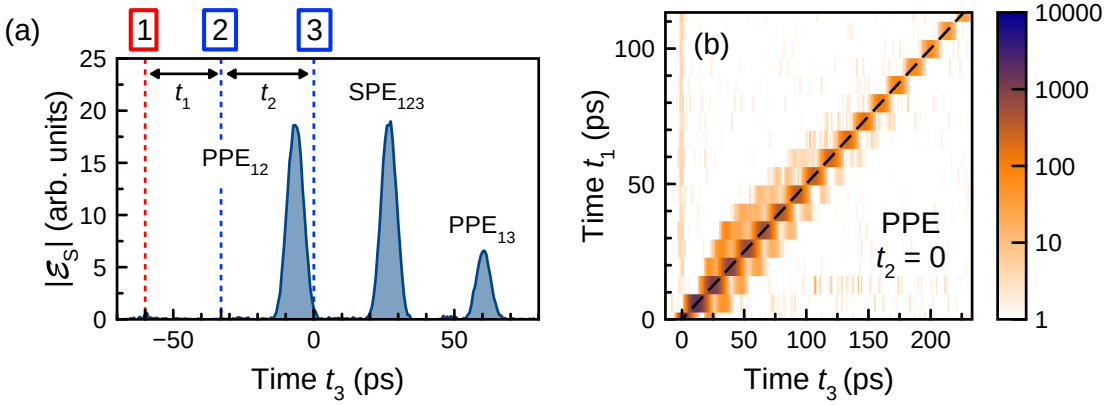

Figure 7.6: (a) Time-resolved cross-correlation of the FWM signal $|\mathcal{E}_S(t_3)|$ measured for $t_1 = 27\,\text{ps}$ and $t_2 = 33\,\text{ps}$. The signal is given by photon echoes involving different pulse sequences: PPE_{12} and PPE_{13} correspond to the two-pulse sequences 1-2 and 1-3, respectively. SPE_{123} corresponds to the three-pulse sequence 1-2-3. (b) Color map of $|\mathcal{E}_S(t_1,t_3)|$ showing the PPE for $t_2 = 0$. The dashed line shows the expected trajectory of the PPE, i.e., $t_3 = 2t_1$. Experimental parameters: temperature $T = 2\,\text{K}$, photon energy $\hbar\omega = 1.597\,\text{eV}$.

The weak inhomogenous broadening of the transitions enables the selective excitation of trions, donor-bound excitons, and excitons by the use of spectrally narrow picosecond pulses (cf. Fig. 4.1). Similar structures with this feature were studied in Refs. [Lan12, Lan14].

7.3.2 Coherent optical spectroscopy in zero magnetic field

Figure 7.6(a) shows a typical time-resolved FWM signal $|\mathcal{E}_S(t_3)|$ from our CdTe QW measured for $t_1 = 27\,\text{ps}$ and $t_2 = 33\,\text{ps}$ with excitation at photon energy $\hbar\omega = 1.597\,\text{eV}$. The coherent optical response is fully given by photon echoes. The energy density of each pulse is kept below $30\,\text{nJ/cm}^2$ in order to remain in the $\chi^{(3)}$-regime; i.e., the photon echo intensity depends linearly on the intensity of each of the beams. Due to $\boldsymbol{k}_2 = \boldsymbol{k}_3$ several echoes are emitted along the phase matching direction $\boldsymbol{k}_S$. The two that appear at $t_3 = t_1 \pm t_2$ correspond to primary photon echoes (PPE), which result from the two-pulse sequences 1-2 and 1-3 and are labeled correspondingly as PPE_{12} and PPE_{13} in Fig. 7.6(a). The peak located at $t_3 = t_1$ corresponds to the stimulated photon echo (SPE) which is induced by the three-pulse sequence 1-2-3. Figure 7.6(b) demonstrates that the PPE in $|\mathcal{E}_S(t_1,t_3)|$ follows precisely the dashed line with $t_3 = 2t_1$. Thus, the use of heterodyne detection (cf. Sec. 4.4) allows one to measure the PPE amplitude, $A_{\text{PPE}}(2t_1)$, for a dual delay scan of t_1 and t_3. In analogy, the SPE follows in $|\mathcal{E}_S(t_2,t_3)|$ the trajectory $t_3 = t_2$ (not shown here) and one measures its amplitude, $A_{\text{SPE}}(t_2)$, for a dual delay scan of t_2 and t_3. The vertical line in Fig. 7.6(b) at $t_3 = 0$ results from a residual interference of reference with pulse 2.

Figure 7.7 summarizes the spectral dependence of the coherent optical response measured in the co-polarized configuration at $B = 0$. Note that in absence of a magnetic

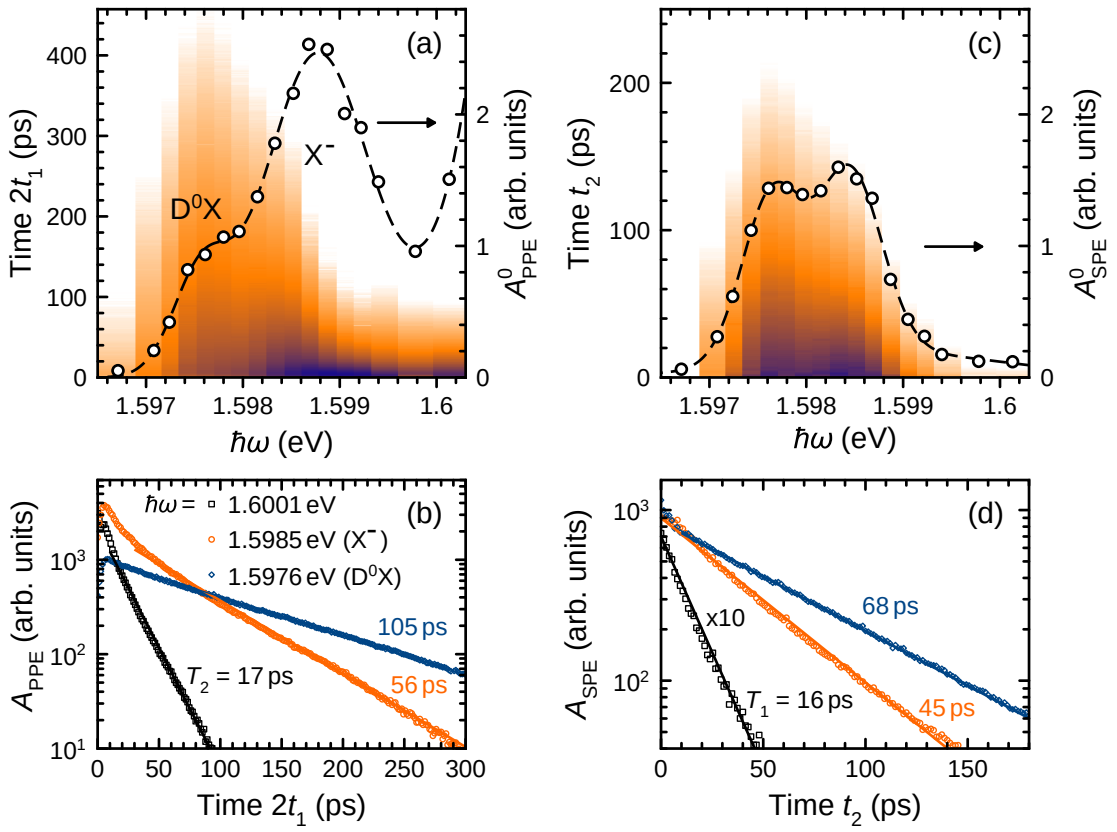

Figure 7.7: Spectral dependences of the A_{PPE} and A_{SPE} transients at $B = 0$. (a) and (c) Colormaps of $A_{\mathrm{PPE}}(2t_1)$ and $A_{\mathrm{SPE}}(t_2)$ measured as function of the excitation energy $\hbar\omega$. The SPE is measured for $t_1 = 27\,\mathrm{ps}$. Dots correspond to the amplitude at time zero, $A^0_{\mathrm{PPE}}(t_1 = 0)$ and $A^0_{\mathrm{SPE}}(t_2 = 0)$, respectively. Dashed lines as guide for the eye. (b) and (d) Cross-sections of the echo transients for selected energies and exponential fits for the evaluation of the coherence time T_2 and lifetime T_1, respectively. Colormaps in logarithmic scale according to (b) and (d). White indicates the near zero level and dark-blue corresponds to the maximum signal.

field one expects no difference between co- and cross-polarized configuration. The peak amplitudes $A_{\mathrm{PPE}}(2t_1)$ and $A_{\mathrm{SPE}}(t_2)$ as function of the excitation energy $\hbar\omega$ are shown in Figs. 7.7(a) and 7.7(c), respectively. The amplitudes of $A^0_{\mathrm{PPE}} = A_{\mathrm{PPE}}(t_1 = 0)$ and $A^0_{\mathrm{SPE}} = A_{\mathrm{SPE}}(t_2 = 0)$ are shown by the dots. For $t_1 = 27\,\mathrm{ps}$, only the trion and donor-bound exciton are seen in the SPE, while the PPE reveals also a signal from the exciton. It manifests itself also in the strongly enhanced X^- line in A^0_{PPE}. From the cross-sections of the PPE transient in Fig. 7.7(b) (orange dots) it is seen that $A_{\mathrm{PPE}}(2t_1)$ decays in fact bi-exponential. The fast component $\sim 10\,\mathrm{ps}$ might be addressed to localized exciton states, such as $\mathrm{D}^+\mathrm{X}$ which is energetically between X and $\mathrm{D}^0\mathrm{X}$. Another explanation could be fast energy relaxation of higher excited trion states. Together with Fig. 7.7(d), one extracts from the exponential decays the coherence time T_2 and the lifetime T_1 of the photoexcited complexes following Eqs. (7.5) and (7.7).

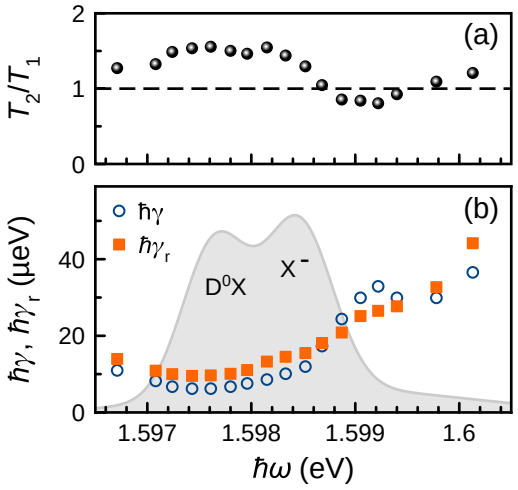

Figure 7.8: Spectral dependences of $\hbar\gamma = \hbar/T_2$ and $\hbar\gamma_r = \hbar/T_1$, evaluated from the exponential fits to the echo transients for different photon energies $\hbar\omega$ in Figs. 7.7(b) and 7.7(d). (a) shows the ratio T_2/T_1 which equals 2 if the coherence is pureley radiatively limited. (b) Decay rates and amplitude $A^0_{\mathrm{SPE}}(t_2 = 0)$ from Fig. 7.7(b) as grey shaded curve.

For resonant excitation of the low energy tail of the localized excitons at $\hbar\omega = 1.601\,\mathrm{eV}$ one obtains short decoherence times limited to 17 ps, i.e., $\hbar\gamma = 38\,\mu\mathrm{eV}$ (Fig. 7.8(b)). For higher $\hbar\omega$ corresponding to excitation of free excitons (X) the linewidth becomes even larger reaching values of $150\,\mu\mathrm{eV}$ [Lan12, Moo14]. For the trions and donor-bound excitons the homogeneous linewidths are significantly narrower due to the stronger localization of these complexes. Here, one obtains $\hbar\gamma \approx 12\,\mu\mathrm{eV}$ for X^- and $\hbar\gamma \approx 6\,\mu\mathrm{eV}$ for D^0X. At lower energies $\hbar\omega \leq 1.598\,\mathrm{eV}$ one observes that the linewidth is determined mainly by the radiative decay to the ground state, i.e. $T_2 \sim 2T_1$ and thus, the pure dephasing is weak (Fig. 7.8(a)). Note, that the intentionally chosen spectrally narrow laser pulses ($\hbar\delta\omega = 0.9\,\mathrm{meV}$) also help to suppress many-body interactions between different photoexcited complexes. For example, using spectrally-broad femtosecond pulses one would simultaneously excite excitons and trions. As a result, the exciton-trion interaction would lead to a significant increase of the homogeneous linewidth for the trion transition, which would become comparable to the one measured for the X [Moo14].

7.3.3 Coherent optical spectroscopy in a transverse magnetic field

Figure 7.9 shows a magnetic field scan of the SPE amplitude, A_{SPE}, fixed at a long time delay $t_2 > 1\,\mathrm{ns}$. In accordance with Eq. (7.5), the co-polarized signal (HHH in Fig. 7.9(a)) shows slow oscillations $\sim \sin^2(\omega_L t_1/2)$. Much faster oscillations, with a 90° phase shifted envelope function with respect to HHH, are seen in the cross-polarized signal (HVV in Fig. 7.9(b)) following $\sim \cos[\omega_L(t_1 + t_2)]$, according to Eq. (7.8). The data are simulated using a theoretical model that takes the inhomogeneous broadening of electron g factors due to Δg into account [Lan14]. Particularly interesting is the observation of weak, faster oscillations in Fig. 7.9(a). While resonant spin amplification is well known from Kerr- or Faraday rotation in pump-probe experiments [Kik98], it has not been reported using coherent optical methods. Since RSA does not follow from the formula in Eq. (7.5), one can speculate whether the effective polarization in the experiment was

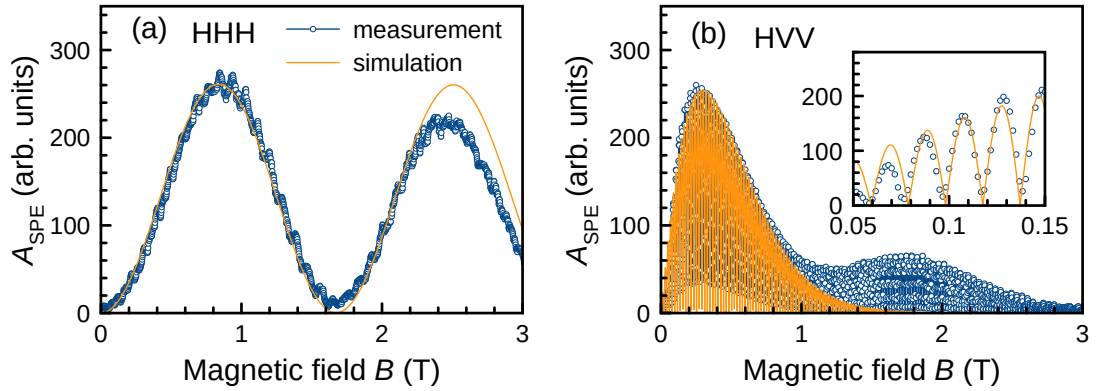

Figure 7.9: Transverse magnetic field dependence of the SPE amplitude, A_{SPE}, for co-polarized configuration (a) and cross-polarized configuration (b). Experimental parameters: $\hbar\omega = 1.5976\,\mathrm{eV}$ ($\mathrm{D^0X}$), $t_1 = t_3 = 27\,\mathrm{ps}$, $t_2 = 1147\,\mathrm{ps}$, $T = 2\,\mathrm{K}$. Additional parameters in the simulation: $|g_\mathrm{e}| = 1.6$, $\Delta g = 0.018$, $\tau_\mathrm{r} = 31\,\mathrm{ps}$, $\tau_\mathrm{sh} = 1\,\mathrm{ns}$, $T_{2,\mathrm{e}} \approx 30\,\mathrm{ns}$, $T_{1,\mathrm{e}} \approx 75\,\mathrm{ns}$.

100% linear. For excitation with circular polarized pulses a macroscopic spin polarization with relaxation times much longer than the pulse repetition will be induced. However, a closer study of the RSA effect and the deviations between simulation and experiment in Fig. 7.9 is out of the scope of this thesis.

As discussed in Sec. 7.2.3, stimulated Raman processes in cross-polarized configuration can be used for detailed spectroscopy of the ground state electron spins. For the measurement in the time domain, the applied magnetic field is fixed at $B = 260\,\mathrm{mT}$. With the g factor from Fig. 7.9 this results in a Zeeman energy splitting of the ground electronic states of $\hbar\omega_\mathrm{L} = 24\,\mu\mathrm{eV}$, which is small compared to the thermal energy $k_\mathrm{B}T = 170\,\mu\mathrm{eV}$. A_{SPE} transients are measured, setting the reference pulse delay $t_3 = t_1$ and performing scans as function of t_2 for different excitation photon energies $\hbar\omega$. The data are summarized in Fig. 7.10. Contour plots of the SPE peak amplitude as function of t_2 and $\hbar\omega$ measured for $t_1 = 27\,\mathrm{ps}$ are shown in Fig. 7.10(a). Exemplary curves taken at $\hbar\omega = 1.5972\,\mathrm{eV}$ and $1.5985\,\mathrm{eV}$, corresponding to excitation of the $\mathrm{D^0X}$ and $\mathrm{X^-}$ optical transitions, respectively, are shown in Fig. 7.10(b). When t_2 is varied, one observe an oscillatory signal that decays on a long time-scale of several ns. Note that the long-lived signal is present only in the spectral region 1.597-1.599 eV, where the $\mathrm{X^-}$ and the $\mathrm{D^0X}$ resonances are located; i.e., it is necessary to address resident carriers for storing optical information on such long time scales.

Using Eq. (7.8), one evaluates the spectral dependence of the long-lived SPE signal strength $A^{\mathrm{e},0}_{\mathrm{SPE}}$, the absolute value of the electron g factor $|g_\mathrm{e}| = \hbar\omega_\mathrm{L}/\mu_\mathrm{B}B$, and the decay rate $\gamma_{2,\mathrm{e}}$, which are plotted in Fig. 7.10(c). Note that we measure in fact the dephasing time of the inhomogeneous ensemble, and thus $\gamma_{2,\mathrm{e}} = 1/T^*_{2,\mathrm{e}}$. Simulations taking Δg into account could be used to estimate the spin coherence time $T_{2,\mathrm{e}}$ (cf. Fig. 7.9). Precise knowledge, however, requires spin echo experiments. In accordance with Eq. (7.15), the

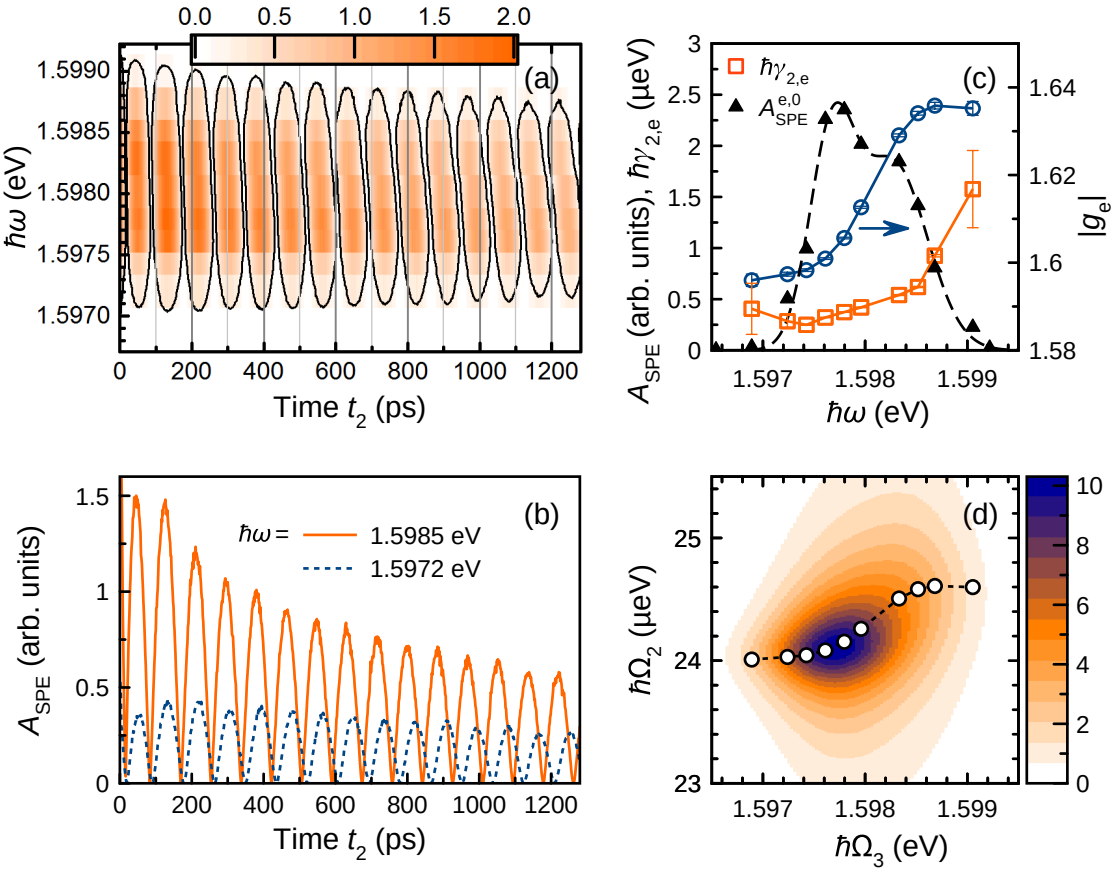

Figure 7.10: (a) Contour plot of the long-lived SPE measured in the HVV polarization configuration as function of the excitation photon energy $\hbar\omega$ and delay time t_2. The data are taken at $B = 260\,\mathrm{mT}$, $t_1 = 27\,\mathrm{ps}$. The solid black lines indicate the signal level with 10% of the maximum intensity. (b) Exemplary transients for given photon energies of 1.5972 eV and 1.5985 eV corresponding to optical excitation of the D^0X and X^- complexes, respectively. (c) Spectral dependence of the long-lived SPE signal strength $A^{e,0}_{SPE} = A_{SPE}(t_2 = 0)$ (left axis), the linewidth $\hbar\gamma_{2,e}$ (left axis), and the electron g factor (right axis) evaluated from the $A_{SPE}(t_2)$ transients at $B = 260\,\mathrm{mT}$. (d) The 2DFTS Raman coherence image $|S^{\perp}_I(\Omega_2,\Omega_3)|$ reconstructed from (c) using Eq. (7.16). The spectral dependence of $\hbar\omega_L$ is shown by the dots.

mentioned parameters allow one to restore the 2DFTS Raman coherence image

$$|S^{\perp}_I(\Omega_2,\Omega_3)| \approx \sum_{\omega} A^{e,0}_{SPE} |S^{\perp}_{I,e}(\Omega_2)| \exp\left(-\frac{\sigma^2(\Omega_3-\omega)^2}{2}\right), \tag{7.16}$$

where the inhomogenity is taken from the pulse width, $2/\sigma = \delta\omega$, and the $S^{\perp}_{I,T}$ term is neglected since $\gamma_T \gg \gamma_{2,e}$. The sum is taken over all excitation energies $\hbar\omega$ used in the experiment. The resulting contour plot is shown in Fig. 7.10(d). Note that one cannot distinguish between real and imaginary contributions to the 2DFTS signal. However, as follows from the theoretical description in Sec. 7.2, this is not crucial for

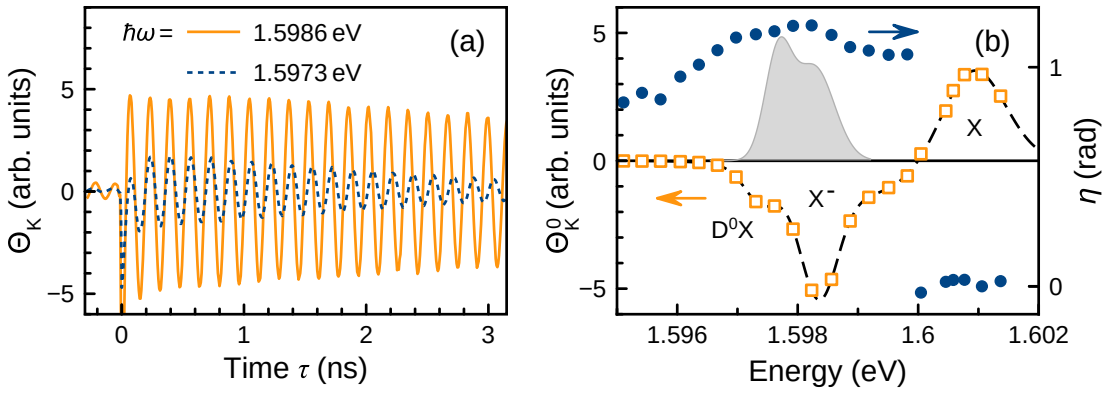

Figure 7.11: (a) Oscillating Kerr rotation angle Θ_K in a transverse magnetic field $B = 270\,\mathrm{mT}$ as function of the pump-probe pulse delay τ. The curves are shown for photon energies of 1.5973 eV and 1.5986 eV corresponding to optical excitation of the D^0X and X^- complexes, respectively, and can be fitted using Eq. (7.17). The power of probe and pump pulses is 0.5 and 2.5 mW, respectively. Temperature $T = 2\,\mathrm{K}$. (b) The amplitude of the long-lived Kerr oscillations, Θ^0_K, as function of the photon energy (right axis). Dashed line as guide for the eye. For comparison, the grey shaded curve shows the SPE amplitude $A^{e,0}_{SPE}$ from Fig. 7.10(c). The phase η is shown on the left axis.

the evaluation of the energy splitting in the ground state in case of isolated localized electrons. Nevertheless, phase stabilized measurements have great potential for in-depth studies of many-body interactions in an ensemble of resident electrons similar to that obtained for photoexcited exciton complexes [Cun09].

The most striking feature of Fig. 7.10(d) is the variation of the Raman coherence peak with photon energy $\hbar\Omega_3$ demonstrating a steplike behavior and clearly showing that $\hbar\omega_L$ increases from 24.0 to 24.6 μeV when the excitation energy is varied from D^0X to X^-. The extracted g factors are $|g_e| = 1.595$ and 1.635 for the resident electrons bound to a donor and localized in a potential fluctuation, respectively (see also Fig. 7.10(c)). The small difference between these values have the opposite trend to that expected for free electrons in CdTe/(Cd,Mg)Te QWs and (Cd,Mg)Te [Sir97]. The electron g factor is controlled by the admixture of valence band states to the conduction band, which in turn is dependent not only on the band gap energy but also on the electron and hole localization. This localization is different for the D^0X and X^- complexes, which results in the measured differences of the g values.

7.3.4 Pump-pobe spectroscopy in a transverse magnetic field

Finally, we discuss the spectral dependence of $\gamma_{2,e}$ in Fig. 7.10(c). It turns out, that it is useful to compare the results with spin relaxation times obtained from time-resolved Kerr rotation using the pump-probe technique (cf. Sec. 4.3.1). Figure 7.11(a) shows strong oscillations of the Kerr rotation angle Θ_K as function of the pump-probe delay τ in presence of a magnetic field $B = 270\,\mathrm{mT}$ for two exemplary curves corresponding

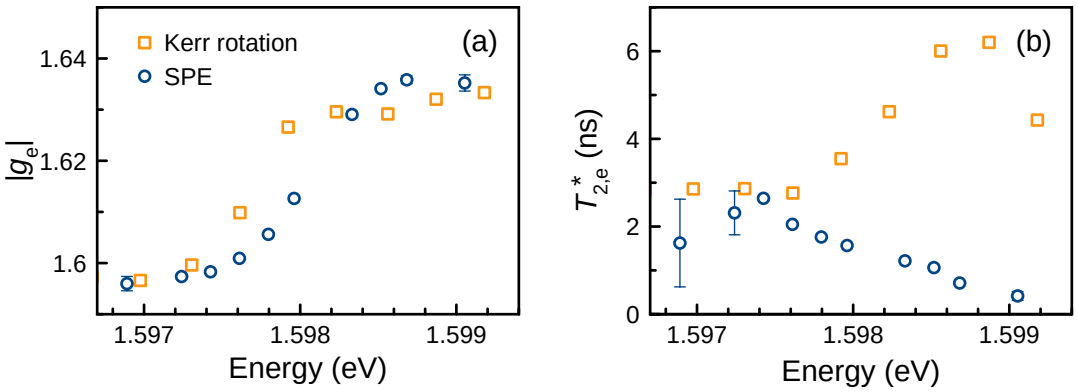

Figure 7.12: Comparison of the results from long-lived SPE in Fig. 7.10 and pump-probe Kerr rotation in Fig. 7.11. Transverse electron g factors in (a) and effective transverse electron spin life times $T_{2,e}^*$ in (b).

to excitation of the D^0X and X^- optical transitions, respectively. As in Fig. 7.10(b), slightly different oscillation frequencies become visible for time delays $\tau > 1\,\text{ns}$. They can be quantified (Figs. 7.11(b) and 7.12(a)) by fitting the data with

$$\Theta_K(\tau) \propto \left|\Theta_K^0\right| e^{-\frac{\tau}{T_{2,e}^*}} \cos(\omega_L \tau + \eta), \tag{7.17}$$

where the phase η is needed for small corrections and determination of the sign of the amplitude Θ_K^0 in the spectra shown in Fig. 7.11(b). Here, clear features of the optical transitions D^0X, X^-, and X are seen. The discussion of the remaining fitting parameters limits on the transitions with resident electrons, that are seen in the coherent optical response from the SPE.

In Fig. 7.10(c) it is shown that the decay rate $\gamma_{2,e}$ from SPE increases from $0.25\,\mu\text{eV}$ for donor-bound electrons to $1.5\,\mu\text{eV}$ for high energy trions. An alternative way of presenting the same data is given in Fig. 7.12(b). Here, $T_{2,e}^* = 1/\gamma_{2,e}$ is compared for both experimental techniques, FWM and pump-probe, respectively. While the same times, $T_{2,e}^* \sim 3\,\text{ns}$, are measured for donor-bound electrons, strong discrepancies are observed for high energy trions. In pump-probe, spin relaxation times up to 6 ns are measured, while in SPE, the times shorten down to $< 1\,\text{ns}$.

There are several mechanisms which can contribute to the decay of the long-lived SPE with increasing t_2. For localized noninteracting electrons, spin relaxation and hopping between localization sites are relevant. The latter mechanism deserves special attention as it may be spin conserving and, therefore, does not give a contribution to conventional pump-probe measurements where the decay of the signal is determined solely by the electron spin relaxation. At each hop the electron changes its localization energy, which acts as a dephasing mechanism that is directly seen in an echo experiment. Thus, $T_{2,e}^*$ from SPE can be identified with a waiting (correlation) time of the localized electron before a hop. The decrease of $T_{2,e}^*$ from SPE with increasing $\hbar\omega$ indicates that hopping

of electrons between localization sites plays an important role for states with weaker localization. Simultaneously, for the donor-bound electrons with strongest localization, the signal decay approaches the values measured by pump-probe.

Thus, the decay of Raman coherence in an electron spin ensemble measured by photon echoes provides access to local relaxation processes, such as hopping of carriers between localization sites or, additionally, spin interactions between electrons within the ensemble causing spin flip-flops. This is because every individual electron in the ground state contributes to the coherent optical response only if it is addressed by all three optical pulses sequentially. Moreover, in photon echo experiments no macroscopic spin polarization is created in the ground state after the stimulated Raman process, because the optically excited states relax between the first and second optical pulses. This reduces the energy input in the system which may destroy coherence even faster. In contrast, time-resolved pump-probe Faraday rotation [Cro97a, Zhu07, Yug09] and transient spin-grating techniques [Cam96, Car06, Wan13] detect the evolution of the macroscopic spin polarization for a large electron ensemble, and local relaxation processes cannot be probed directly. Therefore, a comparison of the signal decays recorded with different experimental techniques can be used to obtain the full and self-consistent physical picture of the spin dynamics in electron ensembles.

7.4 Conclusions

In conclusion, it has been demonstrated that two-dimensional Fourier spectroscopy addressing photon echoes can be successfully applied for the evaluation of tiny splittings between ground state energy levels which are optically coupled to a common excited state in, e.g., a Λ-type scheme. The stimulated steplike Raman process induced by the sequence of two pulses creates a coherent superposition of the ground state doublet which can be retrieved only by optical means due to selective excitation of the same spin sub-ensemble with the third pulse. This provides the unique opportunity to distinguish between several electron spin species in a large ensemble of emitters. As a proof of principle, this method has been applied to an n-type CdTe/(Cd,Mg)Te quantum well system for which the Zeeman splitting difference in the sub-μeV range between donor-bound electrons and electrons localized on potential fluctuations has been resolved, while the homogeneous linewidth of the optical transitions is two orders of magnitude larger than this splitting. The results pave the way for further developing two-dimensional Fourier imaging into a high resolution spectroscopy tool, independent on the nature of the energy splitting in the ground state.

Chapter 8

Summary and outlook

In this thesis semiconductor quantum dots and wells, some of them combined with ferromagnetic or plasmonic metals to hybrids, are investigated by multiple techniques of optical spectroscopy. They are ranging from linear methods like photoluminescence to the nonlinear four-wave mixing and magneto-optical Kerr effect.

In Ch. 5 we investigate a new ferromagnet-semiconductor hybrid material system synthesized of a thin Co ferromagnetic layer and a CdTe quantum well (QW), separated by a thin (Cd,Mg)Te barrier. We magnetize the structure using an external magnetic field and detect a spin orientation of 4% from acceptor-bound holes in the QW, as evidenced by the photoluminescence's (PL) circular polarization. The underlying mechanism is based on equilibrium spin polarization due to thermal population of spin levels that are split by p-d exchange interaction with $\Delta E_{\mathrm{ex}} = (50 \pm 10)\,\mu\mathrm{eV}$. Exchange interaction between hole spins (p-band) and magnetic ions (d-band) typically depends on wave function overlap and is therefore short-ranged. Enhanced PL decay in the vicinity of the Co layer enables us to determine the wave function overlap being approximately 1 nm. Surprisingly, a long-ranged, robust coupling is observed that does not vary with barrier width up to more than 30 nm. The results can be explained in terms of an effective p-d exchange which is mediated by elliptically polarized phonons generated in the ferromagnet (Fig. 8.1(a)). Surprisingly, this ferromagnet is not the Co layer itself but it results from interfacial ferromagnetism whose origin demands further investigation in future. Moreover, it should be studied as to whether optical or electrical control of carrier spins can be used for manipulation of the ferromagnet's magnetization.

Another focus point of this thesis is the study of coherent optical response from inhomogeneously broadened ensembles of electron-hole pairs excited by picosecond optical pulses. In Ch. 6 we investigate excitons from self-assembled (In,Ga)As QDs embedded in two different types of microcavities with moderate quality factors of about 100. Significant enhancement of the light-matter interaction is demonstrated under selective laser excitation of QDs which are in resonance with the electric field mode of a Tamm-plasmon (TP) microcavity, as required for many applications in photonics or optoelectronics. The TP structure comprises one metal layer as mirror combined with a distributed Bragg reflector (Fig. 8.1(b)). The metal layer may turn out to be useful, e.g., for injecting

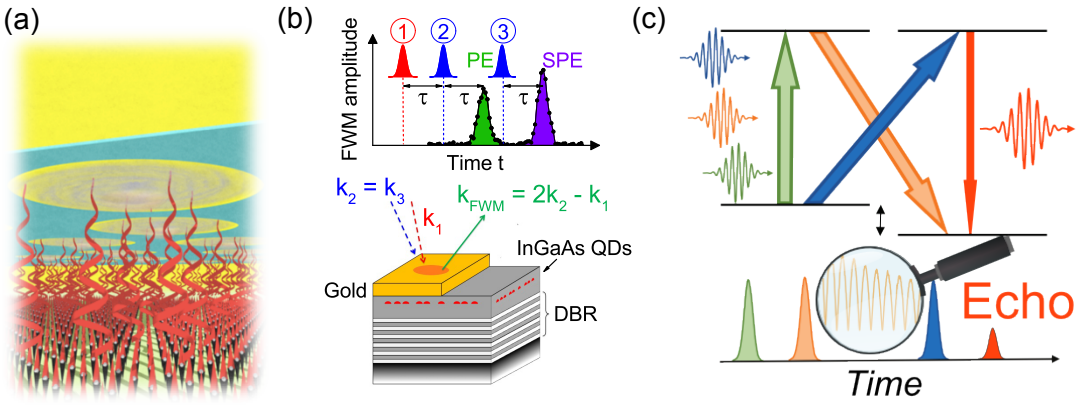

Figure 8.1: Summary of the main results of this thesis. The spin-spin interaction of magnetic ions with holes via elliptically polarized phonons inside a ferromagnet-semiconductor hybrid structure (cf. Ch. 5) is highlighted by the comic in (a). Coherent optical response from a single layer of (In,Ga)As quantum dots inside a Tamm-plasmon microcavity (cf. Ch. 6) is depicted in (b). Finally, (c) shows a steplike Raman process exploiting a sequence of three optical pulses in order to store optical coherence inside a pure spin coherence of the trion ground states (cf. Ch. 7).

carriers or applying an electric field. In our studies, we used Rabi oscillations of the photon echo (PE) to demonstrate that coherent manipulation of QDs in the microcavity is achieved with picosecond pulses at intensity levels more than one order of magnitude smaller as compared with bare QDs. This is the first report on nonlinear optical phenomena under resonant excitation in TP resonators. The decay of PE transients is weakly changed by the TP resonator, indicating a small decrease of the coherence time T_2 which we attribute to the interaction with the electron plasma in the metal layer close (40 nm) to the QD layer. Simultaneously, we see a reduction of the population lifetime T_1 which results from the Purcell effect with an enhancement factor of 2, while nonradiative processes are negligible, as confirmed by time-resolved photoluminescence measurements.

Strong inhomogeneous broadening can lead to a significant deviation from the conventional PE timing sequence, as studied in the second part of Ch. 6. We measure the temporal PE profile of (In,Ga)As QDs inside a DBR microcavity as function of the initial rotation pulse area. We observe a retarded PE for $\pi/2$ pulses, while for $3\pi/2$ the PE is advanced in time as evidenced through monitoring Rabi oscillations. The experimental results are confirmed by detailed calculations that are further used for the simulation of two-dimensional Fourier spectroscopy.

In Ch. 7 we combine methods of spin control with techniques of coherent optical spectroscopy. We investigate an n-type CdTe/(Cd,Mg)Te QW with focus on trion-like transitions that are characterized by an electron ground state with spin projections $\pm\hbar/2$. Although the optical transitions given by inhomogeneous broadening are very broad, tiny Zeeman splittings on the order of 20 μeV can be measured by three pulse

PE transients in a transverse magnetic field. The sub-μeV resolution of our approach exceeds the homogeneous linewidth of the optical transitions by two orders of magnitude. This provides for the unique opportunity to distinguish between different, energetically close spaced complexes in an ensemble; in our case different types of electrons, namely, electrons either bound to donors or localized on QW potential fluctuations. The high-resolution is provided by a stimulated steplike Raman process induced by a sequence of two laser pulses that create a coherent superposition of the ground state doublet which can be retrieved only optically due to selective excitation of the same sub-ensemble with a third pulse (Fig. 8.1(c)). The approach allows us to measure the spin dynamics of carriers in the ground state without creating a macroscopic spin polarization. This is attractive for fundamental studies of spin ensembles, verified by comparison of the relaxation times with results obtained from pump-probe Kerr rotation spectroscopy using a circularly polarized pump pulse. Local relaxation processes, such as spin-conserving hopping of electrons between localization sites, violate the optical coherence stored in the ground state spin system while magneto-optical effects remain unchanged.

To summarize, this thesis puts the properties of novel spintronic devices into a context with coherent optical phenomena that can lead to implementations in future quantum information technologies.

Bibliography

[Afi13] B. I. Afinogenov, V. O. Bessonov, A. A. Nikulin, A. A. Fedyanin. Observation of hybrid state of Tamm and surface plasmon-polaritons in onedimensional photonic crystals. *Appl. Phys. Lett.* **103**, 061112 (2013).

[Aki11] I. A. Akimov, R. I. Dzhioev, V. L. Korenev, Yu. G. Kusrayev, V. F. Sapega, D. R. Yakovlev, M. Bayer. Optical orientation of Mn^{2+} ions in GaAs in weak longitudinal magnetic fields. *Phys. Rev. Lett.* **106**, 147402 (2011).

[Aki14] I. A. Akimov, V. L. Korenev, V. F. Sapega, L. Langer, S. V. Zaitsev, Yu. A. Danilov, D. R. Yakovlev, M. Bayer. Orientation of electron spins in hybrid ferromagnet–semiconductor nanostructures. *Phys. Status Solidi B* **251**, 1663 (2014).

[Aki17] I. A. Akimov, M. Salewski, I. V. Kalitukha, S. V. Poltavtsev, J. Debus, D. Kudlacik, V. F. Sapega, N. E. Kopteva, E. Kirstein, E. A. Zhukov, D. R. Yakovlev, G. Karczewski, M. Wiater, T. Wojtowicz, V. L. Korenev, Y. G. Kusrayev, M. Bayer. Direct measurement of the long-range p-d exchange coupling in a ferromagnet-semiconductor Co/CdMgTe/CdTe quantum well hybrid structure. *Phys. Rev. B* **96**, 184412 (2017).

[Ala01] H. Alawadhi, I. Miotkowski, V. Souw, M. McElfresh, A. K. Ramdas, S. Miotkowska. Excitonic Zeeman effect in the zinc-blende II-VI diluted magnetic semiconductors $Cd_{1-x}Y_xTe$ (Y = Mn, Co, and Fe). *Phys. Rev. B* **63**, 155201 (2001).

[Alb13] F. Albert, K. Sivalertporn, J. Kasprzak, M. Strau, C. Schneider, S. Höfling, M. Kamp, A. Forchel, S. Reitzenstein, E. A. Muljarov, W. Langbein. Microcavity controlled coupling of excitonic qubits. *Nature Commun.* **4**, 1747 (2013).

[All75] N. Allen, J. H. Eberly. *Optical Resonance and Two-Level Atoms.* Wiley, New York (1975).

[Ash76] N. W. Ashcroft, N. D. Mermin. *Solid state physics.* Saunders College, Fort Worth (1976).

[Aws02] D. D. Awschalom, D. Loss, N. Samarth (Eds.). *Semiconductor spintronics and quantum computation*. NanoScience and Technology. Springer, Berlin/Heidelberg (2002).

[Azz16] S. Azzini, G. Lheureux, C. Symonds, J.-M. Benoit, P. Senellart, A. Lemaitre, J.-J. Greffet, C. Blanchard, C. Sauvan, J. Bell. Generation and spatial control of hybrid Tamm plasmon/surface plasmon modes. *ACS Photonics* **3**, 1776 (2016).

[Bab17] I. A. Babenko, I. A. Yugova, S. V. Poltavtsev, M. Salewski, I. A. Akimov, C. Schneider, M. Kamp, S. Höfling, D. R. Yakovlev, M. Bayer. Spontaneous photon echo from an ensemble of (In,Ga)As quantum dots. In *Proc. of the 25th Int. Symp. "Nanostructures: Physics and Technology"* (2017).

[Bal12] R. v. Baltz. Semiconductor bloch equations. In *Semiconductor Optics*, edited by C. F. Klingshirn, Fourth Edition. Graduate Texts in Physics. Ch. 27, 813–833. Springer, Berlin/Heidelberg (2012).

[Bar98] T. Baron, K. Saminadayar, N. Magnea. Nitrogen doping of Te-based II-VI compounds during growth by molecular beam epitaxy. *J. Appl. Phys.* **83**, 1354 (1998).

[Bar11] G. Bartsch, M. Gerbracht, D. R. Yakovlev, J. H. Blokland, P. C. M. Christianen, E. A. Zhukov, A. B. Dzyubenko, G. Karczewski, T. Wojtowicz, J. Kossut, J. C. Maan, M. Bayer. Positively versus negatively charged excitons: A high magnetic field study of CdTe/$Cd_{1-x}Mg_x$Te quantum wells. *Phys. Rev. B* **83**, 235317 (2011).

[Bas86] G. Bastard, J. Brum. Electronic states in semiconductor heterostructures. *IEEE J. Quantum Electron.* **22**, 1625 (1986).

[Bay01] M. Bayer, T. L. Reinecke, F. Weidner, A. Larionov, A. McDonald, A. Forchel. Inhibition and enhancement of the spontaneous emission of quantum dots in structured microresonators. *Phys. Rev. Lett.* **86**, 3168 (2001).

[Bay02] M. Bayer. Semiconductor physics: One at a time, please. *Nature* **418**, 597 (2002).

[Bea59] C. P. Bean, J. D. Livingston. Superparamagnetism. *J. Appl. Phys.* **30**, S120 (1959).

[Bea96] E. Beaurepaire, J.-C. Merle, A. Daunois, J.-Y. Bigot. Ultrafast spin dynamics in ferromagnetic nickel. *Phys. Rev. Lett.* **76**, 4250 (1996).

[Ben11] O. Benson. Assembly of hybrid photonic architectures from nanophotonic constituents. *Nature* **480**, 193 (2011).

[Ber11] P. R. Berman, V. S. Malinovsky. *Principles of Laser Spectroscopy and Quantum Optics*. Princeton Univ. Press, New Jersey (2011). Ch. 9.

[Bim99] D. Bimberg, M. Grundmann, N. N. Ledentsov. *Quantum Dot Heterostructures*. John Wiley & Sons, Chichester (1999).

[Bio00] E. Biolatti, R. C. Iotti, P. Zanardi, F. Rossi. Quantum information processing with semiconductor macroatoms. *Phys. Rev. Lett.* **85**, 5647 (2000).

[Blo28] F. Bloch. Über die Quantenmechanik der Elektronen in Kristallgittern. *Z. Phys.* **52**, 555 (1928).

[Blo46] F. Bloch. Nuclear induction. *Phys. Rev.* **70**, 460 (1946).

[Blo55] A. L. Bloom. Nuclear induction in inhomogeneous fields. *Phys. Rev.* **98**, 1105 (1955).

[Boh51] D. Bohm. *Quantum Theory*. Dover Books on Physics Series. Dover Publications, New York (1951).

[Boh58] N. Bohr. *Atomic physics and human knowledge*. Wiley, New York (1958).

[Bom13] M. Bombeck, J. V. Jäger, A. V. Scherbakov, T. Linnik, D. R. Yakovlev, X. Liu, J. K. Furdyna, A. V. Akimov, M. Bayer. Magnetization precession induced by quasitransverse picosecond strain pulses in (311) ferromagnetic (Ga,Mn)As. *Phys. Rev. B* **87**, 060302 (2013).

[Bor01] P. Borri, W. Langbein, S. Schneider, U. Woggon, R. L. Sellin, D. Ouyang, D. Bimberg. Ultralong Dephasing Time in InGaAs Quantum Dots. *Phys. Rev. Lett.* **87**, 157401 (2001).

[Bor02] P. Borri, W. Langbein, S. Schneider, U. Woggon, R. L. Sellin, D. Ouyang, D. Bimberg. Rabi oscillations in the excitonic ground-state transition of InGaAs quantum dots. *Phys. Rev. B* **66**, 081306 (2002).

[Bor08] P. Borri, W. Langbein. Transient four-wave mixing of excitons in quantum dots from ensembles and individuals. In *Semiconductor Quantum Bits*, edited by F. Henneberger, O. Benson. Ch. 12, 269–319. Pan Stanford, Singapur (2008).

[Bou00] D. Bouwmeester, A. Ekert, A. Zeilinger (Eds.). *The physics of quantum information*. Springer, Berlin (2000).

[Bra15] T. Braun, V. Baumann, O. Iff, S. Höfling, C. Schneider, M. Kamp. Enhanced single photon emission from positioned InP/GaInP quantum dots coupled to a confined Tamm-plasmon mode. *Appl. Phys. Lett.* **106**, 041113 (2015).

[Bra16] T. Braun, S. Betzold, N. Lundt, M. Kamp, S. Höfling, C. Schneider. Impact of ex situ rapid thermal annealing on magneto-optical properties and oscillator strength of In(Ga)As quantum dots. *Phys. Rev. B* **93**, 155307 (2016).

[Bri99] D. Brinkmann, J. Kudrna, P. Gilliot, B. Hönerlage, A. Arnoult, J. Cibert, S. Tatarenko. Trion and exciton dephasing measurements in modulation-doped quantum wells: A probe for trion and carrier localization. *Phys. Rev. B* **60**, 4474 (1999).

[Bro90] S. D. Brorson, H. Yokoyama, E. P. Ippen. Spontaneous emission rate alteration in optical waveguide structures. *IEEE J. Quantum Electron.* **26**, 1492 (1990).

[Bro94] I. Broser, B. Lummer, R. Heitz, A. Hoffmann. Degenerate four-wave mixing at bound excitons in II–VI semiconductors. *J. Cryst. Growth* **138**, 809 (1994).

[Bru09] D. Brunner, B. D. Gerardot, P. A. Dalgarno, G. Wüst, K. Karrai, N. G. Stoltz, P. M. Petroff, R. J. Warburton. A coherent single-hole spin in a semiconductor. *Science* **325**, 70 (2009).

[Brü12] R. Brückner, A. A. Zakhidov, R. Scholz, M. Sudzius, S. I. Hintschich, H. Fröb, V. G. Lyssenko, K. Leo. Phase-locked coherent modes in a patterned metal-organic microcavity. *Nature Photon.* **6**, 322 (2012).

[Cam96] A. R. Cameron, P. Riblet, A. Miller. Spin gratings and the measurement of electron drift mobility in multiple quantum well semiconductors. *Phys. Rev. Lett.* **76**, 4793 (1996).

[Car06] S. G. Carter, Z. Chen, S. T. Cundiff. Optical measurement and control of spin diffusion in n-doped GaAs quantum wells. *Phys. Rev. Lett.* **97**, 136602 (2006).

[Car07] S. G. Carter, Z. Chen, S. T. Cundiff. Ultrafast below-resonance Raman rotation of electron spins in GaAs quantum wells. *Phys. Rev. B* **76**, 201308 (2007).

[Cha72] D. J. Chadi, J. P. Walter, M. L. Cohen, Y. Petroff, M. Balkanski. Reflectivities and Electronic Band Structures of CdTe and HgTe. *Phys. Rev. B* **5**, 3058 (1972).

[Che79] Y. Chen, K. Chiang, S. Hartmann. Photon echo relaxation in LaF3:Pr3+. *Opt. Commun.* **29**, 181 (1979).

[Che01] D. S. Chemla, J. Shah. Many-body and correlation effects in semiconductors. *Nature* **411**, 549 (2001).

[Che14] Y. Chen, D. Zhang, L. Zhu, R. Wang, P. Wang, H. Ming, R. Badugu, J. R. Lakowicz. Tamm plasmon- and surface plasmon-coupled emission from hybrid plasmonic–photonic structures. *Optica* **1**, 407 (2014).

[Chi05] S. Chikazumi. *Physics of Ferromagnetism.* Second Edition. International Series of Monographs on Physics. Oxford University Press, New York (2005).

[Cho92] M. Cho, N. F. Scherer, G. R. Fleming, S. Mukamel. Photon echoes and related four-wave-mixing spectroscopies using phase-locked pulses. *The Journal of chemical physics* **96**, 5618 (1992).

[Cio09] M. Ciorga, A. Einwanger, U. Wurstbauer, D. Schuh, W. Wegscheider, D. Weiss. Electrical spin injection and detection in lateral all-semiconductor devices. *Phys. Rev. B* **79**, 165321 (2009).

[Coh90] A. M. Cohen, G. E. Marques. Electronic structure of zinc-blende-structure semiconductor heterostructures. *Phys. Rev. B* **41**, 10608 (1990).

[Cro66] B. L. Crowder, W. N. Hammer. Shallow Acceptor States in ZnTe and CdTe. *Phys. Rev.* **150**, 541 (1966).

[Cro97a] S. A. Crooker, D. D. Awschalom, J. J. Baumberg, F. Flack, N. Samarth. Optical spin resonance and transverse spin relaxation in magnetic semiconductor quantum wells. *Phys. Rev. B* **56**, 7574 (1997).

[Cro97b] P. A. Crowell, V. Nikitin, D. D. Awschalom, F. Flack, N. Samarth, G. A. Prinz. Magneto-optical spin spectroscopy in hybrid ferromagnetic semiconductor heterostructures. *J. Appl. Phys.* **81**, 5441 (1997).

[Cro05] S. A. Crooker, M. Furis, X. Lou, C. Adelmann, D. L. Smith, C. J. Palmstrøm, P. A. Crowell. Imaging spin transport in lateral ferromagnet/semiconductor structures. *Science* **309**, 2191 (2005).

[CT72] C. Cohen-Tannoudji, J. Dupont-Roc. Experimental study of zeeman light shifts in weak magnetic fields. *Phys. Rev. A* **5**, 968 (1972).

[Cun09] S. T. Cundiff, T. Zhang, A. D. Bristow, D. Karaiskaj, X. Dai. Optical two-dimensional fourier transform spectroscopy of semiconductor quantum wells. *Acc. Chem. Res.* **42**, 1423 (2009).

[Cun12] S. T. Cundiff. Transient four-wave mixing. In *Optical Techniques for Solid-State Materials Characterization*, edited by R. P. Prasankumar, A. J. Taylor. Ch. 10, 371–396. CRC Press, Boca Raton (2012).

[Cun13] S. T. Cundiff, S. Mukamel. Optical multidimensional coherent spectroscopy. *Phys. Today* **66**, 44 (2013).

[Das11] S. P. Dash, S. Sharma, J. C. Le Breton, J. Peiro, H. Jaffrès, J.-M. George, A. Lemaître, R. Jansen. Spin precession and inverted Hanle effect in a semiconductor near a finite-roughness ferromagnetic interface. *Phys. Rev. B* **84**, 054410 (2011).

[Dav12] J. Davis, C. Jagadish. Semicondoctors and their nanostructures. In *Optical Techniques for Solid-State Materials Characterization*, edited by R. P. Prasankumar, A. J. Taylor. Ch. 2, 39–77. CRC Press, Boca Raton (2012).

[De 13] K. De Greve, D. Press, P. L. McMahon, Y. Yamamoto. Ultrafast optical control of individual quantum dot spin qubits. *Rep. Prog. Phys.* **76**, 092501 (2013).

[Deb13] J. Debus, D. Dunker, V. F. Sapega, D. R. Yakovlev, G. Karczewski, T. Wojtowicz, J. Kossut, M. Bayer. Spin-flip Raman scattering of the neutral and charged excitons confined in a CdTe/(Cd,Mg)Te quantum well. *Phys. Rev. B* **87**, 205316 (2013).

[Dem08a] W. Demtröder. *Laser Spectroscopy: Vol. 1: Basic Principles*. Fourth Edition. Springer, Berlin/Heidelberg (2008).

[Dem08b] W. Demtröder. *Laser Spectroscopy: Vol. 2: Experimental Techniques*. Fourth Edition. Springer, Berlin/Heidelberg (2008).

[Die10] T. Dietl. A ten-year perspective on dilute magnetic semiconductors and oxides. *Nature Mater.* **9**, 965 (2010).

[Din74] R. Dingle, W. Wiegmann, C. H. Henry. Quantum states of confined carriers in very thin $Al_xGa_{1-x}As$-GaAs-$Al_xGa_{1-x}As$ heterostructures. *Phys. Rev. Lett.* **33**, 827 (1974).

[Dya71] M. I. Dyakonov, V. I. Perel. Spin orientation of electrons associated with the interband absorption of light in semiconductors. *Sov. Phys. JETP* **5**, 1063 (1971).

[Dya72] M. I. Dyakonov, V. I. Perel. Spin relaxation of conduction electrons in noncentrosymmetric semiconductors. *Sov. Phys. Solid State* **13**, 3023 (1972).

[Dya84] M. I. Dyakonov, V. I. Perel. Theory of optical spin orientation of electrons and nuclei in semiconductors. In *Optical Orientation*, edited by F. Meier, B. P. Zakharchenya, Modern Problems in Condensed Matter Sciences. Ch. 2, 11–71. Elsevier, Amsterdam/Oxford/New York/Tokyo (1984).

[Dya08] M. I. Dyakonov. Basics of semiconductor and spin physics. In *Spin Physics in Semiconductors*, edited by M. I. Dyakonov, Springer Series in Solid-State Sciences. Ch. 1, 1–26. Springer, Berlin/Heidelberg (2008).

[Dzh95] R. I. Dzhioev, B. P. Zakharchenya, V. Korenev. Optical orientation study of thin ferromagnetic films in a ferromagnet/semiconductor structure. *Phys. Solid State* **37**, 1929 (1995).

[Ein05] A. Einstein. Über einen die Erzeugung und Verwandlung des Lichtes betreffenden heuristischen Gesichtspunkt. *Ann. Phys.* **322**, 132 (1905).

[Far46] M. Faraday. Experimental researches in electricity. nineteenth series. *Philos. Trans. Roy. Soc. London* **136**, 1 (1846).

[Fle05] M. Fleischhauer, A. Imamoglu, J. P. Marangos. Electromagnetically induced transparency: Optics in coherent media. *Rev. Mod. Phys.* **77**, 633 (2005).

[Fox10] M. Fox. *Optical Properties of Solids*. Second Edition. Oxford Master Series in Physics. Oxford University Press, Oxford/New York (2010).

[Fra16] F. Fras, Q. Mermillod, G. Nogues, C. Hoarau, C. Schneider, M. Kamp, S. Höfling, W. Langbein, J. Kasprzak. Multi-wave coherent control of a solid-state single emitter. *Nature Photon.* **10**, 155 (2016).

[Fre31a] J. Frenkel. On the Transformation of light into Heat in Solids. I. *Phys. Rev.* **37**, 17 (1931).

[Fre31b] J. Frenkel. On the Transformation of Light into Heat in Solids. II. *Phys. Rev.* **37**, 1276 (1931).

[Fu05] K.-M. C. Fu, C. Santori, C. Stanley, M. C. Holland, Y. Yamamoto. Coherent population trapping of electron spins in a high-purity n-type GaAs semiconductor. *Phys. Rev. Lett.* **95**, 187405 (2005).

[Fur88] J. K. Furdyna. Diluted magnetic semiconductors. *J. Appl. Phys.* **64**, R29 (1988).

[Gaj78] J. A. Gaj, J. Ginter, R. R. Gałazka. Exchange interaction of manganese $3d^5$ states with band electrons in $Cd_{1-x}Mn_xTe$. *Phys. Status Solidi B* **89**, 655 (1978).

[Gaj11] J. Gaj, J. Kossut. *Introduction to the Physics of Diluted Magnetic Semiconductors*. Springer Series in Materials Science. Springer, Heidelberg/Dordrecht/London/New York (2011).

[Gam96] D. Gammon, E. S. Snow, B. V. Shanabrook, D. S. Katzer, D. Park. Homogeneous linewidths in the optical spectrum of a single gallium arsenide quantum dot. *Science* **273**, 87 (1996).

[Gam13] A. Gamouras, R. Mathew, S. Freisem, D. G. Deppe, K. C. Hall. Simultaneous deterministic control of distant qubits in two semiconductor quantum dots. *Nano Letters* **13**, 4666 (2013).

[Gaz11] O. Gazzano, S. M. de Vasconcellos, K. Gauthron, C. Symonds, J. Bloch, P. Voisin, J. Bellessa, A. Lemaître, P. Senellart. Evidence for confined Tamm plasmon modes under metallic microdisks and application to the control of spontaneous optical emission. *Phys. Rev. Lett.* **107**, 247402 (2011).

[Ges14] J. Gessler, V. Baumann, M. Emmerling, M. Amthor, K. Winkler, S. Höfling, C. Schneider, M. Kamp. Electro optical tuning of Tamm-plasmon exciton-polaritons. *Appl. Phys. Lett.* **105**, 181107 (2014).

[Gre06] A. Greilich, D. R. Yakovlev, A. Shabaev, Al. L. Efros, I. A. Yugova, R. Oulton, V. Stavarache, D. Reuter, A. Wieck, M. Bayer. Mode locking of electron spin coherences in singly charged quantum dots. *Science* **313**, 341 (2006).

[Gre12] A. Greilich, A. Pawlis, F. Liu, O. A. Yugov, D. R. Yakovlev, K. Lischka, Y. Yamamoto, M. Bayer. Spin dephasing of fluorine-bound electrons in ZnSe. *Phys. Rev. B* **85**, 121303 (2012).

[Gro52a] E. F. Gross, N. A. Karryev. Pogloshchenie sveta kristallom zakisi medi v infrakrasnoi i vidimoi chasti spektra. *Dokl. Akad. Nauk SSSR [Sov. Phys. Dokl.]* **84**, 261 (1952).

[Gro52b] E. F. Gross, N. A. Karryev. Opticheskii spektr eksitona. *Dokl. Akad. Nauk SSSR [Sov. Phys. Dokl.]* **84**, 471 (1952).

[Gro11] C. Grossmann, C. Coulson, G. Christmann, I. Farrer, H. E. Beere, D. A. Ritchie, J. J. Baumberg. Tuneable polaritonics at room temperature with strongly coupled Tamm plasmon polaritons in metal/air-gap microcavities. *Appl. Phys. Lett.* **98**, 231105 (2011).

[Gub17] A. R. Gubaydullin, C. Symonds, J. Bellessa, K. A. Ivanov, E. D. Kolykhalova, M. E. Sasin, A. Lemaitre, P. Senellart, G. Pozina, M. A. Kaliteevski. Enhancement of spontaneous emission in Tamm plasmon structures. *Sci. Rep.* **7**, 9014 (2017).

[Hah50] E. L. Hahn. Spin echoes. *Physical Review* **80**, 580 (1950).

[Hal07] S. Halm, G. Bacher, E. Schuster, W. Keune, M. Sperl, J. Puls, F. Henneberger. Local spin manipulation in ferromagnet-semiconductor hybrids. *Appl. Phys. Lett.* **90**, 051916 (2007).

[Ham10] K. Hammerer, A. S. Sørensen, E. S. Polzik. Quantum interface between light and atomic ensembles. *Rev. Mod. Phys.* **82**, 1041 (2010).

[Han03] A. T. Hanbicki, O. M. J. van 't Erve, R. Magno, G. Kioseoglou, C. H. Li, B. T. Jonker, G. Itskos, R. Mallory, M. Yasar, A. Petrou. Analysis of the transport process providing spin injection through an Fe/AlGaAs Schottky barrier. *Appl. Phys. Lett.* **82**, 4092 (2003).

[Han14] J. Hansom, C. H. Schulte, C. Le Gall, C. Matthiesen, E. Clarke, M. Hugues, J. M. Taylor, M. Atatüre. Environment-assisted quantum control of a solid-state spin via coherent dark states. *Nature Phys.* **10**, 725 (2014).

[Har68] S. Hartmann. Photon, spin, and Raman echoes. *IEEE J. Quantum Electron.* **4**, 802 (1968).

[Hau98] A. Haury, A. Arnoult, V. Chitta, J. Cibert, Y. M. d'Aubigné, S. Tatarenko, A. Wasiela. Observation of charged $X^-$and X^+excitons and metal-to-insulator transition in CdTe/CdMgZnTe modulation-doped quantum wells. *Superlattices Microstruct.* **23**, 1097 (1998).

[Hei79] W. Heisenberg. *Quantentheorie und Philosophie: Vorlesungen und Aufsätze.* Reclams Universal-Bibliothek. Reclam (1979).

[Her89] M. A. Herman, H. Sitter. *Molecular Beam Epitaxy.* Springer, Berlin/Heidelberg/New York (1989).

[icvac04] I. Žutić, J. Fabian, S. Das Sarma. Spintronics: Fundamentals and applications. *Rev. Mod. Phys.* **76**, 323 (2004).

[Ivc95] E. Ivchenko, G. Pikus. *Superlattices and other heterostructures: symmetry and optical phenomena.* Springer series in solid-state sciences. Springer, Berlin/Heidelberg/New York (1995).

[Jof89] M. Joffre, D. Hulin, A. Migus, M. Combescot. Laser-induced exciton splitting. *Phys. Rev. Lett.* **62**, 74 (1989).

[Joh08] M. Johnson. Spin injection. In *Spin Physics in Semiconductors*, edited by M. I. Dyakonov, Springer Series in Solid-State Sciences. Ch. 10, 279–307. Springer, Berlin/Heidelberg (2008).

[Jon03] F. Jonsson. *Lecture notes on nonlinear optics.* Royal Institute of Technology, Stockholm (2003).

[Jon07] B. T. Jonker, G. Kioseoglou, A. T. Hanbicki, C. H. Li, P. E. Thompson. Electrical spin-injection into silicon from a ferromagnetic metal/tunnel barrier contact. *Nature Phys.* **3**, 542 (2007).

[Jur17a] D. M. Juraschek, M. Fechner, A. V. Balatsky, N. A. Spaldin. Dynamical multiferroicity. *Phys. Rev. Materials* **1**, 014401 (2017).

[Jur17b] D. M. Juraschek, N. A. Spaldin. Sounding out optical phonons. *Science* **357**, 873 (2017).

[Kal07] M. Kaliteevski, I. Iorsh, S. Brand, R. A. Abram, J. M. Chamberlain, A. V. Kavokin, I. A. Shelykh. Tamm plasmon-polaritons: Possible electromagnetic states at the interface of a metal and a dielectric Bragg mirror. *Phys. Rev. B* **76**, 165415 (2007).

[Kas98] A. Kastler. Optical methods for studying hertzian resonances. In *Nobel Lectures in physics 1963-1970*, edited by Nobel Foundation, 186–204. World Scientific, Singapore (1998).

[Kas11] J. Kasprzak, B. Patton, V. Savona, W. Langbein. Coherent coupling between distant excitons revealed by two-dimensional nonlinear hyperspectral imaging. *Nature Photon.* **5**, 57 (2011).

[Kav08] A. Kavokin, J. J. Baumberg, G. Malpuech, F. P. Laussy. *Microcavities*. Oxford University Press, New York (2008).

[Kaw01] R. K. Kawakami, Y. Kato, M. Hanson, I. Malajovich, J. M. Stephens, E. Johnston-Halperin, G. Salis, A. C. Gossard, D. D. Awschalom. Ferromagnetic imprinting of nuclear spins in semiconductors. *Science* **294**, 131 (2001).

[Kaz14] T. Kazimierczuk, D. Frohlich, S. Scheel, H. Stolz, M. Bayer. Giant Rydberg excitons in the copper oxide Cu_2O. *Nature* **514**, 343 (2014).

[Ker77] J. Kerr. XLIII. On rotation of the plane of polarization by reflection from the pole of a magnet. *Philos. Mag.* **3**, 321 (1877).

[Khe93] K. Kheng, R. T. Cox, M. Y. d' Aubigné, F. Bassani, K. Saminadayar, S. Tatarenko. Observation of negatively charged excitons X^- in semiconductor quantum wells. *Phys. Rev. Lett.* **71**, 1752 (1993).

[Kik98] J. M. Kikkawa, D. D. Awschalom. Resonant Spin Amplification in n-Type GaAs. *Phys. Rev. Lett.* **80**, 4313 (1998).

[Kil98] I. G. Kiliptari, V. I. Tsifrinovich. Single-pulse nuclear spin echo in magnets. *Phys. Rev. B* **57**, 11554 (1998).

[Kim11] D. Kim, S. G. Carter, A. Greilich, A. S. Bracker, D. Gammon. Ultrafast optical control of entanglement between two quantum-dot spins. *Nature Phys.* **7**, 223 (2011).

[Kit58] C. Kittel. Interaction of spin waves and ultrasonic waves in ferromagnetic crystals. *Phys. Rev.* **110**, 836 (1958).

[Kit04] C. Kittel. *Introduction to Solid State Physics*. Eighth Edition. Wiley, Hoboken (2004).

[Kli12a] C. F. Klingshirn. *Semiconductor Optics*. Fourth Edition. Graduate Texts in Physics. Springer, Berlin/Heidelberg (2012).

[Kli12b] C. F. Klingshirn, B. K. Meyer, A. Waag, A. Hoffmann, J. Geurts. *Zinc Oxide: From Fundamental Properties Towards Novel Applications* 120 of *Springer Series in Materials Science*. Springer, Berlin/Heidelberg (2012).

[Kno63] R. Knox. *Theory of excitons*. Solid state physics: Supplement Vol. 5. Academic Press, New York/London (1963).

[Kob14] J. Kobak, T. Smoleński, M. Goryca, M. Papaj, K. Gietka, A. Bogucki, M. Koperski, J.-G. Rousset, J. Suffczyński, E. Janik, M. Nawrocki, A. Golnik, P. Kossacki, W. Pacuski. Designing quantum dots for solotronics. *Nature Commun.* **5** (2014).

[Koc93] M. Koch, D. Weber, J. Feldmann, E. O. Göbel, T. Meier, A. Schulze, P. Thomas, S. Schmitt-Rink, K. Ploog. Subpicosecond photon-echo spectroscopy on GaAs/AlAs short-period superlattices. *Phys. Rev. B* **47**, 1532 (1993).

[Koh12] V. Kohnle, Y. Leger, M. Wouters, M. Richard, M. T. Portella-Oberli, B. Deveaud. Four-wave mixing excitations in a dissipative polariton quantum fluid. *Phys. Rev. B* **86**, 064508 (2012).

[Kor03] V. L. Korenev. Electric control of magnetic moment in a ferromagnet/semiconductor hybrid system. *JETP Lett.* **78**, 564 (2003).

[Kor08] V. L. Korenev. Optical orientation in ferromagnet/semiconductor hybrids. *Semicond. Sci. Technol.* **23**, 114012 (2008).

[Kor12] V. L. Korenev, I. A. Akimov, S. V. Zaitsev, V. F. Sapega, L. Langer, D. R. Yakovlev, Yu. A. Danilov, M. Bayer. Dynamic spin polarization by orientation-dependent separation in a ferromagnet-semiconductor hybrid. *Nature Commun.* **3**, 959 (2012).

[Kor16] V. L. Korenev, M. Salewski, I. A. Akimov, V. F. Sapega, L. Langer, I. V. Kalitukha, J. Debus, R. I. Dzhioev, D. R. Yakovlev, D. Müller, C. Schröder, H. Hövel, G. Karczewski, M. Wiater, T. Wojtowicz, Yu. G. Kusrayev, M. Bayer. Long-range p-d exchange interaction in a ferromagnet-semiconductor hybrid structure. *Nature Phys.* **12**, 85 (2016).

[Kos96] A. O. Kosogov, P. Werner, U. Gösele, N. N. Ledentsov, D. Bimberg, V. M. Ustinov, A. Yu. Egorov, A. E. Zhukov, P. S. Kop'ev, N. A. Bert, Zh. I. Alferov. Structural and optical properties of InAs–GaAs quantum dots subjected to high temperature annealing. *Appl. Phys. Lett.* **69**, 3072 (1996).

[Kro04] M. Kroutvar, Y. Ducommun, D. Heiss, M. Bichler, D. Schuh, G. Abstreiter, J. Finley. Optically programmable electron spin memory using semiconductor quantum dots. *Nature* **432**, 81 (2004).

[Krü05] A. Krügel, V. M. Axt, T. Kuhn, P. Machnikowski, A. Vagov. The role of acoustic phonons for Rabi oscillations in semiconductor quantum dots. *Appl. Phys. B* **81**, 897 (2005).

[Kur64] N. A. Kurnit, I. D. Abella, S. R. Hartmann. Observation of a photon echo. *Phys. Rev. Lett.* **13**, 567 (1964).

[Kur09] H. Kurtze, J. Seebeck, P. Gartner, D. R. Yakovlev, D. Reuter, A. D. Wieck, M. Bayer, F. Jahnke. Carrier relaxation dynamics in self-assembled semiconductor quantum dots. *Phys. Rev. B* **80**, 235319 (2009).

[Lam68] G. Lampel. Nuclear dynamic polarization by optical electronic saturation and optical pumping in semiconductors. *Phys. Rev. Lett.* **20**, 491 (1968).

[Lam69] L. Lambert, A. Compaan, I. Abella. Modulation and fast decay of photon-echos in ruby. *Phys. Lett. A* **30**, 153 (1969).

[Lan06] W. Langbein, B. Patton. Heterodyne spectral interferometry for multidimensional nonlinear spectroscopy of individual quantum systems. *Opt. Lett.* **31**, 1151 (2006).

[Lan12] L. Langer, S. V. Poltavtsev, I. A. Yugova, D. R. Yakovlev, G. Karczewski, T. Wojtowicz, J. Kossut, I. A. Akimov, M. Bayer. Magnetic-field control of photon echo from the electron-trion system in a CdTe quantum well: Shuffling coherence between optically accessible and inaccessible states. *Phys. Rev. Lett.* **109**, 157403 (2012).

[Lan14] L. Langer, S. V. Poltavtsev, I. A. Yugova, M. Salewski, D. R. Yakovlev, G. Karczewski, T. Wojtowicz, I. A. Akimov, M. Bayer. Access to long-term optical memories using photon echoes retrieved from semiconductor spins. *Nature Photon.* **8**, 851 (2014).

[Lea02] J. Leach, M. J. Padgett, S. M. Barnett, S. Franke-Arnold, J. Courtial. Measuring the orbital angular momentum of a single photon. *Phys. Rev. Lett.* **88**, 257901 (2002).

[Lev68] R. Levy. *Principles of Solid State Physics.* Academic Press, New York/London (1968).

[LG14] M. Lopez-Garcia, Y. l. D. Ho, M. P. C. Taverne, L.-F. Chen, M. M. Murshidy, A. P. Edwards, M. Y. Serry, A. M. Adawi, J. G. Rarity, R. Oulton. Efficient out-coupling and beaming of Tamm optical states via surface plasmon polariton excitation. *Appl. Phys. Lett.* **104**, 231116 (2014).

[Li03] X. Li, Y. Wu, D. Steel, D. Gammon, T. H. Stievater, D. S. Katzer, D. Park, C. Piermarocchi, L. J. Sham. An all-optical quantum gate in a semiconductor quantum dot. *Science* **301**, 809 (2003).

[Lod15] P. Lodahl, S. Mahmoodian, S. Stobbe. Interfacing single photons and single quantum dots with photonic nanostructures. *Rev. Mod. Phys.* **87**, 346 (2015).

[Lou07] X. Lou, C. Adelmann, S. A. Crooker, E. S. Garlid, J. Zhang, K. S. M. Reddy, S. D. Flexner, C. J. Palmstrom, P. A. Crowell. Electrical detection of spin transport in lateral ferromagnet-semiconductor devices. *Nature Phys.* **3**, 197 (2007).

[Lun16] N. Lundt, S. Klembt, E. Cherotchenko, S. Betzold, O. Iff, A. V. Nalitov, M. Klaas, C. P. Dietrich, A. V. Kavokin, S. Höfling, C. Schneider. Room-temperature Tamm-plasmon exciton-polaritons with a WSe_2 monolayer. *Nature Commun.* **7**, 13328 (2016).

[Mai14] S. Maier, P. Gold, A. Forchel, N. Gregersen, J. Mørk, S. Höfling, C. Schneider, M. Kamp. Bright single photon source based on self-aligned quantum dot–cavity systems. *Opt. Express* **22**, 8136 (2014).

[Mar94] J. Y. Marzin, J. M. Gérard, A. Izraël, D. Barrier, G. Bastard. Photoluminescence of Single InAs Quantum Dots Obtained by Self-Organized Growth on GaAs. *Phys. Rev. Lett.* **73**, 716 (1994).

[Mar99] X. Marie, T. Amand, P. Le Jeune, M. Paillard, P. Renucci, L. E. Golub, V. D. Dymnikov, E. L. Ivchenko. Hole spin quantum beats in quantum-well structures. *Phys. Rev. B* **60**, 5811 (1999).

[Max65] J. C. Maxwell. VIII. a dynamical theory of the electromagnetic field. *Philosophical Transactions of the Royal Society of London* **155**, 459 (1865).

[Mer02] I. A. Merkulov, Al. L. Efros, M. Rosen. Electron spin relaxation by nuclei in semiconductor quantum dots. *Phys. Rev. B* **65**, 205309 (2002).

[Mer16] Q. Mermillod, D. Wigger, V. Delmonte, D. E. Reiter, C. Schneider, M. Kamp, S. Höfling, W. Langbein, T. Kuhn, G. Nogues, J. Kasprzak. Dynamics of excitons in individual InAs quantum dots revealed in four-wave mixing spectroscopy. *Optica* **3**, 377 (2016).

[Mis17] A. K. Mishra, O. Karni, I. Khanonkin, G. Eisenstein. Controlling photon echo in a quantum-dot semiconductor optical amplifier using shaped excitation. *Phys. Rev. Applied* **7**, 054008 (2017).

[Moo13] G. Moody, R. Singh, H. Li, I. A. Akimov, M. Bayer, D. Reuter, A. D. Wieck, S. T. Cundiff. Fifth-order nonlinear optical response of excitonic states in an InAs quantum dot ensemble measured with two-dimensional spectroscopy. *Phys. Rev. B* **87**, 045313 (2013).

[Moo14] G. Moody, I. A. Akimov, H. Li, R. Singh, D. R. Yakovlev, G. Karczewski, M. Wiater, T. Wojtowicz, M. Bayer, S. T. Cundiff. Coherent coupling of excitons and trions in a photoexcited cdte/cdmgte quantum well. *Phys. Rev. Lett.* **112**, 097401 (2014).

[Mor79] J. B. Morsink, W. H. Hesselink, D. A. Wiersma. Photon echo stimulated from optically induced nuclear spin polarization. *Chem. Phys. Lett.* **64**, 1 (1979).

[Muk95] S. Mukamel. *Principles of nonlinear optical spectroscopy.* Oxford series in optical and imaging sciences. Oxford University Press (1995).

[Mye04] R. C. Myers, A. C. Gossard, D. D. Awschalom. Tunable spin polarization in III-V quantum wells with a ferromagnetic barrier. *Phys. Rev. B* **69**, 161305 (2004).

[Nag88] E. L. Nagaev. Photoinduced Magnetism and Conduction Electrons in Magnetic Semiconductors. *Phys. Status Solidi B* **145**, 11 (1988).

[Nie13] S. H. Nie, Y. Y. Chin, W. Q. Liu, J. C. Tung, J. Lu, H. J. Lin, G. Y. Guo, K. K. Meng, L. Chen, L. J. Zhu, D. Pan, C. T. Chen, Y. B. Xu, W. S. Yan, J. H. Zhao. Ferromagnetic interfacial interaction and the proximity effect in a Co_2FeAl/(Ga,Mn)As bilayer. *Phys. Rev. Lett.* **111**, 027203 (2013).

[Nol90] G. Noll, U. Siegner, S. G. Shevel, E. O. Göbel. Picosecond stimulated photon echo due to intrinsic excitations in semiconductor mixed crystals. *Phys. Rev. Lett.* **64**, 792 (1990).

[Nov17] T. F. Nova, A. Cartella, A. Cantaluppi, M. Forst, D. Bossini, R. V. Mikhaylovskiy, A. V. Kimel, R. Merlin, A. Cavalleri. An effective magnetic field from optically driven phonons. *Nature Phys.* **13**, 132 (2017). Letter.

[Pag98] N. Paganotto, J. Siviniant, D. Coquillat, D. Scalbert, J.-P. Lascaray, A. V. Kavokin. Donor bound or negatively charged excitons in thin CdTe/$Cd_{1-x}Mn_x$Te quantum wells. *Phys. Rev. B* **58**, 4082 (1998).

[Pan09] M. A. Pankov, B. A. Aronzon, V. V. Rylkov, A. B. Davydov, E. Z. Meĭlikhov, R. M. Farzetdinova, E. M. Pashaev, M. A. Chuev, I. A. Subbotin, I. A. Likhachev, B. N. Zvonkov, A. V. Lashkul, R. Laiho. Ferromagnetic transition in GaAs/Mn/GaAs/In_xGa_{1-x}As/GaAs structures with a two-dimensional hole gas. *J. Exp. Theor. Phys.* **109**, 293 (2009).

[Par69] R. R. Parsons. Band-to-band optical pumping in solids and polarized photoluminescence. *Phys. Rev. Lett.* **23**, 1152 (1969).

[Par71] R. R. Parsons. Optical pumping and optical detection of spin-polarized electrons in a conduction band. *Can. J. Phys.* **49**, 1850 (1971).

[Pat05] B. Patton, U. Woggon, W. Langbein. Coherent control and polarization readout of individual excitonic states. *Phys. Rev. Lett.* **95**, 266401 (2005).

[Per84] V. I. Perel, B. P. Zakharchenya. Major physical phenomena in the optical orientation and alignment in semiconductors. In *Optical Orientation*, edited by F. Meier, B. P. Zakharchenya, Modern Problems in Condensed Matter Sciences. Ch. 1, 1–10. Elsevier, Amsterdam/Oxford/New York/Tokyo (1984).

[Pet08] M. Yu. Petrov, I. V. Ignatiev, S. V. Poltavtsev, A. Greilich, A. Bauschulte, D. R. Yakovlev, M. Bayer. Effect of thermal annealing on the hyperfine interaction in InAs/GaAs quantum dots. *Phys. Rev. B* **78**, 045315 (2008).

[Pfa05] S. Pfalz, R. Winkler, T. Nowitzki, D. Reuter, A. D. Wieck, D. Hägele, M. Oestreich. Optical orientation of electron spins in GaAs quantum wells. *Phys. Rev. B* **71**, 165305 (2005).

[Pla01] M. Planck. Ueber das Gesetz der Energieverteilung im Normalspectrum. *Ann. Phys.* **309**, 553 (1901).

[Pol16a] S. V. Poltavtsev, M. Salewski, Yu. V. Kapitonov, I. A. Yugova, I. A. Akimov, C. Schneider, M. Kamp, S. Höfling, D. R. Yakovlev, A. V. Kavokin, M. Bayer. Photon echo transients from an inhomogeneous ensemble of semiconductor quantum dots. *Phys. Rev. B* **93**, 121304 (2016).

[Pol16b] S. V. Poltavtsev, L. Langer, I. A. Yugova, M. Salewski, Yu. V. Kapitonov, D. R. Yakovlev, G. Karczewski, T. Wojtowicz, I. A. Akimov, M. Bayer. Access to long-term optical memories using photon echoes retrieved from electron spins in semiconductor quantum wells. In *Proc. SPIE* 9931, 99311V–99311V–9 (2016).

[Pol16c] S. V. Poltavtsev, M. Salewski, Yu. V. Kapitonov, I. A. Yugova, I. A. Akimov, C. Schneider, M. Kamp, S. Höfling, D. R. Yakovlev, A. V. Kavokin, M. Bayer. Advance and delay effects in photon echo from a highly inhomogeneous ensemble of InGaAs/GaAs quantum dots. In *Proc. of the 24th Int. Symp. "Nanostructures: Physics and Technology"* (2016).

[Pol17a] S. V. Poltavtsev, A. N. Kosarev, I. A. Akimov, D. R. Yakovlev, S. Sadofev, J. Puls, S. P. Hoffmann, M. Albert, C. Meier, T. Meier, M. Bayer. Time-resolved photon echoes from donor-bound excitons in ZnO epitaxial layers. *Phys. Rev. B* **96**, 035203 (2017).

[Pol17b] S. V. Poltavtsev, M. Reichelt, I. A. Akimov, G. Karczewski, M. Wiater, T. Wojtowicz, D. R. Yakovlev, T. Meier, M. Bayer. Damping of Rabi oscillations in intensity-dependent photon echoes from exciton complexes in a CdTe/(Cd,Mg)Te single quantum well. *Phys. Rev. B* **96**, 075306 (2017).

[Pre08] D. Press, T. D. Ladd, B. Zhang, Y. Yamamoto. Complete quantum control of a single quantum dot spin using ultrafast optical pulses. *Nature* **456**, 218 (2008).

[Pri98] G. A. Prinz. Magnetoelectronics. *Science* **282**, 1660 (1998).

[Rae88] H. Raether. *Surface plasmons on smooth and rough surfaces and on gratings.* Springer tracts in modern physics. Springer, Berlin/Heidelberg (1988).

[Ram07] A. J. Ramsay, R. S. Kolodka, F. Bello, P. W. Fry, W. K. Ng, A. Tahraoui, H. Y. Liu, M. Hopkinson, D. M. Whittaker, A. M. Fox, M. S. Skolnick. Coherent response of a quantum dot exciton driven by a rectangular spectrum optical pulse. *Phys. Rev. B* **75**, 113302 (2007).

[Ram10] A. J. Ramsay, T. M. Godden, S. J. Boyle, E. M. Gauger, A. Nazir, B. W. Lovett, A. M. Fox, M. S. Skolnick. Phonon-induced Rabi-frequency renormalization of optically driven single InGaAs/GaAs quantum dots. *Phys. Rev. Lett.* **105**, 177402 (2010).

[Rei14] D. E. Reiter, T. Kuhn, M. Glässl, V. M. Axt. The role of phonons for exciton and biexciton generation in an optically driven quantum dot. *J. Phys.: Condens. Matter* **26**, 423203 (2014).

[Roz15] I. V. Rozhansky, K. S. Denisov, N. S. Averkiev, I. A. Akimov, E. Lähderanta. Spin-dependent tunneling in semiconductor heterostructures with a magnetic layer. *Phys. Rev. B* **92**, 125428 (2015).

[Sal14] M. Salewski, L. Langer, S. V. Poltavtsev, I. A. Yugova, D. R. Yakovlev, G. Karczewski, T. Wojtowicz, I. A. Akimov, M. Bayer. Magnetic field induced oscillations of photon echoes in semiconductor nanostructures. In *Proc. of the 22nd Int. Symp. "Nanostructures: Physics and Technology"*, 172–173 (2014).

[Sal17a] M. Salewski, S. V. Poltavtsev, Yu. V. Kapitonov, J. Vondran, D. R. Yakovlev, C. Schneider, M. Kamp, S. Höfling, R. Oulton, I. A. Akimov, A. V. Kavokin, M. Bayer. Photon echoes from (In,Ga)As quantum dots embedded in a Tamm-plasmon microcavity. *Phys. Rev. B* **95**, 035312 (2017).

[Sal17b] M. Salewski, S. V. Poltavtsev, I. A. Yugova, G. Karczewski, M. Wiater, T. Wojtowicz, D. R. Yakovlev, I. A. Akimov, T. Meier, M. Bayer. High-resolution two-dimensional optical spectroscopy of electron spins. *Phys. Rev. X* **7**, 031030 (2017).

[Sal17c] M. Salewski, N. V. Kozyrev, Yu. V. Kapitonov, S. V. Poltavtsev, I. A. Yugova, E. A. Zhukov, G. Karczewski, M. Wiater, T. Wojtowicz, D. R. Yakovlev, I. A. Akimov, M. M. Glazov, L. E. Golub, M. Bayer. Four-wave mixing and pump-probe Kerr rotation spectroscopy of electron spins in a CdTe/(Cd,Mg)Te quantum well. *In preparation for submission to Phys. Rev. Lett.* (2017).

[Sam78] V. V. Samartsev, R. G. Usmanov, G. M. Ershov, B. S. Khamidullin. Advance and delay effects in photon echo signals. *Sov. Phys. JETP* **47**, 1030 (1978).

[Sap94] V. F. Sapega, T. Ruf, M. Cardona, K. Ploog, E. L. Ivchenko, D. N. Mirlin. Resonant Raman scattering due to bound-carrier spin flip in GaAs/Al_xGa_{1-x}As-GaAs quantum wells. *Phys. Rev. B* **50**, 2510 (1994).

[Sch76] G. Schaack. Observation of circularly polarized phonon states in an external magnetic field. *J. Phys. C: Solid State Phys.* **9**, L297 (1976).

[Sch85] L. Schultheis, M. D. Sturge, J. Hegarty. Photon echoes from two-dimensional excitons in GaAs-AlGaAs quantum wells. *Appl. Phys. Lett.* **47**, 995 (1985).

[Scu97] M. Scully, M. Zubairy. *Quantum Optics.* Cambridge University Press, Cambridge (1997).

[Seb15] K. Sebald, S. S. Rahman, M. Cornelius, J. Gutowski, T. Klein, S. Klembt, C. Kruse, D. Hommel. Tailoring the optical properties of wide-bandgap based microcavities via metal films. *Appl. Phys. Lett.* **107**, 062101 (2015).

[Sha99] J. Shah. *Ultrafast Spectroscopy of Semiconductors and Semiconductor Nanostructures* 115. Springer Series in Solid-State Sciences, New York (1999).

[She84] Y. Shen. *The Principles of Nonlinear Optics.* Wiley-Interscience, New York (1984).

[Sim16] S. Sim, D. Lee, M. Noh, S. Cha, C. H. Soh, J. H. Sung, M.-H. Jo, H. Choi. Selectively tunable optical Stark effect of anisotropic excitons in atomically thin ReS2. *Nature Commun.* **7**, 13569 (2016).

[Sin60] R. N. Sinclair, B. N. Brockhouse. Dispersion relation for spin waves in a fcc cobalt alloy. *Phys. Rev.* **120**, 1638 (1960).

[Sir97] A. A. Sirenko, T. Ruf, M. Cardona, D. R. Yakovlev, W. Ossau, A. Waag, G. Landwehr. Electron and hole g factors measured by spin-flip Raman scattering in CdTe/$Cd_{1-x}Mg_x$Te single quantum wells. *Phys. Rev. B* **56**, 2114 (1997).

[Sla10] M. Sladkov, A. U. Chaubal, M. P. Bakker, A. R. Onur, D. Reuter, A. D. Wieck, C. H. van der Wal. Electromagnetically induced transparency with an ensemble of donor-bound electron spins in a semiconductor. *Phys. Rev. B* **82**, 121308 (2010).

[Son11] C. Song, M. Sperl, M. Utz, M. Ciorga, G. Woltersdorf, D. Schuh, D. Bougeard, C. H. Back, D. Weiss. Proximity induced enhancement of the curie temperature in hybrid spin injection devices. *Phys. Rev. Lett.* **107**, 056601 (2011).

[Sta07] C. D. Stanciu, F. Hansteen, A. V. Kimel, A. Kirilyuk, A. Tsukamoto, A. Itoh, Th. Rasing. All-optical magnetic recording with circularly polarized light. *Phys. Rev. Lett.* **99**, 047601 (2007).

[Ste70] P. J. Stephens. Theory of magnetic circular dichroism. *J. Chem. Phys.* **52**, 3489 (1970).

[Sti01] T. H. Stievater, X. Li, D. G. Steel, D. Gammon, D. S. Katzer, D. Park, C. Piermarocchi, L. J. Sham. Rabi oscillations of excitons in single quantum dots. *Phys. Rev. Lett.* **87**, 133603 (2001).

[Stö06] J. Stöhr, H. Siegmann. *Magnetism: From Fundamentals to Nanoscale Dynamics.* Springer Series in Solid-State Sciences. Springer, Berlin/Heidelberg (2006).

[Sto09] K. W. Stone, K. Gundogdu, D. B. Turner, X. Li, S. T. Cundiff, K. A. Nelson. Two-quantum 2D FT electronic spectroscopy of biexcitons in GaAs quantum wells. *Science* **324**, 1169 (2009).

[Sto10] S. Stobbe, T. W. Schlereth, S. Höfling, A. Forchel, J. M. Hvam, P. Lodahl. Large quantum dots with small oscillator strength. *Phys. Rev. B* **82**, 233302 (2010).

[Str11] D. Strauch. GaAs: lattice parameters. In *New Data and Updates for IV-IV, III-V, II-VI and I-VII Compounds, their Mixed Crystals and Diluted Magnetic Semiconductors*, edited by U. Rössler, 169–172. Springer, Berlin, Heidelberg (2011).

[Str12] D. Strauch. CdTe: lattice parameters. In *New Data and Updates for several III-V (including mixed crystals) and II-VI Compounds*, edited by U. Rössler, 147–149. Springer, Berlin, Heidelberg (2012).

[Sve79] E. Svensson, B. Powell, A. Woods, W.-D. Teuchert. Phonon dispersion in $Co_{0.92}Fe_{0.08}$. *Can. J. Chem.* **57**, 253 (1979).

[Sym13] C. Symonds, G. Lheureux, J. P. Hugonin, J. J. Greffet, J. Laverdant, G. Brucoli, A. Lemaître, P. Senellart, J. Bellessa. Confined Tamm Plasmon Lasers. *Nano Lett.* **13**, 3179 (2013).

[Tah14] H. Tahara, Y. Ogawa, F. Minami, K. Akahane, M. Sasaki. Generation of undamped exciton-biexciton beats in InAs quantum dots using six-wave mixing. *Phys. Rev. B* **89**, 195306 (2014).

[Tru13] K. Truex, L. A. Webster, L.-M. Duan, L. J. Sham, D. G. Steel. Coherent control with optical pulses for deterministic spin-photon entanglement. *Phys. Rev. B* **88**, 195306 (2013).

[Tuc72] J. W. Tucker, V. W. Rampton. *Microwave ultrasonics in solid state physics.* North-Holland, Amsterdam (1972).

[Vah09] K. Vahaplar, A. M. Kalashnikova, A. V. Kimel, D. Hinzke, U. Nowak, R. Chantrell, A. Tsukamoto, A. Itoh, A. Kirilyuk, Th. Rasing. Ultrafast path for optical magnetization reversal via a strongly nonequilibrium state. *Phys. Rev. Lett.* **103**, 117201 (2009).

[Wan12] H. Wang, S. O'Leary. Electromagnetically induced transparency from electron spin coherences in semiconductor quantum wells. *J. Opt. Soc. Am. B* **29**, A6 (2012).

[Wan13] G. Wang, B. L. Liu, A. Balocchi, P. Renucci, C. R. Zhu, T. Amand, C. Fontaine, X. Marie. Gate control of the electron spin-diffusion length in semiconductor quantum wells. *Nature Commun.* **4**, 2372 (2013).

[Web91] M. D. Webb, S. T. Cundiff, D. G. Steel. Observation of time-resolved picosecond stimulated photon echoes and free polarization decay in GaAs/AlGaAs multiple quantum wells. *Phys. Rev. Lett.* **66**, 934 (1991).

[Wei88] S.-H. Wei, A. Zunger. Role of metal d states in II-VI semiconductors. *Phys. Rev. B* **37**, 8958 (1988).

[Wei91] C. Weisbuch, B. Vinter. *Quantum Semiconductor Structures: Fundamentals and Applications*. Academic Press, San Diego (1991).

[Wil10] M. J. Wilson, M. Zhu, R. C. Myers, D. D. Awschalom, P. Schiffer, N. Samarth. Interlayer and interfacial exchange coupling in ferromagnetic metal/semiconductor heterostructures. *Phys. Rev. B* **81**, 045319 (2010).

[Wil15] B. L. Wilmer, F. Passmann, M. Gehl, G. Khitrova, A. D. Bristow. Multidimensional coherent spectroscopy of a semiconductor microcavity. *Phys. Rev. B* **91**, 201304 (2015).

[Wog97] U. Woggon. *Optical Properties of Semiconductor Quantum Dots*. Springer Tracts in Modern Physics. Springer, Berlin/Heidelberg/New York (1997).

[Wol01] S. A. Wolf, D. D. Awschalom, R. A. Buhrman, J. M. Daughton, S. von Molnár, M. L. Roukes, A. Y. Chtchelkanova, D. M. Treger. Spintronics: A spin-based electronics vision for the future. *Science* **294**, 1488 (2001).

[Xia89] J.-B. Xia. Electronic structures of zero-dimensional quantum wells. *Phys. Rev. B* **40**, 8500 (1989).

[Xu08] X. Xu, B. Sun, P. R. Berman, D. G. Steel, A. S. Bracker, D. Gammon, L. J. Sham. Coherent population trapping of an electron spin in a single negatively charged quantum dot. *Nature Phys.* **4**, 692 (2008).

[Yak08] D. R. Yakovlev, M. Bayer. Coherent spin dynamics of carriers. In *Spin Physics in Semiconductors*, edited by M. I. Dyakonov, Springer Series in Solid-State Sciences. Ch. 6, 135–177. Springer, Berlin/Heidelberg (2008).

[Yan07] L. Yang, I. V. Schweigert, S. T. Cundiff, S. Mukamel. Two-dimensional optical spectroscopy of excitons in semiconductor quantum wells: Liouville-space pathway analysis. *Phys. Rev. B* **75**, 125302 (2007).

[Yan16] Y. Yang, M. Yang, K. Zhu, J. C. Johnson, J. J. Berry, J. Van De Lagemaat, M. C. Beard. Large polarization-dependent exciton optical Stark effect in lead iodide perovskites. *Nature Commun.* **7**, 12613 (2016).

[Yu10] P. Y. Yu, M. Cardona. *Fundamentals of Semiconductors: Physics and Materials Properties*. Fourth Edition. Graduate texts in physics. Springer, Heidelberg/Dordrecht/London/New York (2010).

[Yug09] I. A. Yugova, M. M. Glazov, E. L. Ivchenko, Al. L. Efros. Pump-probe Faraday rotation and ellipticity in an ensemble of singly charged quantum dots. *Phys. Rev. B* **80**, 104436 (2009).

[Zai10] S. V. Zaitsev, M. V. Dorokhin, A. S. Brichkin, O. V. Vikhrova, Yu. A. Danilov, B. N. Zvonkov, V. D. Kulakovskii. Ferromagnetic effect of a Mn delta layer in the GaAs barrier on the spin polarization of carriers in an InGaAs/GaAs quantum well. *JETP Lett.* **90**, 658 (2010).

[Zak82] B. P. Zakharchenya, D. N. Mirlin, V. I. Perel, I. I. Reshina. Spectrum and polarization of hot-electron photoluminescence in semiconductors. *Sov. Phys. Usp.* **25**, 143 (1982).

[Zak05] B. P. Zakharchenya, V. L. Korenev. Integrating magnetism into semiconductor electronics. *Phys. Usp.* **48**, 603 (2005).

[Zha05] T. Zhang, C. N. Borca, X. Li, S. T. Cundiff. Optical two-dimensional Fourier transform spectroscopy with active interferometric stabilization. *Opt. Express* **13**, 7432 (2005).

[Zha07] T. Zhang, I. Kuznetsova, T. Meier, X. Li, R. P. Mirin, P. Thomas, S. T. Cundiff. Polarization-dependent optical 2D Fourier transform spectroscopy of semiconductors. *Proc. Natl. Acad. Sci.* **104**, 14227 (2007).

[Zhu07] E. A. Zhukov, D. R. Yakovlev, M. Bayer, M. M. Glazov, E. L. Ivchenko, G. Karczewski, T. Wojtowicz, J. Kossut. Spin coherence of a two-dimensional electron gas induced by resonant excitation of trions and excitons in CdTe/(Cd,Mg)Te quantum wells. *Phys. Rev. B* **76**, 205310 (2007).

[Zre02] A. Zrenner, E. Beham, S. Stufler, F. Findeis, M. Bichler, G. Abstreiter. Coherent properties of a two-level system based on a quantum-dot photodiode. *Nature* **418**, 612 (2002).

List of Figures

1.1 Crystal structure and first Brillouin zone 8
1.2 Band structure for a bulk crystal 9
1.3 Band structure for a quantum well 11
1.4 Scanning electron microscope image of quantum dots 12
1.5 3D representation of a quantum mechanical two-level system 14
1.6 Dipole moments between the heavy hole valence and conduction bands . . 16
1.7 Exciton complexes 18

2.1 Grating picture of transient four-wave mixing 24
2.2 Principle of the photon echo 26
2.3 Double-sided Feynman diagrams 27
2.4 Principle of two-dimensional rephasing spectra for the two-level system . . 28
2.5 Principle of two-dimensional Raman coherence spectroscopy 29

3.1 Ferromagnetism 36
3.2 Dispersion relation of magnons and TA phonons 37

4.1 Characterization of the picosecond laser pulses 42
4.2 PL setup 43
4.3 Pump-probe Kerr rotation setup 45
4.4 FWM setup 47
4.5 Dual delay scan 48

5.1 Sample information about the Co-CdTe hybrid 52
5.2 Co-CdTe hybrid band structure 53
5.3 FM induced proximity effect 54
5.4 Co-CdTe time-resolved spin dynamics 56
5.5 FM-induced spin polarization of the QW heavy holes bound to acceptors 57
5.6 Hanle and “inverted” Hanle effect 59
5.7 Modulation parameter 60
5.8 Temperature dependence of the proximity effect 62
5.9 Magneto-optical Kerr effect 63
5.10 Proximity effect as function of the Co thickness 64
5.11 Circular polarization in a big magnetic field range 65

5.12 Magnetic circular dichroism 66
5.13 Illustration of a circularly polarized phonon mode 67
5.14 Phonon a.c. Stark effect 68

6.1 Sample information about the InGaAs QDs inside the Tamm structure . . 74
6.2 Sample information about the InGaAs QDs inside the DBR structure . . 75
6.3 Photon echoes from the TP structure 76
6.4 Rabi-oscillations from PPE for variation of the second pulse 77
6.5 Rabi-oscillations from SPE for variation of the second and third pulse . . 79
6.6 Photon echoes from the DBR structure 80
6.7 Coherent dynamics from the TP structure 81
6.8 TRPL from the TP structure 82
6.9 Measured and calculated Rabi oscillations from the first pulse 84
6.10 Theory of the PE temporal profile as function of the first pulse 86
6.11 Explanation of the PE timing modifications using the Bloch sphere 87
6.12 Simulations of 2DFTS for strong inhomogeneous broadening 89

7.1 Optical selection rules for the four-level system 93
7.2 Double-sided Feynman diagrams for the four-level system. 95
7.3 Calculated 2DFS rephasing spectra 98
7.4 Calculated 2DFS Raman spectra 99
7.5 Sample information about the CdTe QW 101
7.6 Photon echoes from the CdTe QW 102
7.7 Spectral dependence of the FWM transients at $B = 0$ 103
7.8 Spectral dependence of the FWM decay rates 104
7.9 Magnetic field dependence of the SPE 105
7.10 Spectral dependence of the SPE transients in a magnetic field 106
7.11 Spectral dependence of the Kerr rotation transients in a magnetic field . . 107
7.12 Comparison of the pump-probe and FWM results 108

8.1 Summary of the main results 112

List of publications

1. Access to long-term optical memories using photon echoes retrieved from semiconductor spins,

   L. Langer, S. V. Poltavtsev, I. A. Yugova, **M. Salewski**, D. R. Yakovlev, G. Karczewski, T. Wojtowicz, I. A. Akimov, and M. Bayer,

   Nature Photon. **8**, 851–857, 2014.

2. Long-range p-d exchange interaction in a ferromagnet-semiconductor hybrid structure,

   V.L. Korenev, **M. Salewski**, I. A. Akimov, V. F. Sapega, L. Langer, I. V. Kalitukha, J. Debus, R. I. Dzhioev, D. R. Yakovlev, D. Müller, C. Schröder, H. Hövel, G. Karczewski, M. Wiater, T. Wojtowicz, Yu. G. Kusrayev, and M. Bayer,

   Nature Phys. **12**, 85–91, 2016.

3. Photon echo transients from an inhomogeneous ensemble of semiconductor quantum dots,

   S.V. Poltavtsev, **M. Salewski**, Yu. V. Kapitonov, I. A. Yugova, I. A. Akimov, C. Schneider, M. Kamp, S. Höfling, D. R. Yakovlev, A. V. Kavokin, and M. Bayer,

   Phys. Rev. B **93**, 121304, 2016.

4. Photon echoes from (In,Ga)As quantum dots embedded in a Tamm-plasmon microcavity,

   M. Salewski, S. V. Poltavtsev, Yu. V. Kapitonov, J. Vondran, D. R. Yakovlev, C. Schneider, M. Kamp, S. Höfling, R. Oulton, I. A. Akimov, A. V. Kavokin, and M. Bayer,

   Phys. Rev. B **95**, 035312, 2017.

5. High-resolution two-dimensional optical spectroscopy of electron spins,

   M. Salewski, S. V. Poltavtsev, I. A. Yugova, G. Karczewski, M. Wiater, T. Wojtowicz, D. R. Yakovlev, I. A. Akimov, T. Meier, and M. Bayer,

   Phys. Rev. X **7**, 031030, 2017.

6. Direct measurement of the long-range p-d exchange coupling in a ferromagnet-semiconductor Co/CdMgTe/CdTe quantum well hybrid structure,

   I. A. Akimov, **M. Salewski**, I. V. Kalitukha, S. V. Poltavtsev, J. Debus, D. Kudlacik, V. F. Sapega, N. E. Kopteva, E. Kirstein, E. A. Zhukov, D. R. Yakovlev, G. Karczewski, M. Wiater, T. Wojtowicz, V. L. Korenev, Yu. G. Kusrayev, and M. Bayer,

   Phys. Rev. B **96**, 184412, 2017.

Conference contributions

2013-03 Regensburg, Germany. DPG Spring Meeting, contributed talk *Polariton condensates in GaAs-based microcavities: influence of the spot size.*

2013-07 Cluij-Napoca, Romania. 3rd Workshop on Nanoscale Spin and Charge Dynamics, contributed talk and poster *Magnetic-field induced oscillations of spontaneous and stimulated photon echoes from the electron-trion system.*

2013-11 Paderborn, Germany. Graduiertenkolleg 1464, contributed talk *Long-lived stimulated photon echoes from semiconductor nanostructures in a magnetic-field.*

2014-03 Dresden, Germany. DPG Spring Meeting, contributed talk *Photon echoes from CdTe quantum wells in a magnetic-field*

2014-06 Saint Petersburg, Russia. 22nd International Symposium - Nanostructures: Physics and Technology, contributed talk *Magnetic field induced oscillations of photon echoes in semiconductor nanostructures.*

2014-08 Konstanz, Germany. 2nd School and conference on Spin-based quantum information processing, contributed poster *Magnetic field induced oscillations of photon echoes in semiconductor nanostructures.*

2014-09 Bremen, Germany. NOEKS 12, contributed poster *Rabi-oscillations of photon echo in (In,Ga)As quantum dots.*

2014-11 Bad Sassendorf, Germany. 1st internal workshop of the SFB/TRR 142, contributed talk *Coherent spectroscopy of excitons and trions in CdTe quantum wells.*

2015-03 Berlin, Germany. DPG Spring Meeting, contributed poster *Rabi oscillations of photon echo in (In,Ga)As quantum dots.*

2015-05 Bad Sassendorf, Germany. 2nd internal workshop of the SFB/TRR 142, contributed talk *Time-resolved four-wave mixing spectroscopy in CdTe quantum wells.*

2015-10 Jerusalem, Israel. OECS 2015, contributed talks *Photon echo from quantum dots in Tamm-plasmon microcavity* and *Long-range p-d exchange interaction in a ferromagnet-semiconductor hybrid structure.*

2015-10 Nijmegen, The Netherlands. UMC 2015, contributed poster *Magnetic field induced oscillations of photon echoes in semiconductor nanostructure.*

2016-03 Regensburg, Germany. DPG Spring Meeting, contributed talk *Long-range p-d exchange interaction in a ferromagnet- semiconductor hybrid structure.*

2016-06 Saint Petersburg, Russia. 24th International Symposium - Nanostructures: Physics and Technology, contributed poster *Photon echo from quantum dots in Tamm-plasmon microcavity.*

2016-10 Dortmund, Germany. NOEKS 13, contributed poster *Photon echo from InGaAs quantum dots embedded in Tamm-plasmon microcavity.*

2017-07 Würzburg, Germany. PLMCN18, contributed posters *Photon echoes from (In,Ga)As quantum dots embedded in a Tamm-plasmon microcavity* and *High resolution two-dimensional optical spectroscopy of electron spins in a n-type CdTe quantum well.*

2017-10 Saint Petersburg, Russia. Excitons in crystals and nanostructures, contributed posters *Long-range p-d exchange interaction in a ferromagnet-semiconductor Co/CdMgTe/CdTe quantum well hybrid structure* and *Photon echoes from exciton complexes in CdTe/(Cd,Mg)Te quantum well structures.*

Acknowledgments

This work was created in the research group Experimentelle Physik 2 headed by Prof. Dr. Manfred Bayer. It is largely thanks to him that I had the chance to meet so many wonderful people and great scientists from the Russian Federation. I was lucky to be part of the International Collaborative Research Center TRR 160, bringing together researchers from the Technische Universität Dortmund, the Ioffe Physical-Technical Institute, and the State University in St. Petersburg.

I would like to thank my supervisor PD Dr. Ilya A. Akimov. He has an unerring sense for interesting and fruitful research projects and it is very pleasant to work with him. Especially, I want to thank him for sending me to the conference on ultrafast magnetism in Nijmegen 2015 where I met my future wife Anna.

I had the pleasure to work together with Dr. Sergey V. Poltavtsev on photon echoes. Building an highly complex experimental setup, measuring on it, and analyzing the data with an almost childish enthusiasm, Sergey became my mentor and friend. I also remember with a smile the lab time hand in hand with Dr. Lukas Langer, explaining me our experiment by the runners in a stadium. In 2015 Dr. Yury V. Kapitonov joined our echo team, and soon Sasha N. Kosarev will start his PhD in Dortmund. They are all great people and I am happy to know them.

The second big project for this thesis developed in collaboration with Prof. Dr. Volodya L. Korenev and Ina V. Kalitukha. Working in a "TU-Ioffe hybrid" on ferromagnets and semiconductors was always nice and I learned a lot from, and with them.

I will never forget the time as a PhD student in St. Petersburg. Starting in 2014 with the touristic support of my dear colleague Prof. Dr. Zhenia A. Zhukov (born in Moscow!), I could visit "Piter" until now already six times. Special pleasure was my in total four-month research exchange, working under the supervision of Prof. Dr. Vladimir K. Kalevich in the group of Prof. Dr. Yury G. Kusrayev at the Ioffe institute. In particular, I remember the interesting measurements together with Erik Kirstein and Nikolay V. Kozyrev, and of course, the "Wohngemeinschaft" together with Felix Spitzer, Dion Braukmann, and Janina Rautert. I thank you all very much for the wonderful time, not only in the "Ulitsa Butlerova 40" but also being colleagues in Dortmund and providing me with many useful advices in various aspects.

In this context, I want to thank Dr. Steffen Varwig, Dr. Fabian Heisterkamp, and Dr. Johannes Schmutzler who became good friends, Johannes Thewes and Johannes Mund, Daniel Schmidt, Jonas Vondran, Dennis Kudlacik, Janina Schindler, Dr. Marco Lafrenz,

Dr. Martin Pohl, Dr. Benjamin Siebers, Jun.-Prof. Dr. Marc A. Aßmann, Dr. Jörg Debus, and many others. Special thanks to Dr. Lars Erik Kreilkamp, Dr. Sebastian Tempel, Dr. Franziska Wishahi, and Markus Kuhnert for the great time together in the old building's office. I am grateful to Lars Wieschollek and Klaus Wiegers for vast amounts of helium and technical support, and to Michaela Wäscher and Nina Collette for their great patience with me, when I struggled with placing orders or filling out the SAP.

In particular I want to thank Dr. Vasilii Belykh, Dr. Elena Kozhemyakina, Alexey Danilov, Pavel Sokolov, and Dr. Alex Greilich for speaking with so much patience russian with me in Dortmund. I owe the fact that this is possible to Prof. Dr. Dima R. Yakovlev's initiative and most of all, my dedicated teacher Luba A. Yakovleva. I also want to acknowledge Sergey Nekrasov's and Misha Petrov's contribution during the time they had been my guests in Witten.

Finally, I want to thank Anna, my parents Susanne and Kurt, my sister Lara, and my grandfather Franz-Josef for their love and support in every moment of my life.